The University of Sheffield
Faculty of Engineering
Department of Electronic & Electrical Engineering

Experimental Analysis, Modelling and Optimisation of Large Scale Lithium-ion Batteries

---

A thesis submitted in partial fulfilment of the requirements for the degree of Doctor of Philosophy

T. L. Fantham

2021

The University of Sheffield

Faculty of Engineering

Department of Electronic & Electrical Engineering

Experimental Analysis, Modelling and Optimisation of Large Scale Lithium-ion Batteries

---

A thesis submitted in partial fulfilment of the requirements for the degree of Doctor of Philosophy

Thomas Louis Fantham
September 2021

Abstract

Globally, there is a substantial increase in the use of large batteries. One key application of these is grid-connected batteries. To maximise revenue, it is important that the full capacity of the battery is used. To achieve this, an operator must be confident of the capability of a battery at any given time.

For grid-connected batteries consisting of upwards of tens of thousands of cells, this can be challenging. This is because the cells all behave slightly differently due to manufacturing tolerances, with effects combining to give the observed output behaviour. Two main model-based approaches for these large batteries are observed in literature - a cell model for each cell, or modelling the battery with a single cell model. The former results in high computation demand while the latter is less accurate, ignoring the cell behaviour.

This thesis investigates the means for maximising the useable capacity of a large battery, through the consideration of cell level behaviour. This behaviour is demonstrated experimentally using a 2MW/1MWh system, with the behaviour examined through rigorous testing at the lab scale. A new model is proposed which considers nine cell models to represent a large battery to achieve accurate estimation. This is validated and shown to be computationally efficient while giving cell-level detail. A method is then explored to identify model parameters for cells within a large battery, which is successful at parameterising a model to match a physical system. It is demonstrated using 1584 cells in-situ, showing the variance of capacity and impedance in a large battery. The model and parameter identification method are then combined to produce an online state estimator to estimate key battery metrics in real-time, considering cell behaviour. The observations and methodologies presented thus far are then applied to consider maximising the capacity of a grid-connected battery. It is shown through simulation that choosing an appropriate SoC at which to perform cell voltage equalisation can increase the capacity, and that this is dependant on the cell parameter variance. Additionally, it is shown that rearranging modules in a large system based on temperature can further improve the system capacity. This can be as high as 5% depending on the capacity variance.

List of Publications

Parts of the work presented in this thesis have been reported in the following internationally-respected publications:

Published

T. L. Fantham and D. T. Gladwin, "Impact of cell balance on grid scale battery energy storage systems," in *Energy Reports*, 2020, vol. 6 supp. 5, pp209-216, http://dx.doi.org/10.1016/j.egyr.2020.03.026.

T. L. Fantham and D. T. Gladwin, "An overview of safety for laboratory testing of lithium-ion batteries" in *Energy Reports*, 2020, vol. 7 supp. 2, pp2-8, http://dx.doi.org/10.1016/j.egyr.2021.03.004.

H. Alnuman, D. T. Gladwin, M. P. Foster and **T. L. Fantham**, "Adaptive Control Method to Manage SOC for Energy Storage in DC Electric Railways," *IECON 2019 - 45th Annual Conference of the IEEE Industrial Electronics Society*, 2019, pp. 261-266, doi: 10.1109/IECON.2019.8927602.

Submitted for Review

T. L. Fantham and D. T. Gladwin, "In-situ Parameter Identification of Cells in Grid-Connected Batteries" in *IECON2021 - 47th Annual Conference of the IEEE Industrial Electronics Society*

Z. Wang, D. T. Gladwin, M. J. Smith and **T. L. Fantham**, "Data-selection for state estimation of large-scale battery system" in *IECON2021 - 47th Annual Conference of the IEEE Industrial Electronics Society*

T. L. Fantham and D. T. Gladwin, "A fast variance based Grid Scale Battery Model" in *Journal of Power Sources*

Manuscripts in Preparation

T. L. Fantham and D. T. Gladwin, “Online parameter estimation for grid connected batteries” in *2022 IEEE 31st International Symposium on Industrial Electronics*

Acknowledgements

I extend sincere gratitude to my supervisor and mentor, Dan Gladwin for his support and encouragement throughout the course of my PhD.

I would like to give much thanks to my family for their kindness, moral support and understanding, particularly when the end was seemingly always one month away. To my wife, who particularly practically supported me during the writing period and showed much love and grace.

A big thank you must go to all of my colleagues at the University of Sheffield, both in the Energy Storage CDT and CREESA, it has been a joy and pleasure working with you all during the past years.

Finally, I would like to gratefully acknowledge support from the EPSRC via grant EP/L016818/1 which funds the Centre for Doctoral Training in Energy Storage and its Applications (CDT-ESA), and Siemens for funding this PhD through the CDT-ESA.

Contents

List of Figures

List of Tables

Nomenclature

9CM 9 Cells Model.

ACM All Cells Model.

BESS Battery Energy Storage Systems.

BM Balancing Mechanism.

BMS Battery Management System.

CC Constant Current.

CCCV Constant Current, Constant Voltage.

CE Coulombic Efficiency.

CPE Cell-level Parameter Estimator.

CV Constant Voltage.

DCIR DC Internal Resistance.

DFR Dynamic Firm Frequency Response.

DoD Depth-of-Discharge.

ECM Equivalent Circuit Model.

EIS Electrochemical Impedance Spectroscopy.

EKF Extended Kalman Filter.

ESA Electrode-Separator Assembly.

ESO Electricity System Operator.

ESS Energy Storage System.

EV Electric Vehicle.

FFR Firm Frequency Response.

GB Great Britain.

HGV Heavy Goods Vehicle.

HPPC Hybrid Pulse Power Characterization.

HVAC Heating, Ventilation and Air Conditioning.

NGESO National Grid Electricity System Operator.

OCV Open Circuit Voltage.

P2D Pseudo-2D.

RC Resistor-Capacitor.

SCiB Super Charge ion Battery.

SCM Single Cell Model.

SoC State-of-Charge.

SoH State-of-Health.

SoP State-of-Power.

TUoS The University of Sheffield.

WESS Willenhall Energy Storage System.

List of Symbols

Symbol	**Description**	**Unit**
C	Capacity or 1-hour discharge rate	-
Q	Electrical Charge	C
R_0	Ohmic Resistance	Ω
R_{DCIR}	DC Internal Resistance	Ω
R_{CT}	Charge Transfer Resistance	Ω
R_P	Polarisation Resistance	Ω
T	Temperature	°C
V_{OCV}	Open Circuit Voltage	V

Chapter 1

Introduction

1.1 Motivation

Globally, there is a push to reduce greenhouse gas emissions and limit global warming to below 1.5°C, with The Paris Agreement [21] being adopted by 196 parties. This agreement is rapidly increasing the penetration of renewable energy sources on electricity grids. To best use this clean energy, Lithium-ion batteries are seen as a way for storing energy for many applications, particularly where fossil fuels are traditionally used.

As such, the production of Lithium-ion batteries is rapidly increasing, set to triple between 2020 and 2025, from 455GWh in 2020 to 1,447GWh in 2025, shown in figure 1.1.

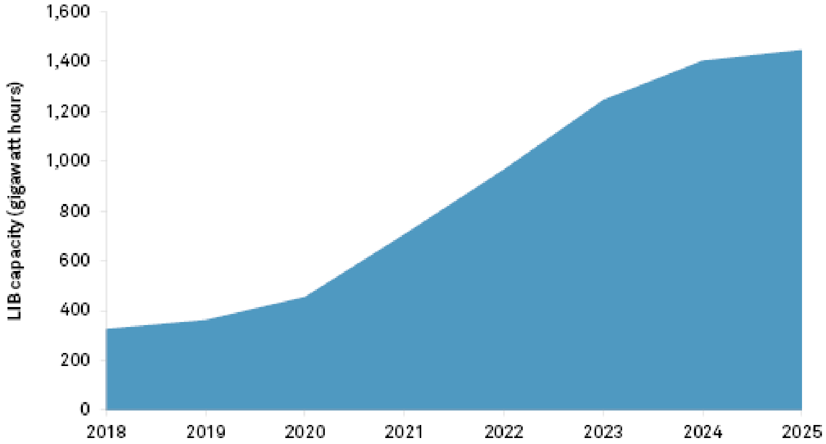

Figure 1.1: Global predicted Lithium-ion battery capacity production [1].

Meanwhile, according to Benchmark Mineral Intelligence, the price for Lithium ion batteries has been dropping, from approximately 300\$/kWh to approaching 100\$/kWh at the end of 2020 [22]. There appears to be two main drivers for this - Electric Vehicles (EVs) and grid-connected Battery Energy Storage Systems (BESS).

Globally, EV sales are expected to triple between 2020 and 2025 and a similar story is seen with grid-connected BESS, with the global installed capacity set to reach 135GW in 2030, from 8.5GW in 2020 [23].

These applications are both for large battery packs, with an EV battery pack consisting of hundreds to thousands of cells [24,25]. and upwards of tens of thousands in a large grid-connected BESS [26]. These can be even larger when using smaller cells in these large packs, such as the cylindrical 2170 cell which is used in the Hornsdale Power Reserve - a 100MW/129MWh BESS built by Tesla [27,28]. With a cell capacity of 17.3Wh, it can be estimated that the system consists of 7.5 million cells.

It can be challenging to estimate the energy stored in a large pack such as these at any given moment - it is however important. With EVs, it is obvious that being depleted of charge unexpectedly is problematic, as it results in the vehicle occupants becoming stranded, resulting in a costly tow or call-out.

Similarly, it is costly when the same happens with grid-connected BESS. When trading on the Great Britain (GB) electricity grid, an amount of energy is bid in advance, to be delivered in a specified half-hour period. Failure to deliver the energy results in extra charges, in the form of the shortfall in energy being charged at the Balancing Mechanism (BM) rate, which is likely to be high. Naturally, this is undesirable for a BESS owner/operator, and would be caused by poor estimation of the battery states. For a system consisting of a single cell, this could be a fairly simple fix, by adjusting the expected capacity of the battery to correct the SoC estimation. For a large battery, however, there are many thousands of cells to consider, which all interact and contribute to the output behaviour.

Being able to understand and estimate this output behaviour to maximise capacity is a key aspect to maximising profitability for grid-connected storage, which this thesis considers.

1.2 Thesis Contributions

This thesis presents five research chapters which consider cell level behaviour to develop modelling, estimation and optimisation of large packs. The first three chapters detail a novel model for a large pack, with a focus on electricity grid applications. The final two chapters then use the findings to propose state estimation and optimisation of large packs.

Investigation into Cell Voltage Imbalance in Grid-Connected Batteries

The cells that form a grid-connected battery have small variations between them, resulting in a deviation in cell voltages under cycling. This chapter presents cycles observed from a grid-connected battery, focusing on the trends of these cell voltage deviations for the first time. Lab scale experiments are performed, recreating the cycles from the larger system, showing the cell level data and providing detail of how cell voltages interact in a large pack. The results presented verify assumptions that are used when modelling large packs and sets the requirements for the model and subsequent online parameter estimator.

A fast variance based Grid Scale Battery Model

Two methods are seen in literature to model large packs - represent the pack with a single cell model, or represent the pack with a cell model for every cell. The former is computationally efficient and suitable for real-time applications but lacks cell level detail, whilst the latter possesses the detail, yet due to the model size, is unsuitable for real-time applications. Thus, a novel model is presented which represents any sized pack using up to nine cell-models. This is then verified experimentally with two lab scale tests, and a method for identifying parameters for a large sample of cells is evaluated.

In-situ Parameter Identification of cells in Grid Connected batteries

To identify parameters for the model introduced in the previous chapter, ideally, every cell in the pack should have its parameters identified. Typically, this requires dismantling a pack and performing a parameter identification test on every cell. For a grid-connected pack, with upwards of tens of thousands of cells, this would take an enormous amount of time. Therefore, this chapter presents a method for identifying the parameters for cells within a large pack in-situ. The method is demonstrated through rigorous experimentation on two systems, where it is shown to be effective. The results show that compensating for cell temperature significantly improves the accuracy of the parameters. For the larger system used for demonstration, it was shown that there can be as much as 4°C difference in temperature between cells in a string, highlighting the need for this.

Online parameter estimation for grid connected batteries

The State-of-Charge (SoC) and State-of-Power (SoP) define the energy and power management for a grid-connected battery, and confident estimates of these are crucial for maximising use and revenue of such systems. With packs consisting of upwards of tens of thousands of cells, there are many variables which are contributing factors to that estimate. This chapter combines the outcomes of the investigation into cell voltages in a large pack from chapter 4, the computationally efficient and accurate model from chapter 5 and the parameter identification procedure from chapter 6 to define a new open-loop state estimator for SoC, SoP and State-of-Health (SoH). The estimator considers both cell temperature and voltage in real-time to provide an accurate measure for the three states. This is a significant step forward in estimation for large BESS, giving confidence to push a battery to it's operating limits.

Optimising energy storage capability of grid connected batteries
Once a BESS system is commissioned, there are few changes which can be easily made to improve performance of the system. This chapter uses findings and techniques from the previous three chapters to evaluate two methods for minimising the cell voltage imbalance to maximise cell utilisation. It is shown with simulation and experimentation that when using passive balancing techniques, the SoC at which cell voltage equalisation is performed can affect the overall system capacity. The point at which it is best to balance is highly system dependant, but the chapter explains the principles behind optimising cell voltage equalisation to maximise system capacity. Secondly, optimally arranging modules by capacity in a pack to maximise system capacity is shown to be effective through simulation, using the previously gathered experimental parameters. This is in agreement with other work. Further to this, it is shown for the first time using simulation that arranging the poorest performing cells into the warmest areas of the battery can give a further improvement to the overall capacity of the system.

Chapter 2

Background

The work proposed in this project considers the use of large battery packs consisting of lithium-ion cells and how cells of slightly differing performance behave in a pack. This chapter consists of two main sections - the first provides an overview of the lithium-ion cell technology as a means to understand the cause of these performance differences. The second gives a view of large battery packs as a whole, considering their use and behaviour.

2.1 Lithium-ion Battery Cells

According to a report, annual production capacity of lithium-ion cells is estimated at 455 GWh/yr, with this being expected to increase to 1447 GWh/year in 2025 [1]. This section aims to give a broad overview of these cells, including the physical attributes, modelling and diagnostics of these cells.

2.1.1 Physical Attributes

Considering the physical attributes, the following section aims to give a background in the chemistry, packaging and manufacture of lithium-ion cells. The purpose of this is to give an insight into the results that are later presented, providing sound reasoning for trends observed, particularly for cell voltage imbalance.

2.1.1.1 Chemistry

Secondary (rechargeable) lithium-ion cells consist of Li^+ ions moving through an electrolyte between two electrodes. The lithium ions then intercalate into the cathode or anode depending on whether it is being charged or discharged as shown in the figure 2.1 below. [2]

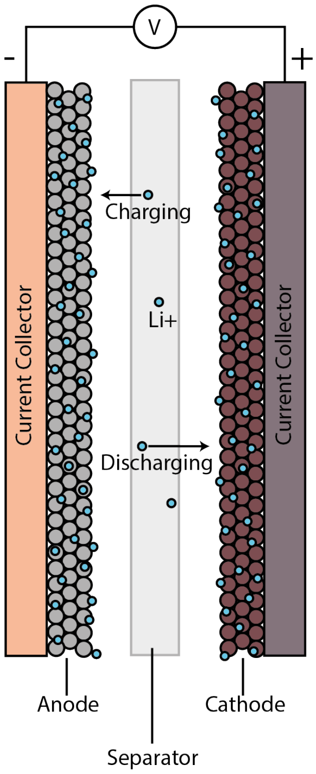

Figure 2.1: Movement of Li^+ ions in a lithium-ion Cell (adapted from [2])

The anode (negative electrode) typically contains graphite or another form of carbon. Other anode materials include Lithium Titanate (LTO) and silicon. [29] The cathode (positive electrode) material generally has more variation, where typical materials include: Lithium Cobalt Oxide (LCO), Lithium Nickel Cobalt Manganese Oxide (NMC), Lithium Nickel Cobalt Aluminum Oxide (NCA) and Lithium Iron Phosphate (LFP) [29]. The voltage of a cell occurs due to the difference in potential between the anode and cathode. Combining different anode and cathode materials gives a range of characteristics, with some typical combinations shown in table 1, presented by Burke et al [20]. Despite the differing characteristics, they generally behave in a similar way in terms of charge and discharge behaviour, which can be seen in figure 2.2.

Chemistry Anode / Cathode (Common Name)	**Cell Voltage / V Max / nominal / min (typical)**	**Capacity Density / Ah/g Anode/Cathode**	**Energy Density Wh/kg**	**Cycle life (deep)**	**Thermal stability**
Graphite/ NiCoMnO2 (NMC)	4.2/3.6/2.5	0.36/0.18	100-170	2000-3000	fairly stable
Graphite/ Mn spinel (LMO)	4.0/3.6/3.0	0.36/0.11	100-120	1000	fairly stable
Graphite/ NiCoAlO2 (NCA)	4.2/3.6/3.0	0.36/0.18	100-150	2000-3000	least stable
Graphite/ FePO4 (LFP)	3.65/3.25/2.0	0.36/0.16	90-115	>3000	stable
Lithium titanate/ Mn spinel (LTO)	2.8/2.4/1.5	0.18/0.11	60-75	>5000	most stable

Table 2.1: Properties of common Li-ion battery chemistries. (adapted from [20])

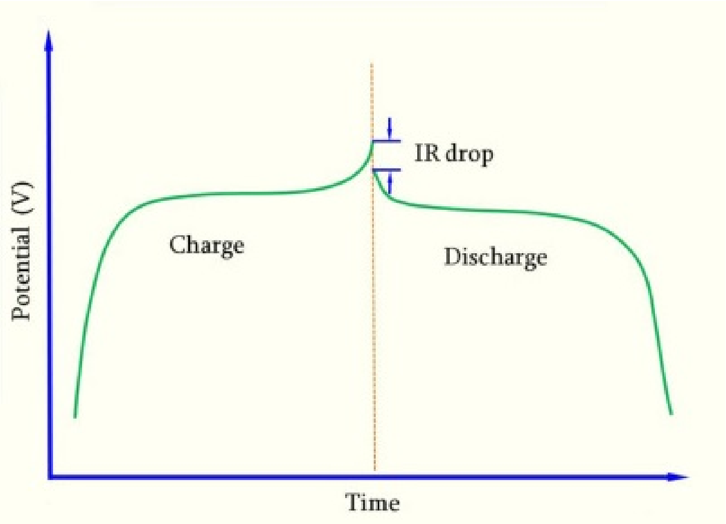

Figure 2.2: Typical charge and discharge curve in a lithium-ion battery where IR drop is the drop in voltage due to internal resistance. (adapted from [3])

The charge and discharge curves both have relatively flat portions in the middle part of the cycle, and a steep curve towards high and low states of charge. It can also be seen that the shapes are virtually the same, but the charge curve is shifted higher and the discharge curve is shifted lower due to the voltage drop from the impedance.

The reason for the curve shape in figure 2.2 is due to the chemical processes occurring in the battery related to the way in which lithium intercalates into the electrodes, where one electrode has an abundance of lithium and the other very little towards the end of charge or discharge.

The figure also shows an IR drop - a drop in voltage due to internal resistance. All lithium-ion batteries demonstrate this property and the amount of voltage drop corresponds to the current draw of the battery and the internal resistance. A higher current draw or higher internal resistance will result in a larger voltage drop [3], demonstrated in figure 2.3

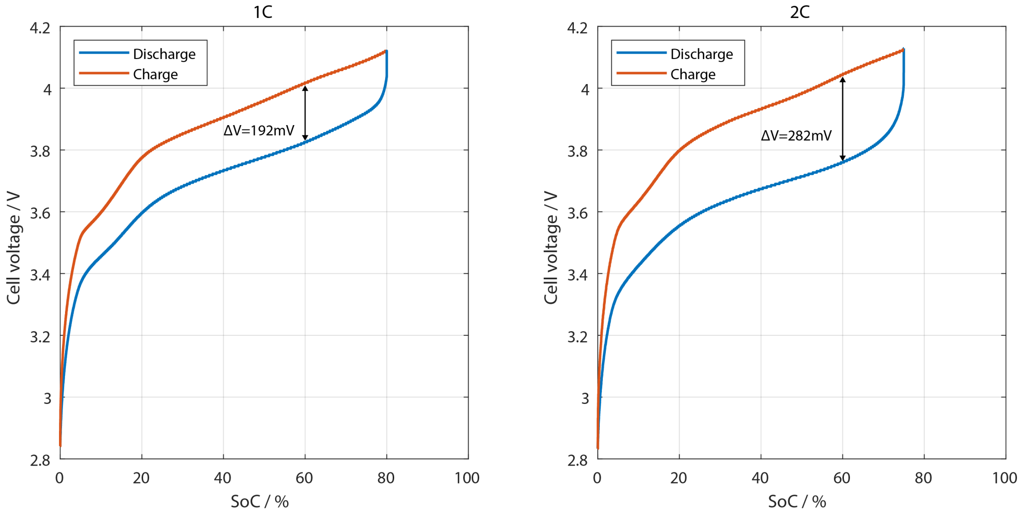

Figure 2.3: Charge/Discharge voltage vs SoC at 1C or 2C (50A or 100A) in LIM50E cells. Experimental data from Chapter 6.

2.1.1.2 Cell Packaging

Lithium-ion cells are commercially produced in a large variety of packages [30], all of which can give slightly different properties to other cells of identical chemistry [31]. These can be separated into categories as follows:

Coin / button

These are small cells that are used to power small devices such as hearing aids, watches, etc. Figure 2.4 shows a diagram of a coin cell. They are too small for use in grid scale storage and so will not be considered further.

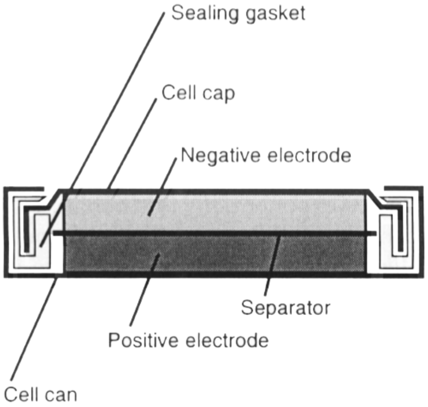

Figure 2.4: Coin / button cell construction [4]

Cylindrical

Cylindrical cells are shaped in a cylinder as the name suggests. The electrodes are wrapped around a central core as per figure 2.5.

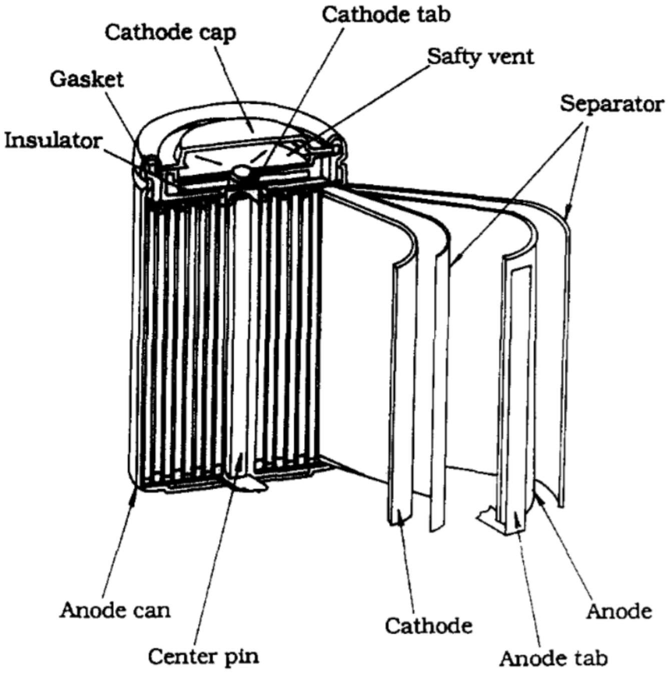

Figure 2.5: Cylindrical Cell Construction [5]

These are named by their width and height - the first two numbers are the diameter in mm and the last three are the height in mm to one decimal place. i.e. 18650 = 18mm diameter, 65.0mm height [32].

They typically also have a safety device built in which has two main purposes. It firstly vents gas if pressure builds up in the cell and disconnects the positive terminal permanently should the pressure threshold be exceeded. This helps to prevent dangerous failure of the cells [5]. Battery safety is a concern [33], so having a safety mechanism is highly desirable in a cell.

Cylindrical cells generally have the highest energy and power densities out of all the cell packaging types [34]. This is as they are generally wound more tightly and are more compacted, giving both better chemical performance and a greater volumetric density.

However, when grouped in a module, their geometric shape limits them as they cannot perfectly pack together. This can negate their improved density over other packaging types.

Prismatic / Pouch Cells

Prismatic and pouch cells are cuboid shaped cells. The difference between them is that the prismatic cells are in a sealed container, where part of that container contains conductive parts attached to the electrodes as the battery terminals. In Pouch cells, tabs are welded to the electrodes and pass through the container into the battery while maintaining a seal.

The electrodes are generally either wound flat or folded back and forth, as shown in figure 2.6.

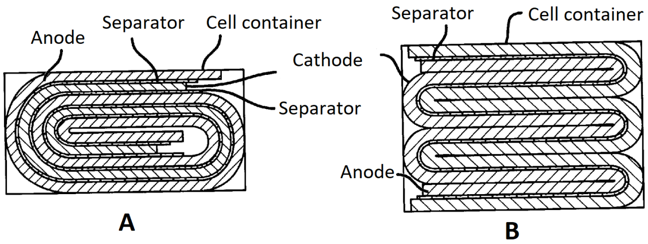

Figure 2.6: Prismatic cell electrode stacking - A: wound flat, B: folded back and forth. (adapted from [6])

As mentioned before, these are not as energy dense as cylindrical type cells, as the electrodes cannot physically be packed as tightly together. However, due to their cuboid shape, they pack much more efficiently when arranged in a module, potentially giving a greater energy density when connected in a pack.

2.1.1.3 Manufacture

With a basic understanding of cell chemistry, it is also important to understand how cells are manufactured. This will give key insights into the factors that impact the capacity, impedance, and other parameters from a manufacturing perspective.

It has been noted that differences in electrical parameters between cells is due to manufacturing tolerances. Lithium-ion battery cells are produced in a long and complex process with many steps where each step introduces the possibility of a difference in the electrical behaviour between cells. Figure 2.7 shows a general manufacturing process for lithium ion cells (based on work presented in [7, 35, 36]) and considers the impact of each step on electrical parameters (i.e. voltage, capacity, impedance, degradation).

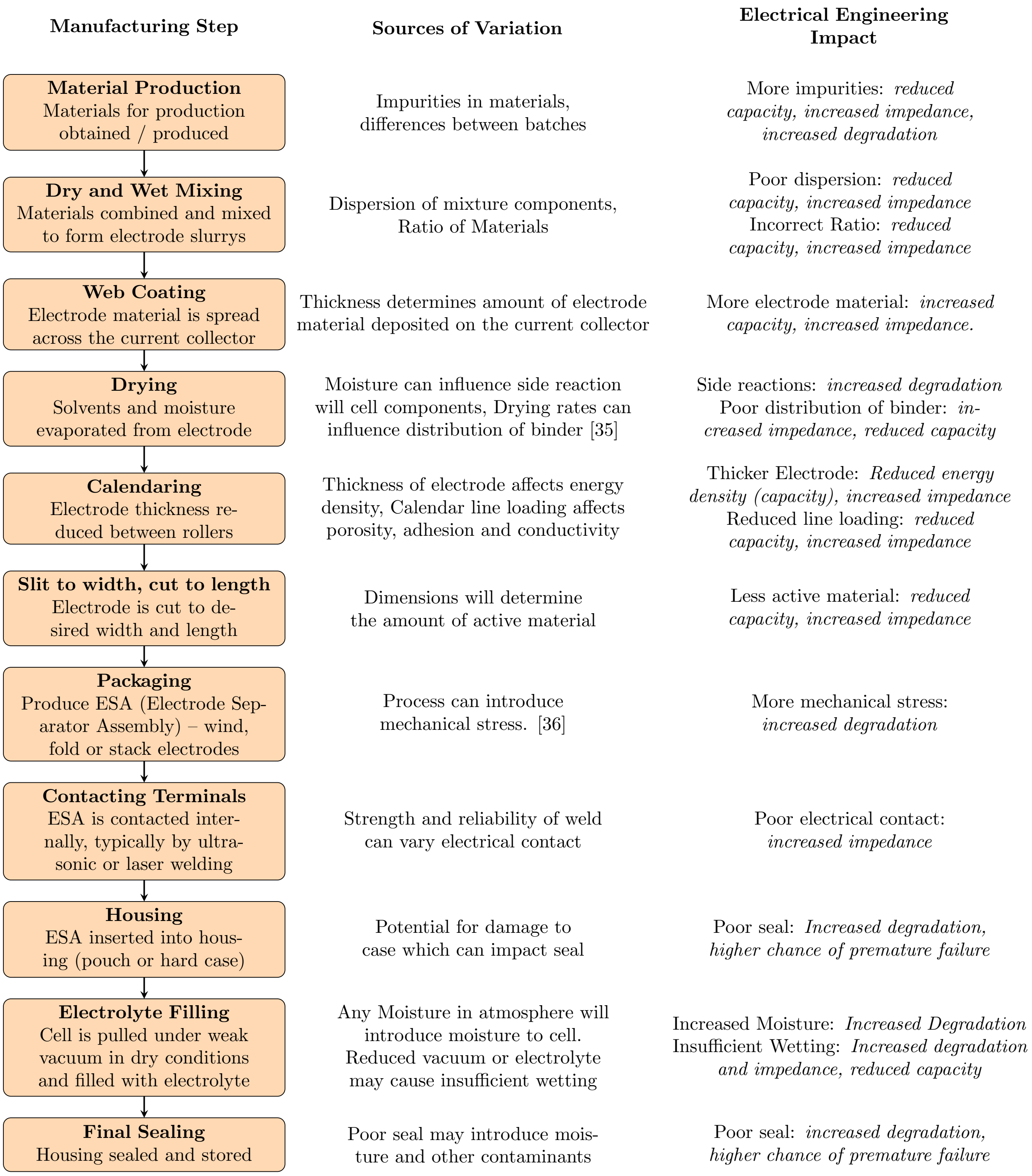

Manufacturing Step	**Sources of Variation**	**Electrical Engineering Impact**
Material Production Materials for production obtained / produced	Impurities in materials, differences between batches	More impurities: *reduced capacity, increased impedance, increased degradation*
Dry and Wet Mixing Materials combined and mixed to form electrode slurrys	Dispersion of mixture components, Ratio of Materials	Poor dispersion: *reduced capacity, increased impedance* Incorrect Ratio: *reduced capacity, increased impedance*
Web Coating Electrode material is spread across the current collector	Thickness determines amount of electrode material deposited on the current collector	More electrode material: *increased capacity, increased impedance.*
Drying Solvents and moisture evaporated from electrode	Moisture can influence side reaction will cell components, Drying rates can influence distribution of binder [35]	Side reactions: *increased degradation* Poor distribution of binder: *increased impedance, reduced capacity*
Calendaring Electrode thickness reduced between rollers	Thickness of electrode affects energy density, Calendar line loading affects porosity, adhesion and conductivity	Thicker Electrode: *Reduced energy density (capacity), increased impedance* Reduced line loading: *reduced capacity, increased impedance*
Slit to width, cut to length Electrode is cut to desired width and length	Dimensions will determine the amount of active material	Less active material: *reduced capacity, increased impedance*
Packaging Produce ESA (Electrode Separator Assembly) – wind, fold or stack electrodes	Process can introduce mechanical stress. [36]	More mechanical stress: *increased degradation*
Contacting Terminals ESA is contacted internally, typically by ultrasonic or laser welding	Strength and reliability of weld can vary electrical contact	Poor electrical contact: *increased impedance*
Housing ESA inserted into housing (pouch or hard case)	Potential for damage to case which can impact seal	Poor seal: *Increased degradation, higher chance of premature failure*
Electrolyte Filling Cell is pulled under weak vacuum in dry conditions and filled with electrolyte	Any Moisture in atmosphere will introduce moisture to cell. Reduced vacuum or electrolyte may cause insufficient wetting	Increased Moisture: *Increased Degradation* Insufficient Wetting: *Increased degradation and impedance, reduced capacity*
Final Sealing Housing sealed and stored	Poor seal may introduce moisture and other contaminants	Poor seal: *increased degradation, higher chance of premature failure*

Figure 2.7: Typical manufacturing process for a lithium-ion cell. (adapted from [7])

It is clear from figure 2.7 that these steps all affect the physical properties of the cell, and so any slight changes between each cell can cause different properties between the different cells produced. Whilst every step introduces an element of variation, Kwade et al. note in [7] that the most crucial parameters with variation are remaining moisture, mechanical stress, connection resistance and wetting consistency of the Electrode-Separator Assembly (ESA). This impacts the properties of the battery pack that is produced. According to experimental work presented in [15], this variation can be as high as 5% for the capacity and impedance of new cells in an EV. Experimental work on cells presented in this thesis however give a lower variation nearer 1%. Therefore, there are extensive steps before producing a battery pack as detailed in figure 2.8.

Figure 2.8: Typical process for producing a lithium-ion battery pack. (adapted from [7])

The cells are sorted to be grouped with other cells with similar properties such as similar capacity and internal resistance, before being assembled into modules. These modules are then sorted in much the same way as the cells to be assembled into packs.

2.1.2 Modelling

Models for battery cells aim to produce a mathematical representation of a cells behaviour, generally for simulation or used alongside model based estimation and control algorithms. These can be broken into three broad categories - physical models, electrochemical models and bucket models, with respectively reducing complexity.

Models can be either empirical - based on observations of the behaviour, or mechanistic - based on theory. The three model types presented have both empirical and mechanistic elements, with observations required to identify the parameters for the models, but the more simplistic models tend to be increasingly empirical.

2.1.2.1 Physical / Electrochemical Models

A typical physical model is a particle model - these are generally single particles or Pseudo-2D particle models. A Pseudo-2D (P2D) model describes the battery electrochemical behaviour based on the porous electrode theory [12] [37].The electrodes are considered separately as a mass of spherical particles submersed in a liquid electrolyte where they diffuse and intercolate during charge and discharge. This is then mathematically represented by a complex set of PDE's which gives a highly accurate yet highly computationally intensive model [38].

This can be simplified to a single particle model - the same as a P2D yet merely a single particle is modelled. This is still fairly complex, but according to authors [39] is noted to be potentially suited to BMS applications.

2.1.2.2 Equivalent Circuit Models

Less complex than an electrochemical model, an Equivalent Circuit Model (ECM) represents the battery as a voltage source (generally dependant on SoC) and a network of resistors and capacitors - generally a resistor in series with a number of parallel pairs, as shown in figure 2.9 [8]. Some ECMs include an element for inductance, such as that in [40], where the author notes that inductive impedance is dominant at frequencies >1kHz, or a time period of <1ms. For battery pack applications, it is typically ignored as it is not measurable, with BMSs typically sampling in the order of 10Hz.

Each RC element refers to the voltage response of a battery to an applied current, with different time constants represented by each element. The output voltage is determined by equation 2.1 below [41]. As noted by Lin et al. in [12], they can be used for real-time applications, using an open-loop or closed loop algorithm to estimate battery states or parameters.

$$V_i = OCV - I\left[R0 + \sum_{i=1}^{n} R_i\left(1 - e^{-t/R_iC_i}\right)\right] \tag{2.1}$$

Increasing n (number of RC elements) increases the complexity, whilst giving a more precise estimate of impedance. It has been shown that despite the increased precision of the model, increasing n does not necessarily improve model accuracy, due to the challenges in identifying the model parameters [41].

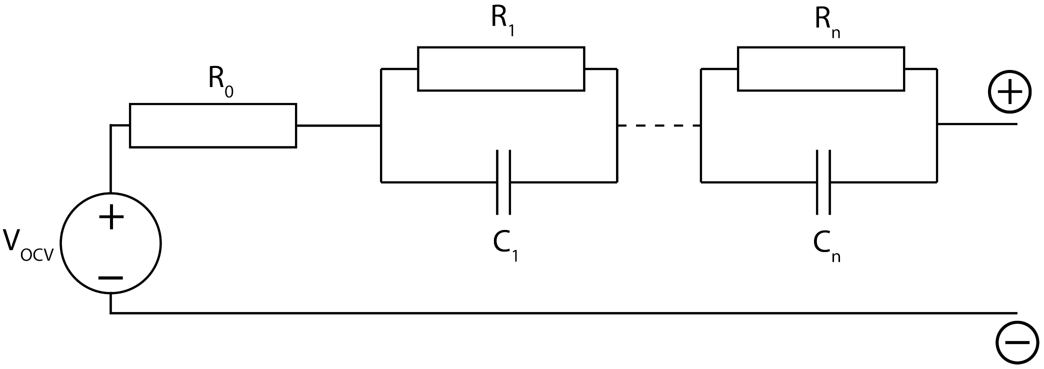

Figure 2.9: Equivalent Circuit Model (adapted from [8])

2.1.2.3 Bucket Models

Less complex still, a bucket model is a highly simplistic model of a battery, considering the battery as a"fuel tank" or energy store with a fixed capacity [42]. Applying power to the model changes the energy stored in the battery through integration of power, so a model can output SoC. Hence the battery model is described in [42] as:

$$\frac{dSoC}{dt} = \frac{P(t)}{E_{Wh}} \tag{2.2}$$

This type of model would typically be used where voltage is not a concern and a high level of detail is not required. Being simple, it is computationally efficient and particularly useful for simulating over long timeframes, or as part of a simulation of a larger model (i.e. a model of an electricity grid).

2.1.2.4 Overview

Overall, models ranging from complex electrochemical models have been shown, down to the very simplistic bucket models. Typically ECMs are used in real-time applications and in BMSs as a fair compromise between performance and detail.

2.1.3 Battery Metrics

For an operator or user of a battery, it is useful to have various performance indicators to understand battery behaviour in a simple manner. Direct battery measurements such as voltage and current alone are not sufficient to determine the future operating limits of a battery without some mathematical processing. Therefore, various metrics are estimated to give a more useful measure of a battery's state at any given time to an operator.

2.1.3.1 SoC

SoC is commonly defined as the total available energy available from a particular cell or battery relative to the total energy the cell or battery can store. In a lithium-ion battery, it is related to the concentration of lithium in each electrode [43] as:

$$SoC = \frac{\theta - \theta_{0\%}}{\theta_{100\%} - \theta_{0\%}}, \tag{2.3}$$

where θ is the normalised lithium-ion concentration, and $\theta_{100\%}$ is the concentration at 100% SoC, and $\theta_{0\%}$ is the concentration at 0% SoC.

It is important to know the remaining charge in a cell for virtually all applications and therefore significant research has been performed around being able to measure it. The vast majority of research considers single cell SoC measurement which this section will explore.

It is worth noting that SoC is not a metric that can be specifically measured like voltage or current. It is always an estimate based on other measurements that can be taken [44]. Typical measurements taken in operational battery systems are voltage, current and temperature, though other measurements have been proposed such as optical [45], strain and ultrasound [46] measurements. From typical measurements from operational battery systems, there are many techniques which are used to estimate the SoC, which can range from very simple to highly complex, both in terms of computation and mathematics.

2.1.3.1.1 Discharge test

This is considered the most basic SoC estimation algorithm [9]. A battery is discharged until it is empty and the energy that has left the battery is measured. It can be found following a Constant Current, Constant Voltage (CCCV) charge as:

$$SoC = \frac{Q_{released}}{Q_{rated}} \tag{2.4}$$

where:

$$Q_{released} = \int_0^t I dt \tag{2.5}$$

where:

$Q_{released}$ = Charge released from the cell [Ah]
Q_{rated} = Rated battery capacity [Ah]
t = Discharge time (h)
I = Current (A)

This method is impractical for most applications as the battery requires a time-consuming recharge, and it is only known what the SoC was at that particular point in the past. Additionally, the primary function of the battery is interrupted. It must be performed under controlled conditions to be accurate, so is only suitable for verifying results.

2.1.3.1.2 Coulomb Counting

Coulomb counting extends the discharge test, continuously measuring the charge in and out of the battery [47]. It requires initial knowledge of SoC and can be found as:

$$SoC(t) = SoC(t_0) + \int_{t_0}^{t_0+T} \frac{I}{Q_{rated}} \tag{2.6}$$

where:

t = Observation time
t_0 = Initial time
T = Operating period

This method is an improvement to the discharge test as it can work during normal operation of the battery. However, with this method, current measurement error causes the value to ‘drift’ over time as all errors are carried through [48]. It can be corrected when the battery reaches a known SoC level - i.e. full charge, however depending on the application, this particular point may never be reached.

2.1.3.1.3 Open Circuit Voltage (OCV)

The open circuit voltage of a battery relates to it’s SoC. It has been used for a long time for lead acid batteries where there is a very strong and linear relationship between OCV and SoC as shown in figure 2.10.

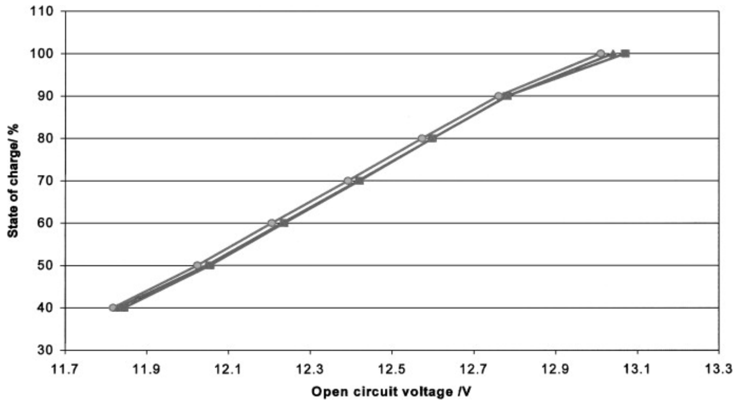

Figure 2.10: Lead acid OCV vs SoC for 4 lead-acid (VRLA) batteries of the same type [9]

This gives a simple linear equation to have a measure of SoC from OCV. Applying this to lithium ion batteries is less straightforward, however. Figure 2.11 shows the OCV plot for a LFP/LTO (cathode/anode) cell, highlighting the issue.

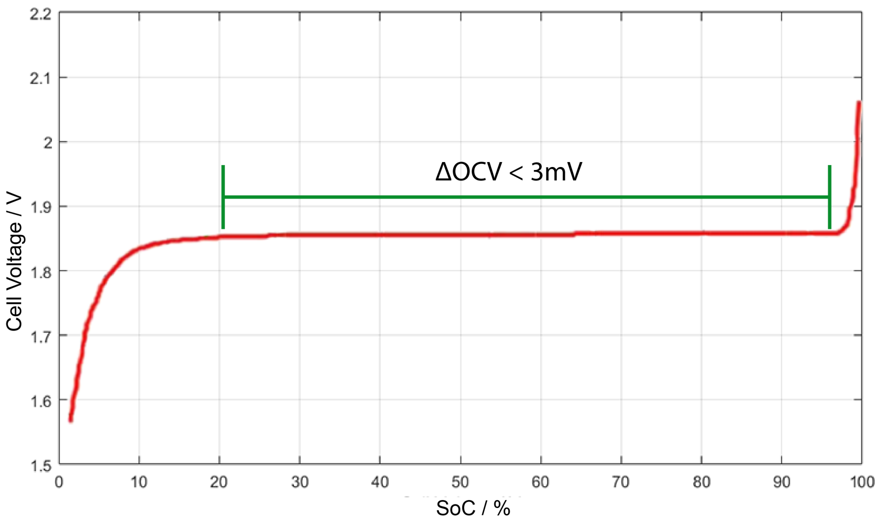

Figure 2.11: OCV vs SoC of an LTO-LFP cell [10]

As can be seen, there is a very flat region of OCV - between 20% & 95% SoC, there is 3mV change in OCV. Furthermore, it is not linear, and the

OCV-SoC relationship cannot be represented by a simple linear equation. This particular chemistry has an especially flat region, but other lithium cells exhibit similar properties, with a range of cell OCVs shown in figure 2.12.

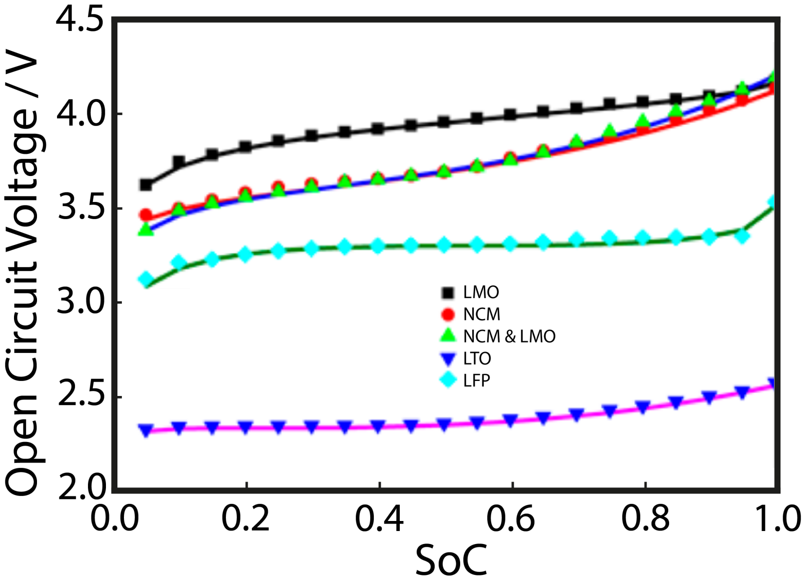

Figure 2.12: Typical OCV vs SoC for a range of lithium cell chemistries (adapted from [11])

Comparing figure 2.11 and figure 2.12 it can be seen that other lithium chemistries still exhibit the flattened region, but to a lesser extent. Regardless, the relationship between SoC and OCV is not linear and therefore a lookup table is more appropriate. This is where the voltage is compared with measured values at known states of charge and interpolating between points [49].

This can be more accurate than coulomb counting, however, to have a true value for SoC a cell is required to be open circuit - i.e. no load, and rested to allow the voltage to settle.

2.1.3.1.4 Electrochemical Impedance Spectroscopy

Another technique that can be used is Electrochemical Impedance Spectroscopy (EIS). This involves measuring the impedance of a cell at a range of frequencies. The impedance of a battery changes with SoC at certain frequencies so can be used to give a metric for SoC. A typical Nyquist plot from an EIS test at different SoCs is shown in figure 2.13

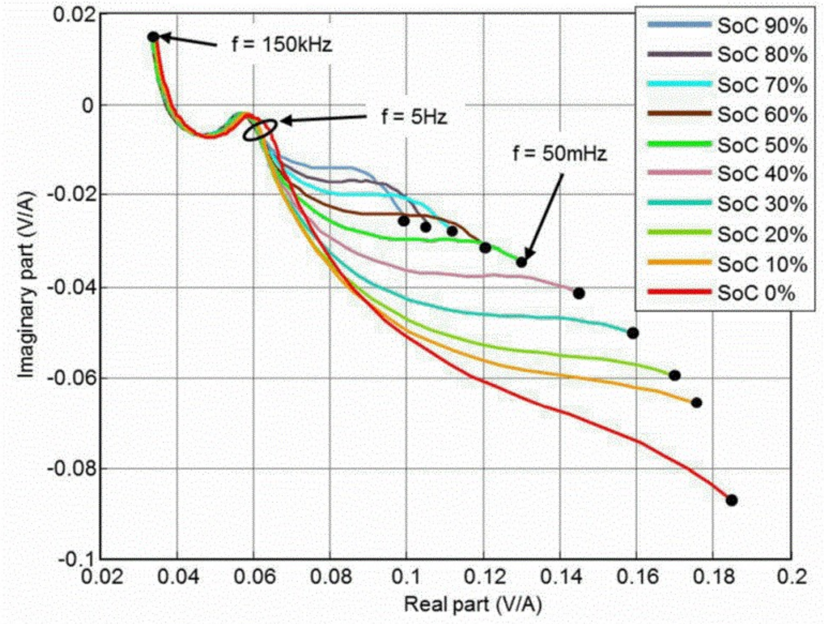

Figure 2.13: Nyquist plot for the typical result of an EIS test at different SoCs. Example shown is an LFP-LTO cell from [10].

This has been demonstrated to give a reasonable estimate whilst the cell is at rest [10], though it is noted that more work is required for the technique to be used in the full operating range of the battery.

2.1.3.1.5 Model Based Approach

Model based approaches estimate SoC based on a model of a cell or battery. An open loop approach runs the model alongside the battery to predict target variables. A disadvantage to this is the susceptibility to uncertainty in the model, input measurement and initial conditions, as noted by [50] and [51].

A closed-loop approach incorporates the model alongside measurements to improve the prediction of target variables. The schematic of a typical closed-loop estimation algorithm is shown in figure 2.14. The state estimator part of the algorithm can take many forms, including a Kalman Filter [52], PDE Observer [53], Neural Networks, Fuzzy Logic and Support Network Machine [54] amongst others.

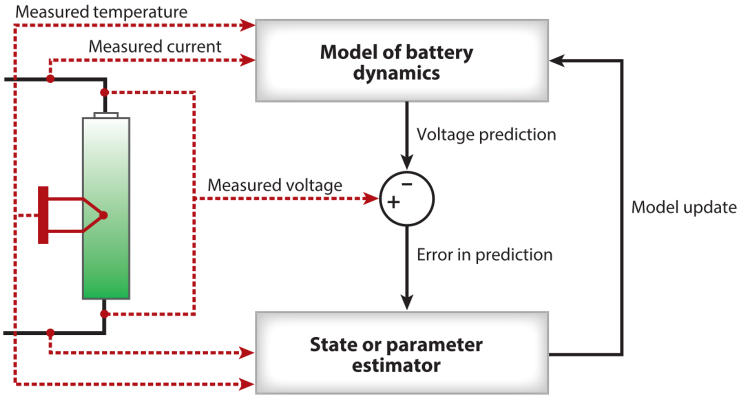

Figure 2.14: Closed-loop battery state estimation algorithm. (Adapted from [12])

2.1.3.2 SoH

State of Health (SoH) is another metric that is closely linked to SoC. It relates to the condition of a particular cell or battery relative to when it was new, or it's rated specification [55] [47]. It is typically reported considering the reduction in capacity, described by the following equation [47]:

$$SoH = \frac{Q_{max}}{Q_{rated}} \times 100\% \tag{2.7}$$

Additionally, [55] notes that a change in OCV and increase in impedance can also be used to contribute to the metric of SoH. Mechanisms for these changes are discussed in section 2.1.4.

With SoH typically being a change in capacity, it is normally estimated by either modelling degradation, or updating an estimate for capacity. This is important for determining SoC, particularly where coulomb counting is involved, as the SoC is estimated relative to capacity.

2.1.3.3 SoF / SoP

State of Function (SoF) has several definitions across literature [56–60], but it is generally considered a binary "Yes/No" for a battery to perform a specified function. This could be for a function such as cranking an engine, or performing a constant current discharge for a set time.

A similar metric, State of Power (SoP) determines the maximum available power a battery can charge or discharge in it's current state. It is noted by Lin et al. in [12] that the estimation is critical in maximising the utilisation of a battery as it increases the operating window of a battery. For instance, as a battery charges, cells within it will approach their upper voltage limits. The SoP indicates that power is needed to reduce to avoid these limits being exceeded. Should the estimate for SoP be too conservative, power will reduce earlier than necessary, reducing the operating window for the battery. Should the opposite be true, a voltage limit may be exceeded, which could result in a battery shutdown to avoid unsafe operating conditions.

These two metrics are less commonly reported than SoC or SoH in literature, but are important from a standpoint of maximising battery utilisation whilst remaining in a safe operating window and considers both SoC and SoH in it's estimation.

2.1.4 Degradation

It is well known that batteries degrade when being used. User experience of a smartphone (or any other rechargeable device) for a matter of months before observing a capacity reduction. The battery cost for this type of device is small, however, for an electric vehicle, or other application with large batteries, there can be a large cost associated with the degradation. [61] For an online algorithm, it is important to understand that there is a degradation associated with each cycle, and it may be beneficial to associate that to a particular degradation mechanism to better model it.

Degradation is caused by a large number of highly complex mechanisms which occur in a lithium ion cell [62] [31]. These mechanisms are shown in figure 2.15 below.

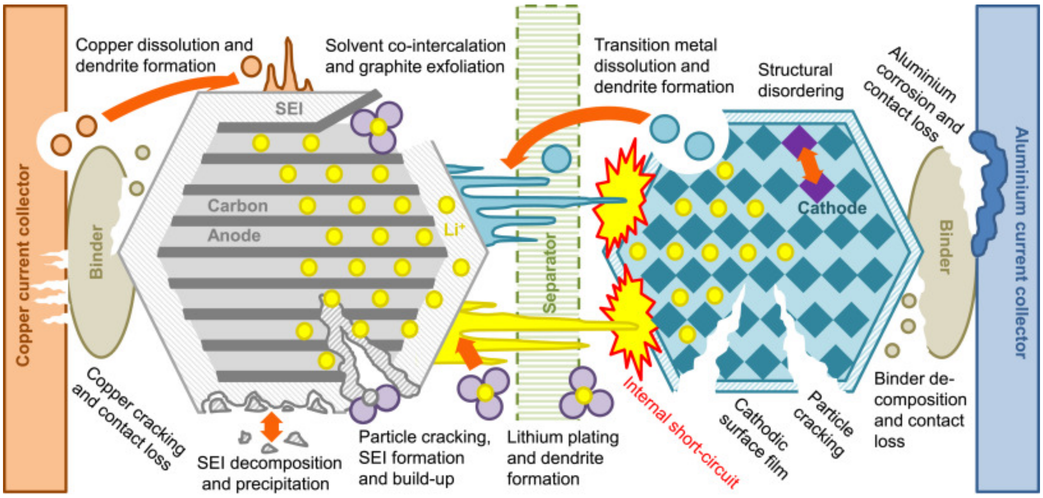

Figure 2.15: Degradation mechanisms in lithium ion cells. [13]

As can be seen, there are many physical and chemical processes occurring in the cell. However, Birkl et al. state in [13] that these mechanisms can be summarised in three modes: Loss of lithium inventory; loss of active cathode material and loss of active anode material.

Electrically, this results in a loss in capacity or power available [63]. There are several factors in the operation of the cells that affect the rate of degradation. C-rate (the rate at which cells are discharged relative to their capacity) is known to be a factor. It has been shown that higher C-rates cause a higher rate of degradation [64]. It causes the loss of the active electrode materials.

Cycling nearer 100% and 0% SoC is also a factor, where this degrades a battery faster [65]. It is theorised as being due to crack propagation in the structure of the electrodes when operating in these SoC areas, meaning there is again reduced active electrode material.

At rest, a cell will degrade over time, theorised due to growth of the SEI [13] and is known as calendar ageing.

Finally, temperature is a factor in degradation. Both high [66] and low [67] temperatures cause accelerated cyclic and calendar ageing. High temperature degradation results in loss of capacity and increase in impedance and it has been observed that this can be due to a low-conductivity SEI forming on the cathode [66]. Low temperature degradation is due to lithium plating occurring on the anode as opposed to intercalation of the ions, causing loss of lithium inventory.

This is summarised in more detail below in figure 2.16.

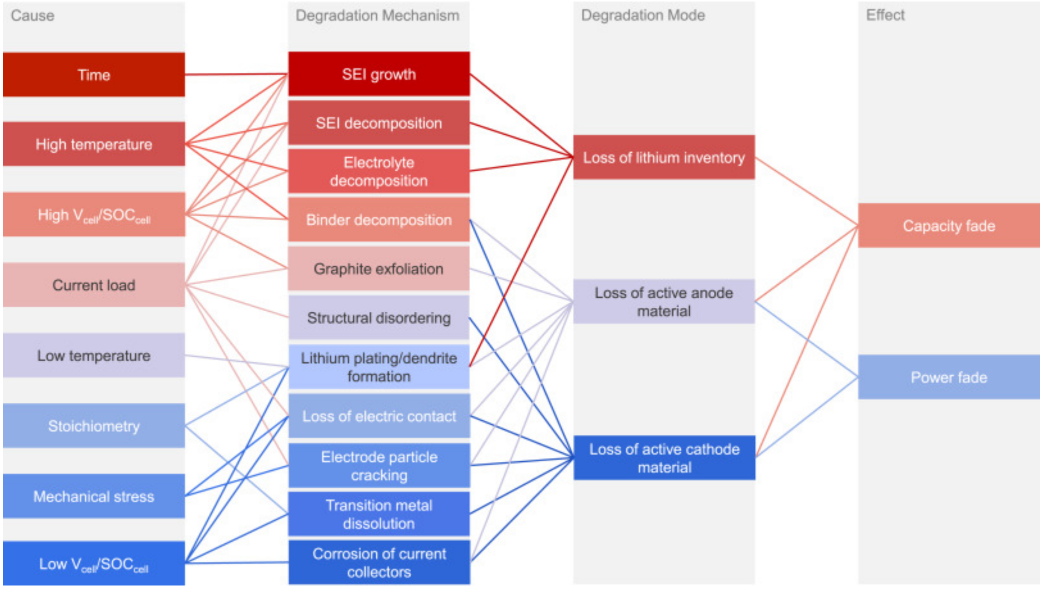

Figure 2.16: Degradation mechanisms in a lithium ion cell [13].

2.2 Large Battery Packs

Considering large battery packs, this work defines a battery “pack” as consisting of multiple cells with series and/or parallel connections, and additional circuitry for monitoring and protection, with an example shown in figure 2.17. It is then considered large in this work when consisting of >100 cells. Other terms that are used include strings and modules. A string refers to a number of cells connected in series. The term module is used to refer to a group of cells with series and/or parallel connection that is a “building block” for a larger system. Modules typically contain some cell monitoring and balancing but not a full BMS, lacking control.

A BMS can be described as a system control unit, primarily to safeguard the battery [68]. This is through measurement of cell voltages, current and temperature [69] and controlling contactors in the system. The scope of a

BMS varies depending upon the application and in thesis, it is defined as a system to monitor the battery, provide battery protection, estimate the battery's operational state and report the battery states to external equipment. In a grid connected system, the external equipment may be a system to control power flow to or from the grid.

The configurations of batteries are named by their series and parallel connections, where 's' is the number of series connections and 'p' is the number of parallel connections. As an example, for a 2p4s8p battery, there are 2 cells connected in parallel, of these there are 4 connected in series. There are then 8 of these 2p4s groups of cells connected in parallel.

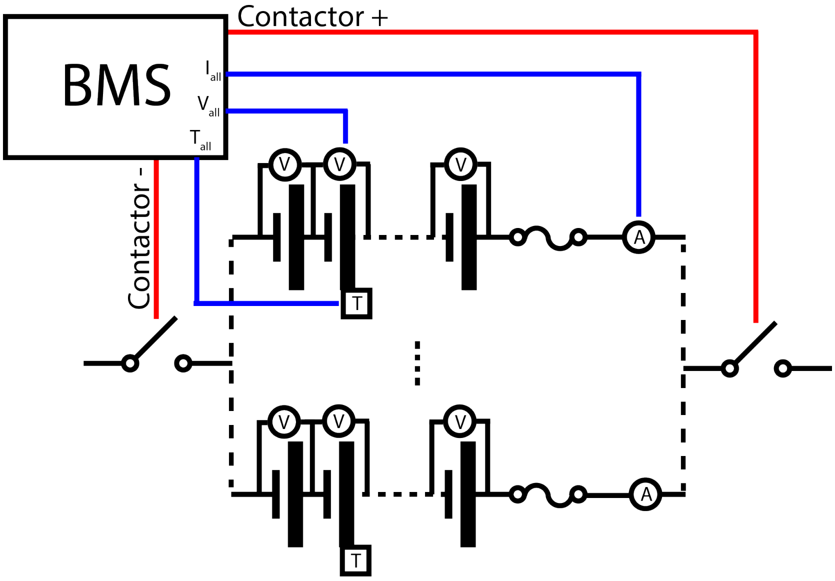

Figure 2.17: Example of a battery "pack", as defined in this work

In this section, studies in differences between cells will be initially considered, including degradation effects, then how this is mitigated through cell balancing mechanisms. Next, the applications of large battery packs will be considered, before discussing the work that this thesis builds upon.

2.2.1 Cell Variations

Several studies show that there there are variations between cells of the same age and type from the same manufacturer [15, 70–74]. When used in a pack, these variations cause a difference in cell voltages and a difference in current between parallel cells / strings during cycling. These voltages and currents must be measured and considered to prevent any cell from exceeding its rated upper or lower voltage or current limit. For example, during the charge of a pack, once any cell reaches the upper voltage limit, the charging current must be reduced or stopped such that the upper voltage is not exceeded. Not doing this and allowing the individual cell to exceed the voltage limit could result in cell damage or catastrophic failure of the cell [75].

2.2.1.1 Capacity Variation

It is shown in the mentioned studies that cells connected in a pack will have different capacities. This is shown to be as high as 5% in new cells [15], though the other previously mentioned studies measure capacity variation to be between 1-2%. If they are connected in series in a fully charged state and discharged, they will end at different states of charge [76]. This is illustrated in figure 2.18 below.

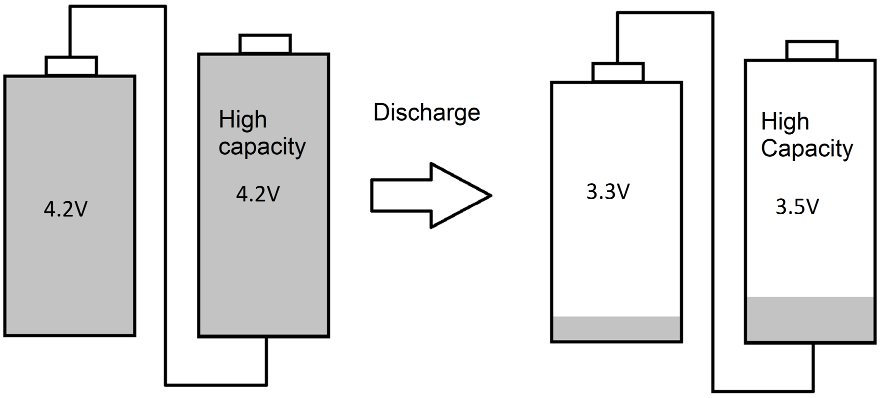

Figure 2.18: Voltage difference between two cells with different capacities discharging.

This is due to the fact that current is constant between the cells, and as such, they discharge to different SoCs, and therefore different voltages.

Manufacturers may deliberately have different “windows” of acceptable variation between cells, depending upon the application. For example, in applications where cells are generally only connected in parallel (i.e. power bank), there will be a wider acceptable variation. Additionally, in applications which rarely reach near full and empty charge, the variation is less impactful, so a wider acceptable variation may be used. Where maximum cell-utilization is important (i.e. in electric vehicles to maximise driving range) a manufacturer might choose a smaller window of variation.

2.2.1.2 Impedance Variation

Additional to capacity variance, cells connected in a pack will also have an impedance imbalance. In series connected cells, it manifests itself as a voltage difference under load. Assuming the cells have the same SoC however, the cells will relax to the same voltage [76].

The variation between cells can however be significant. It is suggested in [76] that a batch of cells may have as much as 20% difference in impedance at production, which agrees with results shown in [70]. This demonstrates a problem with using multiple cells together. Even with identical capacities, the cells will show a variation in voltage under a load, meaning that cells will reach their maximum or minimum voltages at different points. Different manufacturers may have different tolerances as to what is an acceptable difference in impedance, but it is to be expected that cells will have some variation of impedance when new.

2.2.1.3 Degradation Variation

It is important to note that while cells might begin at reasonably consistent capacities and impedances, this can vary throughout their lifetime. Figure 2.19 shows the cell capacity from ageing of 48 cells tested separately by Baumhöfer et al. in [14]. A similar study from Harris et al. agrees with this conclusion [77].

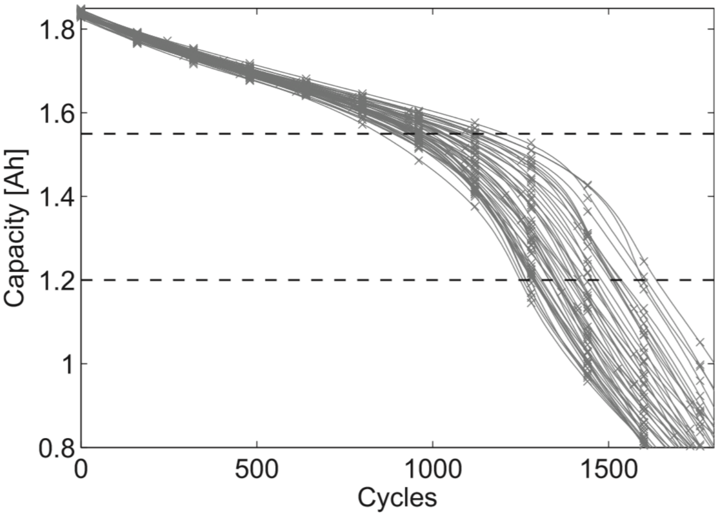

Figure 2.19: Different ageing trends from 48 equal cells under identical ageing conditions and profiles. [14]

These cells were tested independently of each other and exhibited this variation effect. In a series connected battery, this effect would likely be magnified. It is known (section 2.1.4) that discharging and charging cells to lower and higher SoCs results in greater degradation. With some cells reaching a lower SoC than others due to imbalance, degradation will occur faster in these cells. These will then have a further reduced capacity, compounding the issue.

This is further shown in figure 2.20, where Schuster et al. took 3 samples of cells from EVs - one new, and two which had been used for 25,000km and 3 years each [15]. It can be seen that the internal resistance and capacity of the cells are tightly grouped for the new cells, with just one outlier. After ageing, there is a much wider spread of both impedance and capacity.

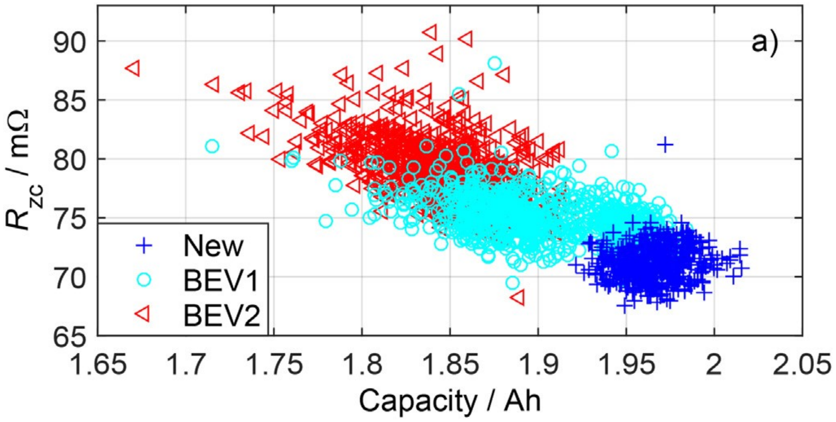

Figure 2.20: Impedance and capacity of cells removed from EV packs, one new and two aged (BEV1/BEV2). (Adapted from [15]).

Additionally to capacity and internal resistance, [13] suggests that the OCV-SoC relationship also changes as cells degrade, therefore it stands to reason that the more degraded cells may have a different OCV-SoV curve compared to less degraded cells.

This unequal degradation is particularly an issue with large batteries, as with a new battery, the cells all perform reasonably equally, but over time it is expected that they will perform differently to each other. Algorithms would be required to track these changes to maintain a good estimation of SoC throughout a battery's lifetime, to know how much energy is available at any given time.

2.2.1.4 Cell Balancing Mechanisms

In order to overcome cell imbalance issues, balancing mechanisms are used to adjust the state-of-charge of individual cells connected in a pack in a process often called cell balancing or charge equalisation. They can be broadly split into passive and active mechanisms [16, 78]. Many balancing mechanisms have been presented in literature [79–94]. The common balancing mechanisms are helpfully summarised in [16], as shown in figure 2.21.

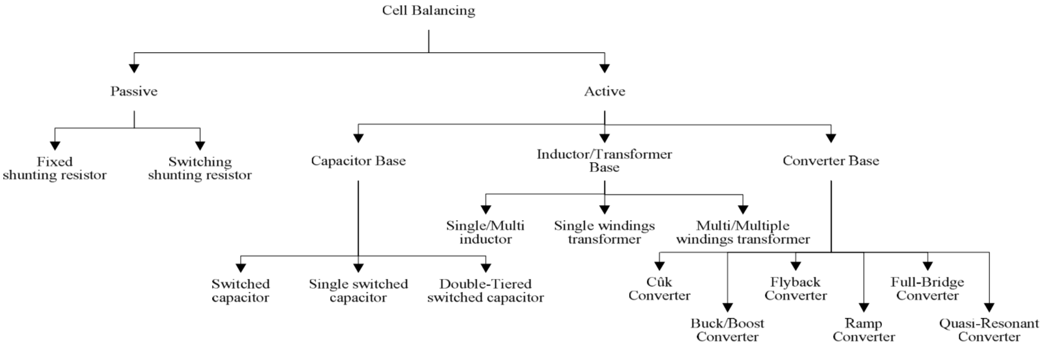

Figure 2.21: Passive and Active Cell Balancing mechanisms. (Adapted from [16].)

Passive balancing mechanisms for lithium ion batteries involves controlling a switched resistor in parallel with an individual cell. This is used to discharge cells with a higher SoC than others. An active balancing mechanism involves shuttling charge between cells using capacitors, inductors, or DC-DC converters. These each have varying costs and complexity, with passive methods being cheaper, however, they are inefficient due to energy being wasted as heat, and active methods being more expensive but with a much greater efficiency. The batteries used experimentally in this thesis all employ a passive balancing mechanism, which seems to be the industry standard based on the commercial modules observed by the author, however the actual balancing mechanisms employed in commercial large batteries are generally not publicised.

2.2.2 Applications

As previously mentioned, the manufacture of lithium-ion batteries is seeing an increase which is forecast to accelerate. This increase is largely due to large battery pack applications, which can be broadly split into static and motive applications. Static applications include use on Electricity Grids [95], Micro Grids [96] and home storage [97]. The motive applications include EVs (cars) [98], Heavy Goods Vehicles (HGVs) [99] and ferries [100] amongst others. The research in this thesis is largely focused upon grid-connected batteries, due to the gap in experimental research of such large systems, so the application of these will be explored in more detail.

For grid-connected batteries, there are several revenue streams. These can be divided into two main categories - frequency services and energy trading. This work focuses on the system in GB, where a rapid growth in the market is forming a large driver for research into grid-connected batteries.

2.2.2.1 Frequency Services

In GB, National Grid Electricity System Operator (NGESO) is the electricity system operator, responsible for maintaining a balance between the supply and demand of electricity on the grid. One means for this is through frequency services, which NGESO pays generators to perform. These aim to balance short-term supply and demand of electricity on the grid. A good example of a typical frequency service is Firm Frequency Response (FFR) - this is traditionally provided by generators by varying their output, with the response of the generator during dynamic FFR shown in figure 2.22. More recently, this service is additionally being provided by batteries.

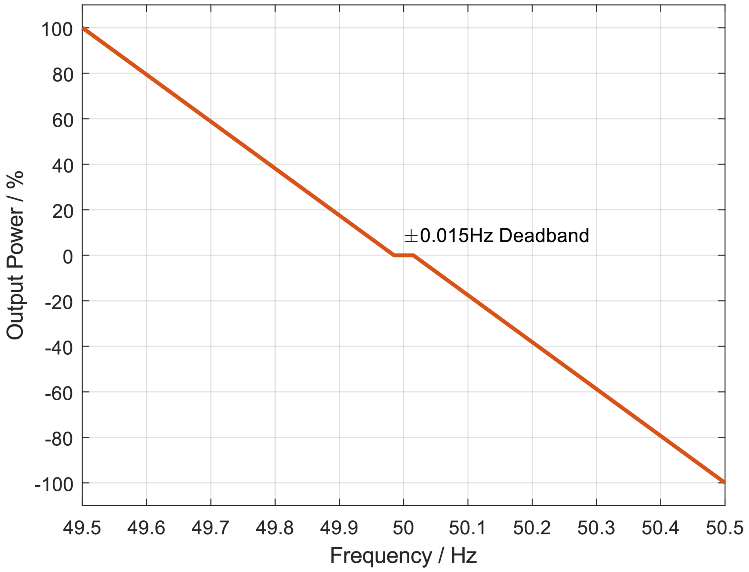

Figure 2.22: Dynamic FFR Output Requirement.

This is an area that is seeing rapid changes in GB, with the latest frequency service offered by NGESO being Dynamic Containment - similar to dynamic FFR but with different response requirements and specifically designed for storage assets. Performing a frequency type service on a battery results in many small cycles, as shown in figure 2.23.

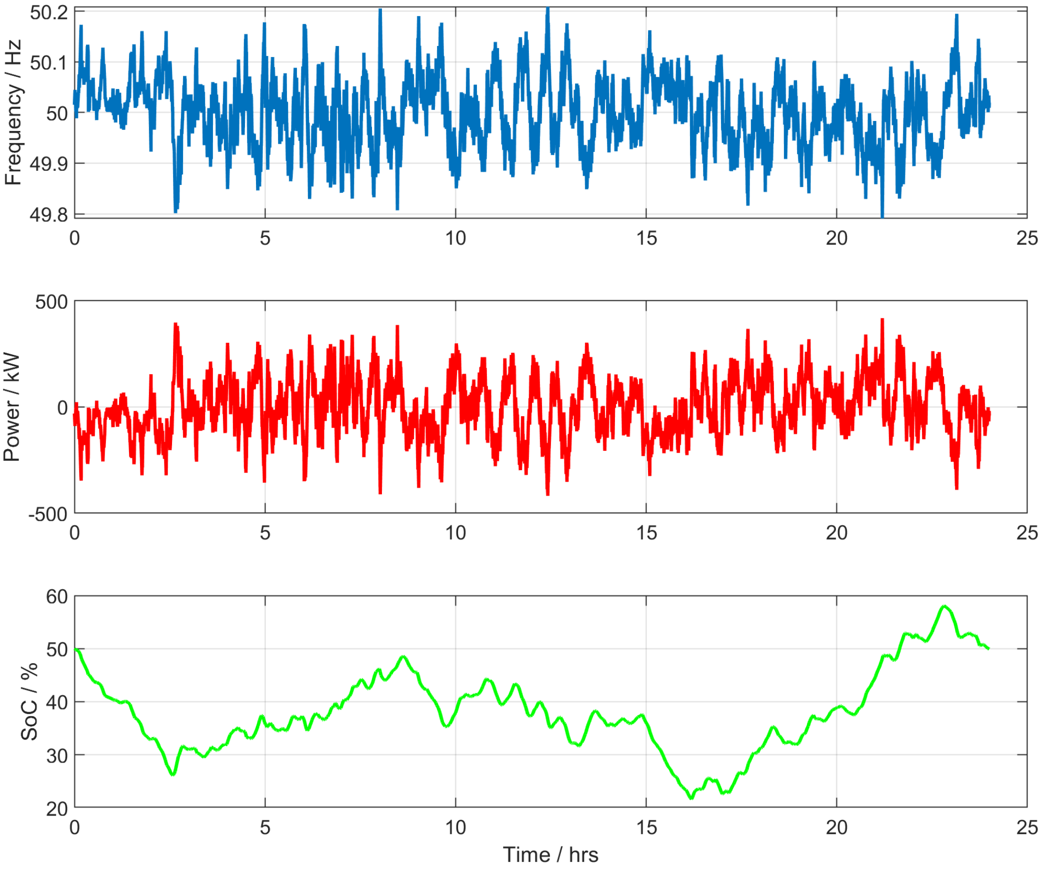

Figure 2.23: Simulated response of a 1MWh battery performing Dynamic FFR over a 24 hour period. (Produced using model of WESS produced for chapter 7.)

Considering the operator of a battery asset, the operator bids a certain power for the service, and the time of delivery. This service is paid in £/MW/hr.

2.2.2.2 Energy Trading

In the UK, there are two main types of energy trading for batteries, which are triad avoidance and energy arbitrage.

Triads are the three half-hour settlement periods with highest demand during one season on the UK electricity grid [101]. These are set by NGESO and are designed to reduce the peak load by charging a substantially higher amount for energy during this time, ranging from £16 to £29 per kWh. Triad information is only published after the triad season, and therefore customers forecast these periods. Predicted triad periods occur around 20-30 times per year and so demand is reduced during these periods [102]. Batteries are well placed to make the most of this high pricing to generate a high income. A battery operating in this manner would likely see a full charge and discharge cycle around 20-30 times per year in line with the number of triad predictions per year.

Arbitrage involves purchasing off-peak electricity at a low price and selling it when the electricity is expensive. There can be multiple price peaks and troughs during a single day, as shown in the EPEX SPOT Power UK Auction chart below.

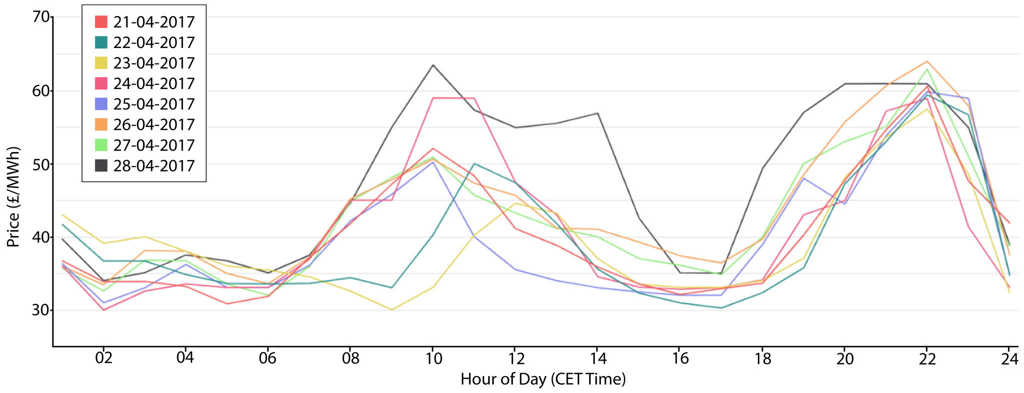

Figure 2.24: The Daily EPEX SPOT Power UK Auction price for a week during April 2017 [17].

It can be seen that there are generally two peak and two off peak periods per day, with varying levels of change between peak and off-peak prices. It can be expected that there might be up to two full charge-discharge cycles per day or 730 per year, with the two periods per day. Considering the effects this might have on the life of a battery is important to determine the profitability of such a grid connected battery energy storage system performing arbitrage on an electricity grid.

For optimal trading, selling electricity will result in a discharge from 100% SoC to 0% SoC and buying electricity will result in a charge from 0% SoC to 100% SoC. Of course, for operational reasons this may not be possible. With charges for non delivery of any bids made in the balancing market (non-delivered energy is charged at the imbalance market rate), and non-delivery of frequency services, it is important to bid an amount of energy that is confidently achievable by a battery system.

2.2.3 State estimation of Large Batteries

With both frequency services and energy trading based on bids that relate to the capacity of a battery, good battery state estimation is required to maximise the bid capacity, and thereby revenue. This thesis aims to improve on the work in this area relating it to large batteries, which will be discussed.

There are a number of studies in literature which consider state estimation of large batteries. These are generally under the application of grid-connected storage or EVs. The latest and majority of these state estimators fall under the category of a closed-loop estimator, introduced in section 2.1.2.

The closed-loop estimators proposed tend to use a single cell model to represent the large battery, which is seen specifically in [58, 103–107]. Other studies or state the application to be for large packs, but merely demonstrating the model experimentally on a single cell [41, 104, 108–112].

Some others will take the opposite approach and model every cell individually. In [89], a model and state estimator is used on each cell. Other studies implementing a model in this way include [71, 113–117], simulating all cells in the model.

Of these, only a small number use experimental data from large packs. Of the examples, only a recent study from Li et al. compares their model to a large pack (>100 cells) - in this case, a 199.4kWh electric bus battery [106]. He et al. test their model against a battery module [103], and small strings are tested in [105], [113] and [71].

With only Li et al. using data from a large pack, this shows a lack of research using large packs for validation. Moreover, the cell level data from the large packs is not shown or considered or shown.

Parameter identification for modelling all cells is generally done from a single cell, although [113] uses various adaptive algorithms to estimate the resistance of 4 cells connected in series. For large groups of cells, packs are dismantled and individually tested to provide capacity and resistance, such as in [15].

Overall, in the research area of modelling large batteries, there is a limited amount of practical experimental results presented from real systems. The primary expected reason for this is due to growth in the area being relatively recent. This means there are a limited number of research facilities and therefore few results. Furthermore, it is expected that most systems do not report or store data for all cells in the system, due to the large storage requirements. This gap in research leads to the outlined research objectives.

2.3 Research objectives

- Little published work presents practical challenges associated with the operation of large batteries. Using data from an operational grid-connected battery, typical cycles should be observed, and behaviour of the system should be noted, with a focus on the behaviour of the cells within the system. Can these observations be reproduced in the lab? This should then be used to inform the design on a grid-scale battery model.

- With current research demonstrating models for large batteries either by modelling every cell individually or modelling the battery as a single cell, a new large battery model should be proposed. This should aim to provide the level of cell detail when modelling all cells whilst being nearer to being computationally efficient as modelling a large pack as a single cell. This should be demonstrated in lab tests.

- It was noted in section 2.2.3 that Identifying the parameters for cells within a pack is generally performed by dismantling the pack and testing cells individually. A method should therefore be proposed to identify the parameters of the model whilst keeping the cells in the pack. This should be performed and analysed on a large battery, with a comparison to cell tests.
- With the model and parameter identification technique proposed, an online estimator for a large battery should be produced which uses both of these. It should be run on a large battery over a period of time, comparing the results to other methods.
- Completing these proposed objectives provides a strong background in the practical challenges associated with large BESS. Using this work, BESS optimisation of a commissioned battery system should be considered.

Chapter 3

Methodology

Throughout the thesis, experimental data is used to verify models, procedures and claims. This section details the various batteries and test rigs that have been used. It highlights key specifications for each piece of equipment and provides some background.

3.1 Battery Modules

A number of battery modules have been tested in various configurations which will be detailed.

3.1.1 Yuasa LIM5H

The Yuasa LIM5H module is primarily used to verify the model proposed in Chapter 4, being dismantled and cycled in various cell configurations. The specification for the cells is shown in table 3.1 and an image of a cell and the assembled LIM5H 10s1p module is shown in figure 3.1.

Chemistry	NMC
Max Cell Voltage	4.2V
Min Cell Voltage	2.4V
Nominal Cell Voltage	3.7V
Capacity	5Ah
Internal Resistance	0.78mΩ (at 45°C)
Max Charge Current (Continuous/Peak)	50/200
Max Discharge Current (Continuous/Peak	50/200
Temperature Limits	-20C - 60C
Package	Prismatic Cell
External Dimensions (mm)	W130, D24, H80

Table 3.1: Specification for Yuasa LIM5H Cells.

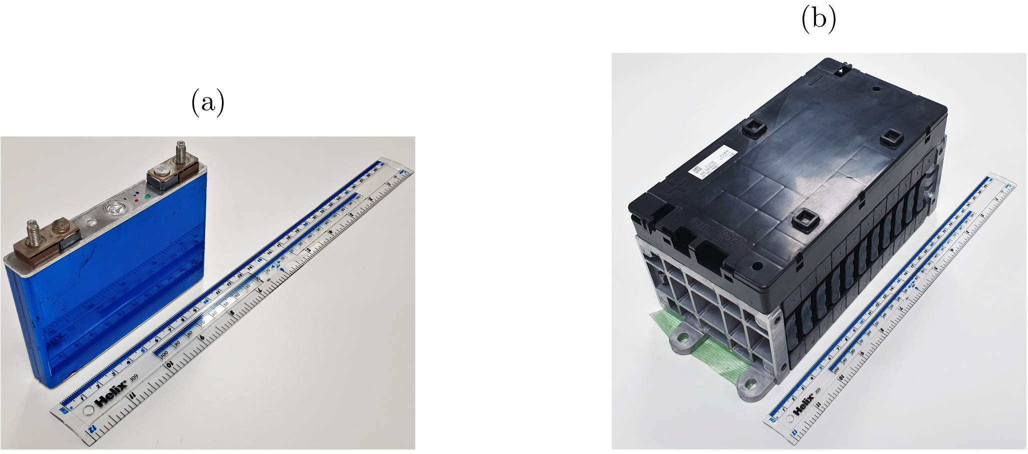
(a)

(b)

Figure 3.1: Yuasa LIM5H cell (a), removed from LIM5H Module (b).

3.1.2 Yuasa LIM50EN

The Yuasa LIM50EN module consists of a 12s1p pack, with cell voltage monitoring (1mV resolution, accuracy not stated), and one temperature sensor per module (1 °C resolution, accuracy not stated). These voltages and temperatures are communicated to a BMS, which can communicate the data via RS-232 serial to a PC at a sample rate of 1Hz. It is tested in various configurations - as a cell (dismantled / removed from a module), module and ESS (in a rack). The specification on these is shown in table 3.2. Images of these systems are shown in figures 3.2 and 3.3.

	Cell	Module	Rack
Chemistry	NMC	NMC	NMC
Max Voltage	4.1V	49.2V	688.8V
Min Voltage	2.75V	33V	462V
Nominal Voltage	3.7V	44.4V	621.6V
Capacity	47.5Ah	47.5Ah	47.5Ah
Max Charge Current	125A	125A	125A
Max Discharge Current	300A	300A	300A
Temperature Limits	-10C - 45C	-10C - 45C	-10C - 45C
Package	Prismatic Cell	Module	19” Rack
External Dimensions (mm)	W180 D45 H110	W215 D180 H125	W600 D800 H1880
Configuration	1s1p	12s1p	168s1p

Table 3.2: Specification of LIM50EN Cell, Module and ESS.

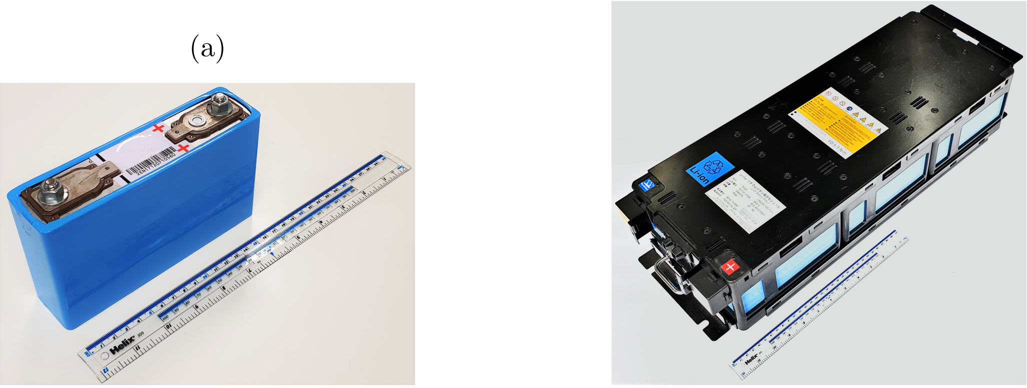
(a)

(b)

Figure 3.2: Yuasa LIM50EN cell (a), removed from LIM50EN Module (b).

Figure 3.3: Yuasa LIM50E ESS

Additionally, there is a passive cell balancing system, where the BMS can control individual cells to discharge through an 82 Ohm resistor. At the maximum cell voltage (4.1V) this gives a maximum balancing current of 0.05A or 0.001C.

3.1.3 Toshiba SCiB

The Toshiba SCiB (Super Charge ion Battery) is used in the Willenhall Energy Storage System (discussed later) and two sample modules and a number of sample cells have been made available for testing. The specification for these are presented in table 3.3 and images are shown in figure 3.4.

	Cell	Module
Chemistry	LTO	LTO
Max Voltage	2.7V	32.4V
Min Voltage	1.5V	18V
Nominal Voltage	2.4V	28.8V
Capacity	20Ah	40Ah
Max Charge Current	120A	120A
Max Discharge Current	120A	120A
Temperature Limits	-20C - 45C	-20C - 45C
Package	Prismatic Cell	Module
External Dimensions (mm)	W115 D20 H135	W190 D360 H125
Configuration	1s1p	2p12s

Table 3.3: Toshiba SCiB Cell and Module Specifications.

(a)

(b)

Figure 3.4: Toshiba SCiB sample cell (a) and Toshiba SCiB Module (b).

The modules have an on-board Cell Monitoring System (CMS), which monitors temperature and voltage. Temperature is reported to the nearest 1°C and Voltage to the nearest 1mV. As with the Yuasa LIM50EN modules, the accuracy of the measurements is not detailed. A schemating showing the positions of the temperature measurements is shown in figure 3.5

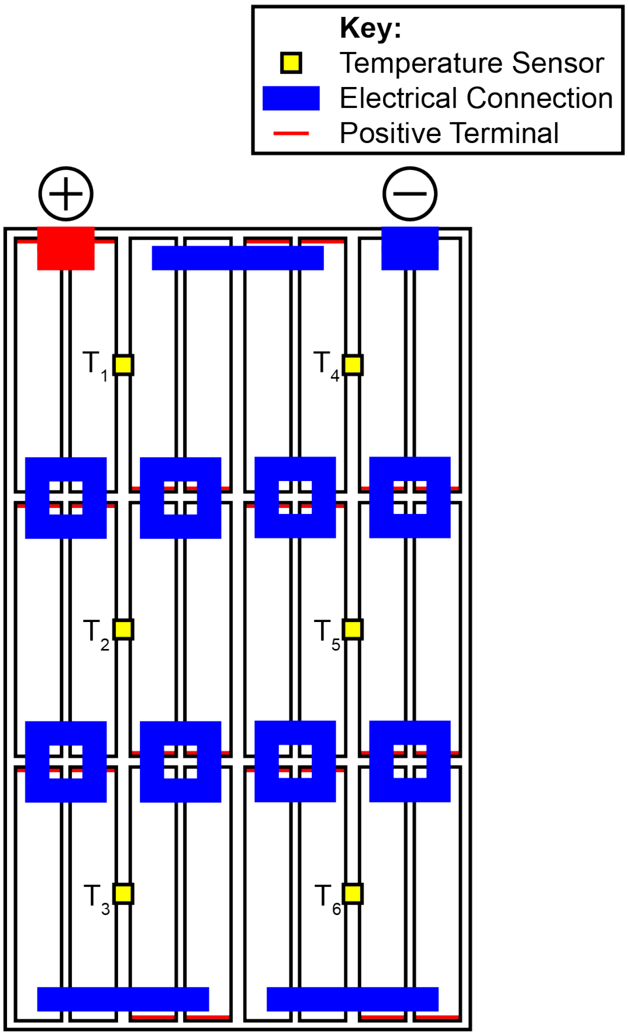

Figure 3.5: Schematic of a Toshiba SCiB module, highlighting the cells which the temperature sensors monitor.

Additionally, similarly to the Yuasa LIM50EN module, there is a passive cell balancing system, where the BMS can control individual cells to discharge through a 22 Ohm resistor. At the maximum cell voltage (2.7V) this gives a maximum balancing current of 0.12A or 0.003C.

3.2 Experimental Test Rigs / Research Facilities

To cycle the aforementioned cells and modules in various configurations, different test rigs and research facilities were used, which this section details.

3.2.1 Cell Level

For cell level testing and small packs, a MACCOR Series 4000, 32 Channel cell tester was used. The specifications are shown in table 3.4 and is depicted in figure 3.6.

Voltage Range	0-20V
Voltage Accuracy	0.02% (4mV)
Voltage Resolution	16 bit (0.3mV)
Current Range	0-10A
Current Accuracy	0.05% (5mA)
Current Resolution	16 bit (0.15mA)
Sample Rate	200Hz max

Table 3.4: Specification for MACCOR Series 4000 cell tester.

Cells were cycled in a PHCBi MIR154-PE Environmental chamber. Specifications for the device are shown in table 3.5 and is depicted in figure 3.6.

Temperature Range	-10°C - +60°C
Temperature Accuracy	±0.2°C (Heated)
	±1.5°C (Cooled)
Temperature Uniformity	±0.5°C
Temperature Resolution	0.1°C

Table 3.5: Specification for PHCBi MIR154-PE Environmental chamber.

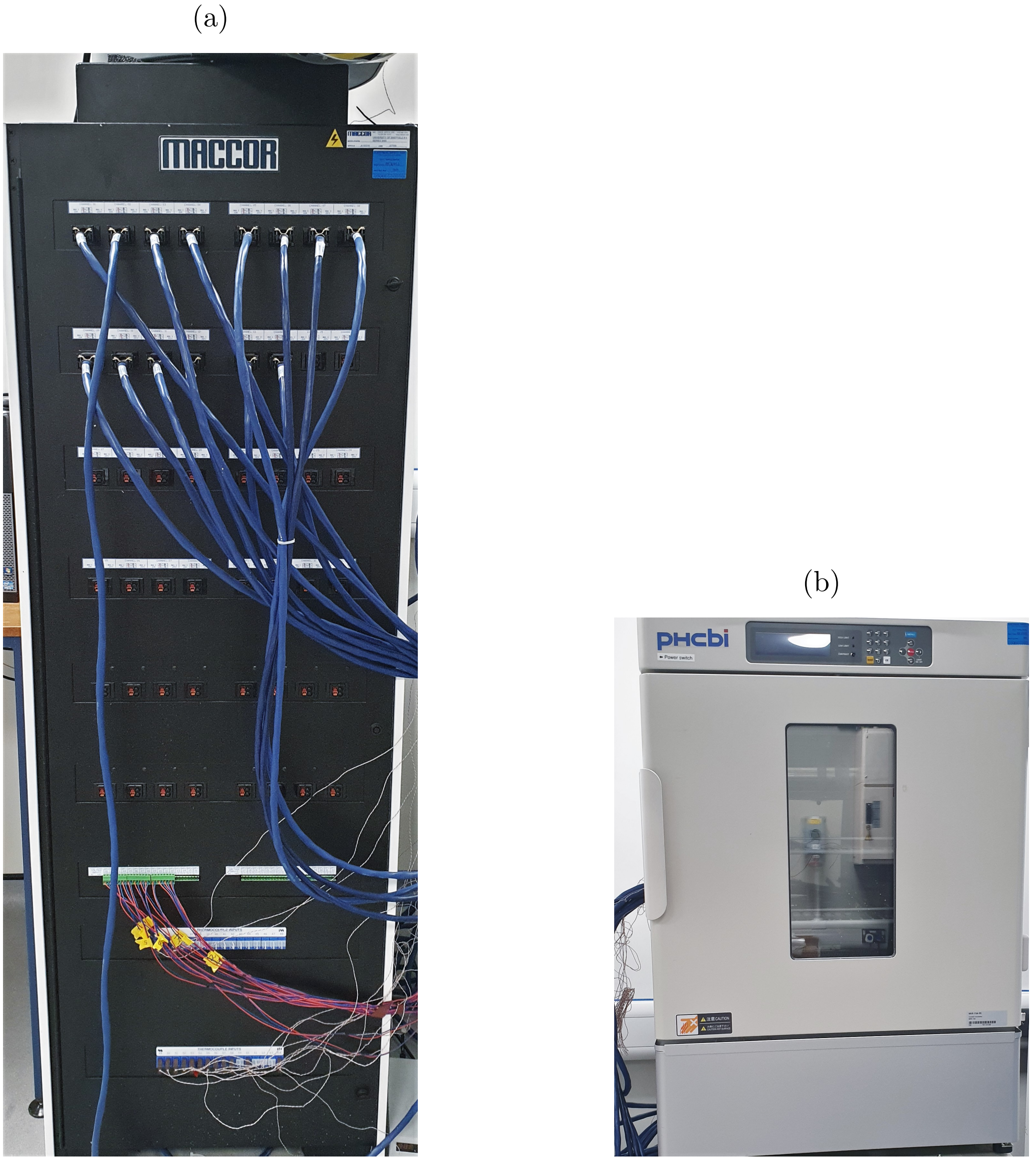
(a)
(b)

Figure 3.6: (a) MACCOR S4000 cell tester, (b) PHCBi MIR-154-PE environmental chamber.

This setup was used to cycle Yuasa LIM5H cells and the LIM50EN cell, where 8 channels were combined in parallel to give a 0-80A current range.

3.2.2 Module / Rack Level

3.2.2.1 Hardware

For cycling modules, Elektro-Automatik EA PSB 9xxx-xxx power supplies were used. Two models were available - the 9080-240 and the 9750-60. The choice of model depends upon the required voltage and current. A table of the specifications for these two models is shown in table 3.6 and a picture is shown in figure 3.7.

	EA-PSB-9080-240	EA-PSB-9750-60
Max Voltage	80V	750V
Voltage Resolution	0.01V	0.1V
Voltage Accuracy	0.1% (80mV)	0.1% (0.75V)
Max Current	240A	60A
Current Resolution	0.01A	0.01A
Current Accuracy	0.2%	0.2%
Max Power	10kW	15kW

Table 3.6: Specification for the EA-PSB-9080-240 and EA-PSB-9750-60 bi-directional power supplies.

Figure 3.7: EA-PSB 9080-240 power supply used for cycling modules below 80V, this is identical in appearance to the EA PSB 9750-60 which is used for cycling modules up to 750V.

For testing the Yuasa ESS, where high current and voltage is required, two EA-PSB-9750-60's were connected in parallel to give a maximum power of 30kW and maximum current of 120A. At the maximum voltage for the Yuasa ESS (688.8V), this is a maximum current of 43.55A, or 0.92C due to the power limit. As such, tests on this system were performed at a maximum of 0.9C.

3.2.2.2 Software

Additionally for this test rig, software was written to control the EA-PSB-9xxx-xxx using a PC, written in Python. This was done so that an upper system could monitor cell voltages reported by the BMS and control the power accordingly. Additionally, the data from the power supply and BMS were stored in a database. A block diagram of the software is shown in figure 3.8.

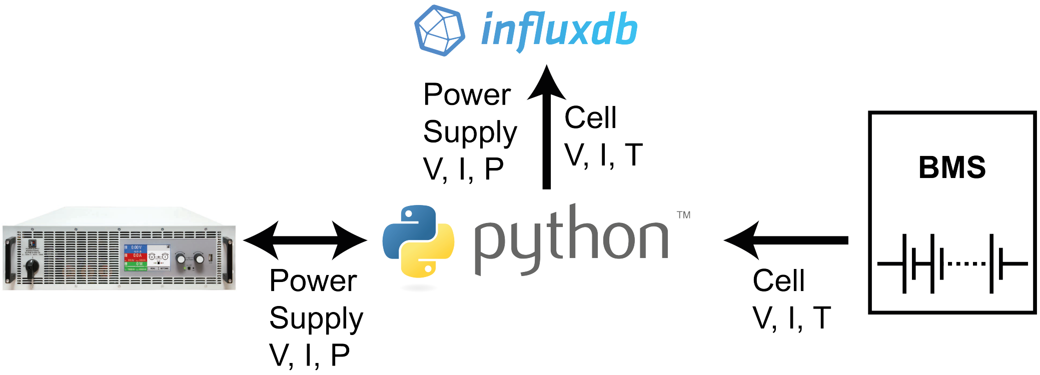

Figure 3.8: Block diagram representing the software controlling cycling and storing data for module and ESS testing.

3.2.3 Safety Considerations

Cycling cells and modules in a laboratory can be hazardous, should any of the safety limits be exceeded (over-voltage, under-voltage, over-current, over-temperature) which can result in a thermal runaway event. Therefore, significant work has been undertaken in order to ensure that experimental work can be performed safely, which is presented in a conference publication [118].

For testing modules and racks, additional safety components were added, as shown in figure 3.9. It can be seen that safety critical components include a contactor, fuse and fireproof enclosure. The contactor is driven by a BMS which considers all cell voltages, currents and module temperatures, ensuring that the contactor opens should any limit be exceeded. A fuse is in place to protect against accidental short-circuit. Finally, where possible, the modules are located in a fireproof enclosure to contain any failure should all protection systems fail.

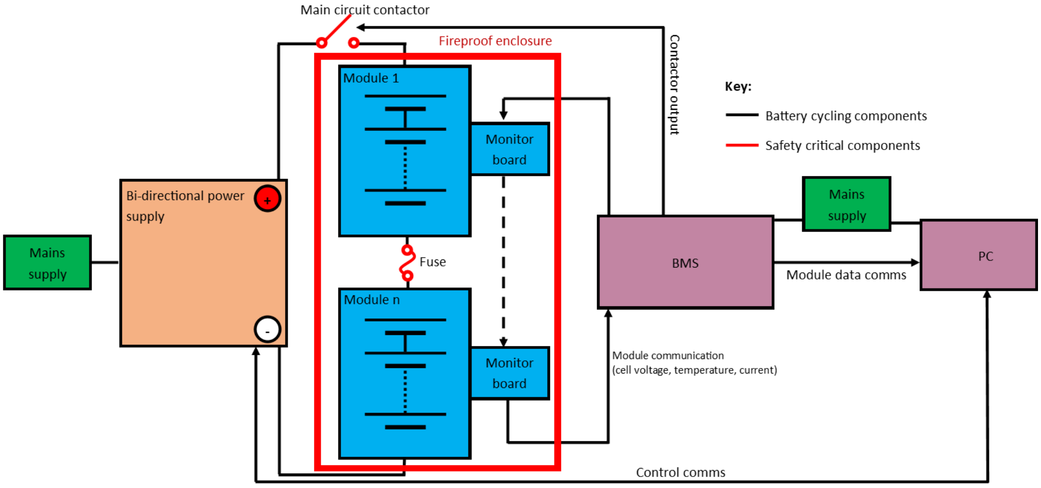

Figure 3.9: Diagram showing safety setup for testing battery modules and racks.

3.2.4 Grid-scale (Willenhall Energy Storage System)

One unique aspect presented in this thesis is thanks to access to Willenhall Energy Storage System (WESS), a 2MW, 1MWh grid connected battery operated by The University of Sheffield (TUoS). It consists of the aforementioned Toshiba SCiB modules, configured with 40 series strings of 22 modules. This gives an overall configuration of 2p268s40p. Key specifications are shown in table 3.7, and a picture of the system site is shown in figure 3.10. More details can be read in [26].

Max Voltage	723.6V (or any cell 2.7V)
Min Voltage	512V (or any cell 1.5V)
Max Current	3200A
Max Power	2MW
Capacity	1600Ah / 0.986MWh
Max Cell Voltage Imbalance	150mV

Table 3.7: Specification for WESS.

Figure 3.10: Image of the battery container (left) and inverter cabin (right) at WESS.

It is noteworthy that the lower limit of the system is 512V. This is due to the limits of the AC/DC converter. Theoretically, if all cells reached their minimum voltage (1.5V), the system would reach 402V. Considering the OCV-SoC relationship, limiting the lower limit to 512V (1.91V per cell) gives a theoretical effective maximum capacity of 0.977MWh.

The stated "Cell Voltage Imbalance" is defined as the voltage difference between the highest cell voltage in the system, and the lowest cell voltage in the system as:

$$V_{imbalance} = V_{cell,max} - V_{cell,min} \tag{3.1}$$

The system is controlled using a CompactRIO in LabVIEW, which communicates with the battery BMS and system inverters over Modbus. The control system samples at 100ms, and the inverters are capable of responding to a maximum power change (-2MW to +2MW) in 40ms. The system architecture is summarised in figure 3.11.

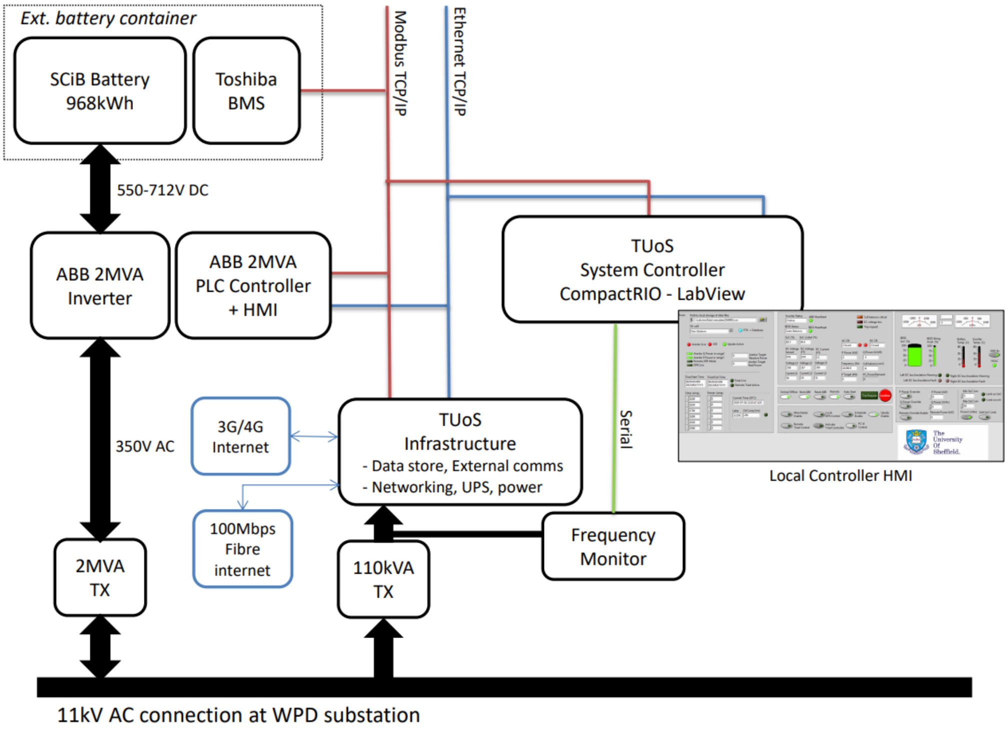

Figure 3.11: System Diagram of WESS. Adapted from [18]

3.2.4.1 Cell Level Monitoring

Modules in the system report cell-level temperature and voltage data over a CAN network to 10 “gateways” in the system. These gateways then report the minimum and maximum cell voltages and temperatures, and current for each series string to the BMS. This means that the full cell level data for the system is not stored, and merely aggregated data is stored.

Towards the mid-point of the PhD, it became clear that full cell-level data from WESS would be immensely useful in terms of verifying the findings of the presented work. To overcome this, 40 USBtin devices (CAN-USB interface) were installed, which are connected to a Raspberry Pi cluster. These report and store the data in a database. Images of these two core components are shown in figure 3.12. The CAN network reports at 120ms intervals. To minimise storage requirements, the Raspberry Pi's report the latest cell data synchronised at 0.5s intervals.

Unfortunately, due to the Covid-19 pandemic, this was not achieved until July 2021, and as such, only limited data is presented and used in the final chapters of this thesis.

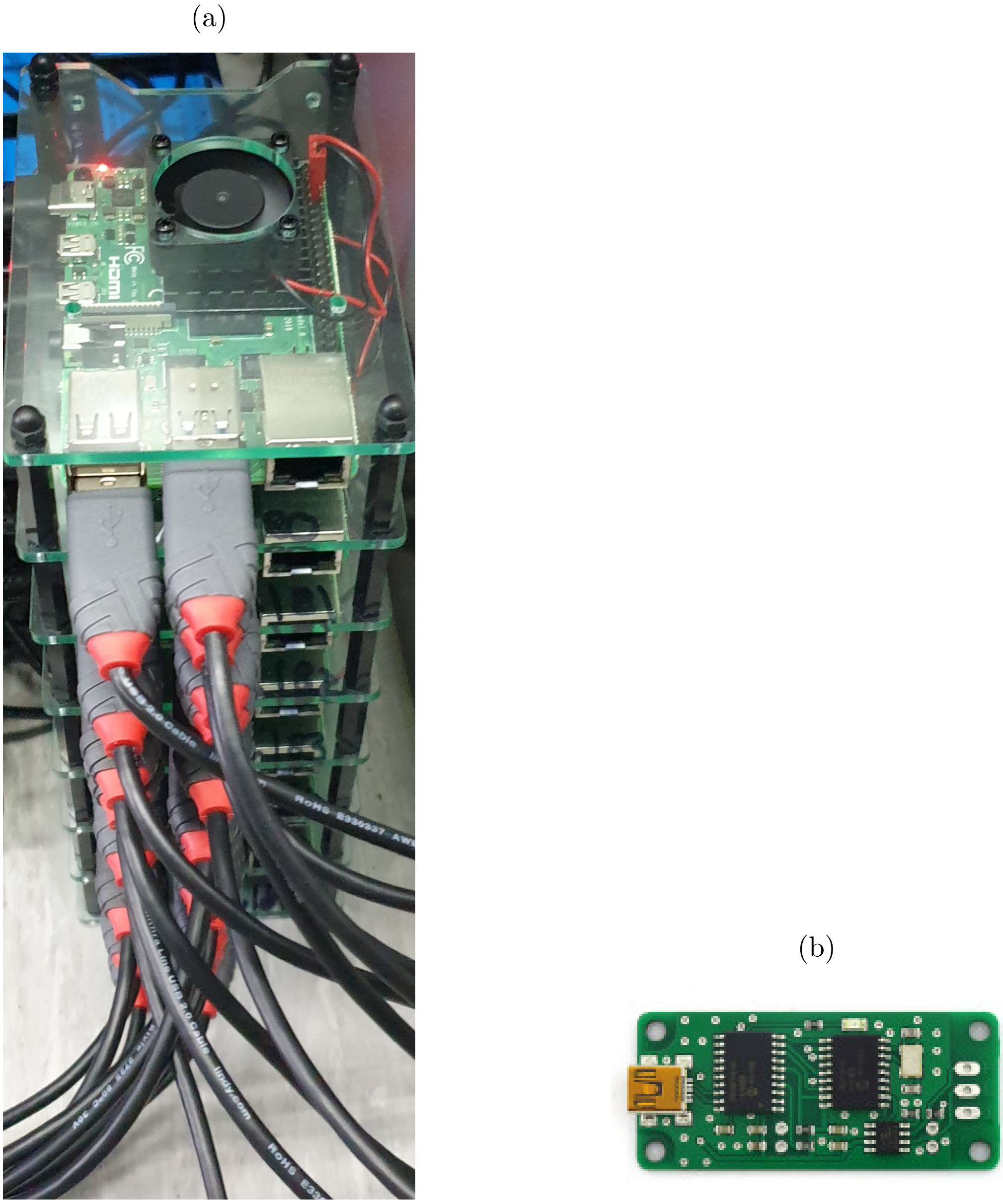

(a)

(b)

Figure 3.12: (a) Raspberry Pi 4 cluster and, (b) USBtin Device, used together to monitor cell voltage at WESS.

Chapter 4

Investigation into Cell Voltage Imbalance in Grid-Connected Batteries

4.1 Introduction

Chapter 2 introduced that differences between cells in a large pack impacts the utilization of the cells within that pack. It is important to understand the behaviour of these cells in grid-connected batteries in order to prevent undesirable operating conditions which could cause an unexpected shutdown and to provide an insight for better design to maximise battery capacity. In this chapter the observations from a WESS are presented and recreated under lab conditions for analysis.

Introduced in chapter 3, WESS is a grid-connected battery operated by TUoS. It is primarily a research battery, however has various revenue streams to help cover costs, which include performing: Dynamic Firm Frequency Response (DFR) (generation only), balancing market trading and triad avoidance to fund it's ongoing use. As a result, it has performed a large number of cycles, with a range of Depth-of-Discharges (DoDs) and C-rates. This chapter observes the data from these different types of cycles at the system level, with a particular focus on the effect of cell voltage imbalance. This is the level of data a system operator would see. The observations are then compared to cycles in a lab-based experiment at the module level, where individual cell voltages are monitored.

4.2 System Level cell voltage imbalance Observations

This section observes the behaviour of cell voltages in a BESS under different cycles, attempting to explain the observations. The following section then investigates whether these are seen at a smaller scale to verify the observations and give more detail on how the cells interact. From analysis of several years of data from WESS, there are two main types of cycles which appear to have an impact on the cell voltage imbalance. These are High DoD cycling and large power changes.

4.2.1 High DoD cycling

High DoD cycling occurs when the battery performs a large charge or discharge. For WESS, this has been observed for characterisation tests, triad avoidance, arbitrage, and recharging after performing grid frequency services. A typical high DoD cycle is shown in figure 4.1. This particular cycle was performed in 2018 for a simulated BM trade.

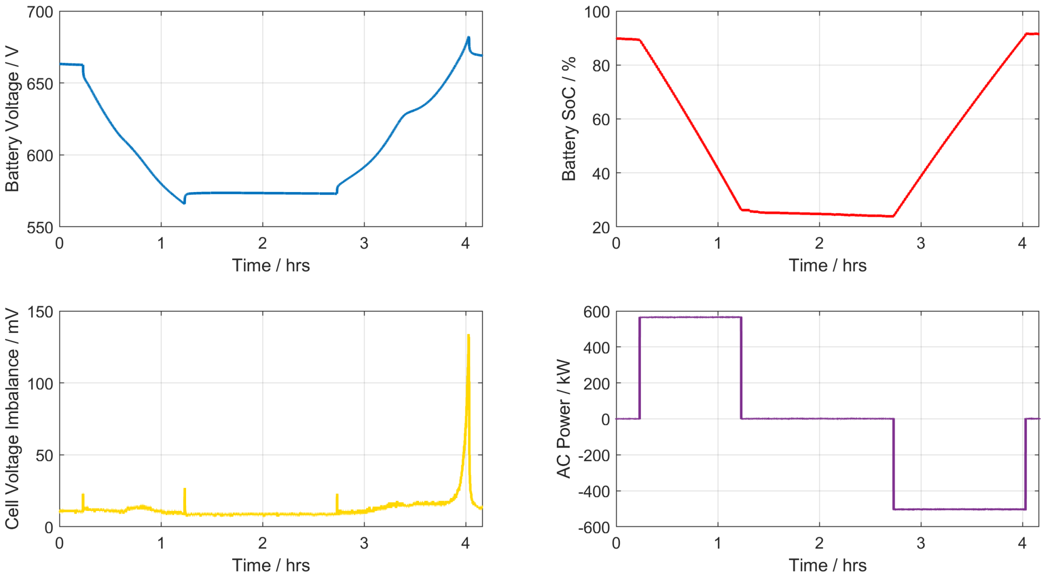

Figure 4.1: A typical discharge-charge cycle from WESS

Considering the cell voltage imbalance, it is immediately clear that there is a large increase as the cycle approaches the end of the charge portion (at ∼4 hours). The likely reason for this is due to a difference in capacity between cells. As the system charges, the cells reach slightly different SoCs due to the capacity difference. Work presented later in figure 5.30 shows that at around 90% SoC during charge, the impedance sharply increases, which would cause a sharp increase in voltage for the cells that have reached that point. For the higher capacity cells which will be at a lower SoC, they will not have reached the sharp increase in impedance and hence there will not be a large voltage change in those cells. This results in the large cell voltage imbalance seen in figure 4.1 at the end of charge, which then returns to the normal cell voltage imbalance upon the current switching to 0A.

It would be expected that this same phenomenon would be observed during discharge, as during charge, as there is a sharp increase in the impedance at around 10% SoC during discharge (again shown by later presented work in figure 6.9). This, however, is not seen. This is due to the operational constraints of WESS. Each cell has a voltage range of 1.5V to 2.7V. At WESS, with 264 cells connected in series, this gives a theoretical voltage range of 396V - 712.8V. However, the AC/DC converters have a minimum DC voltage of 512V, meaning the cells cannot reach the region where there is a sharp increase in impedance. Hence, little change in the cell voltage imbalance is seen during discharge.

It can also be seen in figure 4.1 that during the rest period there is a small discharge. Whilst the AC/DC converters are set to 0kW, there is a parasitic drain of ∼12A from the inverters on the battery. Opening the battery contactors removes this drain and little self-discharge is observed.

4.2.2 Large Power changes

Close inspection of figure 4.1 shows that during the moderate (∼570kW) step change in power at the start or end of the charge and discharge, there is a short "spike" in the cell voltage imbalance.

WESS is capable of 4MW change in power (+2MW to -2MW) in a short period (<80ms [26]). During these large power swings, it has been observed that the cell voltage imbalance increases significantly. One such observation, with a power change of 2MW, (-1C to +1C) is shown in figure 4.2.

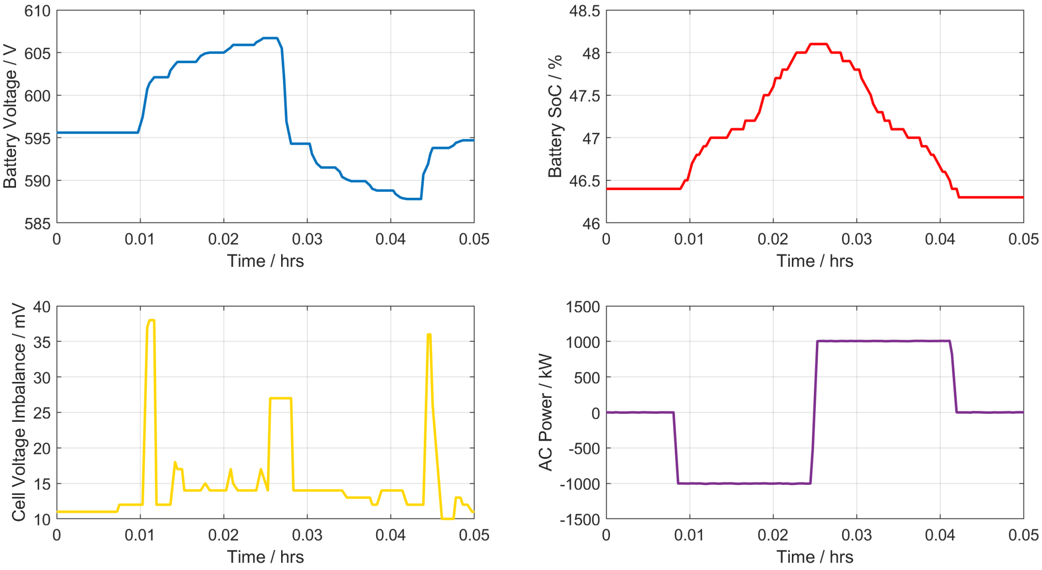

Figure 4.2: Power change at WESS of 2MW (-1MW - +1MW)

There are several potential causes for the imbalance occurring. Firstly, it could be that the BMS brings all cells to an equal voltage during a charge phase through the balancing system, and on changing to discharge, the cells then exhibit a different voltage drop caused by the battery impedance, causing the voltages between the cells to diverge. This seems unlikely, as the balancing does not occur fast enough at 0.003C maximum.

A second potential cause is with differences between the series strings that are combined in parallel to produce the overall battery. As the series strings are connected in parallel, they equalize voltage as current flows between them to bring them to the same charge level. When there is a significant change in current, there is a hysteresis effect, where the voltage of each series string will change due to the impedance in it. Current will then flow between the series strings until the voltage of each string is equal – a process which is not necessarily immediate as there is impedance in the connection between strings.

The final potential and most likely cause is that there is a delay in sampling the cell voltages. The modules report cell voltage every 120ms, however this is reported to a subsystem which then reports back to the BMS which calculates the cell voltage imbalance based on the voltages it receives. The time for the BMS to receive all cell voltages is unknown. This is the most likely cause, as the pattern of cell voltage imbalance has an inconsistent trend - during some of the power changes, there are multiple peaks in balance changes - likely reflected by the different strings returning cell voltages at different points.

4.3 Module Level cell voltage imbalance Observations

A set of experiments were designed and performed to better understand the observations seen on the large scale BESS. These were performed on two types of modules – Toshiba SCiB 2p12s modules (identical to modules in WESS) and Yuasa LIM50EN 12s1p modules. The Yuasa LIM50EN was used in addition to explore the behaviour of different chemistries. Two modules were connected in series to give a total of 24 series cells for both the Toshiba SCiB and Yuasa LIM50EN, providing easily comparable results. The test procedure involved performing 3 cycles at 1C whilst recording the cell voltages. The data for the third cycle is then used, allowing time for the battery to reach a thermal steady state. This test procedure is summarised in table 4.1. This should demonstrate the operational issues that are seen in WESS, with the test giving a large power swing when changing from charge to discharge in a cycle and also allowing the modules to reach cell voltage limits, showing the spread of cell voltages at these points. The results for the Toshiba and Yuasa modules for 1C cycles are shown below in figures 4.3 - 4.6.

	Step	**Sequence**	**Limits**	**End Condition**
Achieve Thermal Equilibrium	1	CC Charge	I = 1C	Any Cell >= Max V
	2	CC Discharge	I = 1C	Any Cell <= Min V
	3	CC Charge	I = 1C	Any Cell >= Max V
	4	Loop	Loop to 2	After 1 loop
Test Cycle	5	CC Discharge	I = 1C	Any Cell <= Min V
	6	CC Charge	I = 1C	Any Cell >= Max V

Table 4.1: Procedure for cycling Toshiba SCiB modules and Yuasa LIM50E Modules.

Initially, the Toshiba SCiB modules were tested. They are the same modules used in WESS, and as such give the most helpful comparison to previous results. It can be seen that similar results are observed at high SoC as with WESS - around 80mV of cell voltage imbalance is seen at the end of CC charge. This is less than the 140mV seen in WESS, however there are fewer cells and it is a newer system, so it is likely the cells are more balanced in the modules than WESS.

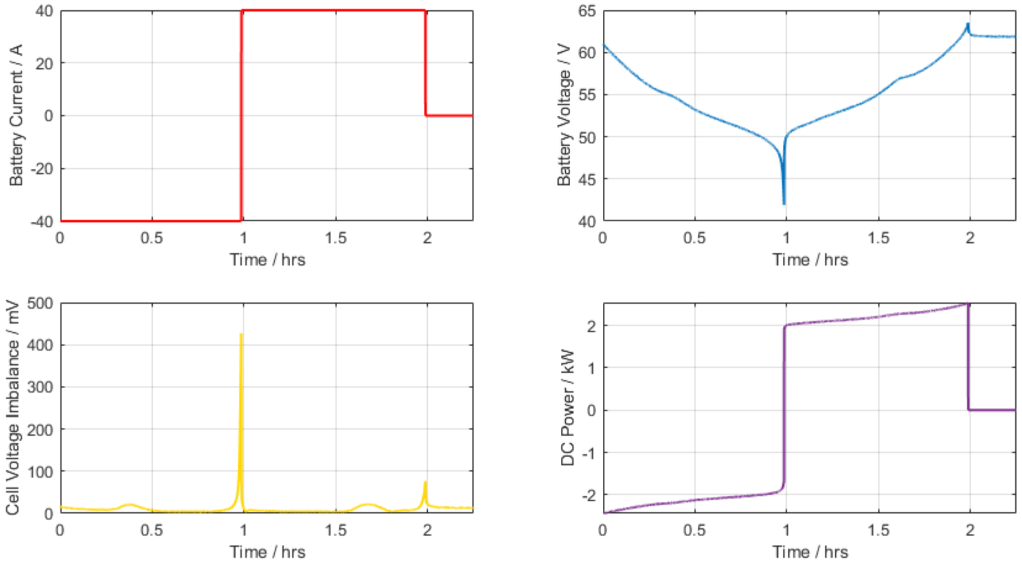

Figure 4.3: 1C test of two Toshiba SCiB modules connected in series.

At low SoC, a large imbalance of 430mV is observed at the end of discharge. This was expected as explained with WESS, as the module test can reach the full voltage range of the cells. It can be seen that the system only reaches 42V, whereas the theoretical minimum module voltage (all cells at 1.5V) is 36V. This is because one cell will have reached 1.5V. This is more clear by observing the cell voltages at the end of charge and discharge, as shown in figure 4.4.

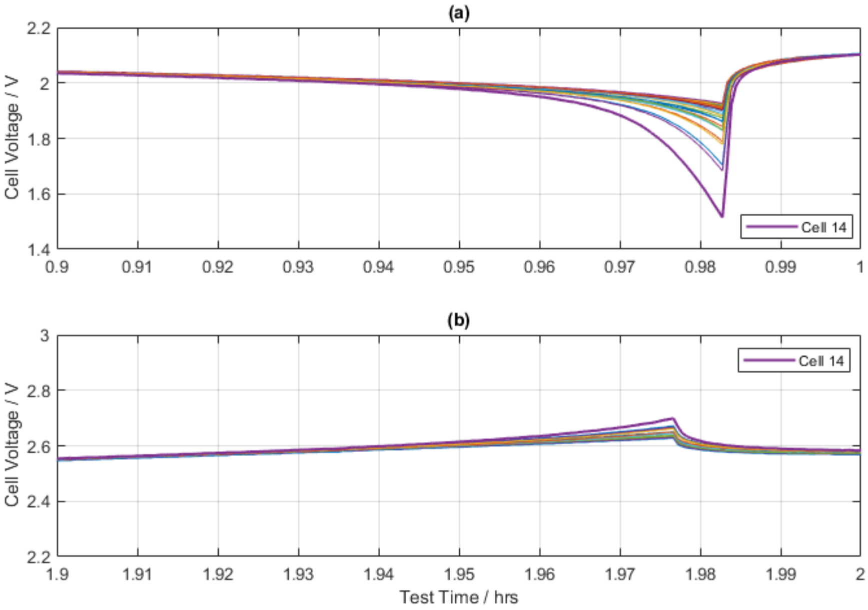

Figure 4.4: Cell voltages of two Toshiba SCiB modules connected in series, (a) approaching end of discharge, (b) approaching end of charge.

This is the same approaching 100% SoC, however there is less deviation in the cell voltages. It is noteworthy that a single cell reaches both the maximum and minimum cell voltages. It is likely that this cell has a lower capacity than the other cell as opposed to the pack being poorly balanced. With the 2C change in power between discharge and charge, it can be seen that there is no significant deviation in cell voltage imbalance. This suggests that it is not related to the cell balancing mechanism. Instead, it could be the sampling rate, or the parallel nature of the system. This could be clarified through collecting cell-level data from WESS.

Considering the Yuasa LIM50E modules, a similar result is seen in figure 4.5, with a large deviation in cell voltage at low SoC and a slight deviation in cell voltage at high SoC. This is different at high SoC due to the difference in the impedance-SoC relationship, shown in figure 6.5, where there is only a small increase in impedance towards 100% SoC. At low SoC, the impedance-SoC relationship is similar to the SCiB cells, where there is a large increase in the impedance.

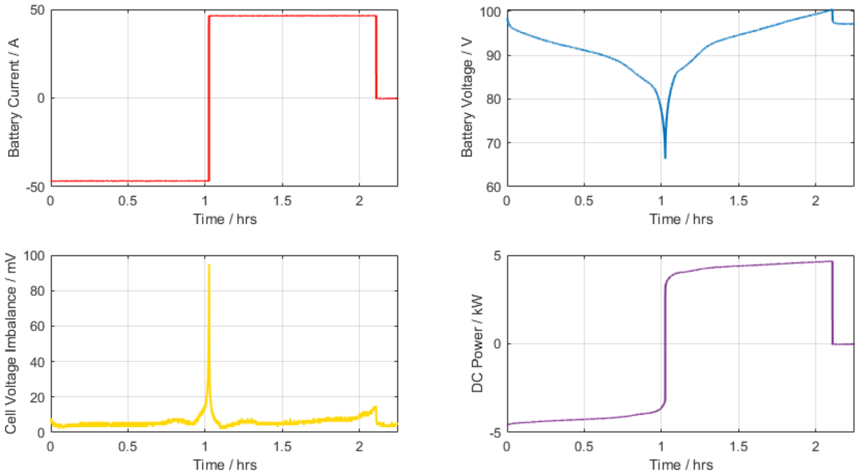

Figure 4.5: 1C test of two Yuasa LIM50EN modules connected in series.

Considering the cell voltages, shown in figure 4.6, as seen with the SCiB modules, a single cell reaches the maximum and minimum cell voltages. This single cell will limit the capacity of the two modules to the capacity of that cell.

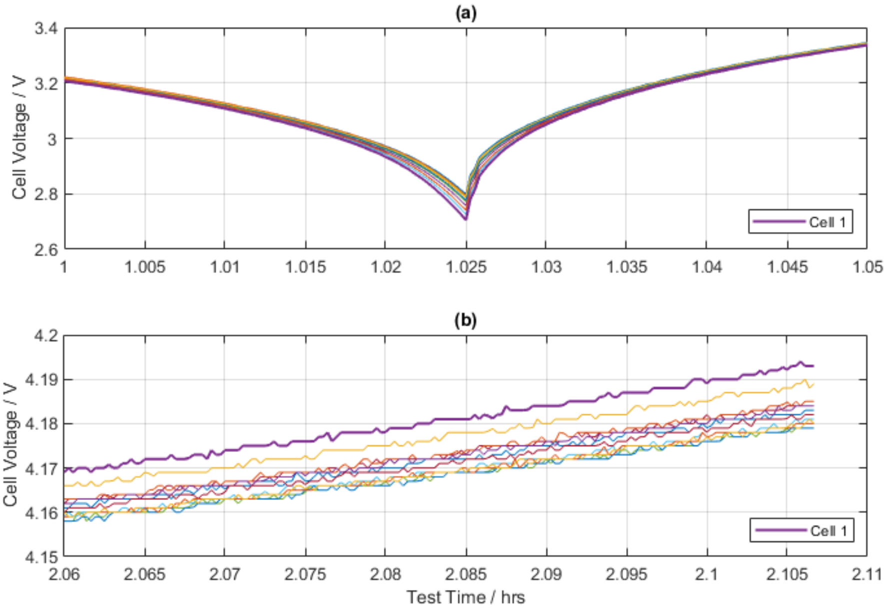

Figure 4.6: Cell voltages of two Yuasa LIM50EN modules connected in series, (a) approaching end of discharge, (b) approaching end of charge.

4.4 Implications for grid scale storage

For WESS, the main implications of a high cell voltage imbalance is that it trips (the main breakers open) when the cell voltage imbalance exceeds 150mV. This is a value set by the manufacturer, and used to prevent high currents between parallel strings. Additionally, the system will trip should any cell exceed the voltage limit. Tripping is not a desirable event as it means a trade or service will not be completed, resulting in monetary charges, and additionally there will be increased wear on the circuit breakers, which could cause early failure or require shorter maintenance intervals.

To prevent this, two main methods could be used which are expected to be used by battery asset owners. Firstly, by limiting the SoC range to be outside the sharp change in impedance, the cell voltage imbalance can be kept to a minimum. Considering the cell impedance for the cells used in WESS (presented in figure 6.9) a reasonable range would be 10% to 90% SoC.

The second method is to curtail power based on the cell imbalance to limit it. This is done simply by applying a power multiplier based on the cell voltage imbalance, where the power will reduce as the cell voltage imbalance increases, shown by figure 4.7. By reducing power, the cell voltage imbalance will reduce as it is caused by the increased impedance increasing the voltage drop. Reducing the current will reduce the voltage drop and therefore the imbalance. This is the method currently used in WESS, an example of which is shown in figure 4.8

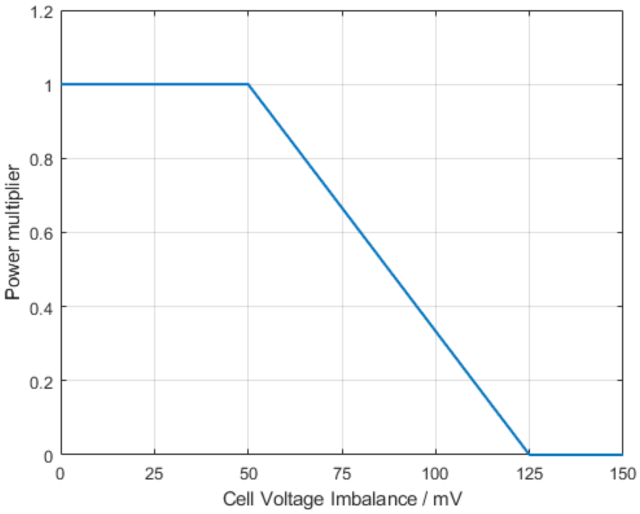

Figure 4.7: Power curtailment method used for WESS.

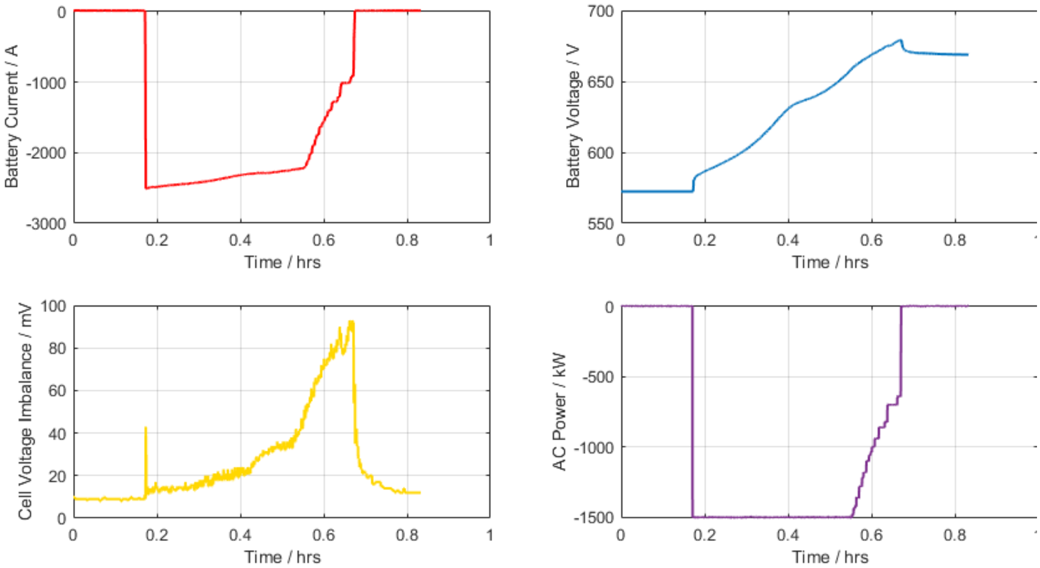

Figure 4.8: A 1.5MW charge cycle at WESS, showing the reduction in power to maintain the cell voltage imbalance below 50mV.

These methods are useful to prevent trips, however, resulting in either a reduced capacity or failure to fully deliver a service, as will be discussed further.

By limiting the useable SoC, the income potential is reduced. As an example, table 4.2 and figure 4.9 show a 41MWh / 41MW BESS performing a 38MWh trade in the EPEX Intraday market with instructions received from NGESO for a change in power [19].

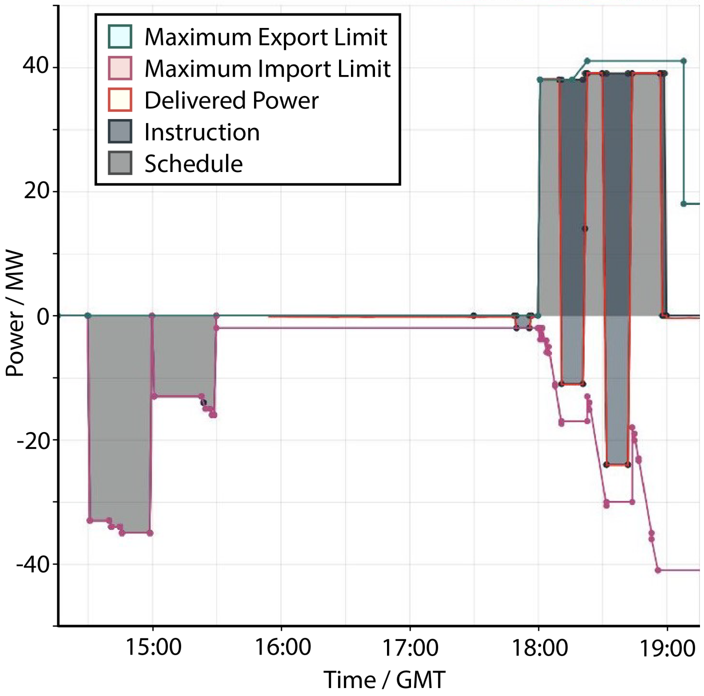

Figure 4.9: Trade by a 41MWh battery in February 2021. (adapted from [19])

Time	**Type**	**Power / MW**	**Price / £/MWh**	**NGESO Instruction / MW**	**Instruction Price / £/MWh**	**Net Power / MW**	**Revenue / £ (Expense is negative)**
15:00-15:30	Scheduled	-34	60 (estimated)	0	n/a	-35	-1050
15:30-16:00	Scheduled	-23	60 (estimated)	0	n/a	-23	-690
16:00-17:45	Scheduled	0	n/a	0	n/a	0	0
17:45-17:55	Scheduled	2	60 (estimated)	0	n/a	2	-20
17:55-18:00	Scheduled	0	n/a	0	n/a	0	0
18:00-18:10	EPEX Intraday Market Trade	38	685	0	n/a	39	4338
18:10-18:20	EPEX Intraday Market Trade	38	685	-49	600	-11	9238
18:20-18:30	EPEX Intraday Market Trade	38	685	0	n/a	38	4338
18:30:18:40	EPEX Intraday Market Trade	39	685	-63	600	-24	10752
18:40-18:59	EPEX Intraday Market Trade	39	685	0	n/a	39	8563

Table 4.2: Trade by a 41MWh battery in February 2021.

The total income for this trade is £37,230. Including the initial charge, during this period the system made a profit of £35,470. Reducing the capacity by 20% (10% to 90% SoC range) would reduce the 38MWh trade to 30.4MWh. This would reduce the income of this trade to £32,024 - a reduction of £5,206 or ∼14%. If this trade were performed daily, this could result in a loss of income of ∼£2 million over a year, or ∼£4000/MW/month.

It does not appear that reality is as extreme as the example for this asset, however, only 38MWh has been bid, where 41MWh is the capacity of the battery. It is possible that this is due to the same power limiting issue, or a lesser understanding of the operating performance leading to increased capacity overhead requirements. Increasing the example trade to 41MWh would give an increased income of £2055 or ∼5%. Over a year, this would be an increase of £750,000. This scenario, with such high prices seems to be a rare occurrence, however, giving a much higher than average revenue. To give an approximate expected income for a BESS, research presented by Brogan et al. suggests a theoretical revenue for a 1MW, 2.5MWh BESS to be ∼£25k/MW/month [119] (converted from Euros) whilst BESS assets from Gresham House achieved ∼£10k/MW/month [120].

Considering instead power curtailment. Trades are made within half hour periods. Should the power curtail, then the full amount of energy would not be delivered or received due to the reduced power. For the example in figure 4.8, 688 kWh were received (battery charging), whereas 750kWh was the bid amount. This is a shortfall of 62kWh. In this case, the energy was paid for which was not charged into the battery. Were this more predictable, the initial power could have been higher, then reduced as the power curtails to charge by the full amount of energy during the half-hourly period.

These examples show that better diagnostics of the system behaviour could provide more confidence when making trades and providing services. Sections 4.2 and 4.3 show the behaviour of cells in these circumstances and will be used to inform the ongoing work in this thesis.

4.5 Conclusions

In this chapter an observed cell voltage imbalance issue from operation of a grid scale BESS is presented. Using modules under lab conditions, the observations are recreated to allow analysis at the cell level. It can be seen from series connected module testing that cell voltage imbalance is an issue when the cells approach the upper and lower limits of the SoC with an increasing spread of voltages across cells. It is possible to mitigate this by limiting the range of the SoC used or by curtailing power as cell imbalance increases, however this reduces the usable capacity at constant power and curtailing power may not be possible depending on the service being provided. From the results of the tests it is shown that large changes in power do not cause increased cell voltage imbalance in series connected strings and therefore is a potential issue limited to parallel connected strings only.

The work presented demonstrates that there is a need to accurately predict available energy to a trader, to maximise revenue from a battery asset. This could be achieved through empirical modelling based on the system power and energy. Alternatively, a more mechanistic model which considers individual cell behaviour could be used, which is the method used going forwards.

Chapter 5

A fast variance based Grid Scale Battery Model

5.1 Introduction

Chapter 4 introduced how cells connected in a pack are not identical, and that this can affect the performance of the overall pack. For a series string, it was shown that the overall capacity of a pack is limited by a single cell. This chapter explores creating an accurate yet computationally efficient model which takes into account this behaviour, combining different approaches

When performing analysis on a multi-cell pack, such as real-time state estimation or simulation, there are two main approaches (introduced in chapter 2) that are used when modelling the pack. The first is to model every cell individually, as represented by figure 5.1, and discussed in [115, 121]. This would give the most complete picture of the state of the battery, with an estimate for every single cell in the pack to give the best understanding of the overall pack performance. However, it is challenging to monitor, store, and process data from every cell in a pack. As an example, in WESS, there are 21,120 cells. There are typically 2 bytes per data frame for each cell containing voltage readings which are reported by the cell management system to the battery management system every 120ms. This is 21.1KB of data per 120ms and therefore 176KB/s. Over a single day, stored with no compression, this would produce 15.2GB of data. While not impossible to deal with, processing all data in real time for every cell in the pack could pose a challenge due to the large processing requirements. Various solutions have been proposed and implemented in different systems, including pre-processing in each battery module and reporting back information such as SoC and SoH for each cell, rather than just voltage data [8]. Even with the processed information for each cell, this will still not be able to give a complete picture of the overall output performance of the battery - the state of charge or the overall available energy capacity at the terminals. This would again mean further processing to give this information.

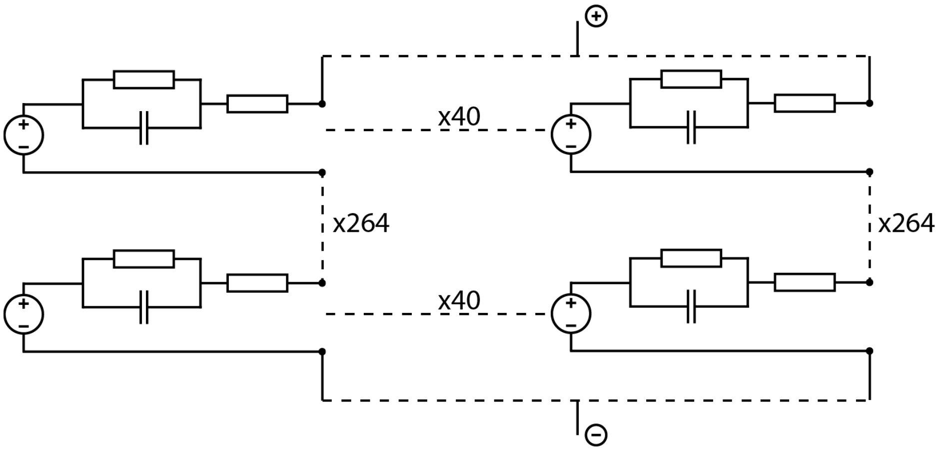

Figure 5.1: A model representation of WESS showing every cell being modelled, with each string containing 264 parallel pairs of 2.7V (max), 20Ah cells. There are 40 strings connected in parallel.

The same issues are faced in the simulation of large-scale packs. As an example, modelling a single cell with a zero-order Equivalent Circuit model (Rint Model [41, 103]) in Simulink as detailed in section 5.2.1, takes 1.7s to perform a single cycle (charge and discharge) at 1C with a 1s sample rate on a modern computer (CPU - i7 7700, 24GB RAM, SSD). A number of simulations were performed with different pack configurations for 7200s simulation time and the results can be seen in figure 5.2 which shows how the real processing time varies with the number of cells being simulated.

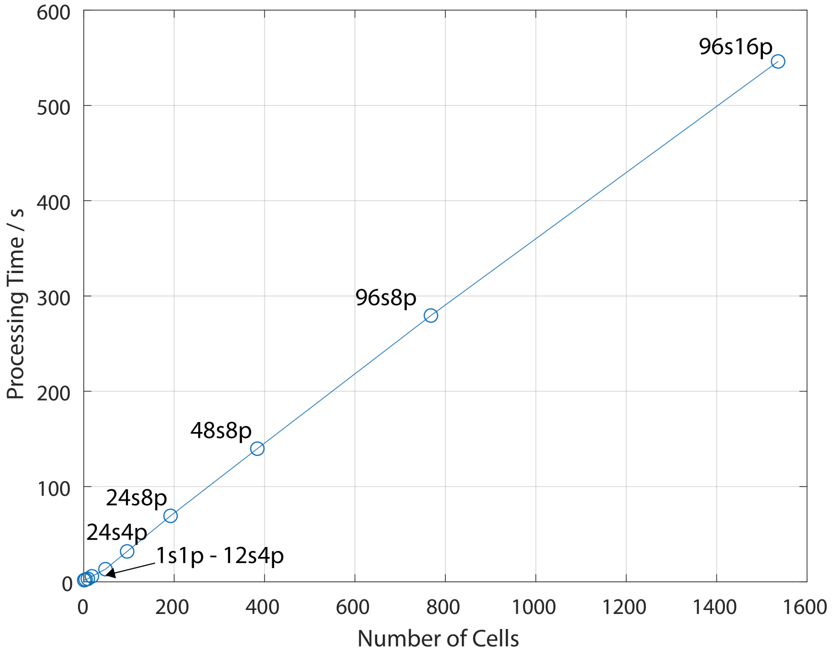

Figure 5.2: Processing time vs number of cells for a Rint model for various pack configurations.

Interpolating figure 5.2 for WESSs 21,120 cells, it can be estimated that simulating WESS for a simulation time of 7200s would take approximately 7500s of processing on a modern computer (specification mentioned previously). With the processing time being longer than the simulation time, it makes the approach unsuitable for real-time applications and time consuming for general simulation, though the ever advancement of computing power may see this approach more feasible in the future.

The second approach is to model the entire pack as a single cell model such as those seen in [106, 122]. It can be effective as it is fast and straightforward to implement and allows the use of a more computationally intensive cell model as only a single cell is simulated. However, the main issue with this is the loss of accuracy in the model due to the cells in the pack not being identical. In other words, at any given time, the cells will not necessarily all have the same voltage and current flow due to differences in capacity, impedance, and other parameters. For a practical system, it is expected that modelling the pack with a single cell model would result in the system reporting a larger amount of energy available than is actually available, due to some cells reaching their voltage limits before others meaning some cells have unreachable capacity. This would vary depending on how well balanced the system is at any given time.

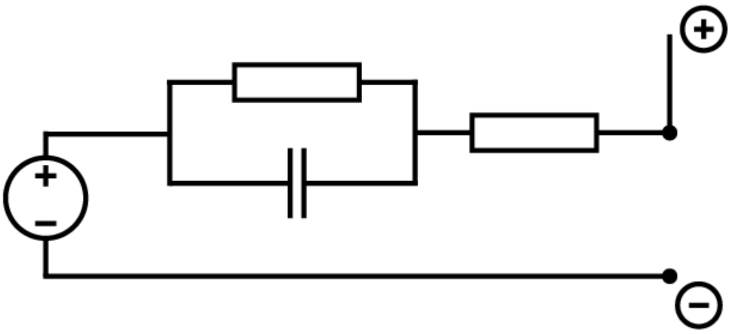

Figure 5.3: A single cell model representation of WESS showing just a single cell being modelled, totalling the voltage and capacity of the model shown in figure 5.1.

In reality, the only important readings are the lowest and highest cell voltage as a full charge / discharge cycle must end or change when one cell reaches its upper or lower voltage limit. The work in chapter 4 has shown that in general, this will always take the place of a single cell which can be considered the “weakest cell”. The weakest cell in a series string will reach its voltage limit before all others, assuming the string is balanced. In this work, a string or pack is considered balanced if the SoCs of all cells become equal at any point during a cycle.

The approach proposed in this chapter aims to improve on these large battery pack models, by producing a model with a sufficient view of the state of the cells within the system, without having to model every single cell. The approach revolves around the concept that its only necessary to know the maximum and minimum cell voltages to predict the remaining charge that can be put into the battery and removed from the battery. One method is to model the single weakest cell (the cell with the lowest capacity and highest impedance) alongside the model representing the whole pack. This results in the model consisting of just two cell models.

This should show an improvement in the accuracy, but the model lacks the data for currents inside the system (such as between parallel strings), so assumes that there is equal current between strings in the system. Furthermore, it cannot give a measure of cell voltage imbalance - the difference between the highest and lowest cell voltages. Many systems operate with cell voltage imbalance as a limit as mentioned in chapter 4, to prevent large currents between parallel strings. These two metrics (cell voltage imbalance and maximum string current) should therefore be output from the model.

To give a value for cell voltage imbalance for a series string, it is proposed that 3 cell models are required. The strongest cell, the weakest cell, and the remaining cells as a single cell model, shown later in figure 5.15. This study defines the weakest cell as the cell which reaches the upper / lower voltage limits under charge / discharge and the strongest cell is defined as the cell which remains furthest from the voltage limits, assuming the pack is balanced at a given SoC (i.e. the cell voltages converge at a the given SoC). This will give the highest, lowest, and average cell voltage, as well as the SoC of each cell model and therefore the overall SoC. Current is constant between cells in the string.

To give a value for the maximum current between any number of cells connected in parallel, it is proposed that 3 cell models are required. Again, the strongest, weakest, and remaining cells, shown later in figure 5.17 As the voltage is constant in the parallel connections, the current between the cells can be calculated. It is expected that this will give the maximum current, as there will be the highest current through either the strongest or weakest cell. From this, to model a pack of any size with any combination of parallel and series connections, at most nine cell models are required as a combination of the series and parallel models, which is the final model proposed in this chapter, represented in figure 5.4. The model can then be used to predict useful metrics including:

1. Available energy capacity in the pack at difference C-rates
2. Capacity of pack in different configurations at different C-rates
3. Efficiency of pack in different configurations

4. Power curtailment curves to manage cell imbalance

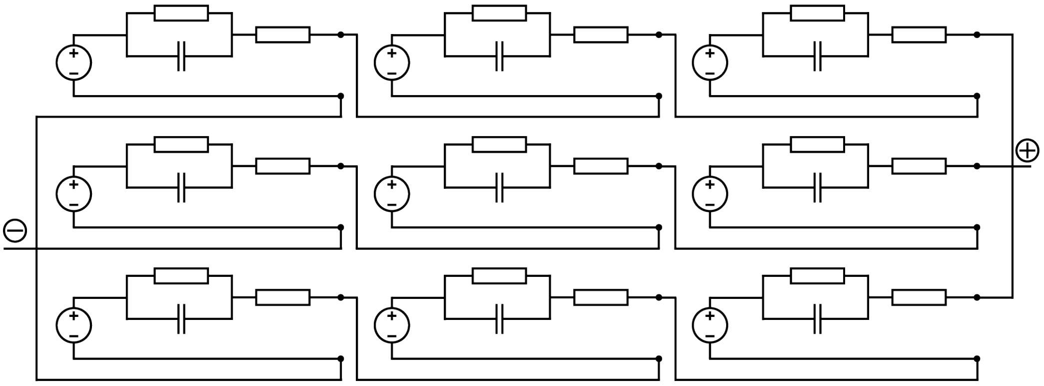

Figure 5.4: Configuration of the 9 cells model proposed in this chapter.

The above list mentions the available energy capacity in a pack. This is different from SoC, where SoC is the total capacity remaining in the cells in the pack, relative to the capacity of the pack. Typically, a large pack cannot reach its true 100% SoC or 0% SoC due to the difference in cell voltage, meaning that one cell may reach a voltage limit, while others have capacity remaining, as discussed in [12]. This is generally caused by varying impedance and capacity between cells. Available energy at different C-rates may be a more suitable metric to a user of a large pack than SoC.

The author hypothesises that this depends on the variation between the cells. That is the difference between cells in the key parameters capacity and impedance. A sample of cells with a greater variance will have a lower capacity as there is a greater chance that there will be a weak cell according to the distribution. And therefore, the larger the sample for a given variance, the weaker the weakest cell will be in comparison to the strongest and the mean.

5.2 Modelling

The proposed model containing 9 cells to make up the overall pack model is produced using Simulink named 9 Cells Model (9CM). This section will discuss the architecture of the model, beginning with the individual cell model, discussing the input parameters, and justifying the details of the model. It will then be shown how the 9CM is scaled from single cell models.

5.2.1 Cell Model

The cell model was built in Simulink, functioning as a Rint model, as shown in figure 5.5 where the internal resistance varies with the current direction (charge or discharge) (seen in [105, 121]) and the temperature. Additionally, the capacity degrades on cycling [41] [103]. One negative aspect of the Rint model is that it will not correctly show the dynamic behaviour of the pack, meaning that during a large change in current, the voltage shown by the model may not exactly match experimental values due to the transient behaviour of the battery. The Rint model was however chosen for several reasons. Firstly, in a grid-scale system, the largest concern is about reaching the voltage limits. The Rint model will show the 'worst case scenario' where the steady-state behaviour will be reached immediately. Next, the study is looking more closely at the variations between large numbers of cells. It is relatively straightforward to identify the parameters for the Rint model, meaning a large dataset can be used to give the variance of a group of cells without the need for impedance measurements at a range of frequencies on individual cells. Finally, this study is more concerned with the process of modelling a large number of cells, rather than producing a unnecessarily complex cell model. The parameters that are considered are those that are most relevant to a grid scale system, however, it would be possible to increase the order of the model if the results show that a Rint model is insufficient. Figure 5.6 shows the design of the cell model in Simulink.

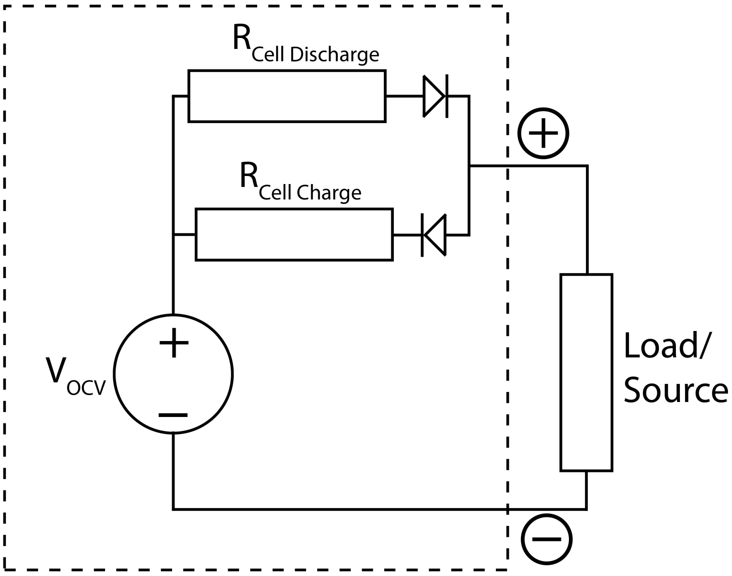

Figure 5.5: The proposed Rint cell model.

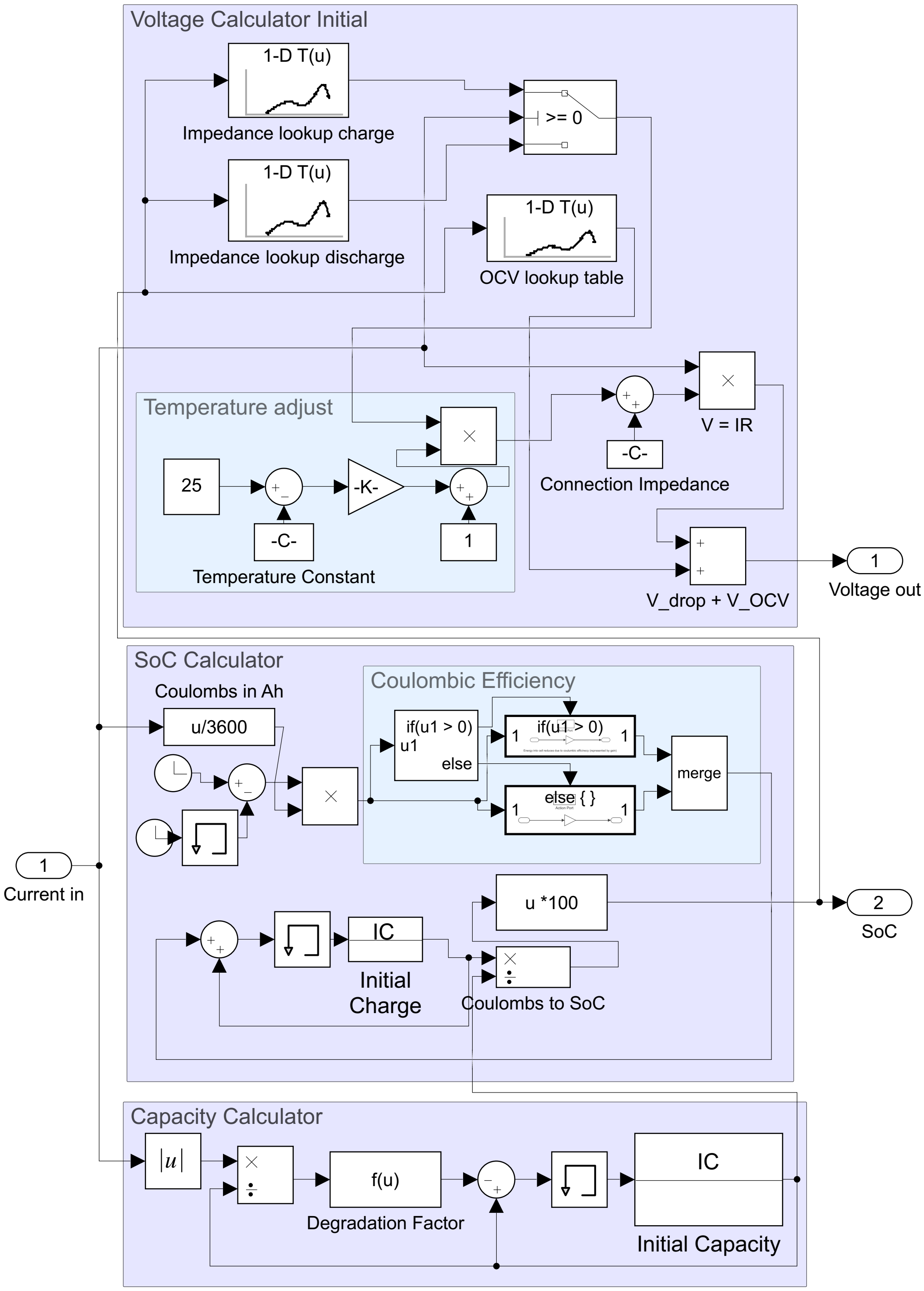

Figure 5.6: Implementation of the Rint model in Simulink

5.2.1.1 Model Parameters

The physical parameters which are used in the model include:

1. Capacity
2. OCV
3. Impedance
4. Temperature
5. Coulombic efficiency
6. Degradation rate.

Each of these parameters has been considered individually and experimentally verified to determine how they are implemented in the cell model. This section describes the chosen implementations for each parameter.

For experimental validation, a sample of ten Yuasa LIM5H cells were used (the specification can be found in chapter 3). Ten cells were used to give nine cells to identify the parameters for the 9CM and a spare. They were chosen as they are of a lithium-NMC type chemistry - a widely used cell chemistry [123].

5.2.1.1.1 Capacity

Introduced in chapter 2, the capacity of a cell describes the Coulombic charge which can be extracted from or input to it, before voltage limits are reached. The capacity of a cell is measured using a CCCV charge / discharge test to determine the maximum capacity of a cell, using the procedure shown in table 5.1. Using a CCCV discharge to measure capacity is atypical, but is used in this case as the capacity must represent the full Coulombic charge stored in the battery.

	Step	**Sequence**	**Limits**	**End Conditions**
Capacity Test	1	CCCV Charge	V >= Max V, I = 1C	I <C/20 A
	2	CCCV Discharge	V <= Min V, I = 1C	I <C/20 A
	3	CCCV Charge	V >= Max V, I = 1C	I <C/20 A

Table 5.1: Test procedure for measuring capacity of cells.

The CV cutoff current used is C/20, a value commonly used in literature [124,125]. This is an important choice as a model would consider the battery to have reached 100% or 0% SoC once a CV charge or discharge has reached C/20, even though more energy could be charged or discharged at lower C-rates. In the literature, C/20 appears to be a suitable balance between having a good measurement for capacity and not having an unnecessarily lengthy test time.

5.2.1.1.2 OCV

Introduced in chapter 2 Open-Circuit Voltage (OCV) refers to how the voltage of a battery at rest (i.e., no current flow and the voltage is unchanging) changes depending on the charge in the battery. It is highlighted in [41,54] the importance of good OCV measurement for having a good SoC estimate.

It is important to understand how the OCV changes depending upon the state of charge. When using a Randles model, OCV is the key in determining the voltage at any point, with the voltage deviating from OCV on the application of current and subsequent voltage drop [126].

The datasheet for any particular cell generally states OCV, however it is useful to perform a test to verify this. This involves discharging in 10% increments of SoC, followed by charging in the same increments as shown in figure 5.7.

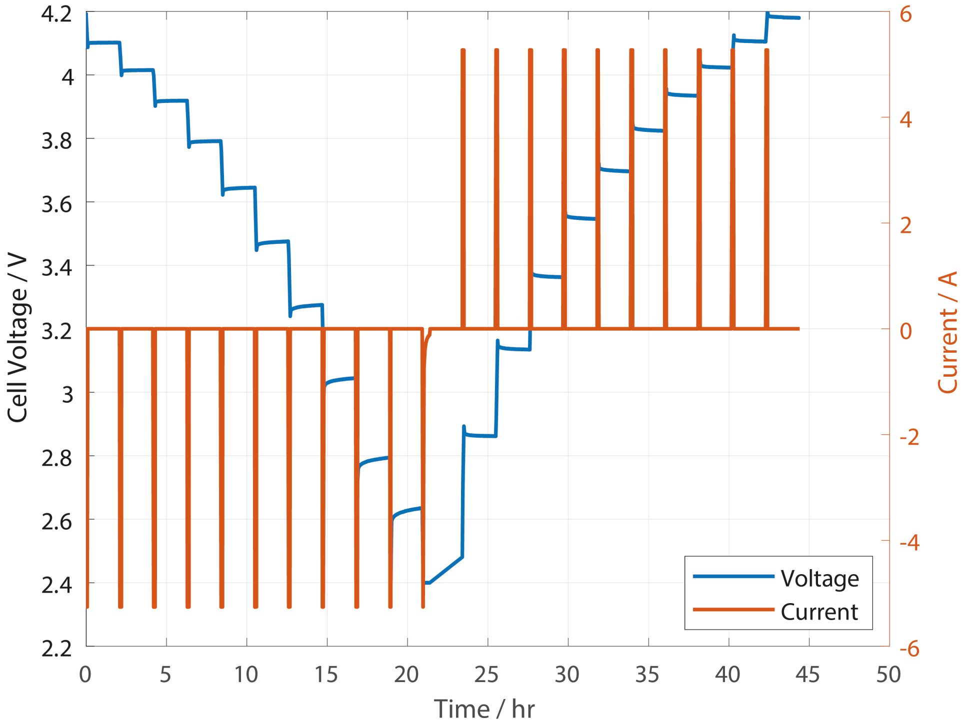

Figure 5.7: Experimental test profile to find the OCV-SoC relationship of LIM5H cells

The test begins with a full 1C cycle to ensure consistent behaviour (not shown in figure 5.7) before performing the OCV test. The capacity test is performed immediately before the OCV test, as the capacity is needed to perform the OCV test. Once the capacity of the pack is known, the pack is discharged and then charged in 10% capacity increments at 1C, with a CV discharge at the end of the last discharge pulse to ensure the cell is at 0% before beginning the first charge pulse - a method seen used in literature [86]. There is a 2 hour rest between each pulse and the average voltage between the charge and discharge for SoC is taken to eliminate any hysteresis or to compensate for where the cell has not completely reached a constant resting voltage - the latter typically occurs at a low SoC as seen in figure 5.7.

Considering SoC accuracy for each pulse point for the OCV test shown in figure 5.7, the discharge capacity measured during the capacity test was 5.256

Ah and the total capacity discharged during the pulse discharges totalled 5.274 Ah. This is a 0.3% difference meaning each OCV measurement is within at least that margin of error in terms of SoC.

5.2.1.1.3 Impedance

Impedance in a cell causes a voltage drop due to the current through it. Various methods have been used to measure the impedance of the LIM5H cells in this study, with varying test times and varying results. These will each be analysed to determine which is the ideal test to use for parameter identification of impedance.

EIS

EIS is a commonly used technique to measure the impedance of a cell across a range of frequencies. It can be used to assist with identifying the parameters of multi-order equivalent circuit models of cells [127] [128]. It is time consuming to perform EIS measurements and the test is unnecessary to identify parameters for a Rint model, as the frequency response of the battery is not represented by the model. Therefore, this will not be considered further.

Single-frequency impedance

Using a 1kHz impedance tester such as a Hioki BT3554 can be a very fast way to measure the impedance at a fixed frequency. While not the most useful measure for the battery model, it could be a good way to track impedance changes over time. One benefit is that the cell is not subject to high currents for any extended period, so it is a useful method to track the change in impedance relative to temperature, as the act of measurement will not affect the cell temperature and therefore the impedance. It is a value often quoted in a cell's datasheet. [129]

DC Internal Resistance

In the Rint model, the voltage is dropped across the series resistance, seen previously in figure 5.5.

The voltage drop can be found as $V_{drop} = IR$ and the impedance (R) can therefore be found through a known change in current and measuring the subsequent change in voltage as:

$$R_{DCIR} = \frac{\Delta V}{\Delta I} \tag{5.1}$$

While straightforward, this presents issues in measurement. Immediately measuring the voltage after a current change will result in a low value for R_{DCIR} due to the transient behaviour. Measuring the voltage after a longer period of time after a current change to a nonzero current would result in a change in SoC and therefore give a larger R_{DCIR} reading. Therefore, a suitable way to calculate R is to measure the voltage once it has reached steady-state and change the current from a specified value to zero to eliminate a change in SoC [125]. The decision then lies on how long a rest period is required to reach the end of the transient behaviour, where the voltage returns to the OCV.

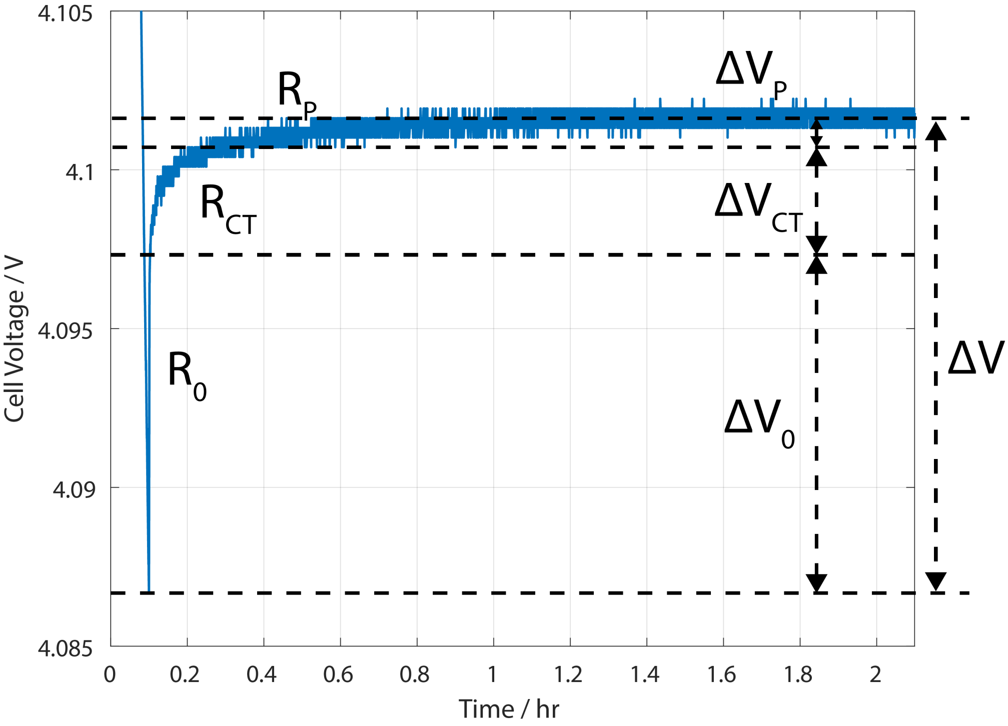

Figure 5.8: The relaxation of the cell voltage for a LIM5H cell, after a 1C charge.

Figure 5.8 shows that measuring for different lengths of time results in a different measurement for impedance. A very short test (¡1s) provides the value known as R_0 - or the purely ohmic component of a multi-order Randles model [125]. A much longer test, in the shown case upwards of 1 hour, shows the the charge transfer resistance [130] (R$_{CT}$) (the resistance due to charge transfer at the interface between the electrode and electrolyte) and the polarisation resistance [105] (R$_{P}$) (the resistance due to ionic diffusion). Inductive impedance is dominant at time periods shorter than 1ms, though ramp current ramp rates ($\frac{dI}{dt}$) and inductance small enough such that it is insignificant to the measurable time domain response. As an example, inductance for a cell is in the order of 10^{-8}H, and the MACCOR S4000 cell tester ramps to it's maximum current (10A) in 500μs. This would give a ΔV of 0.2mV, which is less than the 0.3mV resolution for a time period shorter than the 10ms fastest sample rate. Hence, the inductive impedance is ignored going forwards. Therefore R for the Rint model is:

$$R_{DCIR} = R_0 + R_{CT} + R_P \tag{5.2}$$

A MACCOR S4000 cell tester, which is used to perform the cell testing, has a built-in impedance measurement function - this performs a series of 350ms pulses and uses Ohms law to provide a value for impedance. Considering the above figure 5.8, it can be seen that this provides a value for R_0. While not especially helpful for measuring the overall Rint model resistance, it could be used as a fast method to find the variance between the cells, assuming $R_0 \propto R_{DCIR}$.

The transient behaviour of these cells ends after 2 hours at most SoCs, so 2 hours will therefore be used as the rest time for subsequent impedance experiments using these cells. However, this is only necessary to calculate the open-circuit voltage. If coulomb-counting can be used to estimate the state-of-charge, then the open circuit voltage can be used instead of waiting for 2 hours. This can vastly accelerate the testing procedure. Therefore, instead of $\Delta V = V_{load} - V_{rest}$ to find the voltage drop, $\Delta V = V_{load} - V_{OCV}$ can be used.

Naturally, a lengthy OCV test is still required on at least one cell, as well as high-precision current sensing to provide suitably accurate coulomb-counting to give a good estimate for SoC. It should also be the most accurate method, as in the model, the voltage is estimated based upon the OCV and the voltage drop caused by the impedance under load. For identifying parameters using this method, the impedance is calculated based upon the estimated OCV, the measured voltage under load and the measured current. This is essentially a direct inverse as the OCV-SoC relationship is the same in the model and the parameter identification.

All measured values assume that all resistance is from the cell, and not from any physical connections. This is justified as the tests use remote voltage sense, and due to the very low current in the sense wires, there is an immeasurable loss due to the connection.

However, when connected in a pack, this is not the case for the output, which will experience a voltage drop due to connections within the pack. Therefore, this is an input which is added to the multi-cell model and represents a constant addition to the resistance as:

$$R_{Total} = R_{Cell} + R_{Connection} \tag{5.3}$$

Impedance testing Results

Using the four methods (EIS, 1KHz test, R_{DCIR} 350ms Pulse test, R_{DCIR} comparing OCV to load voltage) the impedance of a cell can be found across a range of SoCs. It was found that using some methods, there was a different measured impedance to charge than discharge. The ten Yuasa LIM5H cells provided a measure for the variance between the cells. Figure 5.9 shows the results for the cells.

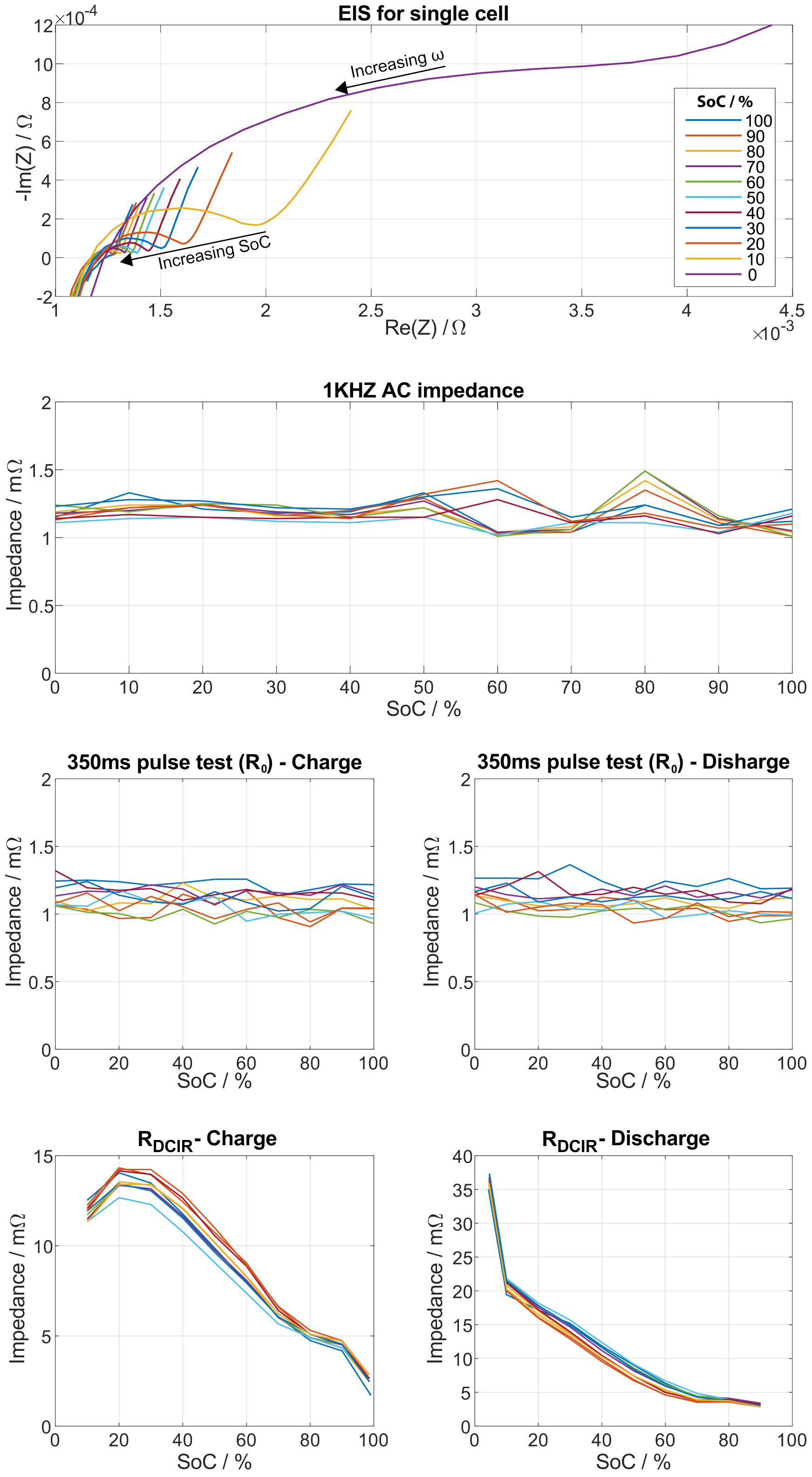

Figure 5.9: Impedance of 10 LIM5H cells measured using different techniques.

Both the 1KHz AC impedance test and the 350ms pulse impedance test show no change in impedance with SoC. This appears to be in agreement with EIS results presented in [72], though this is a different chemistry (NCA instead of NMC), so it is not conclusive. Furthermore, they do not provide the correct R value for the Rint model as they do not take into account the transient behaviour. However, as they are fast tests to perform and are not dependant on SoC, they could be a useful measure for variance, assuming the variance is the same across the different tests.

The impedance test using OCV for V_{rest} provides the best value for the Rint model as it is calculated with the inverse method for how it is used in the model, and is the fastest for finding the impedance across a range of SoCs, it will therefore be the proposed parameter identification method. The measured impedance to charging is different from the impedance to discharging, also observed and modelled in [121]. The impedance changes across the range of SoC, and during charge, there is a mostly linear relationship as shown in figure 5.10. It is clear, however, that there is a small drop in impedance below 20% SoC. Using a linear relationship is ideal due to the simplicity, and should not affect the model in terms of capacity, as during charge it is most important to have an accurate impedance value approaching 100% SoC, as this is the point that the charge phase of a Constant Current (CC) charge would end. Therefore, 20% and 10% values are neglected when producing the linear fit, however, it would be expected that the voltage during charge will not perfectly track an experimental result at low SoCs. It can also be seen that the variance between cells is consistent - where generally a particular cell will have a higher or lower impedance from the average across the full range. For the model, the linear relationship between impedance and SoC can be used to calculate the impedance based on the SoC.

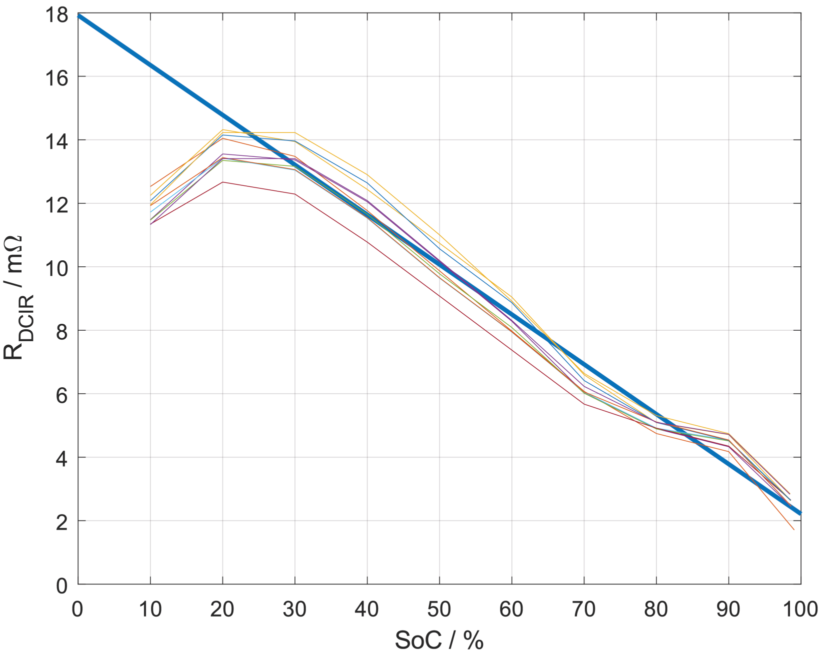

Figure 5.10: R_{DCIR} during charge for a sample of 10 LIM5H cells, showing the proposed relationship in bold.

Discharging relationship

During discharge, the relationship follows the same trend - in other words, higher impedance at low SoC, however, is much less linear, as can be seen in figure 5.11 below.

To find the relationship, the MATLAB curve fitting tool was used, and the best fit was found using a 2-term exponential of the form:

$$R_{DCIR} = ae^{b*SoC} + ce^{d*SoC} \tag{5.4}$$

where a, b, c, d are the terms to be optimised.

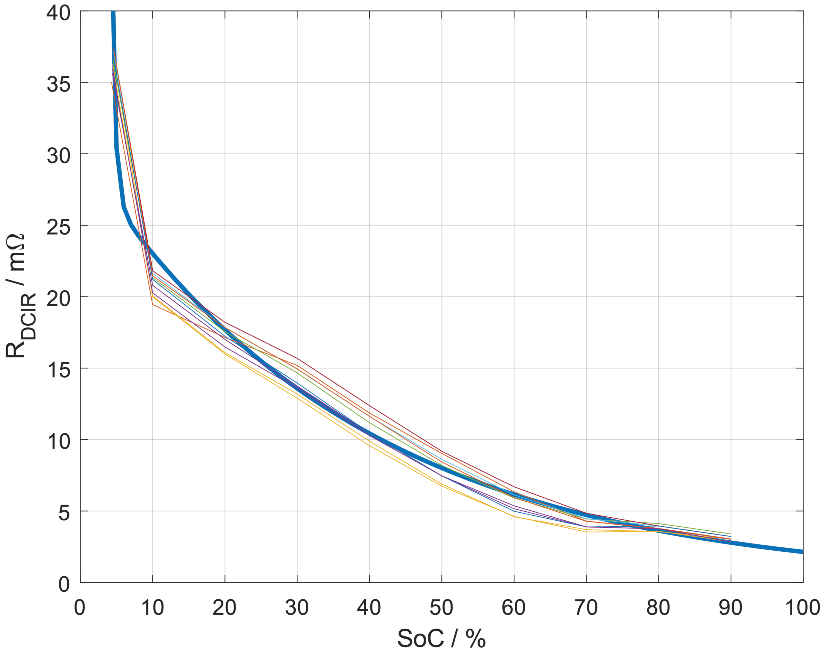

Figure 5.11: R_{DCIR} during discharge for a sample of 10 LIM5H cells, showing the proposed relationship in bold.

5.2.1.1.4 Temperature

The impedance testing thus far has all been performed in an environmental chamber at 25°C. Observations from WESS presented in subsequent chapters suggest that there is often significant non-uniformity in temperature between cells in large-scale battery packs, as they are not in a closely controlled environment, despite the use of Heating, Ventilation and Air Conditioning (HVAC) systems. Therefore, it is helpful for a model to have temperature as an input, to be able to model the effects of changing temperature.

Some have observed that a reduction in temperature results in a reduction in cell voltage [107]. A test of 10 LIM5H cells at rest between 40°C and -10°C, with 2 hours at each temperature at 50% SoC showed no change in cell voltage. However, the impedance was shown to change. Using the 350ms pulse impedance test, the results are as follows:

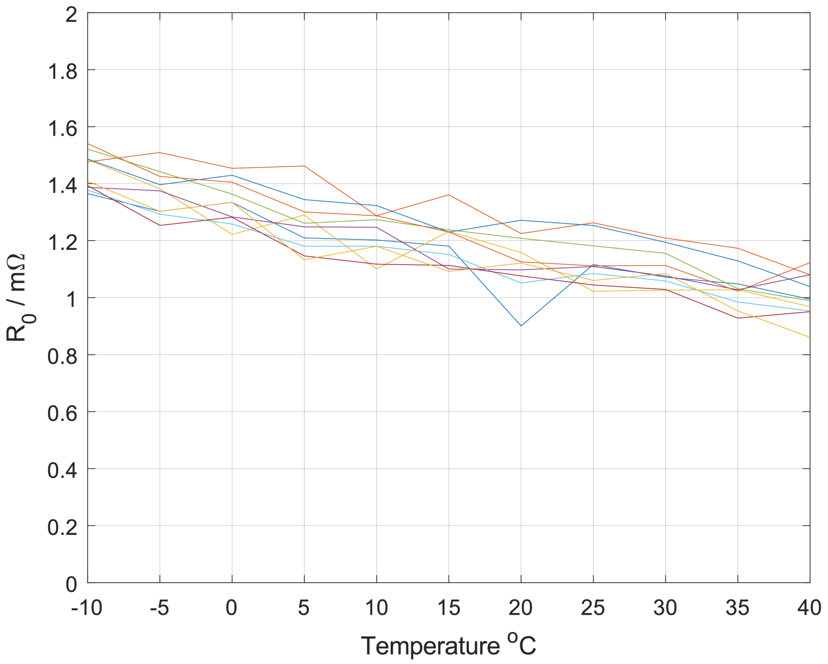

Figure 5.12: R_0 vs temperature for a sample of 10 LIM5H Cells

It can be seen that the impedance is inversely proportional to temperature, which can be approximated with a linear approach as:

$$R_T = (25 - T) * 0.0075 R_{25} \tag{5.5}$$

where R_T is the resistance at T°C and R_{25} is the resistance at 25°C.

This is the purely ohmic impedance R_0, and assumes that $R_0 \propto R_{DCIR}$ for implementing it in the model. This method was chosen as the test is very short, so only a small amount of energy flows in or out of the battery, meaning the total heat generation from I^2R losses is very small. This in turn means that the cell temperature is as close to the environment temperature as possible. Later work involves improved modelling of temperature, but this is sufficient for general validation of the model and should indicate the effect of temperature on a battery, although it may not provide absolute values.

5.2.1.1.5 Coulombic efficiency

Batteries do not have a perfect Coulombic Efficiency (CE), where CE is defined as:

$$CE = \frac{\int_{t_{ch,start}}^{t_{ch,end}} I \; dt}{\int_{t_{dch,start}}^{t_{dch,end}} I \; dt} \tag{5.6}$$

This can be caused through the consumption of lithium or electrolyte and generally by side reactions in the cell during a cycle [131, 132].

This will be calculated and implemented as an efficiency in the model, with half the efficiency factor applied during both charge and discharge, providing the correct overall CE. In reality, it is likely that there is differing CE during the charge and discharge phase [132], however, this would be very dependant on the chemistry as well as the age of the battery. Due to the fact that <1 CE is due to side reactions or lithium consumption, CE can be a factor which indicates degradation [133]. CE will be calculated using coulomb-counting from the capacity test with equation 5.6.

5.2.1.1.6 Degradation

In order to simulate the change in capacity with cycling, the model includes a factor for degradation based on the charge throughput for each cell, similar to the model described in [134–136]. The degradation factor is calculated based on the expected number of full cycles the cell will throughput before degrading to a specific proportion of its original capacity. Generally, a cell datasheet will state the number of cycles before reaching a given SoH. Equation 5.7 shows the relationship implemented in the model.

$$C_t = C_{t-1} - \Delta Q * k, \tag{5.7}$$

where k is the degradation factor.

This is useful in the model as it should highlight whether some cells have a higher capacity throughput and are therefore degrading faster than others.

5.2.1.2 Cell Model Results

To validate the results for the single cell model, the model (shown in Simulink in figure 5.6) was parameterised using the experimental data from one of the LIM5H cells.

Three cycles were then performed on both the model and the physical cell at 2.5A, 5A and 7.5A (0.5C, 1C, 1.5C), so the results could be directly compared as shown below.

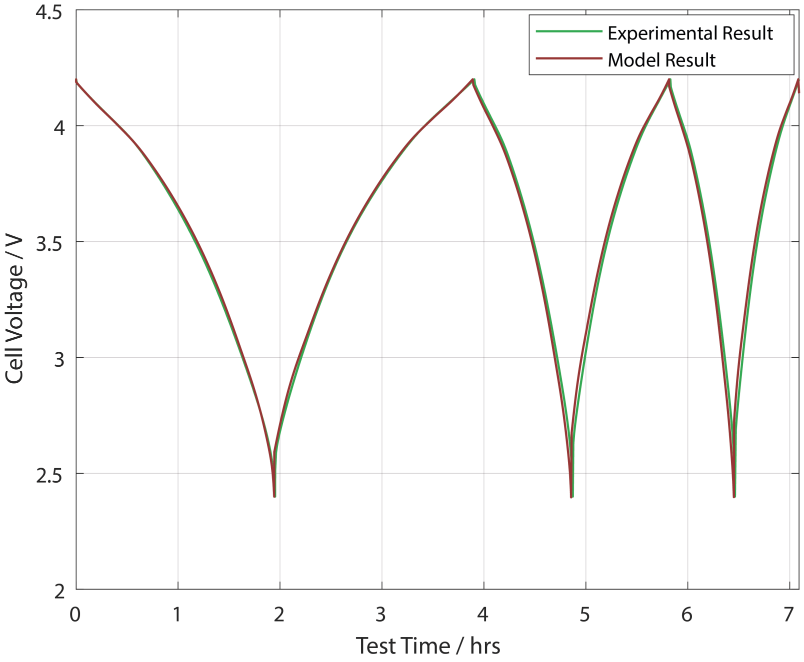

Figure 5.13: Model vs experimental results for a single LIM5H cell.

	Mean Model Result	**Mean Experimental Result**	**Mean Model Error**	**Error Standard Deviation**
Discharge Capacity / Ah	4.818	4.821	0.0035	0.0177
Charge Capacity / Ah	4.804	4.794	-0.0099	0.0230
Discharge Energy / Wh	17.111	17.161	0.0499	0.0288
Charge Energy / Wh	17.474	17.361	-0.1132	0.1571

Table 5.2: Summary of results comparing the model and experimental constant current capacity for a single LIM5H cell across 3 cycles at 0.5C, 1C and 1.5C.

Figure 5.13 shows that that the voltage profiles closely match, with only a small discrepancy. As expected, the dynamic behaviour is not exactly correct, as at the change from charge to discharge, the voltage jumps instantaneously, whereas the experimental result shows the change as somewhat damped due to the relaxation of the cell which is not modelled. This is more clear in figure 5.14.

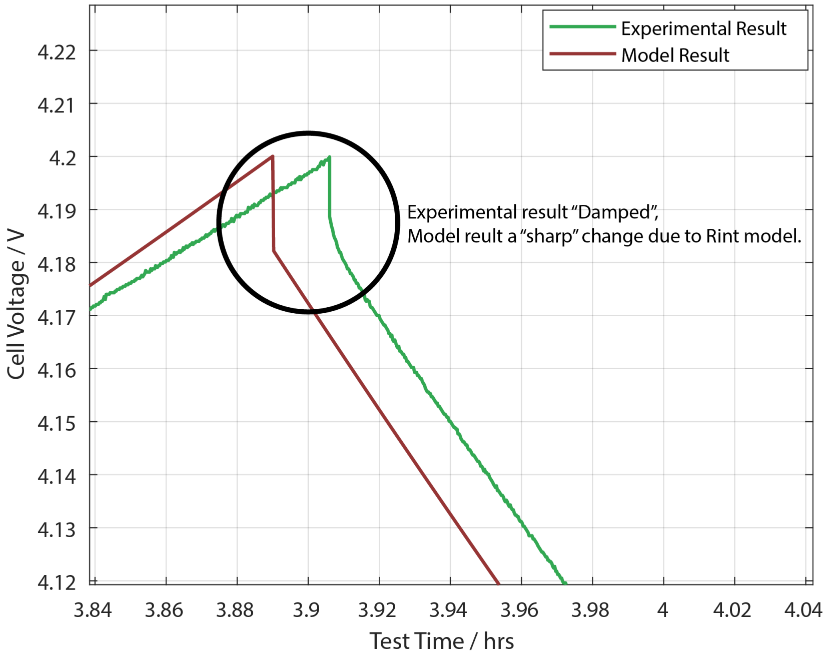

Figure 5.14: Model vs experimental results for a single LIM5H cell, zoomed to the start of the 1C charge to highlight the different curve shape.

The capacity of the pack shows a very accurate result, with a very small error. When considering the energy in the pack, this is slightly less accurate - likely due to the voltage not matching exactly using the relationship chosen in figures 5.10 and 5.11. With only a small error, this model was chosen to be used going forwards.

5.2.2 Pack Model

This section considers using the cell model to produce the proposed model of a large battery pack. Initially a model with just series connections is produced, then a model with both series and parallel connections. These are then combined to give the full pack model. Breaking the model down in this way allows better understanding and verification of the overall pack model.

Each of the three models is verified experimentally using data parameterised from the LIM5H cells. The packs were cycled using the MACCOR S4000. To measure the current in parallel connections, an LEM LTS 15NP current sensor was used, which has an accuracy of 0.2%. These were connected to the MACCOR's 16-bit analogue inputs, each giving 0.0003V resolution and a worst accuracy of 0.02% (0.004V). Using 3 primary turns on the current sensor, this gives a range of ±16A and therefore an accuracy of 32mA at a resolution of 2mA.

The experimental procedure used to validate the model is shown in table 5.3.

Sequence	**Limits**	**End Condition**
CC Charge	I = 1C	Any Cell >= Max V
CC Discharge	I = 1C	Any Cell <= Min V
CC Charge	I = 0.5C	Any Cell >= Max V
CC Discharge	I = 0.5C	Any Cell <= Min V
CC Charge	I = 1C	Any Cell >= Max V
CC Discharge	I = 1C	Any Cell <= Min V
CC Charge	I = 1.5C	Any Cell >= Max V
CC Discharge	I = 1.5C	Any Cell <= Min V

Table 5.3: Test procedure for verification of the model.

This consists of four cycles, a single cycle as to reach thermal equilibrium and three test cycles, each at different C-rates to verify how accurately the model estimated the available capacity under conditions (which should result in differing capacities).

5.2.2.1 Series model

In the series model, the voltage and impedance of each cell are summed to produce the overall battery pack voltage. Three cells are modelled as shown in the diagram below. The cell models are labelled A-C and the cells which the model represents are labelled *1-n* (represented in italics), where n is the number of cells in the string. The cells are ranked strongest to weakest by capacity, with *cell 1* being the weakest and *cell n* being the strongest.

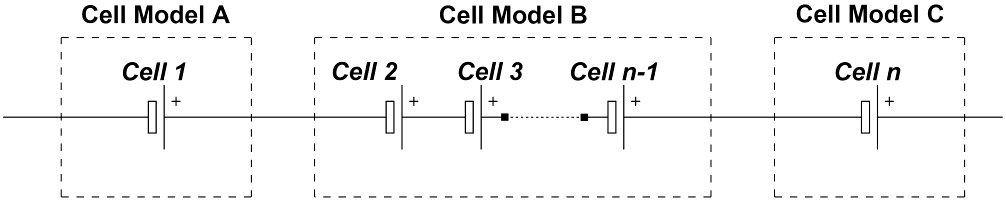

Figure 5.15: Configuration of the cells in the cell models for a pack with series connections.

This results in Cell B being a model of the average capacity of *cell 2* to *cell n-1*, with the voltage being the number of *cells* in Cell B multiplied by the average cell voltage. Then summing the voltage of Cells A, B & C gives the overall pack voltage, shown by equations 5.8 and 5.9.

$$V_A = V_1,\ V_B = V_2 + \cdots + V_{n-1},\ V_C = V_n \tag{5.8}$$

$$V_{pack} = V_A + V_B + V_C \tag{5.9}$$

To compare the model with an experimental result, 3 LIM5H cells were used and 3 CC cycles were performed as per the procedure in table 5.3. The aim is to show that the voltages are different between cells during the cycles, which is reflected both experimentally and using the model in a simulation. The model parameters were found using the experimental data for the 3 cells used. The results are shown in figure 5.16

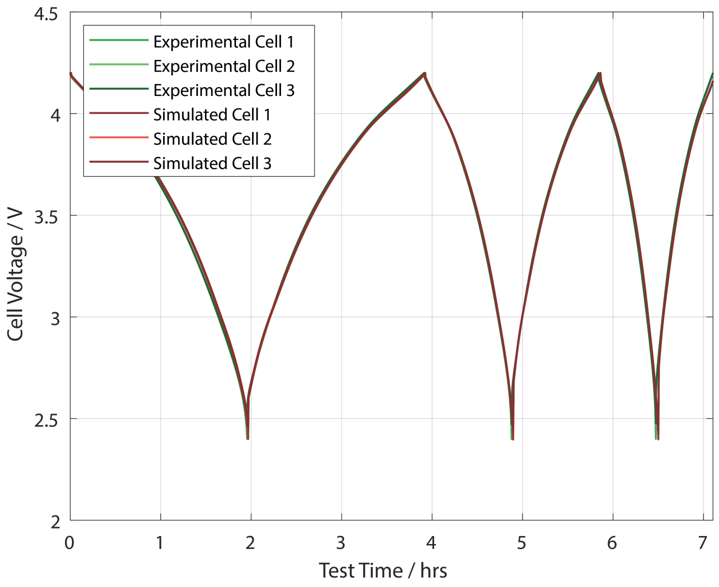

Figure 5.16: Model vs experimental results for a 3 LIM5H cells connected in series

It is clear from the figure that the voltage tracks as accurately as with the single cell model, and the error is in the same order of magnitude as with the single cell test.

5.2.2.2 Parallel Model

The parallel model is modelled similarly to the series model as shown in the diagram in figure 5.17

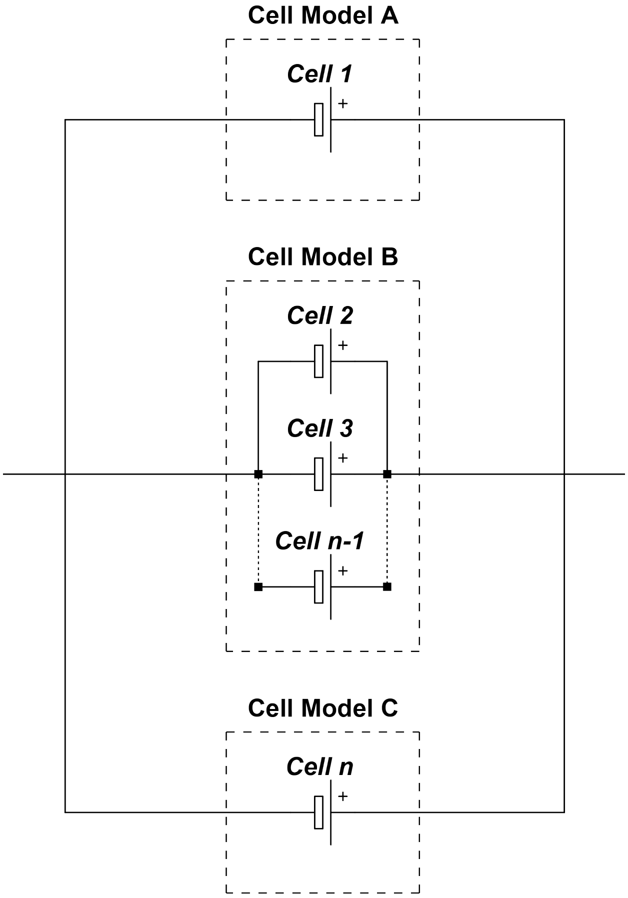

Figure 5.17: Configuration of the cells in the cell models for a pack with parallel connections.

For figure 5.17, again the cells are ranked strongest to weakest by capacity, with *cell 1* being the weakest and *cell n* being the strongest. To identify parameters for cell model B, the capacity 'C' for all *cells* is summed as per equation 5.10, and impedance is calculated using the shown in 5.11:

$$C_A = C_1,\ C_B = C_2 + \cdots + C_{n-1},\ C_C = C_n \tag{5.10}$$

$$R_A = R_1,\ \frac{1}{R_B} = \frac{1}{R_2} + \cdots + \frac{1}{R_{n-1}},\ R_C = R_n \tag{5.11}$$

These are both straightforward, however, the voltage is constant between the cells. Given the same current, the cells would reach different voltages. In reality, different current flows through each cell due to different impedances and SoCs. For the model, a SimScape model was produced to calculate the current in each cell. Each cell consists of a voltage source and a resistor, which have values that are the cell voltage and cell impedance. These are connected in parallel as shown in the figure below.

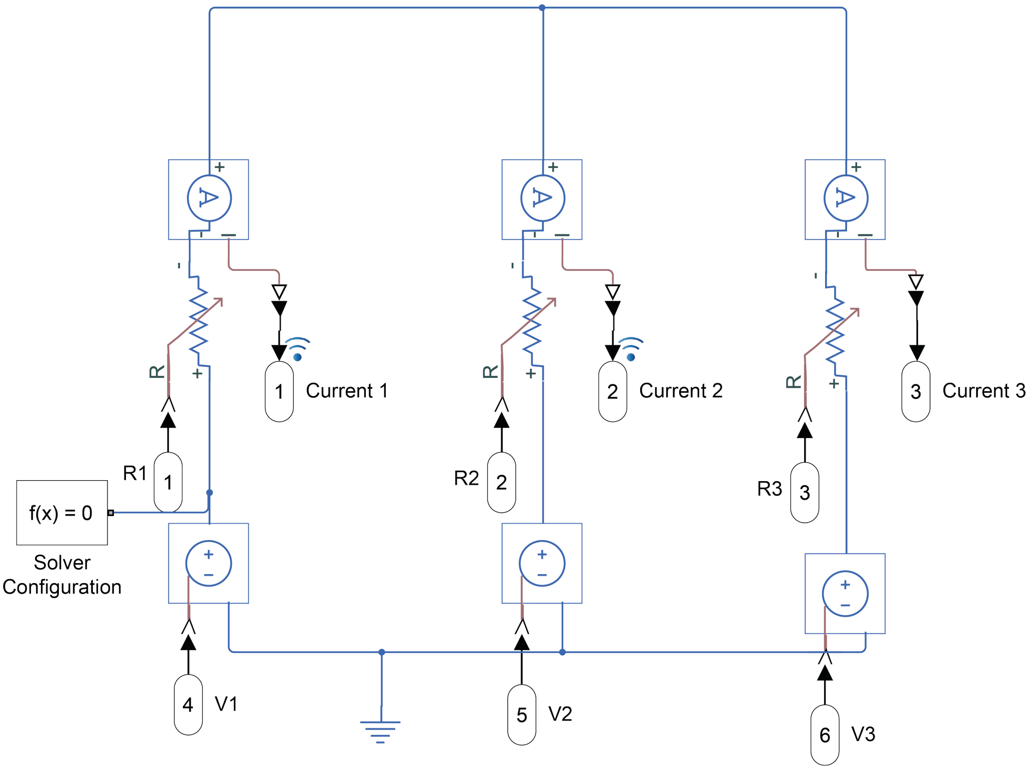

Figure 5.18: Calculation of the current in each cell to ensure constant voltage using Simscape in Simulink.

Again, to compare the model with an experimental result, 3 LIM5H cells were used and 3 CC cycles were performed as per the procedure in table 5.3. The model parameters were identified using the experimental data for the 3 cells used. It is expected that the voltage will be the same between cells and the current will vary between them, as this experiment will demonstrate. The current profile for each cell is shown in figure 5.19.

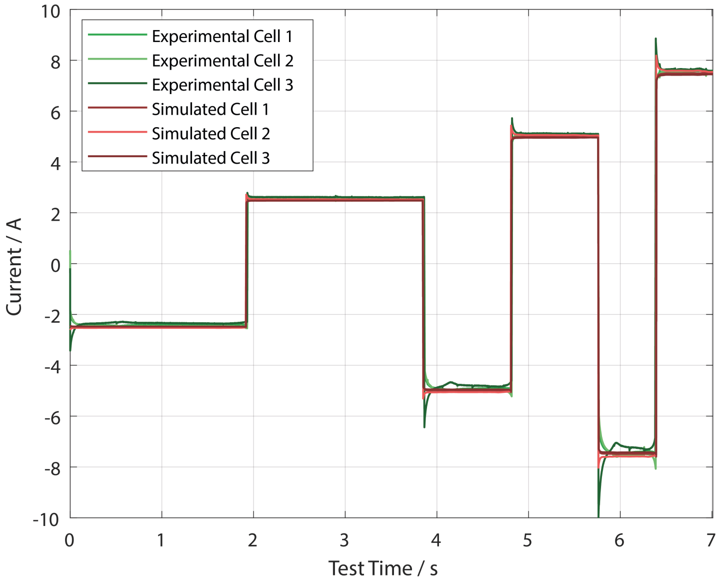

Figure 5.19: Model vs experimental results for a 3 LIM5H cells connected in parallel showing the cell currents.

It can be seen in figure 5.19 that during a change in current, there is initially a large discrepancy in the current between the cells before it settles. In the model, this should show the cell which is working the 'hardest', or the cell that has the most current throughput and therefore will most likely see the most degradation. There is a larger current change seen in the experimental results than in the simulation. It is expected that this is due to a slightly higher connection impedance not accounted for in one cell compared to the others.

5.2.2.3 Series and Parallel Combined Model

Combining the series and parallel models gives a model of the following architecture:

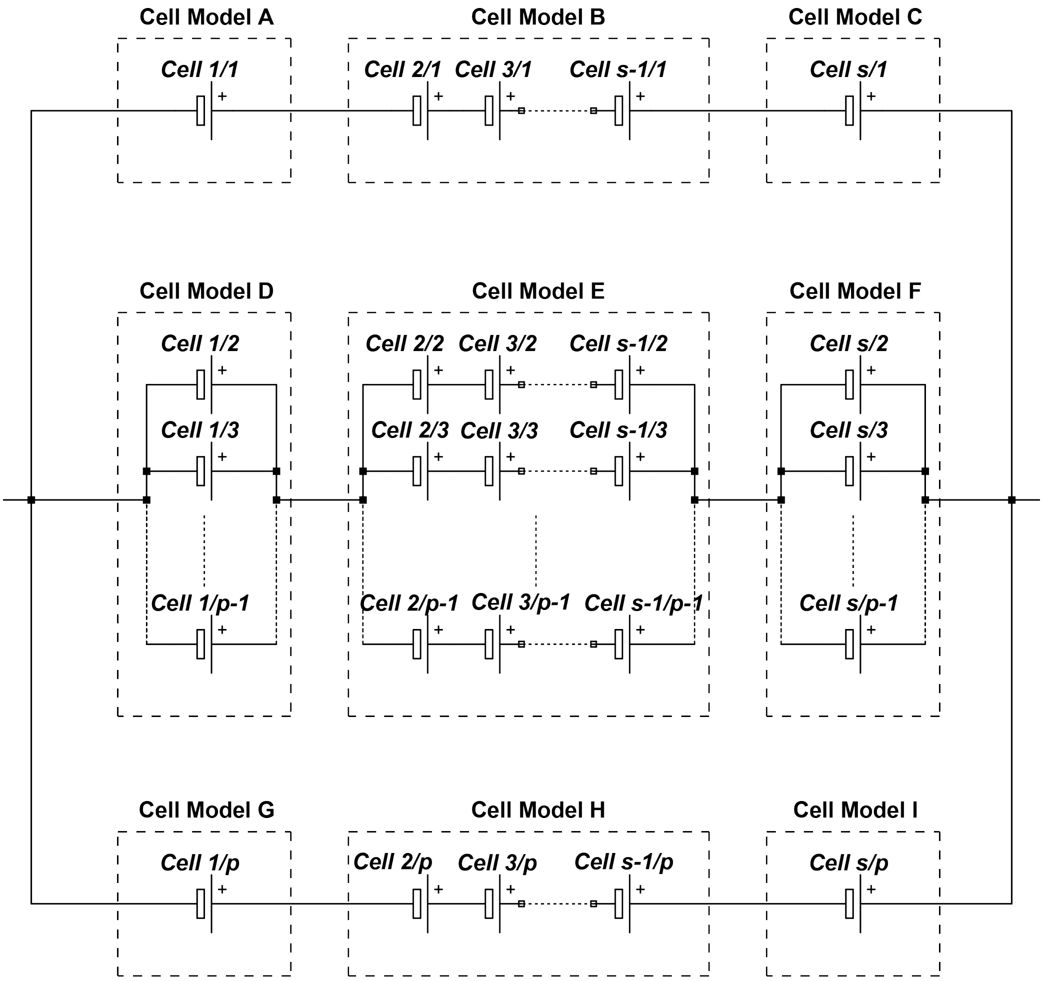

Figure 5.20: Configuration of the cells in the cell models for a pack with series and parallel connections.

The cells are labelled similarly to the series and parallel model, with cells A-I being the 9 cell models which are computed. The *cells* which the model represents are labelled as *cell* x/y where y is the string number and x is the position in that string. p represents the number of parallel connected strings and s represents the number of cells in a series string.

To verify this model, a 3s3p pack was assembled and tested. Each *cell* had individual voltage and temperature measurements and each series string had a current measurement. This provides data points for all the cells being calculated by the model. By having accurate parameters for the 9 *cells*, these can be directly compared to the model results to observe where there are discrepancies between the model and reality, giving a physical demonstration of the limitations. An image of the experimental setup is shown in figure 5.21.

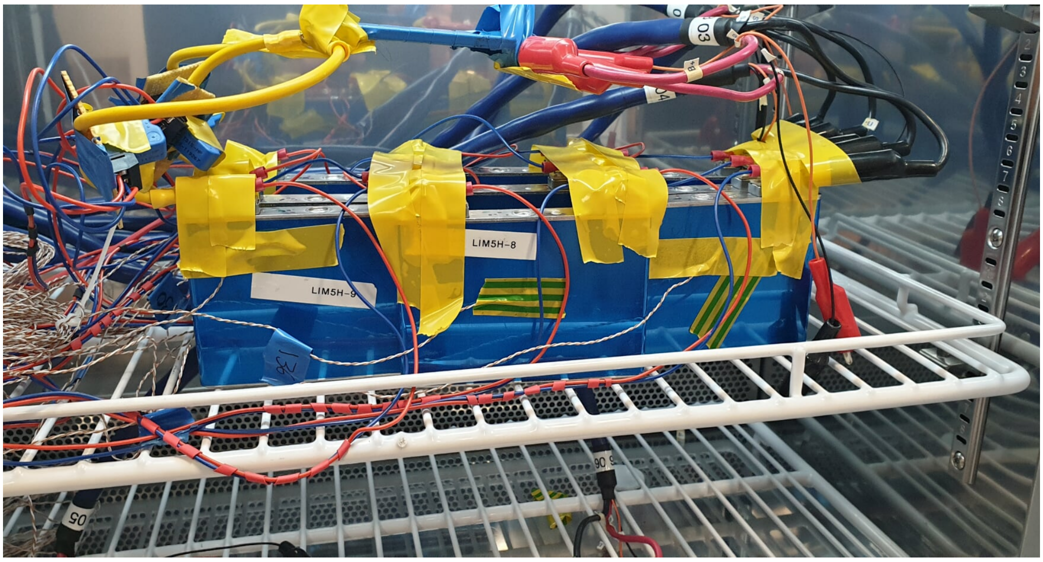

Figure 5.21: An image of the experimental setup for LIM5H cells connected in a 3s3p configuration

It is expected that the model shows the same constant current capacity as the experimental pack, thereby verifying the assumptions made. A result within 1% would be considered sufficient as it allows for the imbalance in SoC due to the accuracy of the MACCOR S4000. The results comparing the model with the experimental results are shown in figure 5.22.

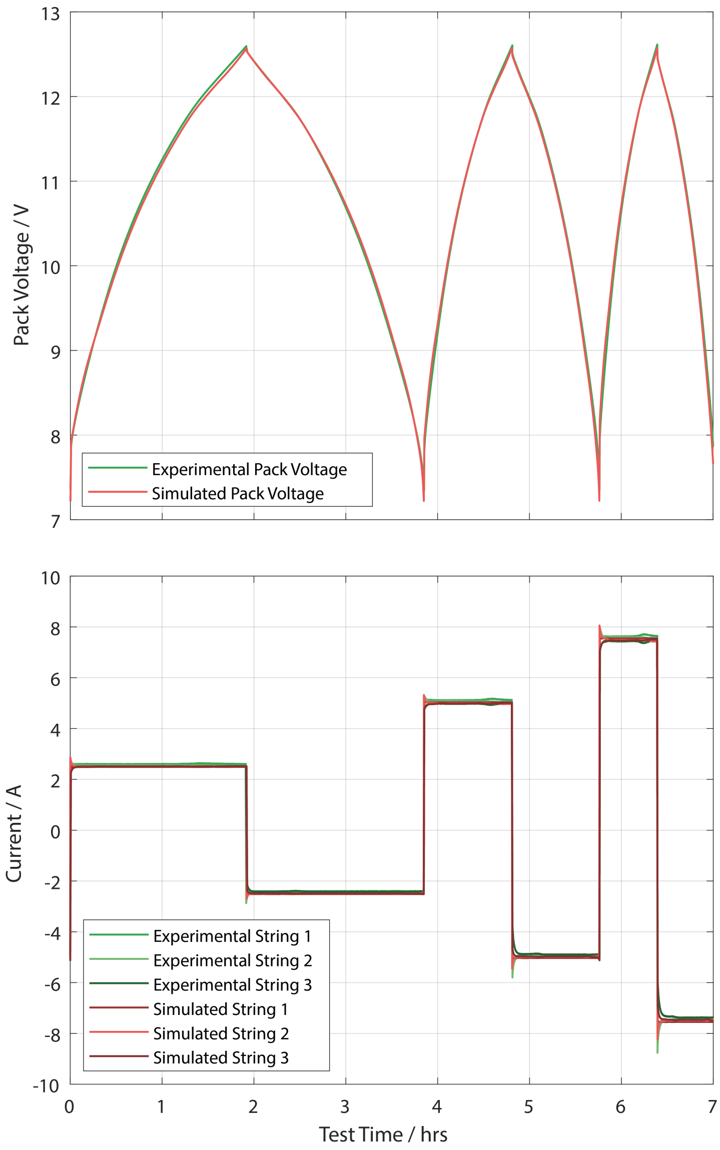

Figure 5.22: Test profile showing the cell voltages in the model and the cell voltages from the experimental data.

	Model Capacity / Ah	**Experimental Capacity / Ah**	**Model Error / %**
0.5C Discharge	14.28	14.24	0.26
0.5C Charge	14.21	14.24	-0.24
1C Discharge	14.08	14.09	-0.02
1C Charge	14.00	13.92	0.57
1.5C Discharge	13.88	13.87	0.08
1.5C Charge	13.79	13.78	0.11

Table 5.4: Summary of results comparing the model and experimental results for a 3s3p pack made from LIM5H cells.

This shows that for CC cycles of a 3s3p pack, the model is to within 1% across a range of C-rates. It is expected that this accuracy would remain for a larger pack, assuming similarly good parameter identification. This notion will be verified in section 5.4.

It can be seen that the current profiles are much better here than with the 3 parallel cells. This is likely due to a better connection which minimises the impedance differences between cells, and the same connection impedance would have less of an impact as there is greater impedance in each string with 3 cells in series.

5.3 Parameter identification

Section 5.2.1.1 discusses methods for identifying the parameters of the individual cells. This section considers how to 'scale up' the model, using a small sample of cells to estimate how a larger pack would behave by producing a sample with the same distribution. This new distribution can be used to populate the model in figure 5.20.

5.3.1 Variance

There is a difference between the capacity and impedance of each cell, considered as the variance. The following plot shows the capacity and impedance of each of the 10 cells.

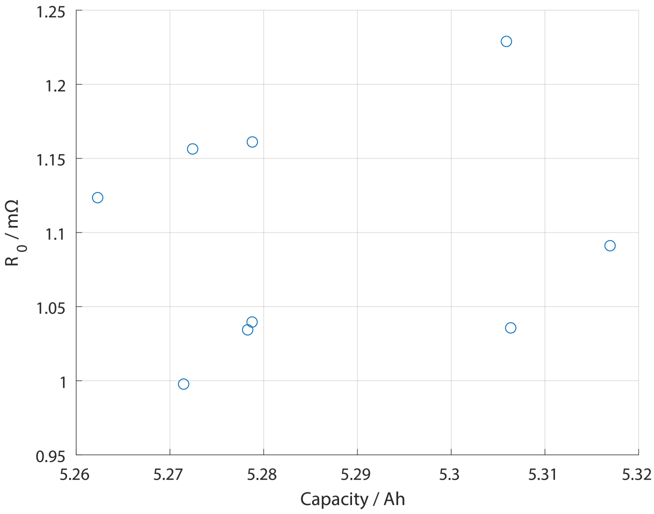

Figure 5.23: R vs Capacity for a sample of 10 LIM5H Cells

As can be seen, there is little correlation between capacity and impedance, which agrees with other studies [15] - particularly with new cells.

Considering just the capacity and applying a normal distribution for the sample produces the distribution shown in figure 5.24.

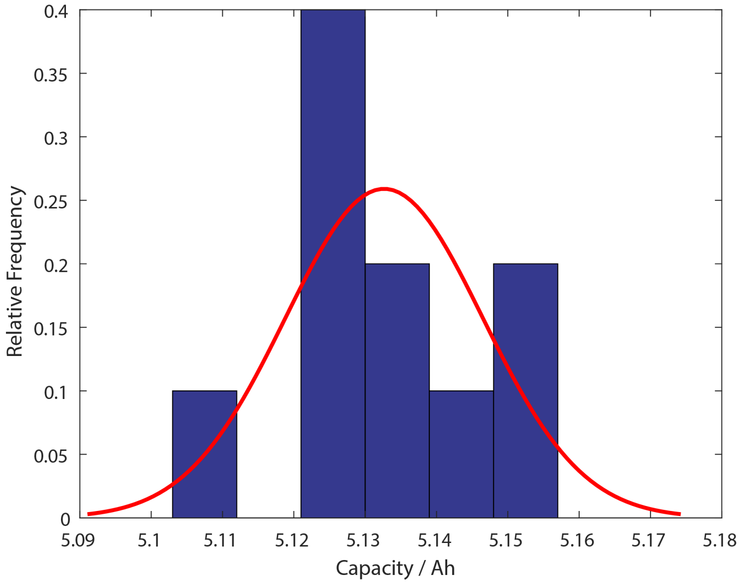

Figure 5.24: Histogram with normal distribution showing distribution of capacities for sample of 10 LIM5H cells

This distribution can be used to produce a new dataset of any number of cells which matches the distribution. It is expected that the larger the dataset, the greater the chance the sample set includes outlier results.

For the impedance, it is not quite so straightforward as the impedance used in the model changes with SoC. Looking back at figures 5.10 and 5.11, as impedance increases, so does the difference in the impedance, suggesting that a multiplication factor would be ideal to define the variance between cells. This is done by taking the mean impedance and multiplying to increase or decrease the impedance by the factor based on the variance, as:

$$R_x = R_{mean} * k_x \tag{5.12}$$

where k_x is the variance factor for cell x and $R_x$is the impedance for cell x.

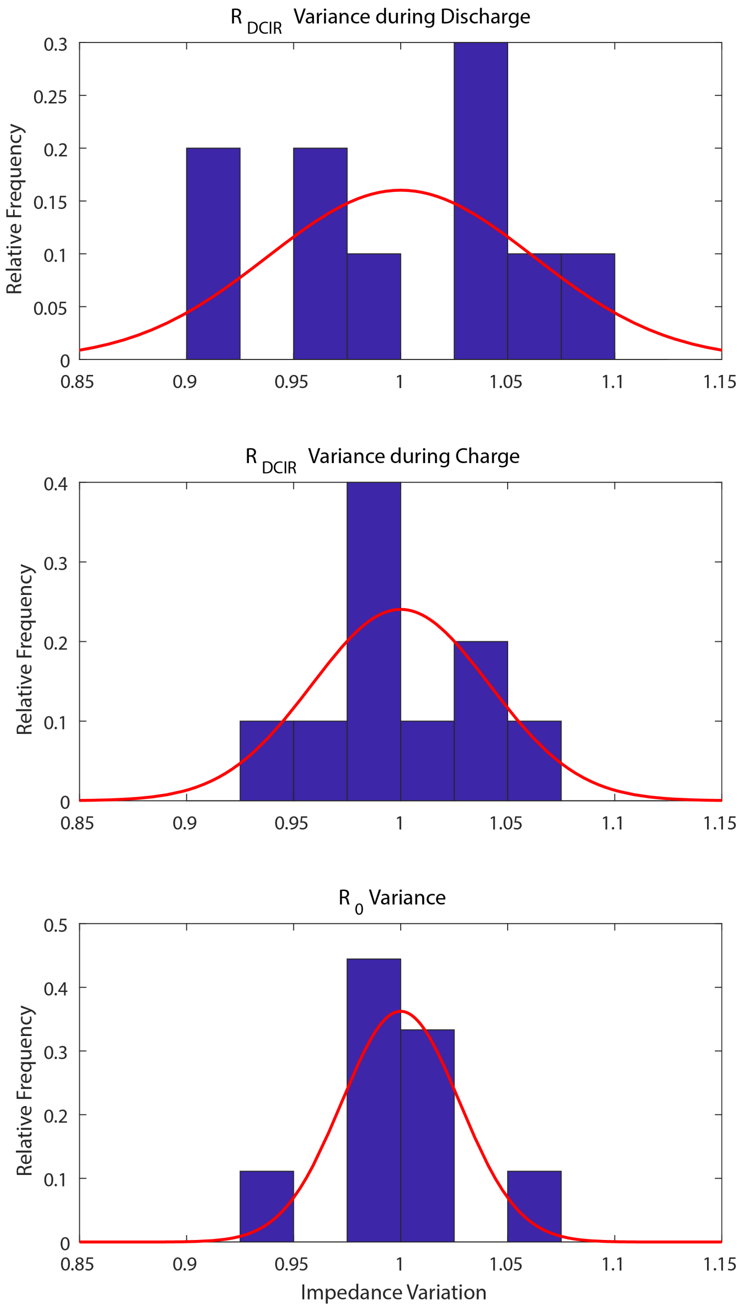

Figure 5.25: Impedance variance from the mean impedance for a sample of 10 LIM5H cells, comparing R_0 with R_{DCIR} during charge and discharge.

Furthermore, comparing the distribution with the trends found for charge and discharge shows that the variance model is sufficient as highlighted in figure 5.26.

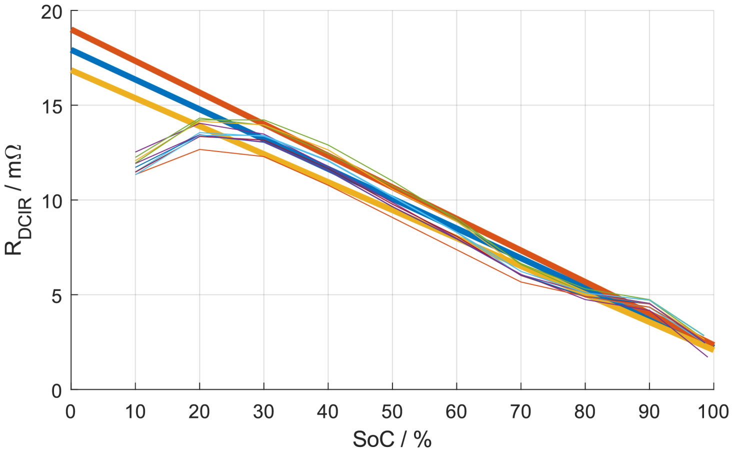

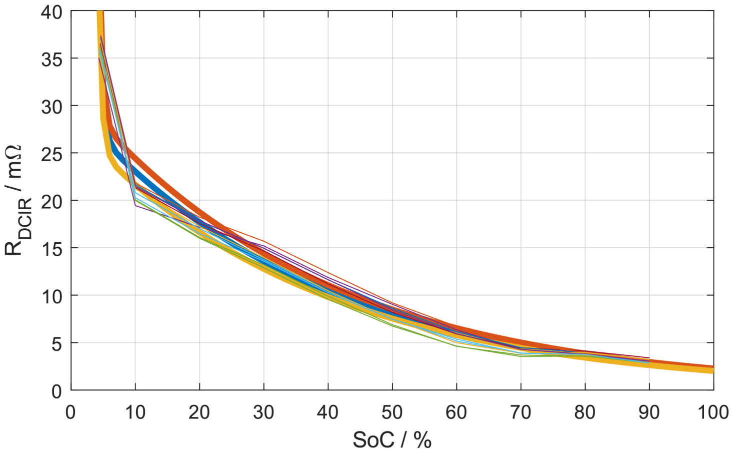

Figure 5.26: R during charge (top) and discharge (bottom) for a sample of 10 LIM5H cells, showing the proposed relationship in Figure 5.10 & Figure 5.11 with the maximum and minimum variance in Figure 5.25 applied, shown by the bold lines.

It can be seen that the fit of the variance matches the variance behaviour of the cells across a range of SoCs, where there is more absolute difference at a higher impedance.

Using the discussed distribution of capacity and impedance, a sample of any number of cells can be produced which match the distribution.

5.3.2 Model Population

To populate the model in figure 5.20 where there are more than 9 cells, it must be decided which cells are represented by which cell models.

In terms of individual cells, it has been shown in figure 5.23 that there is no correlation between capacity and impedance of a cell, so these values are distributed randomly among the sample of cells, except for the strongest and weakest cells. To consider the worst case scenario, the highest impedance cell can be given the lowest capacity for the weakest cell and the lowest impedance cell is given the highest capacity for the strongest cell. The cells are then distributed randomly into the pack, other than the strongest and weakest cells, which should be in different strings. If the worst case scenario is not being considered, then the cells are ranked by capacity to determine the weakest and strongest. The string containing the weakest cell is represented by cells A-C. Cell A represents the weakest cell in the string, cell C represents the strongest cell in the string and cell B represents a model of the remaining cells in the string. Similarly, the string containing the strongest cell is represented by cells G-I. Cell G represents the weakest cell in the string, cell I represents the strongest cell in the string and cell H represents a model of the remaining cells in the string. Finally, for the remaining strings, all weakest cells in each string are represented by a model in Cell D, all strongest cells in each string are represented by a model in Cell F and all remaining cells are represented by a model in cell E. This should give the metric for cell voltage imbalance and an indication of the currents flowing between the strings. This process is outlined in the flowchart and diagram in figures 5.27 and 5.28.

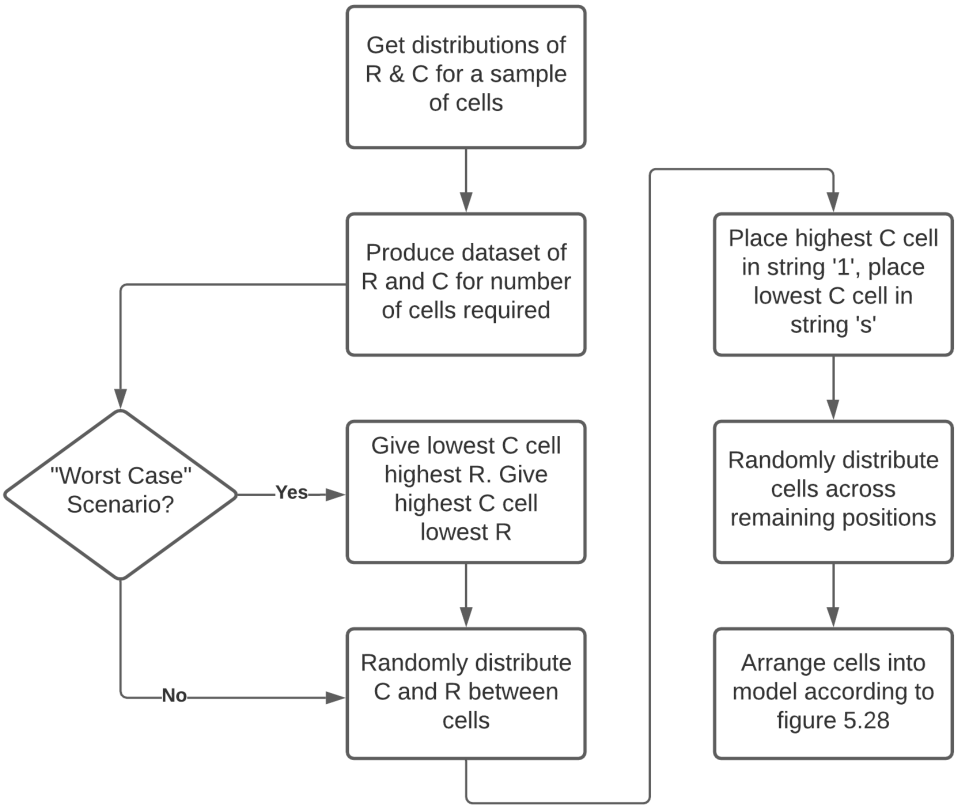

Figure 5.27: Flowchart describing the method for producing a battery pack based on a distribution of Impedance (R) and Capacity (C).

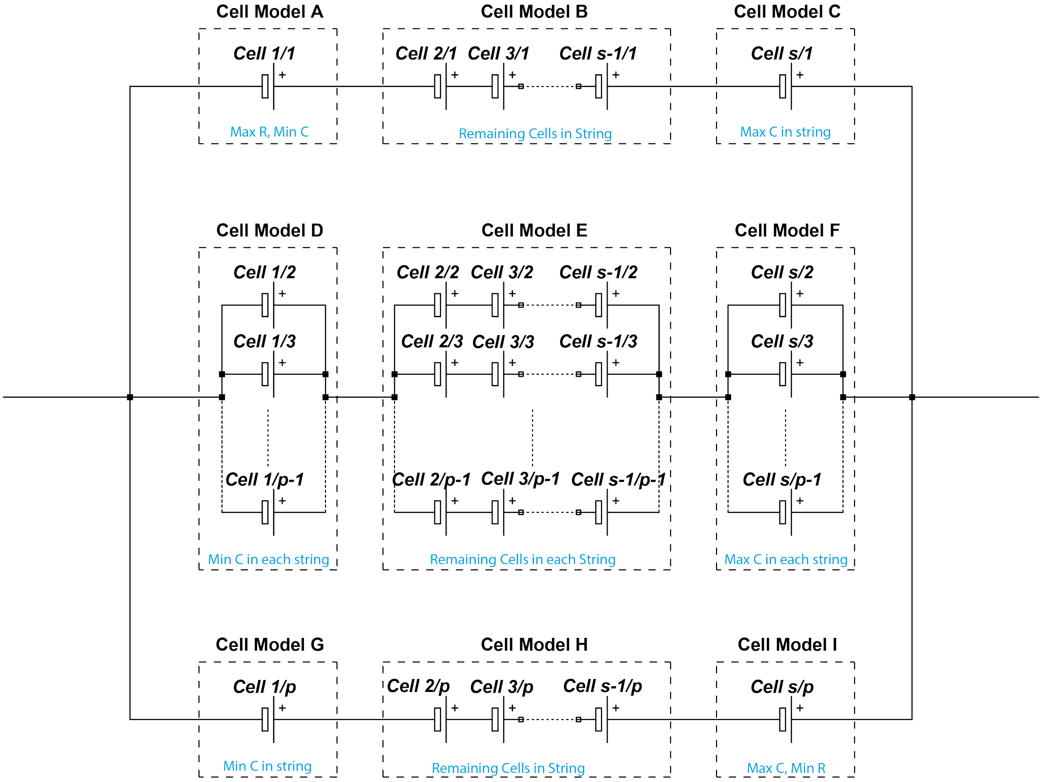

Figure 5.28: Diagram showing where cells in a pack produced from the process in figure are located in the model.

The previous section discussed and validated the model, where the number of cell models and number of cells is the same. For scale-up, a number of assumptions have been made. There is an element of randomness in identifying the parameters of a large model when creating a sample of cells from a distribution. This is because the MATLAB function used to produce the sample (RANDRAW), produces random values based on a distribution. Therefore, each time a set of samples is produced, it will be slightly different. Additionally, decisions have been made regarding which cells should be replaced by a single cell model and which ones should be grouped together into a single cell model. Therefore, to verify these assumptions, experimental work has been completed on a 12s4p pack, which will be discussed in the following section.

5.4 Model Evaluation

This study aims to produce a large battery pack model with a shorter simulation time than modelling every cell individually, but provides a more accurate model than modelling all cells as a single cell. This section will compare the modelling approach outlined in this chapter to these two types of models. The same cell model will be used for each. For an experimental comparison, a 12s4p pack is used which is comprised of 4 Yuasa LIM50E modules connected in parallel. This configuration was chosen to verify the model population procedure outlined in section 5.3.2 as there are greater than 3 cells with series connections and greater than 3 strings with parallel connections. This means that the model will be combining both parallel and series connections.

The cell model parameters were identified using an in-situ test method (explored in chapter 6), and the impedance and OCV relationships are shown in figures 5.29 & 5.30. A variance model was produced using the sample of 48 cells in the 12s4p pack giving the distribution of impedance and capacity shown in figure 5.31. This data was then used to populate the model using different methods, as will be discussed.

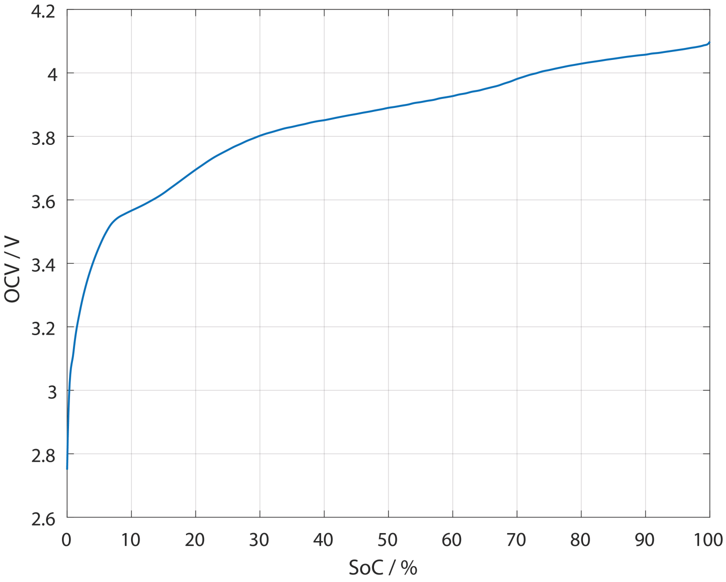

Figure 5.29: OCV vs SOC relationship for LIM50E cells used to identify the parameters for the model.

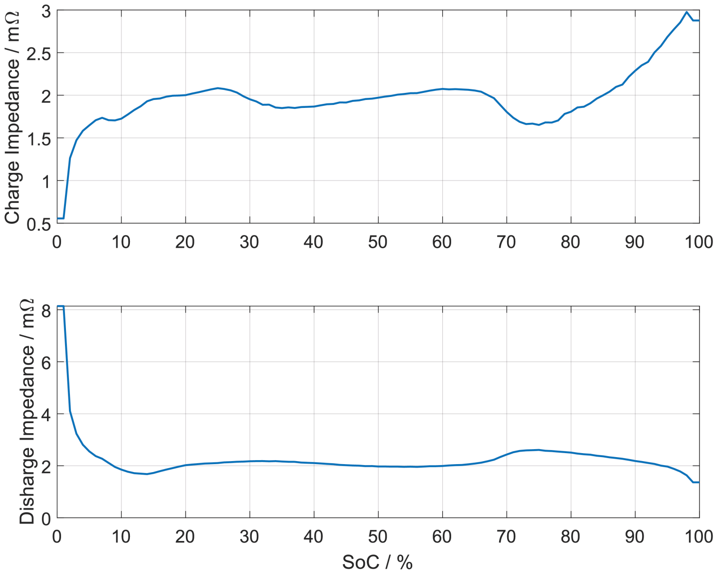

Figure 5.30: Mean impedance relationship for LIM50E cells used to identify the parameters for the model.

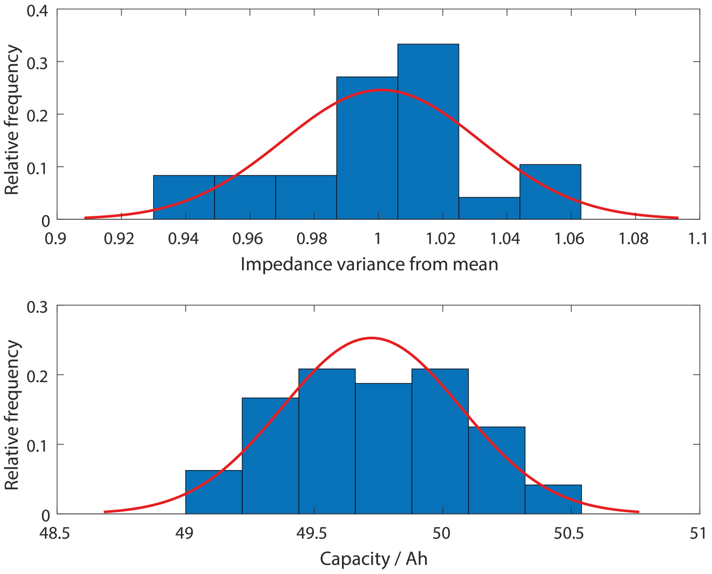

Figure 5.31: Impedance and Capacity distributions for a sample of 48 LIM50E cells used to identify the parameters for the model.

The tests performed experimentally and on the models were CC cycle tests at 0.25C, 0.5C, 0.75C and 1C. These C-rates were chosen as the maximum charge rate given by the manufacturer is 1C, and a range of C-rates were used to observe the model under different operating conditions. The test profile was as shown in table 5.5.

Sequence	**Limits**	**End Condition**
CC Charge	I = 1C	Any Cell >= Max V
CC Discharge	I = 1C	Any Cell <= Min V
CC Charge	I = Test C-rate	Any Cell >= Max V
CC Discharge	I = Test C-rate	Any Cell <= Min V
CC Charge	I = Test C-rate	Any Cell >= Max V

Table 5.5: Test sequence for testing a 12s4p pack of LIM50E cells. The portion of the test sequence used for the results is shown in bold.

The test was performed experimentally at the different C-rates and simulated under different scenarios. Two main experiments were performed:

- Comparison between models of varying numbers of cell models

- Comparison between using experimentally derived parameters and using parameters generated from a distribution.

5.4.1 Varying numbers of Cell Models

For a baseline, an All Cells Model (ACM) was simulated - a model consisting of a cell model representing each cell. The parameters used in the model were those which were experimentally measured. Additionally, a model consisting of a single cell model Single Cell Model (SCM) which represents the entire pack was also simulated, again using the parameters experimentally measured. These were then compared to the 9CM. Parameters were chosen using the weakest cell ranked as the cell with the lowest capacity and equally the strongest cell ranked as the cell with the highest capacity. The model was populated respecting the configuration of the parameters in the experimental pack. The results for the CC cycle tests at different C-rates found experimentally, and using these models are shown in table 5.6. The average percentage error of each model compared to the experimental result is shown in table 5.7, along with the standard deviation across C-rates.

Capacity / Ah	**0.25C**	**0.5C**	**0.75C**	**1C**
Experimental	180.1	169.6	159.6	150.0
ACM	184.6	170.6	159.1	150.8
SCM	186.3	172.5	161.0	152.7
9CM	184.6	170.6	159.1	150.8

Table 5.6: Comparison for the capacity across a range of C-rates for the 3 different model types

	Error	**Std. Deviation**
ACM	0.82%	1.00%
SCM	1.90%	0.90%
9CM	0.82%	1.00%

Table 5.7: Comparison of the error for simulations of the 3 different model types compared to the experimental results.

It can be seen that the ACM performs identically to the proposed 9CM. These are not perfect, however, are within a 1% tolerance, with different errors at different C-rates. The model correlates best at 1C, which is unsurprising, as the parameters were identified using tests at 1C. The errors are likely due to inconsistent temperatures between the different tests (later chapters attempt to compensate for this temperature inconsistency). The SCM is notably worse, with approximately 2% error on average.

Considering the simulation time, it can be seen in table 5.8 that simulation of the ACM took 80s, whereas the proposed 9CM only took 4s. For virtually the same result, this is a significant improvement.

	Test Time for 10hrs simulation / s
Experimental	36000.0
ACM	79.6
SCM	1.2
9CM	3.7

Table 5.8: Comparison of test times for the 3 different model types for a 10 hour experiment

5.4.2 Generating Parameters from a Distribution

The 9CM simulation result using experimental parameters can then be compared to using the variance relationship to identify the parameters for the model. The distribution shown in figure 5.31 was used to produce a sample of 48 cells. The sample was then used to populate the model for a “worst case” scenario according to the method outlined in 5.3.2, where the “weakest cell” has the lowest capacity and highest impedance. Additionally, the model was populated with impedance and capacity distributed randomly, with the weakest cell ranked by capacity as with the simulation of the 9CM in table 5.6. The capacity for these is shown in tables 5.9 and 5.10.

Capacity / Ah	**0.25C**	**0.5C**	**0.75C**	**1C**
Experimental	180.1	169.6	159.6	150.0
Generated Parameters Impedance / Capacity distributed randomly	182.8	168.5	156.9	148.4
Generated Parameters Pack configured as weakest cell has highest impedance	182.1	167.7	156	147.3

Table 5.9: Comparison for the capacity across a range of C-rates for the 9CM for different model population methods, where parameters are generated from the variance relationship.

Capacity	**Mean Error**	**Std. Dev.**
Generated Parameters Impedance / Capacity distributed randomly	-0.47%	1.20%
Generated Parameters Pack configured as weakest cell has highest impedance	-1.03%	1.29%

Table 5.10: Comparison of the error compared to the experimental result across a range of C-rates (shown in table 5.9 for the 9CM for different model population methods, where parameters are generated from the variance relationship.

Using variance to produce a dataset produced a similar result, however, with a lower constant current capacity (2%) than using the parameters found experimentally.

5.4.3 Discussion

The results show that modelling all cells in the 12s4p pack will give virtually the same capacity as the proposed model which considers nine cells in a 3s3p configuration when simulating cycles at a constant current different C-rates. With just a single cell model, the result is around 1% worse across the range of C-rates.

Generating parameters from a distribution gives a similar error to using experimental parameters, however gives lower capacity estimations than were experimentally found. This is likely due to the distribution producing more outliers than are in the experimental pack. A reason for this could be due to manufacturer selection, where new cells are tested, and poorer performing cells removed.

One error is that at lower C-rates, the experimental capacity was found to be lower than the expected capacity from the simulations. It is expected that this is due to temperature, which was not compensated for as there is poor temperature sensing on the LIM50E modules, with only one measurement for all of the 12 cells in each module. At a lower C-rate, the cell will generate less heat over a given time period, meaning the cell temperature is lower, thereby reducing the impedance according to the relationship found in section 5.2.1.1. Work in later chapters involves sensing temperature for each cell individually to be able to compensate for the temperature-related errors and producing a model to simulate changes in temperature.

5.5 Conclusions

In conclusion, the proposed model consisting of 9 cell models, has been shown to model a large battery with the same accuracy as modelling all cells, yet with a reduced simulation time comparable to that of simulating a single cell. It has been shown that it is a viable option to model a sample of cells from a distribution to simulate the behaviour of a different sample of cells which follow the same distribution. These will enable fast modelling of large batteries to predict how they will behave under different conditions.

Subsequent chapters involve using the model to investigate how different scenarios can affect a battery, for example, the optimal SoC to perform cell balancing at and determining a level of cell voltage imbalance that is safely acceptable. Furthermore, further experimentation using cell-level data from WESS is used to evaluate the model at a larger scale, using the model to inform a real-time estimator.

Chapter 6

In-situ Parameter Identification of cells in Grid Connected batteries

The model proposed in chapter 5 explores the use of 9 cell models to describe a large battery. It proposed a method to identify parameters for the model using a test sequence performed on individual cells. This is useful, but from the author's experience, individual cells are often unavailable or difficult to source from a manufacturer. Whilst dismantling a pack or module is often physically possible, the process can often be unsafe and will void the warranty or any manufacturer responsibility. Also, cells in packs may be welded in place [137] and therefore very challenging to remove without damaging the cell. Dismantling of packs has been observed in literature [15, 74] to identify parameters for cells in a lengthy process.

Therefore, identifying the parameters of cells for a system is ideally performed whilst the cells are in-situ, as part of the system. This is particularly true if model parameters are being updated as a system degrades. It is also beneficial when attempting to produce a large dataset of cells - testing a large sample of cells individually can be very resource intensive as each cell requires a channel of battery testing hardware. Testing enough cells to produce a sample that is the same size as the number of cells in a grid-connected system would be immensely impractical. Two examples have been observed in literature, the first where cells had their parameters identified using a Kalman filter, under carefully controlled conditions [113], albeit only four cells. The second is in [71], where results for 96 cells are presented, where it appears these were measured while in the pack, although it is not explicitly mentioned, and the method is not evaluated or discussed.

Chapter 5 demonstrated some experimental techniques for identifying the parameters of cells. This chapter explores the methods used for identifying the parameters of cell models from the mentioned experimental work and literature, and considers the scale-up of these methods to identify parameters of multiple cells with both series and parallel connections in-situ.

6.1 Model

The model for which parameters will be identified is the equivalent circuit model discussed previously in chapter 5. The same Rint Model will be considered, however, it will also be proposed how multi-order ECMs with one or two Resistor-Capacitor (RC) components may be identified in-situ. Figure 6.1 shows a block diagram for how the model is configured, with parameters to be found highlighted. These parameters will each be discussed in section 6.2

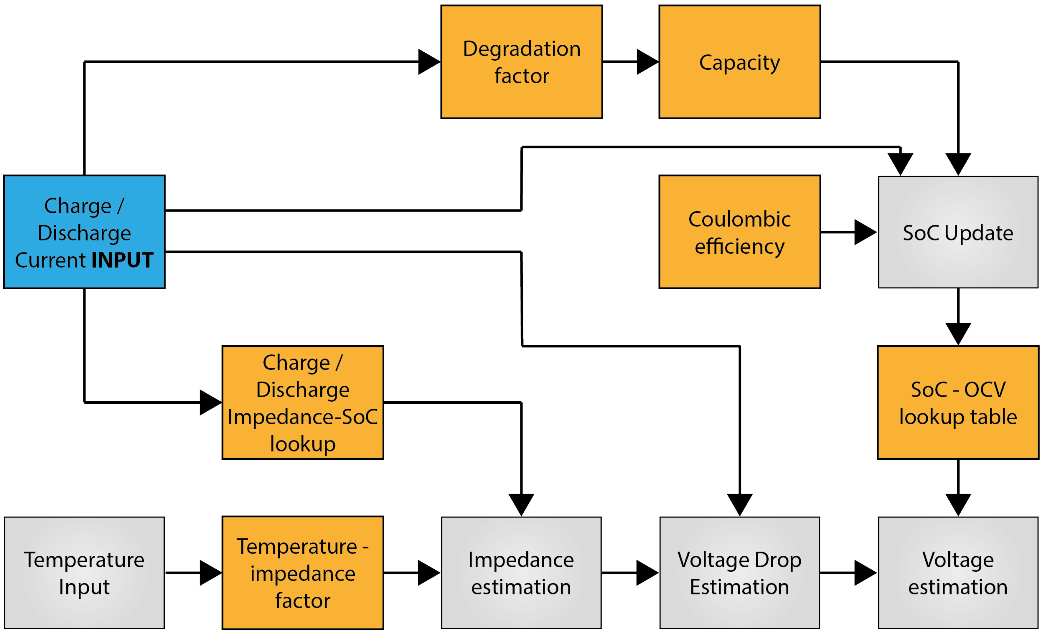

Figure 6.1: Rint model block diagram used in this chapter, with parameters to be found highlighted by a yellow box.

6.2 Parameters to Identify

This section discusses the experimental methods to identify the model parameters for a cell. It considers both the methods reported in literature, as well as those used in chapter 5. For each parameter, it is then considered which of those is best suited to in-situ parameter identification of a large pack.

6.2.1 OCV-SoC

6.2.1.1 Analysis of Cell Level Techniques

Throughout literature, there are several techniques which are both used and proposed in terms of estimating the OCV-SoC relationship, which will be explored.

Pulse Discharge

A pulse discharge test is overwhelmingly the most commonly used technique found reported in literature [8, 54, 86, 94, 138–141]. It involves discharging by known increments of SoC, resting the cell between each increment until the voltage is unchanging. This is then typically followed by charging and resting incrementally in the same way, and averaging the two results. Resting times were reported between 3 minutes [94] and 3 hours [86], with the most commonly used rest period of 2 hours. The rest time is cell dependent, and the rest time should be carefully considered to ensure that the voltage and temperature have reached a constant state.

Using this method requires the test to be preceded by an accurate capacity test, used to determine the pulse time or the capacity to be charged or discharged from the battery during each pulse.

Slow Discharge/Charge

Another commonly reported technique is using low C-rate cycling at a constant current, seen used in [39,58,113,142] and discussed as a method in [139]. In [39], the cell is discharged from 100% SoC to the lower voltage limit at a rate of C/100 and the voltage measured is used for the OCV-SoC relationship. In [58, 113, 142], a test is used involving a discharge at constant current from 100% SoC to the lower voltage limit, followed by a charge at constant current to the upper voltage limit. The OCV-SoC relationship is then determined by taking the average of the charge and discharge voltage. In these cases, a C-rate of C/25 was used. While a reason for the chosen C-rate was not specified, a sensible value might be the same C-rate used as the cut-off current used for a CCCV cycle, given that this is where SoC is defined as 100% or 0%. This c-rate should be sufficiently low to minimise the effects of hysteresis and minimise any temeperature change.

As long as a constant current is used, or the current is accurately measured, the capacity of the pack doesn't need to be known, and SoC can be interpolated based on the fact that at the upper voltage limit the SoC is 100% and at the lower voltage limit SoC is 0%.

Other

One other technique demonstrated in literature involved estimating OCV-SoC relationship based on the impedance-SoC relationship [78] during cycling. This method seems valid, although it relies on calculating the impedance-SoC relationship first and having a good estimate of SoC using coulomb counting or another method.

Finally, many papers state the OCV of a particular cell but do not state how it was measured. It is suspected that some used one of the techniques presented, but that others used an OCV-SoC relationship provided in the cell datasheet by the manufacture. This is a simple solution for defining the relationship without performing an explicit test, however, as the test methodology is often unknown, the relationship may not be reliable.

6.2.1.2 Scale-up to in-situ measurement

The only test found which considers parameter identification tests on multiple cells simultaneously is in [94], where the whole pack is tested as one - i.e., the results are for the overall pack and not the individual cells.

When attempting to estimate the OCV-SoC relationship, the assumption made throughout literature is that the relationship is constant between cells. This is useful, as a relationship for OCV-SoC does not need to be obtained for every cell, just one. For individual cells connected in a pack, the challenge is due to the cell voltage imbalance, where it is difficult to ensure that a single cell reaches both 0% SoC and 100% SoC. In theory, the weakest cell in the pack should take that position, as discussed in chapter 4. However, this relies on a battery being well balanced.

For a pulse test, the cell balance may not remain consistent between the capacity test and the OCV-SoC test, thereby affecting the SoC of the weakest cell being observed.

A low C-rate discharge / charge test seems more appropriate, as it does not rely on an additional capacity test. Performing cell balancing (bringing all the cells to the same voltage) at 50% SoC should give the best chance for an individual cell to reach the minimum and maximum SoC. Due to the low currents used, the voltage imbalance due to differences in impedance is also minimised, thereby increasing the likelihood that a single cell will reach both maximum and minimum voltage limits.

Of course, if a separate single cell is available, the chosen method would be to perform the test using a single cell method, but in the absence of that, a low C-rate charge / discharge is proposed with the pack balanced at 50% SoC. The C-rate will be the C-rate used as the CCCV cutoff current, which for the purposes of this thesis is C/20 as discussed in chapter 5.

6.2.2 Impedance-SoC

6.2.2.1 Analysis of Cell Level Techniques

Impedance in the model describes how the voltage of a battery deviates from OCV depending upon the applied current. For an equivalent circuit model this could be as simple as modelling the impedance as a single resistor, or more complex, including modelling a number of additional RC circuits. The measurement techniques used in literature involve stimulating the battery with AC or DC signals and taking measurements which are used to calculate the impedance used in a battery model, which will be discussed [125, 130].

AC measurement

As with techniques to find the OCV-SoC curve, there is a single technique which the majority of researchers use to find battery impedance. This involves driving the battery with an alternating current. This can be a fixed frequency - generally 1kHz is used for a fixed frequency [125, 129, 143], or a varying frequency such as EIS. As mentioned in the previous chapter, EIS involves measuring the impedance of a battery at many different frequencies. It is widely used to identify parameters for an equivalent circuit model [10, 15, 59, 125, 127, 128, 139, 144, 145]. Frequency ranges used in the mentioned papers generally measure impedance in the 10's of kHz range to 1's-10s of mHz range. A typical test as seen in [15] performs EIS in a frequency range of 10kHz to 10mHz.

The higher frequency measurements describe the inductive components and the lower frequency describes the capacitive components of impedance. In between on the real axis intercept is the purely ohmic component which typically is close to the 1kHz measurement [125], hence suggesting why 1kHz impedance is often quoted in datasheets.

EIS is an effective method for characterising a cell's impedance and should be performed at a range of SoC's as demonstrated in [59,139] as the impedance is likely to change with SoC.

6.2.2.2 Current Pulses

Other researchers use a current pulse technique. This involves applying a current for a period of time, and calculating the impedance based on the voltage response. This may be with a generic test, specifically designed test [14, 111, 125, 130, 139] or the standardised test sequence such as Hybrid Pulse Power Characterization (HPPC) [49,110,146,147]. On the whole, these compare the voltage change from rest to load in order to find the impedance parameters for models of varying order. The voltage is measured at rest, a current is applied - generally for 10 seconds, and the voltage response is recorded. For a Rint model, the voltage difference between rest and the end of the current pulse is used to calculate R_{DCIR}, and for higher order models, curve fitting is used to estimate the RC parameters.

One example considers the relaxation profile rather than the load profile to fit the model [147]. It is expected that this would produce a more accurate model, given that during the pulse there will be a change in SoC. This may be small generally, but at low SoCs where the change in voltage relative to SoC is high, there may be a greater effect, suggesting that there may be a higher impedance than reality.

6.2.2.3 Scale-up to in-situ measurement

For identifying the impedance characteristics of multiple cells in-situ, EIS is an unsuitable measurement technique, as the cell voltage response from a BMS is not fast enough. The BMS for WESS returns cell voltage data every

120ms. According to the Nyquist criterion, the sample frequency should be double the signal frequency, meaning that the highest frequency EIS that could be measured is around 4Hz - too low to estimate battery parameters.

A pulse test instead would be more suited, with cell voltage measurements being able to show the long period cell voltage transient behaviour. The method proposed in chapter 5 using OCV instead of waiting for a cell to rest after a pulse would be suitable for cells within a pack.

This could be further extended to estimating the impedance with a good estimate of SoC as was demonstrated in chapter 5. As a rest is unnecessary when using OCV in place of the resting voltage, a continuous constant current charge or discharge between voltage limits could be used to calculate the impedance at any point in the charge or discharge. This would only work for a Rint model, but would provide a high resolution for the impedance-SoC relationship. This is shown in figure 6.2. A test procedure could involve charge at 1C to the voltage limit, then resting until OCV is reached to set the start SoC. Then a 1C discharge to the lower voltage limit followed by a rest to set the end SoC. This can then be repeated during charge to find the discharging and charging impedance across the range of SoCs reached at 1C.

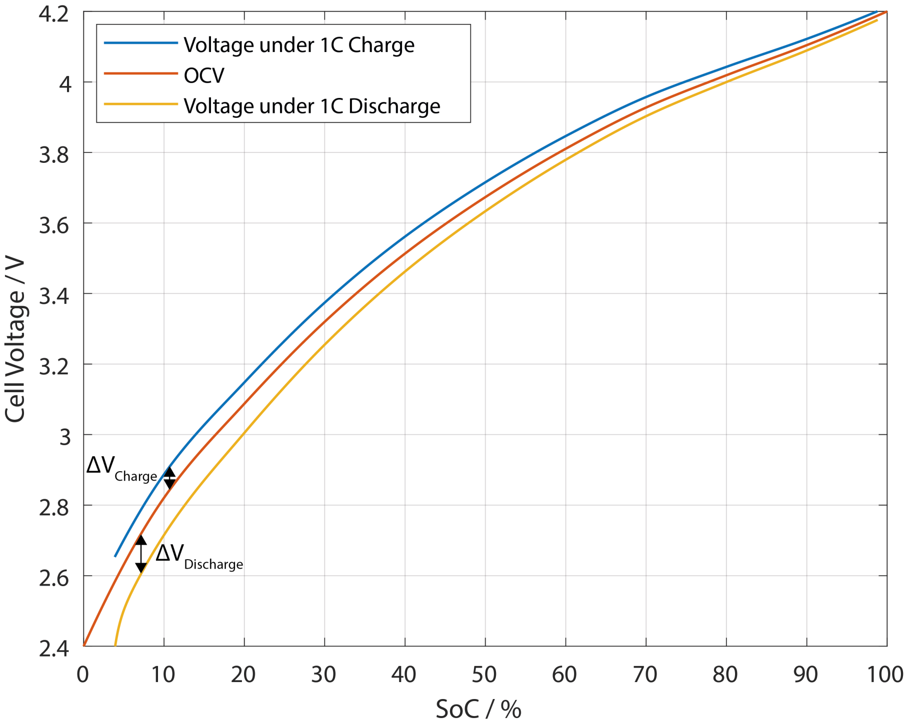

Figure 6.2: Cell voltage at 1C charge and discharge compared to SoC, showing the voltage drop used to calculate R_{dcir} for a Rint model.

If identifying the parameters of a model containing RC components, then a pulse test is necessary - using the cell rest profile to curve fit the RC components.

6.2.3 Capacity

6.2.3.1 Analysis of Cell Level Techniques

Cycle Test

In general, capacity tests are performed with a charge-discharge cycle test, with the procedure explicitly mentioned in many sources [8, 14, 15, 111, 148–151]. Typically a CCCV charge is used to reach the maximum SoC, then a CCCV discharge to measure discharge capacity and a CCCV charge once more to measure charge capacity. The capacity is measured as:

$$\Delta Q = \int_{t_1}^{t_2} I \; dt \tag{6.1}$$

$$C = \frac{\Delta Q_{charge} + \Delta Q_{discharge}}{2} \tag{6.2}$$

A variety of C-rates and CCCV cutoff currents are used. A sensible approach would be to measure capacity based on the application and according to manufacturer recommendations. C-rate can affect capacity measurements [152] and lower CCCV cutoff currents will give a higher capacity measurement.

Change in SoC

Another method has been observed in literature involving partial charge / discharge cycles and instead estimating the change in SoC and calculating the capacity based on the change in charge during the cycle [152, 153]. This is described in [153] as:

$$C = C_{1,2} = \frac{Q_1 - Q_2}{SoC_1 - SoC_2} \tag{6.3}$$

Naturally, this relies on a good estimate of SoC and accurate current measurement for precise coulomb counting. It is suggested in [152] that a change in SoC of >60% is recommended for accurate measurements, which agrees with the experimental results in [153] which states that for well-defined test procedures, the accuracy can be as high as 99.9%.

6.2.3.2 Scale-up to in-situ measurement

Measuring the capacity of many cells in-situ is challenging for performing capacity measurement cycles at constant voltage between voltage limits. This is due to the difference in voltage between cells, so only one cell can reach the voltage limits, and the same cell may not necessarily take the maximum and minimum voltages, for reasons discussed previously.

The technique using the change in charge and SoC to calculate capacity is more feasible, as it does not rely on all cells reaching a voltage limit. It does however, rely on accurate voltage measurements to estimate SoC of each individual cell and accurate current measurement for each string in order to calculate the charge. Assuming those measurements are accurate, equation 6.3 can be used for each cell to estimate the capacity of each cell.

6.2.4 Temperature

Temperature is shown to have an effect on the impedance of a cell [111, 130, 154, 155], where there is an increased impedance at lower temperatures and vice versa. There is some discrepancy between results in literature, but it is agreed that, the CC discharge capacity reduces as temperature reduces [143,156,157]. In [156], which uses Constant Voltage (CV) charge and discharge cycles, there is a less pronounced effect, suggesting that impedance change with temperature has a greater effect.

6.2.4.1 Analysis of Cell Level Techniques

In the aforementioned sources, the relationship between temperature and impedance were calculated using the various measurement techniques discussed in section 6.2.2 and 6.2.3 at different temperatures. The temperatures were controlled in a thermal chamber or other closely temperature controlled manner. It appears in to be assumed across literature in the mentioned references that the relationship is constant between cells (of the same type and age). One challenge appears to be maintaining a constant temperature in the cells, as whilst the environment temperature can be well controlled, performing lengthy tests with higher currents affects the cell temperature, changing the results. Chapter 7 shows how temperature varies across 6 strings at WESS - an example with a strong HVAC system, but still a spread of temperatures ($\sim$4°C average during a 1C cycle). Furthermore, [155] points out that there is a difference between the internal cell temperature and surface temperature.

6.2.4.2 Scale-up to in-situ measurement

For in-situ measurement, it is usually difficult to control the temperature precisely due to the size and location of them. Furthermore, even with temperature control of the environment, cells will not have an even distribution of temperature due to some having greater airflow - i.e. cells situated at the edge of a module. Therefore, it can be difficult to measure the temperature relationship in situ.

Instead, it will be assumed that the temperature relationship is the same between cells. Therefore, where possible, measurements should be performed with an individual cell in a thermal chamber and applied to all cells with the same relationship. In the absence of the necessary resources to do this (i.e. a spare cell), the relationship should be assumed the same as a different cell, or ignored all together, and parameter identification of impedance performed in conditions that are generally experienced by the battery system.

6.2.5 Coulombic Efficiency

Coulombic efficiency defines the efficiency of the electrical transfer of charge [132] between charge and discharge, defined in [132,133] as:

$$CE = \frac{\Delta Q_{Discharge}}{\Delta Q_{Charge}} \tag{6.4}$$

It is noted in [135]that the CE for Lithium-ion batteries is very close to 1 (results in [133,158] suggest around 0.999), and so it is often an parameter which is ignored.

6.2.5.1 Analysis of Cell Level Techniques

For the measurement of CE, typically a charge / discharge cycle is performed, and the charge measured during charge and discharge is used to calculate CE according to equation 6.4. There are no other electrical methods reported, but it is worth noting that the cell should reach the same SoC at the beginning of the cycle to the end.

6.2.5.2 Scale-up to in-situ measurement

For in-situ measurement, cell balance again can cause an issue, as the same SoC may not be reached for each cell in a pack. However, this can be overcome by comparing the estimated charge capacity and discharge capacity calculated in the capacity measurement for each cell. It is expected that the coulombic efficiency will be constant between cells, and any deviation will be within the measurement noise.

6.2.6 Proposed parameter identification procedure

Using this research and discussion, a test procedure for identifying the parameters of cells with many connections is proposed. Table 6.1 shows the procedure for identifying the parameters of multiple cells with series and parallel connections in a pack. It makes several assumptions about the system design in order for parameters to be determined:

- Every cell has individual voltage measurements.
- Every series string has individual current measurements.
- The sample rate for all measurements is >1Hz.
- Where there are parallel connections between individual cells without individual current monitoring, it is considered that the parallel connected cells are one cell. (i.e., series connections of 1s2p cell pairs would be considered as series connections of a single cell with double the capacity).
- The temperature in the pack is constant or there is an accurate cell-level temperature measurement.
- The pack is well balanced

Different configurations may require a tweaked parameter identification process, or may not be possible if sufficient data is unavailable.

Test Phase	**Sequence**	**Limits**	**End Condition**
Balance pack to 50% (nominal)	CCCV Charge / Discharge	V = Average nominal voltage for pack, I = 1C	I <C/20 A
	Hold Voltage	V = Average nominal voltage for pack, I = 1C	Cell imbalance <3mV
OCV - SoC	CC Charge	I = C/20	Any Cell >= Max V
	CC Discharge	I = C/20	Any Cell <= Min V
	CC Charge	I = C/20	Any Cell >= Max V
Capacity / CE / $\mathbf{R_{DCIR}}$	CC Discharge	I = 1C	Any Cell <= Min V
	CC Charge	I = 1C	Any Cell >= Max V
	Rest		dV/dT = 0
	CC Discharge	I = 1C	Any Cell <= Min V
	Rest		dV/dT = 0
	CC Charge	I = 1C	Any Cell >= Max V
	Rest		dV/dT = 0

Table 6.1: The test procedure for identifying the parameters of multiple cells in-situ

This procedure begins with balancing the pack at 50% SoC. This is so the individual cell with the lowest capacity has the greatest chance of reaching 100% SoC and 0% SoC for the OCV-SoC test. As mentioned, 50% is best as there is the greatest change in SoC for charge and discharge, which means small imbalances in SoC should not prevent the lowest capacity cell from reaching both voltage limits. The OCV-SoC test consists of a C/20 charge for the pack to reach 100% SoC, then a C/20 discharge and charge, where the voltage of the cell which reaches the upper and lower voltage limits will be averaged to find the OCV-SoC relationship. Finally, a CC test is performed to find the capacity, CE, and R_{DCIR} for the Rint model. This consists of a CC discharge then charge to normalise the voltage of the pack, where each constant current sequence ends when any cell reaches the upper or lower voltage limit. This is followed by a rest until the cell voltage is constant, which is used to find the SoC of each cell using the OCV-SoC relationship. A CC discharge followed by a rest period until the voltage is constant is used to find the SoC after discharge. The change in SoC and the cell current is used to find the discharge capacity for each cell according to equation 6.3. This is repeated under charge to find the charge capacity for each cell. The CE is therefore calculated using equation 6.4. Using this 1C cycle data, the impedance is found using the process outlined in section 6.2.2, illustrated in figure 6.2, at a resolution of 1% SoC.

As noted when discussing temperature, it is challenging to estimate the Temperature-Impedance-SoC relationship in-situ, due to the lack of precise temperature control in large systems. Therefore, should a single cell be available to test, it should be used individually in conjunction with an environmental chamber to measure the relationship. Should this be unavailable, the temperature relationship should be ignored. The process for determining the Temperature-Impedance-SoC relationship is shown in table 6.2.

Test Phase	**Step**	**Sequence**	**Limits**	**End Condition**
Set Temperature	1	Set Temperature		T >2 hrs
Capacity / R_{DCIR}	2	CCCV Charge	V >= Max V I = 1C	I <C/20 A
	3	CCCV Discharge	V <= Min V I = 1C	I <C/20 A
	4	CCCV Charge	V >= Max V I = 1C	I <C/20 A
Repeat	5	Repeat 1-4 at different temepratures		All temeperatures tested

Table 6.2: The additional test procedure for identifying the parameters of a single cell to find the Temperature-Impedance-SoC relationship

The procedure begins by setting the temperature and waiting for 2 hours for the cell temperature to reach equilibrium. CCCV cycles are then performed to find the capacity and impedance of the cell, using the techniques discussed. This is therefore consistent with the method used ex-situ and in-situ. One potential issue is that there may be a change in temperature due to the relatively long test, however consistency of the method is preferred, and the cell temperature is measured through the test. It is proposed that the temperatures tested should be 5-45 °C, at 10 °C intervals. Furthermore, the capacity and impedance can be compared with the in-situ measurement, verifying the parameter identificaiton process.

6.3 Experimental Setup

In order to validate the proposed test procedure, tests are performed on various systems. These are the Yuasa LIM50E ESS and WESS

6.3.1 LIM50E ESS

As mentioned in chapter 3 the Yuasa LIM50E ESS consists of 168, 47.5Ah cells connected in series, arranged in modules of 12 cells. It is a lab-based battery and as such can be dismantled and reconfigured to provide results under different conditions. For the work presented in this chapter, the system is tested as a whole, an individual module is removed and tested, and a single cell from the removed module is removed to be tested individually. This is used to observe how the in-situ parameter identification test compares to commonly used cell tests. The modules and cells chosen to be removed were those which are most accessible practically.

6.3.2 WESS

WESS consists of 40 series strings connected in parallel, with each series string consisting of 264 series connected parallel pairs of cells, arranged in modules of 12 parallel pairs of cells. At the time the work took place, only six series strings were modified according to section 3.2.4.1 to store individual cell data from each cell pair, giving the data from 1584 pairs of cells.

Unfortunately, due to the operating constraints of the system, the minimum cell voltage cannot be reached so the OCV test cannot be performed on the system. Furthermore, the system is generally used as part of an asset used by an aggregator, meaning specific cycles cannot often be performed. Instead, cycles such as those observed in chapter 4 are used, and the capacity and impedance can be calculated from cycles with a large change in SoC, that match the proposed procedure. This should provide a helpful insight into the practicality and accuracy of performing these types of tests in a “real-world” scenario.

To find OCV, a test cell provided by the manufacturer is used, performing the C/20 test proposed as part of the test procedure. Alongside this, the other parameter identification tests are performed on the cell to compare with the in-situ tests.

6.4 Results

6.4.1 Yuasa LIM50E ESS

6.4.1.1 OCV

The OCV portion of the test was performed using the Yuasa LIM50E ESS and spare module. Following the test of the module, a cell was removed and was tested for OCV using the same procedure. The OCV found for the cell is assumed to correct and the result that should be achieved from the module and ESS if the parameters are identified correctly. The OCV result is shown in figure 6.3

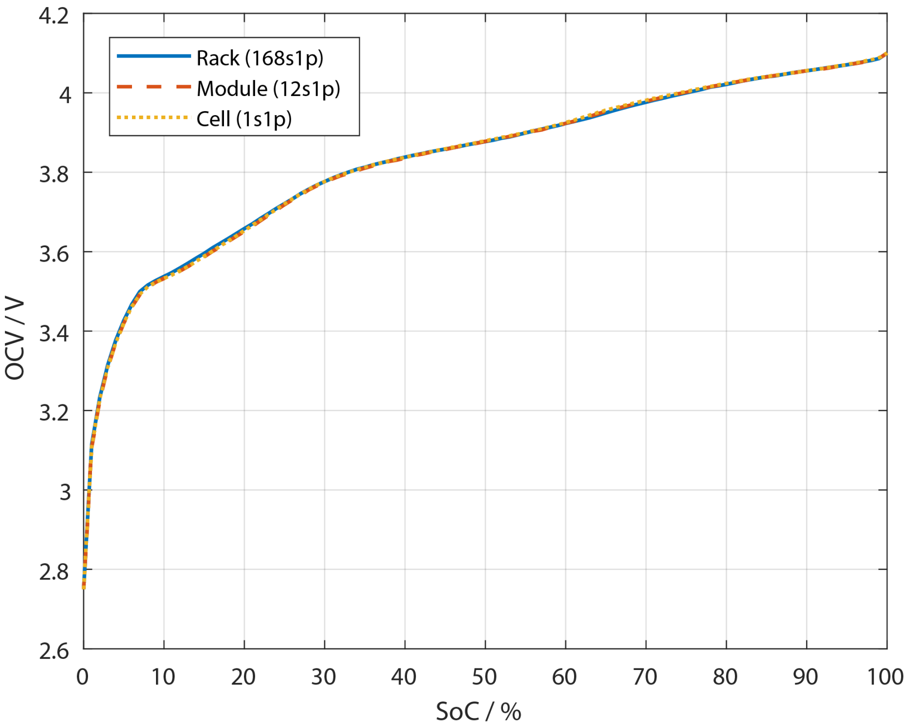

Figure 6.3: OCV for Yuasa LIM50E cells, measured in different contexts.

It can be seen that each of the results is virtually identical. For the ESS and module, it was found that a single cell did not reach both the upper and lower voltage limits. In both the ESS and module, the cell which reached the lower voltage limit came within 2mV of the upper voltage limit during the test, so was used. The OCV relationships shown in figure 6.3 were sampled at 1% SoC intervals and 100% and 0% SoC were set to the minimum and maximum cell voltages. The OCV points from 1% to 99% SoC were determined from the experiment, so a cell not reaching 100% SoC is inconsequential.

6.4.1.2 Capacity

The proposed capacity test was performed using the Yuasa LIM50E ESS and the removed module. The removed cell was tested for capacity using a CCCV charge and CCCV discharge cycle procedure. Considering first the cell which was removed from the system, the capacity found in-situ in the rack was 49.73Ah, the capacity found in-situ in the module was 49.96Ah, and the capacity found by a CCCV cycle test was 50.71Ah. This is a 1.9% difference, and is likely primarily due to differences in temperature, where the tests were not performed in a temperature controlled environment. Additionally, it is expected that some difference is caused by measurement error, where the devices have different calibrations for current. Additionally, cell voltage measurements rely on the BMS which has an unknown accuracy, again providing another source of error.

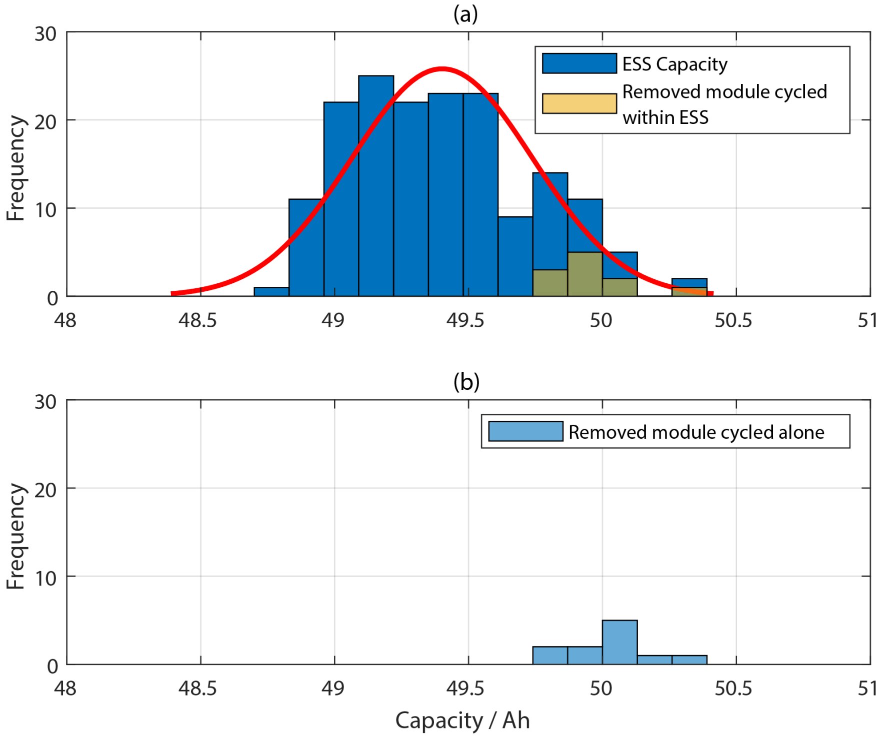

Figure 6.4: Capacity distribution of LIM50E cells, measured from (a) the ESS and (b) the removed module.

Comparing the distribution of capacity between the spare module and the ESS showed a reasonably 'normal' distribution, as seen in figure 6.4. The cells in the removed module measured alone showed virtually the same capacity when cycled alone compared with cycling within the ESS. This is as expected, as very similar hardware was used for cycling in the two tests.

6.4.1.3 Coulombic Efficiency

The coulombic efficiency of the cells in the ESS, removed module and the removed cell was calculated using the capacity measured during charge and discharge in the above capacity tests. The results are shown in table 6.3

	Mean / %	**Std. Dev. / %**
ESS	97.5366	0.0026
Removed Module	100.1979	0.0056
Removed Cell	99.9868	n/a

Table 6.3: Coulombic efficiency of LIM50E cells measured in the ESS, removed module and removed cell.

The value measured directly in the cell is considered the correct value for the cell, as it is measured using the MACCOR S4000 which is highly accurate and regularly calibrated. Additionally, there was no BMS or any other potential loads attached to the cell. In the ESS, the CE was found to be lower than this value, and the module cycled alone was found to be higher. This could be due to a number of reasons - most likely due to inaccuracy in current sensing and losses in the overall system.

6.4.1.4 Impedance

The proposed impedance test was performed using the Yuasa LIM50E ESS, removed module and removed cell. The impedance tested for both the module and the ESS were found to be similar with results shown in figure 6.5.

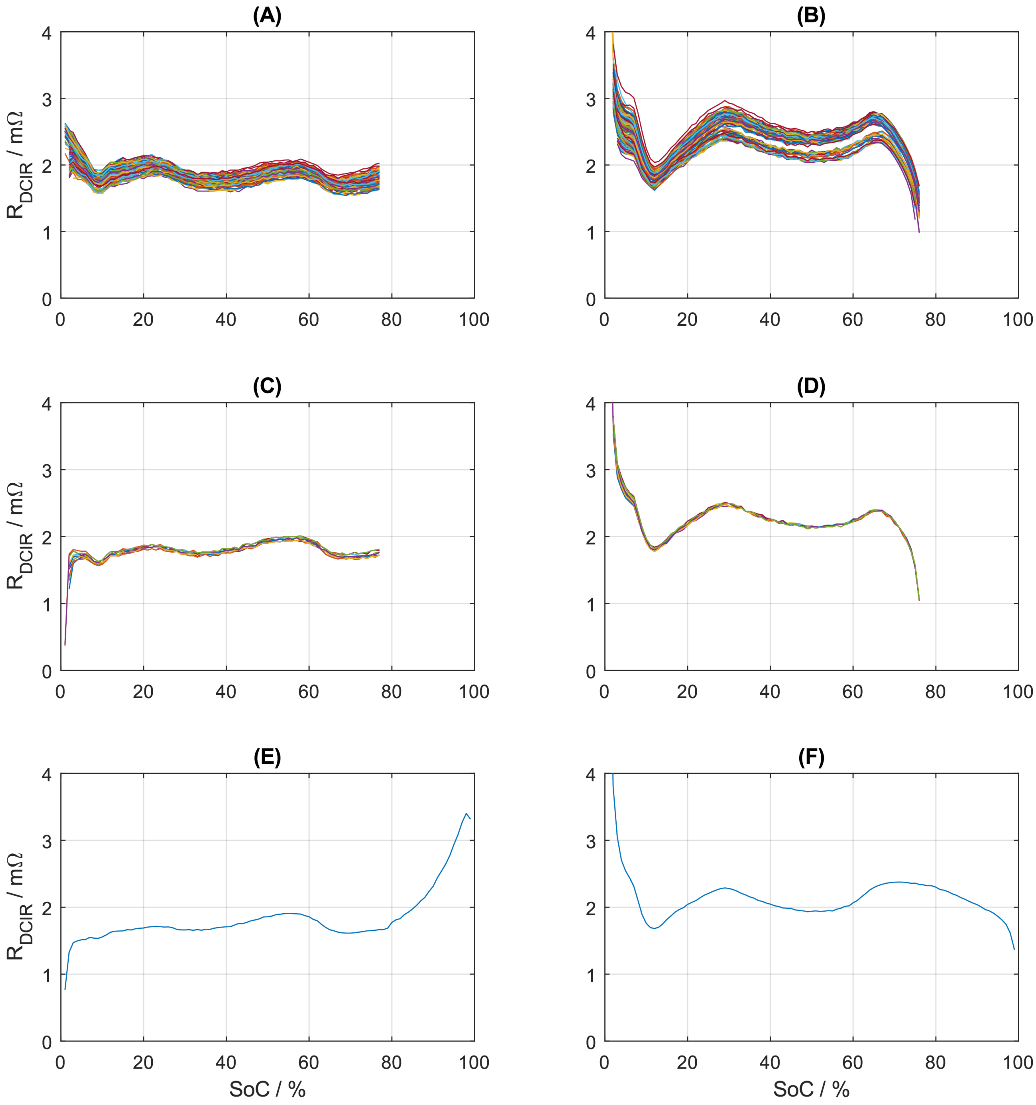

Figure 6.5: Impedance of LIM50E cells, measured in ESS for charge (A) and discharge (B), Module for charge (C) and discharge (D), and single cell for charge (E) and discharge (F)

For all tests, the impedance measurement at the start of each test is notably lower, before reaching the expected value. This can be accounted for by the capacitive components of the impedance, where the voltage takes time to drop to a steady state. Therefore, R_{DCIR} values at low SoC for charge and high SoC for discharge should be discounted. It can be seen in figure 6.5 that in the ESS and module tests, there is no data above ∼78% SoC. This is due to these tests being performed using a CC cycle for safety reasons, where the maximum SoC reached is ∼78%. For the single cell test, the test was performed using a CCCV procedure, hence it reaches the full SoC range.

	Charge / mΩ	Discharge / mΩ
ESS	1.8534	2.0734
Module	1.9021	2.142
Cell	1.8582	1.9401

Table 6.4: R_{DCIR} at 50% SoC for the removed cell, measured in-situ in the ESS and module and measured alone.

Considering the cell which was removed, the impedance measured in-situ and individually is shown to be similar, as can be seen in figure 6.5 and table 6.4, with measurement in the cell being slightly lower in general.

6.4.2 WESS

Performing similar tests on WESS is helpful, as it gives an insight into a larger system with parallel connections, as well as dealing with the constraints of an operational energy storage system. This aims to further test the procedures, comparing the results to a test cell in a new condition provided by the manufacturer.

6.4.2.1 OCV

WESS was unable to perform the OCV test for several reasons. Firstly, it is not possible to reach the full voltage range of the cells given the limits of the inverter system. Secondly, as only 6 strings out of 40 were being measured, the cells in these strings are unlikely to reach the maximum or minimum cell voltages. Therefore, the OCV test was performed with a test cell provided by the manufacturer using the C/20 cycle test. The OCV was found as shown in figure 6.6 and the relationship is used in calculations going forward.

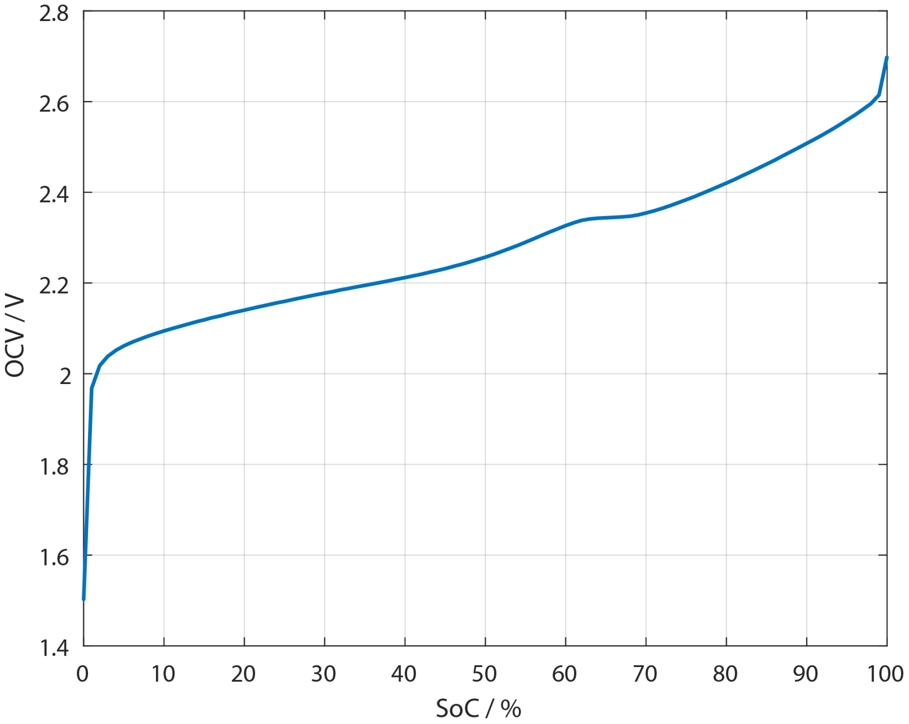

Figure 6.6: OCV for a 20Ah SCiB test cell, identical to those found in WESS.

6.4.2.2 Capacity

To find capacity in WESS, a sequence similar to the proposed CC cycle test followed by a rest is required. With the system performing as part of an aggregator, it often performs arbitrage type cycles - i.e., charging during periods of low energy cost and discharging during periods of high energy cost. This results in large constant power charges and discharges, with a long rest period (while the price changes) - virtually identical for the proposed sequence for measuring capacity using the in-situ technique. A typical sequence is shown in figure 6.7.

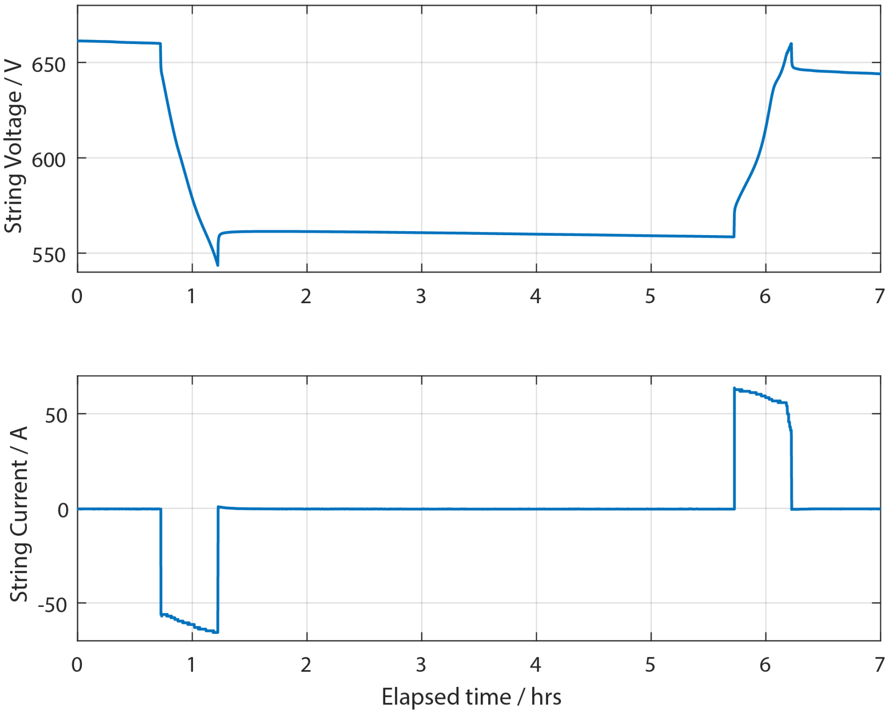

Figure 6.7: A typical charge / discharge sequence from a series string at WESS.

Using this sequence to find capacity gives the distribution of the cells in the 6 strings shown in figure 6.8. Note the result is the capacity for each parallel cell pair. Moreover, it can be seen that the current is not constant, as the system cycles in a constant power mode, as previously mentioned. This is not a significant change, however, it should be taken into account during the calculation of capacity and impedance. Additionally, it can be seen in the string voltage that there is a slight but constant discharge, caused by the parasitic load of the inverters. To determine the OCV at the end of charge or discharge, the method outlined in [130] can be used, linearising and interpolating this slow discharge curve to find OCV at the end of the charge / discharge half cycle.

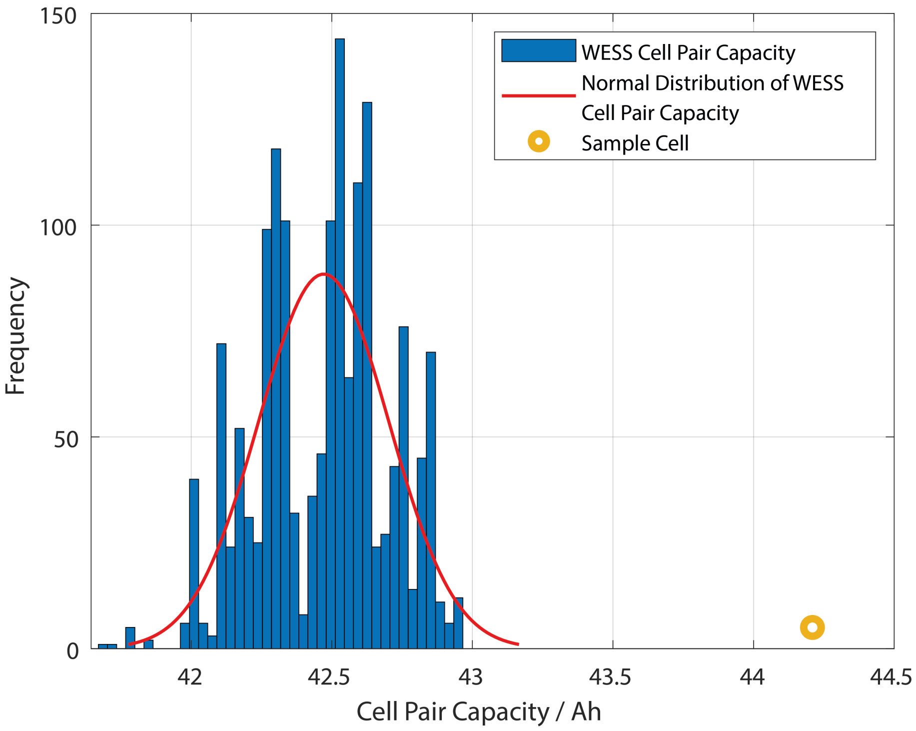

Figure 6.8: Capacity for 1584 parallel cell pairs from WESS compared to a test cell.

The test cell measured individually using a CCCV cycle test showed a capacity of 22.10Ah. Doubling this to compare with the cell-pairs in WESS is 44.21Ah which is shown in figure 6.8.

This is a little higher than the mean value which can be seen in figure 6.8, however the test cell is unused, whereas WESS has been in use for a number of years, so degradation is expected, explaining the higher capacity of the test cell. Further, the cell is from a much newer batch, giving another potential reason for the increased capacity.

The distribution is not as uniform as may have been expected, as was seen in the Yuasa ESS. This may be due to the difference in temperature between cells, where there was a difference of the average cell temperature during the test of 3.9°C.

6.4.2.3 Coulombic Efficiency

As with the Yuasa systems, the CE was measured using the calculated charge and discharge capacity in the above test for WESS and a test cell. The results are shown in table 6.5.

	Mean / %	**Std. Dev. / %**
WESS	95.9934	2.351
Cell	99.9131	n/a

Table 6.5: Coulombic efficiency of cells measured in WESS, compared to a test cell.

Again, the test cell is considered correct, so WESS shows a much lower CE than the test cell. It is expected that the CE of the physical cells is consistent with the test cell, however with losses elsewhere in the system. The CE for cells in each series string is virtually identical and is consistent across different tests. Therefore, it is likely due to some losses or error in current sensing in the system, and demonstrates the sensitivity of CE to measurement and coulomb counting drift.

6.4.2.4 Impedance

To find the impedance in WESS, the same cycle as the capacity test is used, implementing the proposed method. The impedance for each cell pair in the 6 strings as a function of SoC is shown in figure 6.9.

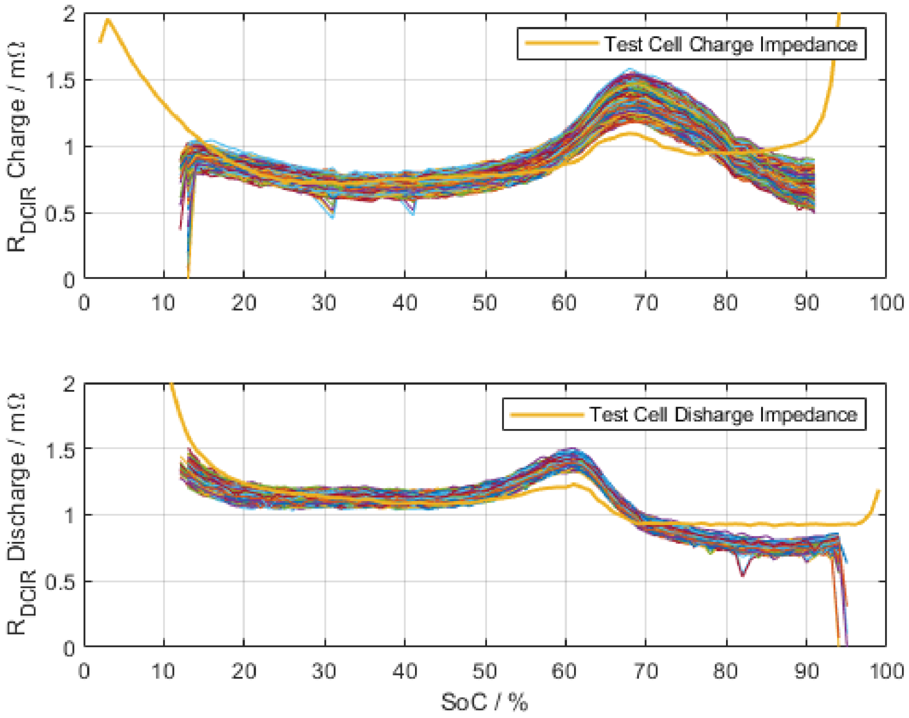

Figure 6.9: R_{DCIR} for 1584 parallel cell pairs from WESS.

The impedance found is very similar, however follows a slightly different trend. This is most likely a result of the ageing, or temperature variations in the system throughout the cycle.

6.4.2.5 Temperature correction

Using the test cell, the temperature relationships were determined using the test procedure in table 6.2. For equation 5.5, the capacity-temperature constant was found to be -0.0022 and the impedance-temperature constant was found to vary with temperature, and is shown in figure 6.10.

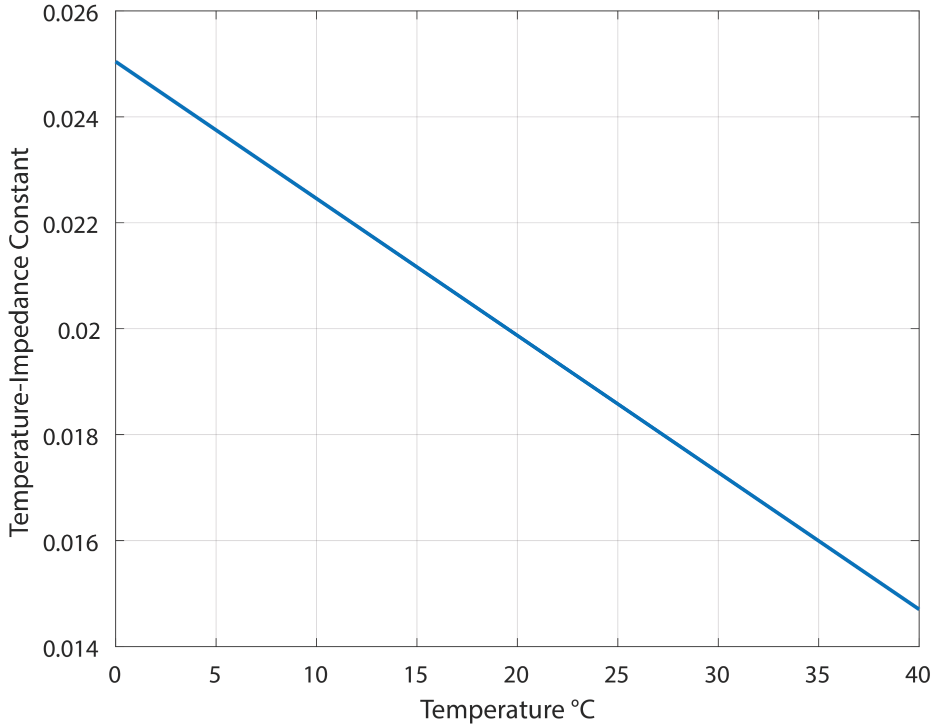

Figure 6.10: The temperature-impedance constant vs temperature for an SCiB test cell used in WESS

Some of the anomalies observed have been accounted to the effects of temperature. Using the temperature relationship, the effects of temperature can be compensated. With a temperature sensor per 2 cell-pairs on the modules, this gives a reasonably good temperature measurement for each cell at WESS. The above temperature relationship is used to normalise the capacity and impedance at 25°C, shown in figures 6.11 and 6.12.

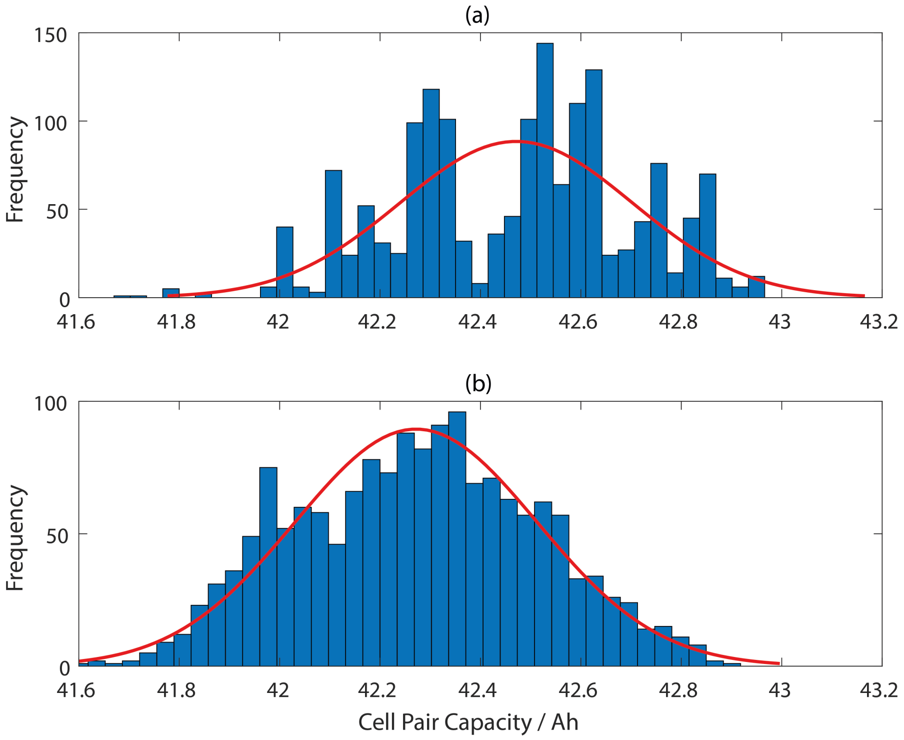

Figure 6.11: The capacity for 1584 parallel cell pairs from WESS (a) as measured and (b) normalised at 25°C.

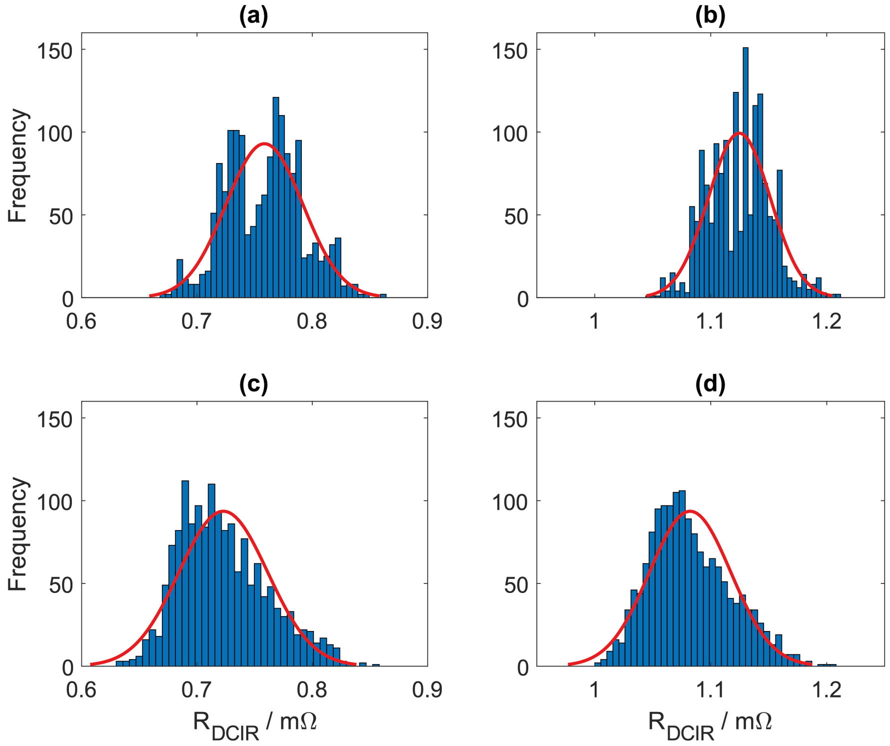

Figure 6.12: R_{DCIR} at 50% SoC for 1584 parallel cell pairs from WESS (a)/(b) as measured (charge)/(discharge) and (c)/(d) normalised at 25°C (charge)/(discharge).

The distributions can be seen to be much more uniform for both impedance and capacity when normalising the parameters at 25°C. This is the result that is expected and explains some of the less uniform results.

6.5 Conclusion

The work presented in this chapter proposes a method for in-situ parameter identification of cells within a large battery system consisting of series and parallel connections. It relies on cell-level voltage data and string current data being reported by the BMS. In-situ parameter results for a Rint model are within the expected range when comparing to tests performed on individual cells. There are several key advantages to using this method when comparing to cycling a large batch of cells individually. Firstly, it is faster and less resource intensive, without having to individually connect cells to channels of a battery tester. Secondly, the measurement error in the system being tested becomes “baked in” to the parameters, so when performing modelling and simulation, the results match.

Chapter 7

Online parameter estimation for grid connected batteries

7.1 Introduction

In chapter 4, the behaviour of cells within large batteries was studied, showing that on the whole, the weakest cell is the limiting factor for overall capacity of the pack. Based on this, chapter 5 proposed a model which considers 9 cell models to represent a large battery. From that, methodology to identify the parameters for all cells, then arrange them into the model was proposed in chapter 6.

This presented work provides the framework to create an online state estimator which is proposed in this chapter, named a Cell-level Parameter Estimator (CPE). Based on discussion throughout this thesis, with the key points highlighted in section 2.1.3, the specifications for the estimator are chosen to be:

- Output SoC Estimate
- Track SoH Diagnostics - Cell & System Capacity
- Output SoP Estimate
- Update Model Parameters

The work presented in this chapter describes the integration of the model and parameter identification methods to produce an online state estimator for SoC, SoH and SoP. This should improve on current methods by the considering the system as more than just a single cell. WESS will be used to evaluate the performance of the estimator.

7.2 Model

7.2.1 Electrical Model

The model for the electrical characteristics of the battery is identical to that proposed in chapter 5, shown in figures 5.20 and 6.1. The Simulink model for each cell is shown in figure 5.6.

Electrical parameters for each cell to be used in the model include: C, $\mathrm{R_{DCIR,Ch}}$ & $\mathrm{R_{DCIR,Dch}}$. The remaining parameters are found for a single cell and are assumed to be constant between cells. Temperature for the cells is estimated separately.

7.2.2 Temperature Model

In addition to the electrical model, a model for temperature of each cell will be considered. It is intended that 9 temperature models will be considered giving a temperature for each of the 9 electrical cell models. This will provide an estimate of temperature for temperature compensation of capacity and impedance.

The thermal model is based on the relatively simple models seen in [159] and [160]. The thermodynamics of the battery is represented by equation 7.1:

$$C_Q \frac{dT_{bat}}{dt} = Q_{Elec} + Q_{\Delta S} - Q_B \tag{7.1}$$

(adapted from [160]).

C_Q represents the heat capacity of the battery, Q_{Elec} represents the electrical heat generation of the battery, $Q_{\Delta S}$ is the entropic heat and Q_B is the dissipated heat. The entropic heat is due to the chemical reaction occurring in the battery, which can be endothermic or exothermic, and is a reversible heat flow [161]. Therefore it will be discounted, as across a cycle it will have a net 0 change in heat in the battery. Further, the process for identifying the the entropic heat is lengthy and requires precise sensing and temperature control [162] which is not present at WESS. Should it be found that a more precise model is required, it would be straightforward to implement in the model, albeit with a lengthy parameter identification procedure, which would have to be performed on an individual test cell.

The electrical heat generation, Q_{Elec}, is calculated as:

$$Q_{Elec} = (V_{OCV} - V_{load})I \tag{7.2}$$

(adapted from [159])

The heat dissipation can be expressed as:

$$Q_B = Ah(T_{bat} - T_{amb}) = k\Delta T \tag{7.3}$$

(adapted from [160])

In equation 7.3, A is the effective surface area of the battery, h is a constant, T_{amb} is the ambient temperature and T_{bat} is the temperature of the battery. With A being constant for each cell, the equation is simplified to $k\Delta T$, where k is a constant to be found for each cell in the system.

Overall, the system can be summarised in figure 7.1

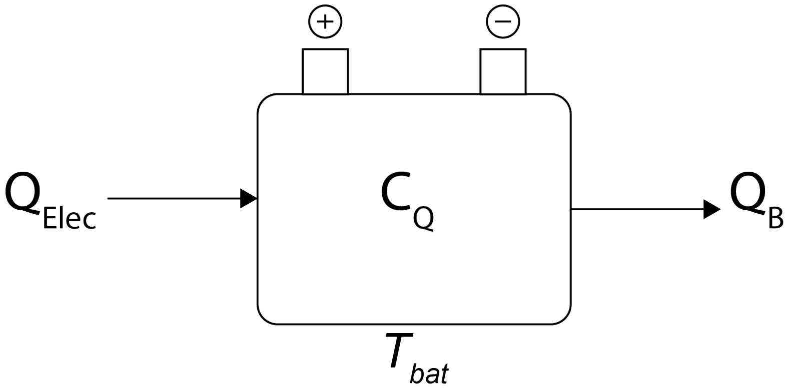

Figure 7.1: Architecture of the Thermal Model.

7.3 Parameter Identification

7.3.1 Electrical Parameters

To identify the electrical model parameters, the calculations presented in chapter 6 are used. The aim is to perform update of the parameters whenever an appropriate cycle is performed by the system which is similar to one of the elements of the test procedure in chapter 6. The method for detecting the cycles, and the type of cycles will be expanded upon in section 7.3.3.

7.3.2 Thermal Parameters

It is intended that the thermal parameters only be identified once, as it should remain constant across the life of a system, unless any physical changes are made. To find thermal parameters, equation 7.1 is integrated and simplified to give:

$$C_Q = \frac{\int_0^t Q_{Elec} - \int_0^t Q_B}{\Delta T} \tag{7.4}$$

Substituting equations 7.2 and 7.3 gives:

$$C_Q = \frac{\int_0^t (V_{OCV} - V_{load})I \quad - k \int_0^t T_{bat} - T_{amb}}{\Delta T} \tag{7.5}$$

This gives two unknowns to be found under a load - C_Q (heat capacity for the cell) and the constant k. Consider a second case where the cells are at rest:

$$C_Q = \frac{-k \int_0^t T_{bat} - T_{amb}}{\Delta T} \tag{7.6}$$

Solving these as a pair of simultaneous equations can give a value for C_Q and k. To give values for equations 7.5 and 7.6, the following test procedure is proposed.

Sequence	**Limits**	**End Condition**
Rest		Δ T = 0 (T$_{\text{cell}}$ = T$_{\text{amb}}$), t >20 min
CC Discharge	I $\approx$ 1C	Δ SoC >50%
Rest		t >20 min
CC Charge	I $\approx$ 1C	Δ SoC >50%
Rest		Delta T = 0 (Tcell = Tamb),

Table 7.1: Procedure for identification of Thermal Parameters

The procedure begins with a rest to set the initial SoC of the cells from OCV, and estimate ambient temperature for each cell. Then a discharge cycle, followed by a rest of 20 minutes to again determine the cell SoCs. Then a charge cycle followed by a long rest period until the cells again reach ambient. The charge and discharge cycles are used in equation 7.5 and equation 7.6 is applied. Solving the two equations gives values for C_Q and k for each cell measured. An example profile is shown in figure 7.2.

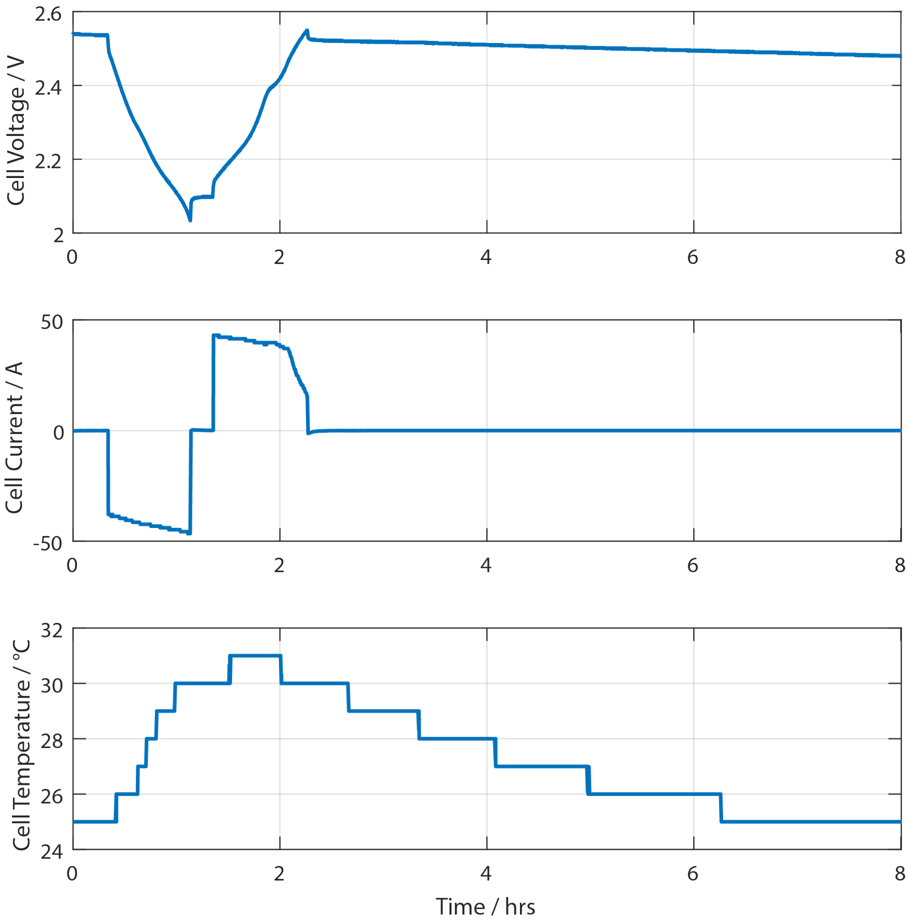

Figure 7.2: Typical test procedure - example taken from a cell in WESS.

7.3.3 Cycle Detection

In order to perform the parameter identification, the cycles must be correctly selected by the system. This is done by producing an array of each sequence the battery has performed, then based on the correct series of sequences, will determine whether the sequence can be used for any parameter identification. An example array is shown in table 7.2

Sequence	**Sequence Parameter**	**Start Time**	**Finish Time**
Rest	2433s	2021-07-02T10:00:00Z	2021-07-02T10:40:33Z
Charge	68.22%	2021-07-02T10:40:34Z	2021-07-02T11:23:35Z
Rest	1867s	2021-07-02T11:23:36Z	2021-07-02T11:54:43Z

Table 7.2: Example Array containing the cycle information used to detect cycles.

Initially, the system categorises the operation of the battery. This can be: charge ($I > 10A$), discharge ($I < -10A$) or rest ($-10A \leq I \leq 10A$). A deadband for rest current is set at 10A for WESS. This is because when the system is set to 0 power, there is around an 8A parasitic load on the battery - the deadband treats this as rest.

The sequence is then stored in the array, writing the sequence type, sequence parameter, start time and end time. If the sequence for the sample being read is the same as the last sequence in the array, it updates the sequence end time and sequence parameter. The sequence parameter refers to a parameter that is considered for whether a cycle is appropriate - for charge and discharge, this is ΔSOC, for rest it is rest time. This can be seen in table 7.2.

The cycles are then detected from this array and cell-level data is downloaded using the saved timestamps, where the parameter identification method is used. For capacity and impedance measures, the system does not currently log the string currents to an accessible database, but the system BMS logs it locally. Therefore, the cell data is written to a file, and the current data can be manually downloaded from the BMS and added, then the parameter identification algorithm is run. This is not perfectly synchronised, but it is thought to be correct to within 10 seconds.

The parameters to determine when to run the in-situ parameter identification are as follows:

7.3.3.1 Capacity

Capacity is split into charge capacity and discharge capacity, and the value for each is a result of an average of the last 5 readings to account for any small errors. The average of the charge and discharge capacity is then taken to give the overall capacity. The last 3 entries in the sequence array should match and meet the following conditions shown in table 7.3:

Sequence	Sequence Parameter
Rest	>1200s
Charge	>60%
Rest	>1200s

Sequence	Sequence Parameter
Rest	>1200s
Disharge	>60%
Rest	>1200s

Table 7.3: Conditions required to update charge (Left) or discharge (right) capacity.

A rest time of 1200s was chosen based on a previous cell-level test, where it was found that it took approximately 20 minutes for the voltage to reach an open-circuit level. A ΔSoC of 60% was chosen as noted in chapter 6 that for the capacity algorithm being used, >60% gave a good estimate for capacity.

7.3.3.2 Impedance

For impedance, the case is similar to capacity, but the charge and discharge impedance are separate. The last 2 entries in the sequence array should meet the following conditions shown in table 7.4:

Sequence	Sequence Parameter
Charge	>20%
Rest	>1200s

Sequence	Sequence Parameter
Disharge	>20%
Rest	>1200s

Table 7.4: Conditions required to update charge (Left) or discharge (right) impedance.

A ΔSoC of 20% is used to ensure that the voltage drop has reached a steady state. The rest time is the same as used in the capacity test, and sets the appropriate SoC which the impedance has been measured at. This is then mapped to the cell measured impedance-SoC relationship to give a value for R_{DCIR}. It is expected that this type of cycle will occur more regularly than a capacity test, and as such, an average of the last 10 readings are used.

7.3.3.3 SoC

This cycle detection will additionally be used to update the SoC. The SoC is estimated through simulation of the model, but this will drift over time due to small errors. To update the SoC, the last sequence in the array merely has to be a 1200s rest. Then the system downloads the cell-level data for the rest period and updates the SoC for each cell in the model. If the system is at rest for a long period, this will only occur a maximum of once every 5 minutes. Additionally, this will update the temperature of the cells in the model.

7.4 Online Estimator Architecture

7.4.1 SoC Estimation

The above model and parameter identification methodology combine to give an online estimator shown in figure 7.3 to estimate SoC.

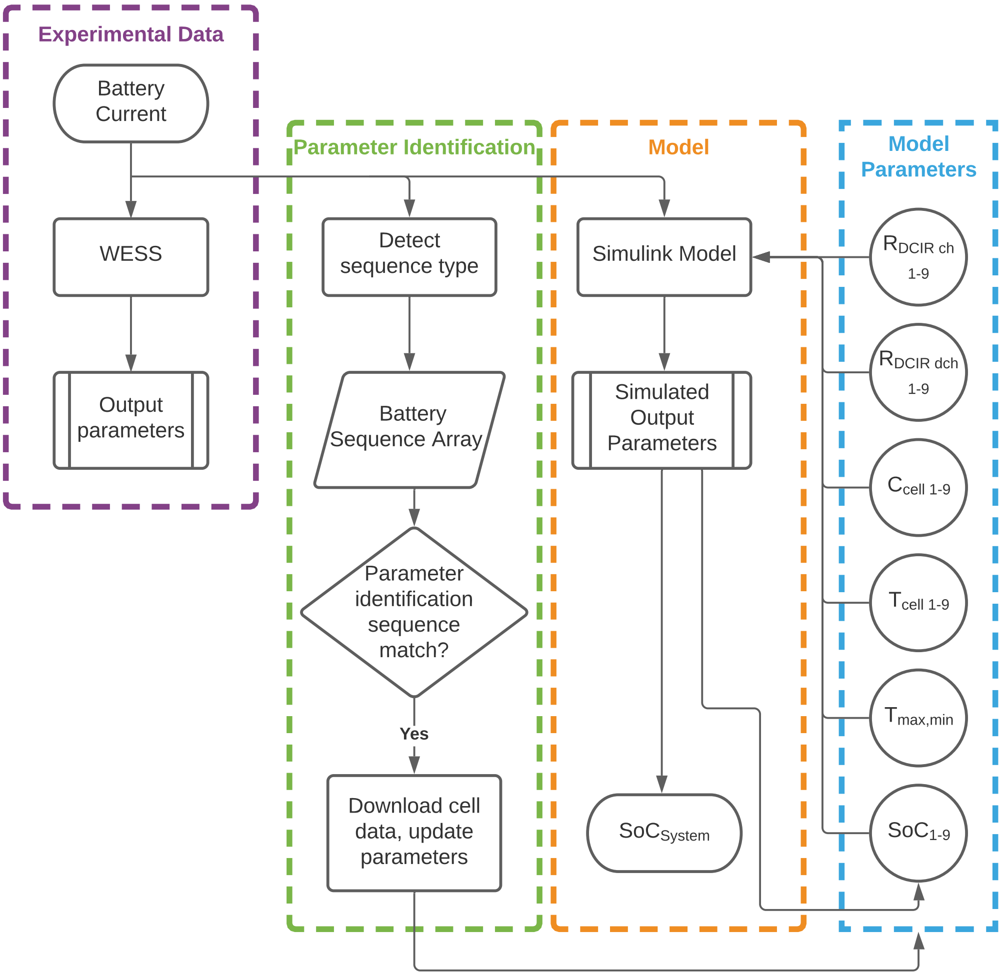

Figure 7.3: Architecture of the Online Parameter Estimator for SoC estimation and parameter updating.

This is an open-loop estimator, in that the model parameters are not updated on every sample, as would be done when using an adaptive state estimator, discussed in chapter 2 and shown in figure 2.14. To estimate SoC, the system initially downloads system level data from the WESS database. This occurs every 10 seconds, and 10 seconds worth of data is downloaded. This is because the time taken to download the data and run the model is 3s. This gives 7s to detect the sequence type for each sample and store it in an array. Should a parameter identification sequence be detected, updating of the parameters occurs. Depending upon the parameter being updated, this can take as long as 100s (mostly time to download the cell level data for all cells).

At this point, running of the model pauses, but once the parameter updating has completed, the SoC estimation resumes, catching up to the present time.

7.4.2 SoH and SoP estimation

To estimate SoH and SoP, simulations will be performed in parallel to the SoC estimator. This will involve simulating CC cycles at different C-rates (0.1C, 0.25C, 0.5C, 0.75C, 1C, 1.25C, 1.5C, 1.75C, 2C) in order to produce a power de-rating curve as a metric for SoP. This can then be used by the experimental system to ensure that cell voltage limits are not exceeded.

The CC capacity of the system at different C-rates provides the estimate for SoH, comparing this to an initial simulation based on a pack built from identical, new cells as a "best case" scenario. In this case, the sample cell presented in chapter 6 is used, with a capacity of 22.10Ah, $\mathrm{R_{DCIR,Ch,50\%}}$ (R_{DCIR} during charge at 50% SoC) of 1.54mΩ & $\mathrm{R_{DCIR,Dch,50\%}}$ of 2.20mΩ. A diagram of this system is shown in figure 7.4. This estimate is performed once per hour - this will be at least once per cycle (considering the maximum C-rate for the system as 2C).

7.4.3 Initialisation

Before the estimator can run, it first requires initialisation. For the model parameters, R_{DCIR} and C are assumed to be the same as the last time it was run, or are found using the parameter identification procedure in 6.1 as the initial parameters. For SoC and Temperature, the system waits until the parameters are updated by detecting the appropriate cycle. Only once this has happened does the simulation of the model begin.

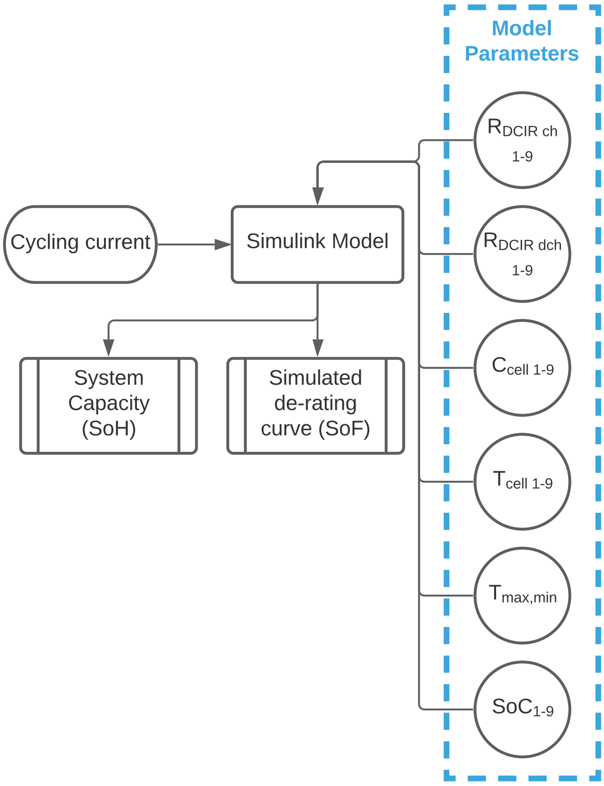

Figure 7.4: Architecture of the SoP and SoH estimation.

7.5 CPE Evaluation

As an online estimator, the CPE is run continuously, and results are presented from the CPE running during July 2021 on WESS. 100 hours of the CPE running is shown in figure 7.5.

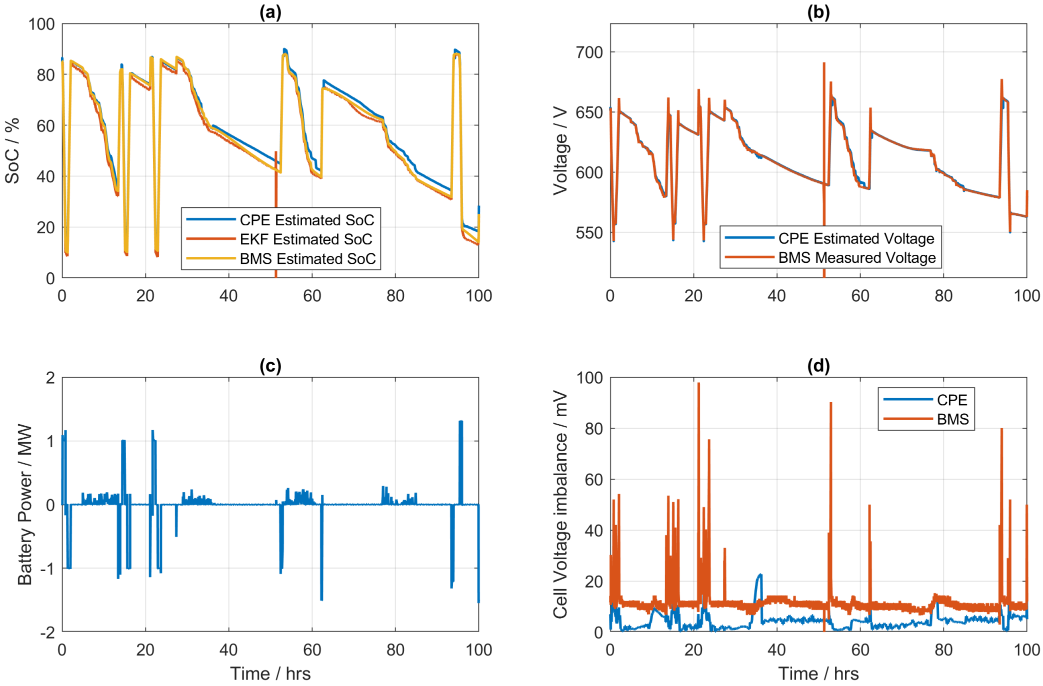

Figure 7.5: Output of the CPE compared to measured results from WESS for 100 hours during July 2021.

From figure 7.5, cycles are chosen which are used to evaluate the CPE in a range of cycle types - High DoD cycling; frequency service type cycling and rest / very low current. A detection and updating of parameters is also shown, and the performance of the SoH and SoP is shown. It can be seen that generally, the CPE correlates well to the experimental data, except for the cell voltage imbalance (difference between highest and lowest cell voltages in the system). The general trends show some correlation, though there is a notable difference. This will be discussed further in section 7.5.2 when discussing power derating.

7.5.1 SoC estimation

The SoC which the SoC estimator output will be presented in comparison to the system BMS and an EKF estimate (detailed in [163]). Figure 7.6 shows the output of the CPE during a high DoD cycle.

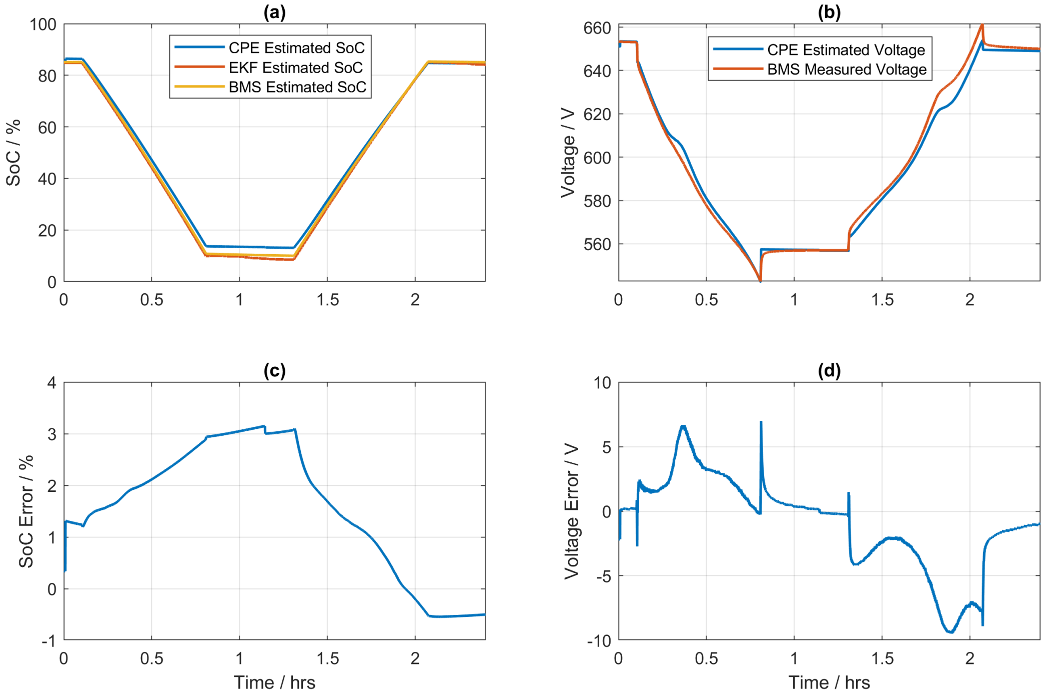

Figure 7.6: A high DoD cycle on WESS. (a) shows the SoC estimate from the CPE compared to the BMS and EKF estimates. (b) shows the system voltage estimate from the CPE compared to the measured value. (c) shows the error for the estimate of SoC compared to the EKF and(d) shows the error for the voltage estimate compared to the measured value.

It can be seen that the estimate for the system is a little higher than the BMS or EKF estimate, particularly at a low SoC. The difference observed in SoC is due to the way in which SoC is calculated. For the CPE, SoC is measured as the total charge remaining in all of the cells in the pack, compared to the total capacity of all of the cells. With the system not being able to utilise all energy in the cells, this means that it reads higher than the BMS, which considers the pack as a single cell with a lower capacity. This should be reflected in the SoP power derating curve, where the system will not be able to reach 100% or 0% SoC, where is has been noted that it is possible to reach 100% and 0% SoC accoridng to the system BMS. Considering the voltage of the system compared to the expected voltage output by the model, it can be seen that this matches more closely - particularly during discharge. During charge however, the error in voltage is greater, though once the current returns to rest, the estimated voltage then matches the measured voltage. As this voltage error is observed under load, it is likely that the error is due to an incorrect estimate of impedance in the model.

Considering frequency type cycles, it can be seen from figure 7.7 that the SoC is again a higher estimate than the BMS and EKF as before, with a larger error at low SoC. It does, however, track the same shape as the BMS and EKF, and the voltage does not appear to drift, with system voltage tracking well. A small drift in the voltage estimation is seen towards the end of the DFR period, though this is less than 3V - an error of under 0.5%.

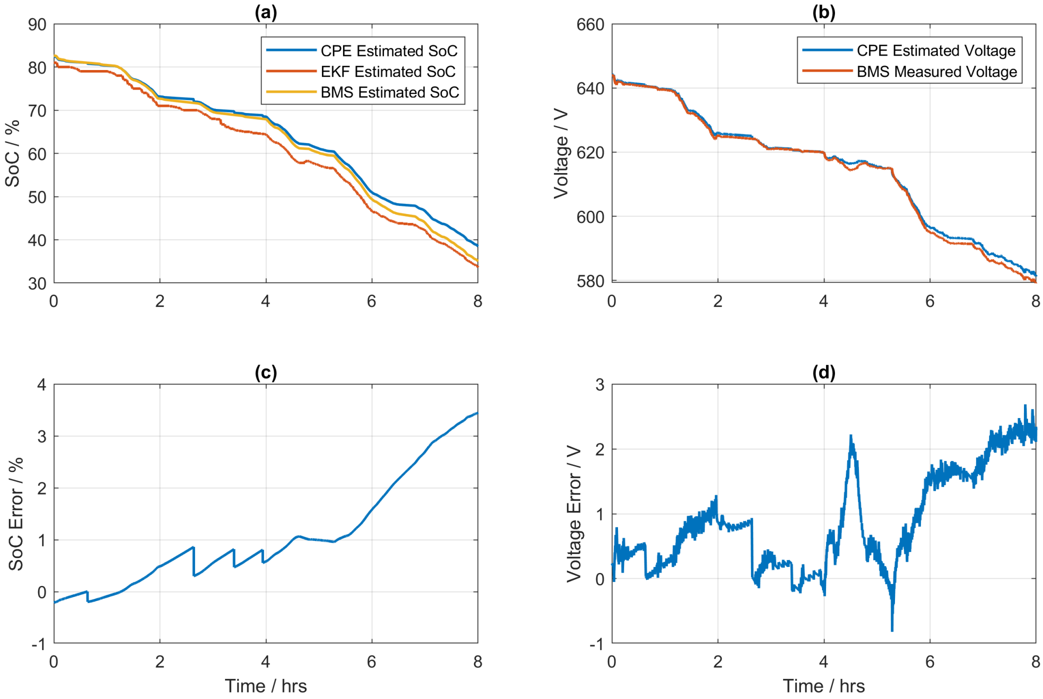

Figure 7.7: WESS performing Dynamic FFR (Discharge only). (a) shows the SoC estimate from the CPE compared to the BMS and EKF estimates. (b) shows the system voltage estimate from the CPE compared to the measured value. (c) shows the error for the estimate of SoC compared to the EKF and(d) shows the error for the voltage estimate compared to the measured value.

At rest, it can be seen in figure 7.8 that the SoC tracks well with the slow discharge created by the parasitic load in the inverters. The very low current is considered as rest, so the SoC is updated from OCV periodically every 20 minutes during this period, hence the “sawtooth” profile. This updating of SoC from OCV suggests that the model does not perfectly match the measurements at low currents, where the performance of the CPE is better at a higher current. It is likely that this is due to current measurement error, although further investigation would be required to conclusively verify this.

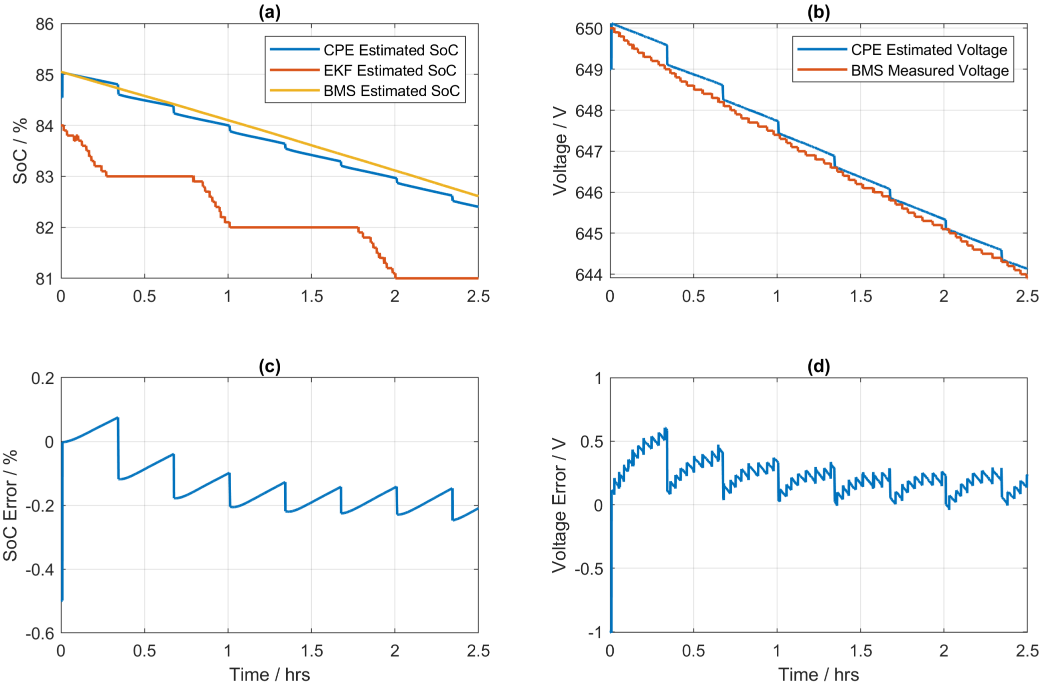

Figure 7.8: WESS during an extended rest period. (a) shows the SoC estimate from the CPE compared to the BMS and EKF estimates. (b) shows the system voltage estimate from the CPE compared to the measured value. (c) shows the error for the estimate of SoC compared to the EKF and(d) shows the error for the voltage estimate compared to the measured value.

7.5.2 SoP & SoH Estimation

Based on the simulation run, the SoH did not notably change during the month of July when the CPE was online. It estimated SoH at 99.24%. It is likely that this would improve should the cells be better equalised.

For SOP, the system initially returned a power derating relationship shown in figure 7.9.

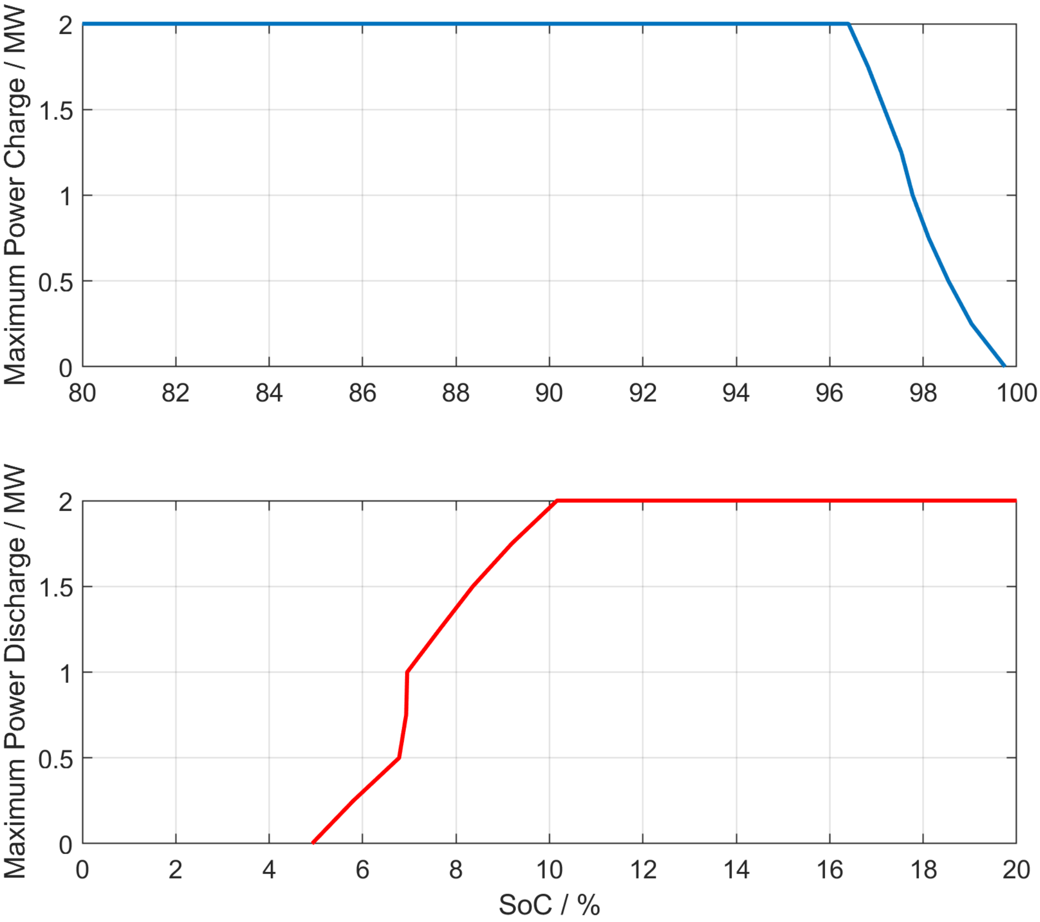

Figure 7.9: CPE estimate of SoP where the system has been resting for a long period (7 hrs).

Testing this is challenging, as it is not feasible to test this on the live system due to operating constraints. Instead an example of the power curtailment to limit power to compensate for a high cell voltage imbalance (discussed in chapter 4) is shown in figure 7.10.

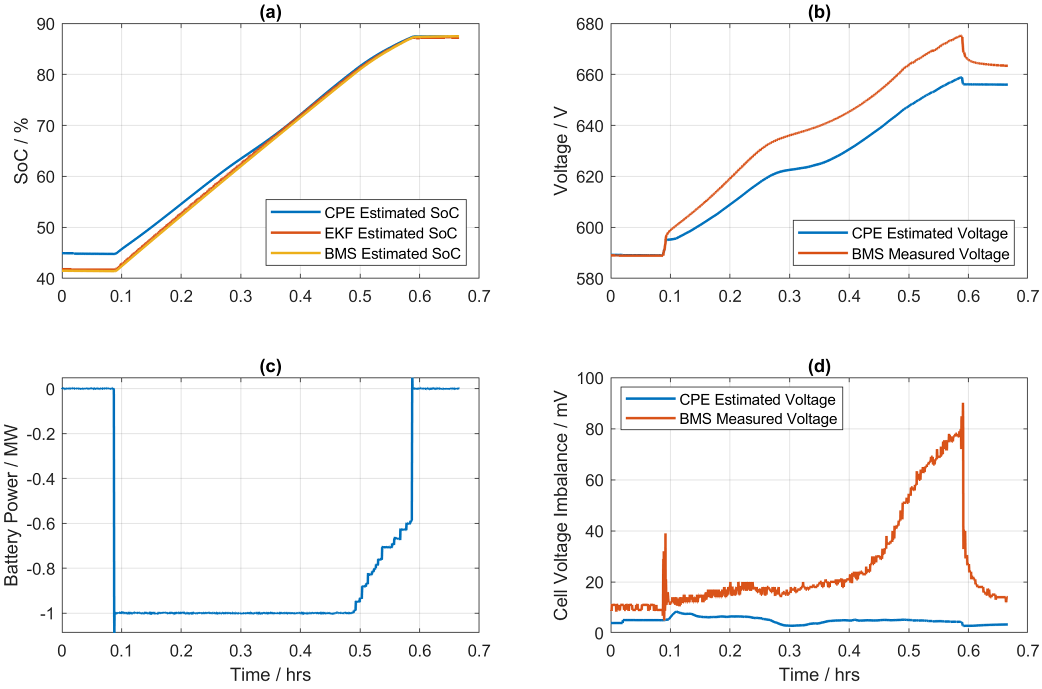

Figure 7.10: Power derating used on WESS, showing the SoC estimate from the CPE.

It can be seen that the power begins to reduce at 81% SoC. This is significantly lower than the CPE SoP estimation. One main reason for this is likely due to the cell balance state. It can be seen in figure 7.10 that the cell voltage imbalance rapidly increases from around 0.4hrs. The estimate of cell voltage imbalance from the CPE does not exhibit this same relationship. It stands to reason that this could be a primary cause of error in the model. With the cell voltage imbalance increasing much sooner in WESS than the CPE, it suggests that the SoC imbalance between cells is greater than the SoC imbalance used in the model. In order to choose parameters for the model, the process in chapter 6 was used, which selects cells for the model based on capacity. This does not consider the differences in SoC between cells, so a cell with a particularly high or low SoC could be the limiting cell, rather than the cell with the lowest capacity, as it is inherently assumed in the model that the pack is well balanced.

During battery operation, the derating curve has been shown to change.

At a higher temperature (after 2 cycles) the derating curve is shown to derate at a higher SoC as shown in figure 7.11.

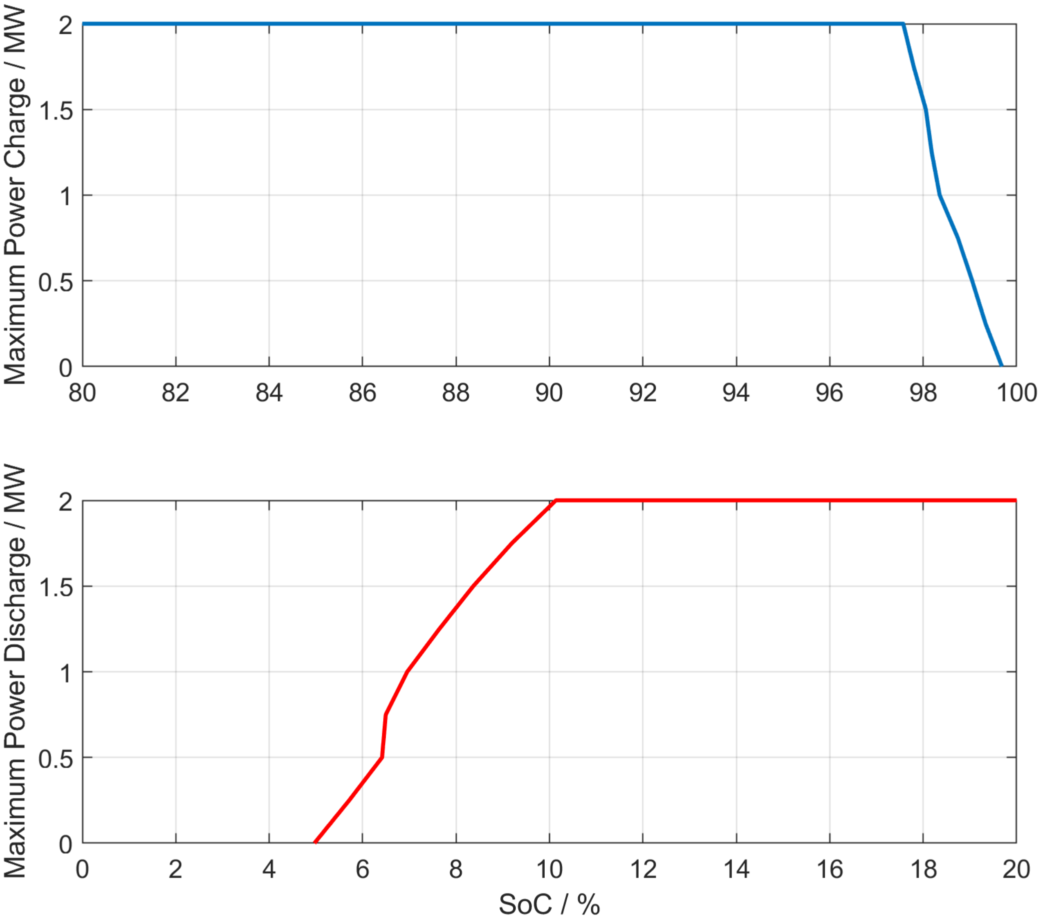

Figure 7.11: CPE estimate of SoP where the system has completed 2 cycles.

It can be seen that the SoP has improved, increasing the operating window for the battery. This is expected, and is due to the reduced impedance of the system at a higher temperature.

7.5.3 Parameter updating

During the month that the CPE was online, the parameters updated a number of times. As there was little to no degradation in this time period, the parameters saw little change. This is a positive result, as it suggests the parameter updating procedures are highly repeatable. It also shows that a suitable sequence for parameter updating can be selected by the CPE. As an example, a charge sequence that was selected is shown in figure 7.12.

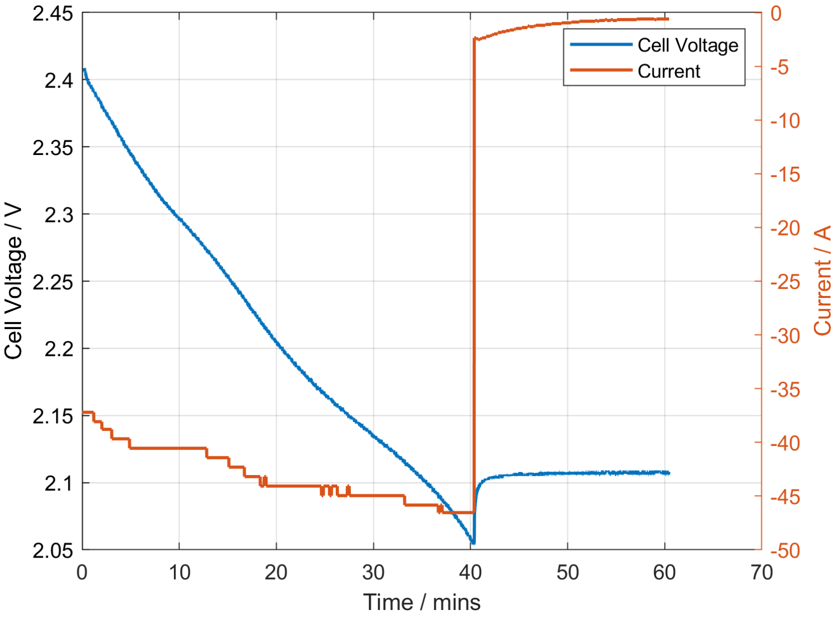

Figure 7.12: Charge sequence selected by the CPE to update parameters.

Table 7.5 shows the previous and new parameters for capacity in the model following the parameter update (and an additional parameter update from a separate discharge capacity sequence).

(a)

Cell Model	Capacity / Ah
A	40.96
B	41.37
C	41.86
D	1579.37
E	1593.56
F	1606.69
G	41.96
H	42.38
I	42.87

(b)

Cell Model	Capacity / Ah
A	40.91
B	41.42
C	41.72
D	1578.64
E	1592.01
F	1604.73
G	41.85
H	42.51
I	42.94

Table 7.5: Capacity for cell models in the CPE (a) before and (b) after parameter updating (from sequence in figure 7.12).

7.6 Conclusions

The CPE presented in this chapter is a culmination of the work presented throughout the thesis. It uses the knowledge learned from the investigation in chapter 4, the model from 5 and the parameter identification procedure from chapter 6 to produce and SoC, SoP and SoH estimator, which has been shown to be effective. The SoC estimate was shown to be slightly different to the BMS or EKF estimates for the battery, though voltage estimates for the overall system were better. It was discussed how errors in the system appear to originate from a lack of the model considering variation in SoC, which should be further considered in future work.

As an open-loop estimator, there is potential to run the system as a closed loop estimator using an adaptive algorithm. This would take some significant work, as the time taken to download cell-level data is too slow, so a solution would have to be devised. The CPE presents a solution to producing an estimator which can run in real-time whilst considering the effects of cell level behaviour.

Chapter 8

Optimising energy storage capability of grid connected batteries

8.1 Introduction

In the previous chapters, the behaviour of large Lithium-ion batteries has been widely explored. It is clear that variations in cell parameters such as capacity and impedance, as well as temperature can have an impact on the energy storage capability of a grid connected battery.

Several studies have considered optimising batteries by changing pack topology - that is changing the number of series and parallel connections. This is generally to maximise cell utilisation [115, 121], but also for other parameters such as minimising size and mass [164] - particularly useful for EVs, or mitigation against failure [165] - useful for many applications.

In this chapter, it will be considered how a grid connected battery can be optimised using different balancing control methodology and changing cell location, as means for optimising an existing battery, where the topology is fixed. Each of the areas to be considered will be discussed, with the expected optimisation proposed, then tested using the cell-model in chapter 5. Where possible, these are considered experimentally, using the Yuasa LIM50E ESS and WESS. For the two optimisation methods, the aim of the optimisation is to maximise the useable capacity at a fixed C-rate, which is strongly related to cell-utilisation. In the model, all cells will be modelled - this is much slower than the model proposed in chapter 5, as per table 5.8, but gives the greatest confidence, where fast simulation time is less of an issue for an application that is not real-time.

8.2 Cell Charge Equalisation

Chapter 4 explores how an imbalance in cell voltage reduces the capacity of a battery. This imbalance results from a variation in capacity, impedance or state of charge. Aside from physically changing out cells, the only variable which could be controlled is SoC through a balancing mechanism. These balancing mechanisms are discussed in section 2.2.1.4 and are a means to change the SoC of individual cells in a series string to equalise the SoC.

Considering passive methods which are widely adopted, they all ultimately change the SoC of individual cells which can be performed at different stages of a battery cycle. These stages could refer to either the load (or lack thereof) or the state of charge of the overall battery. It is hypothesised that from a purely OCV perspective, the capacity of a pack will not change based on which SoC the cell is balanced at. Figure 8.1 considers 2 cells, cell A with 100% of the expected capacity, and cell B with 96% of the expected capacity and is plotted assuming that both cells have the expected capacity.

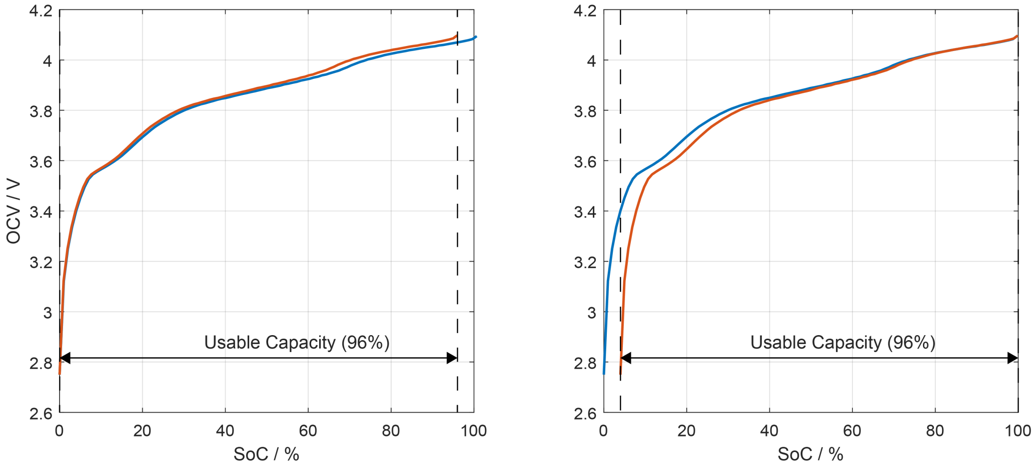

Figure 8.1: The OCV vs SoC relationship for two cells, with a 4% difference in capacity balanced at (a) 0% SoC and (b) 100% SoC.

Figure 8.1 shows that regardless of the balancing point, the usable capacity is the same, as it is limited by the weakest (lowest capacity in this case) cell. This is only the case for a cell at rest (as OCV is used), or if a CCCV charge or discharge is performed as the cells will end at rest.

Under load, or CC cycles, the capacity will however be affected, depending upon the balancing SoC. Figure 8.2 and 8.3 consider the same cell A and cell B but under a load current of 1C (both charge and discharge). This is calculated with the measured impedance to find the voltage drop using equation 8.1 below.

$$V_{load} = V_{OCV} + (I_{bat} * R_{bat}) \tag{8.1}$$

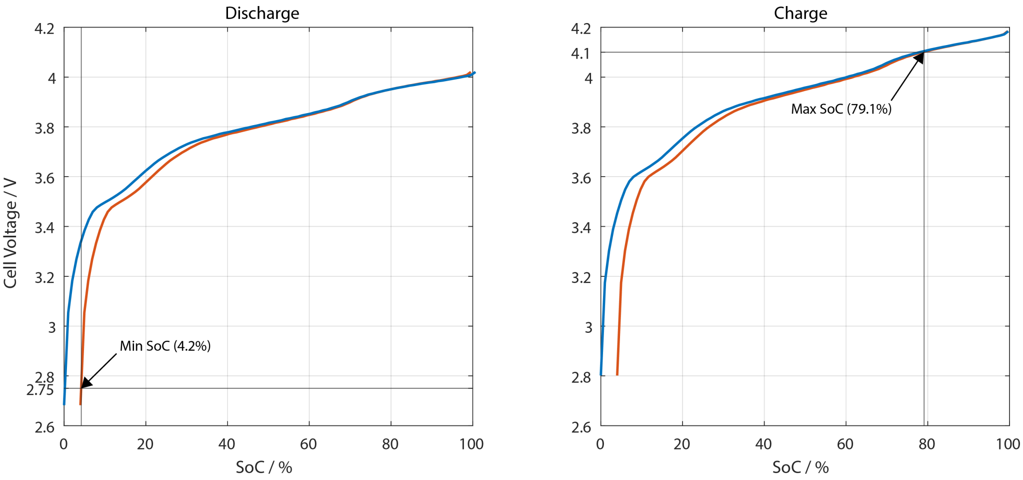

Figure 8.2: The theoretical voltage of 2 cells connected in series with a 4% difference in capacity under a 1C load. The cells are balanced at 100% SoC. The theoretical usable 1C capacity is shown to be 75.7% (relative to the higher capacity cell)

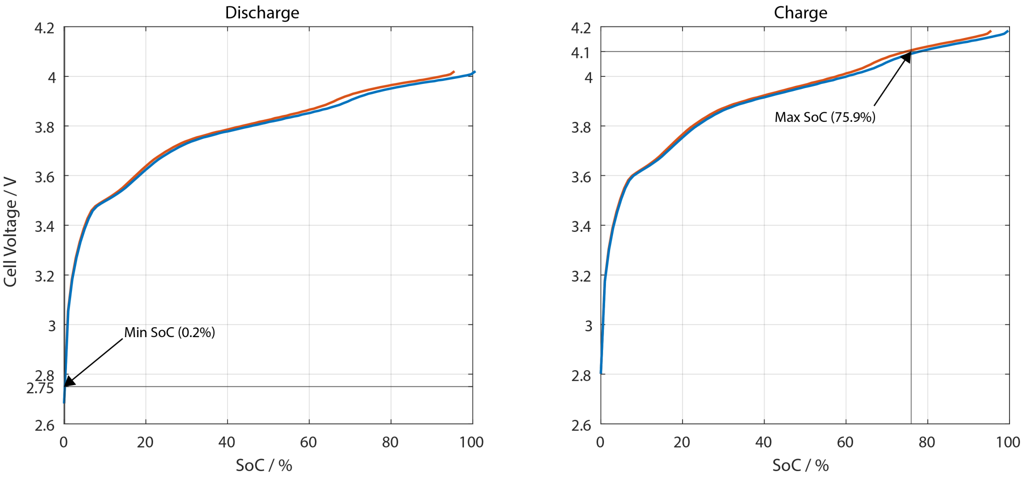

Figure 8.3: The theoretical voltage of 2 cells connected in series with a 4% difference in capacity under a 1C load. The cells are balanced at 0% SoC. The theoretical usable 1C capacity is shown to be 74.9% (relative to the higher capacity cell)

It can be seen from figures 8.2 and 8.3 that with these particular cells, it would be beneficial to balance the cells at 0% SoC rather than 100% SoC as this will give around 0.8% more useable SoC.

The reality is that the difference in SoC between cells is unlikely to be 4%. Therefore, the SoC which is used for balancing is unlikely to make a measurable difference to the CC capacity of a cell, according to the presented figures.

8.2.0.1 Simulation and Experimental

In order to further explore the hypothesis that a pack will have an improved capacity when cell equalisation is performed at different SoCs, a series of simulations and experiments are performed. This will be based around the Yuasa LIM50 ESS, but also considers the implications of other BESS's. With the Yuasa LIM50 ESS, the voltage range of the power supply reaches the full 100% to 0% range of SoC. However, with WESS, the lower voltage limit cannot be reached. This is fairly inconsequential as at a lower SoC, there is a high $\frac{dV}{dSoC}$. However, it may have an impact on cell utilisation when cell equalisation is performed at different SoCs.

Simulations and experiments will follow the same test procedure, where the system is initially balanced using the BMS under constant voltage conditions at different SoC's until the difference in voltage between the highest and lowest cell voltage is <2mV. The system is then charged and discharged at 0.9C (42.75A), ending each charge and discharge sequence when any cell reaches an upper or lower voltage limit (4.1V / 2.75V). Three cycles are performed to ensure temperature has reached a steady state and is consistent between tests. The full test procedure is detailed in table 8.1.

Test phase	**#**	**Sequence**	**Limits**	**End Condition**
Cell Voltage Equalisation	1	CV at fixed SoC	$V = V_{SoC}$, $I_{max} = 0.9C$	V_{max} -V_{min} <2mV
CC Cycles	2	CC Charge	V = System max, I = 0.9C	$V_{max} >= 4.1V$
	3	CC Discharge	V = System min, I = 0.9C	$V_{min} <= 2.75V$
	4	Loop	Loop to #2	3 Loops
Repeat	5	Loop	Loop to #1	All SoC's tested (0% - 100%, 20% steps)

Table 8.1: Test procedure for comparing constant current capacity of a pack when balanced at different SoC's.

Performing this experiment and simulation using the Yuasa LIM50E ESS produced the results shown in figure 8.4.

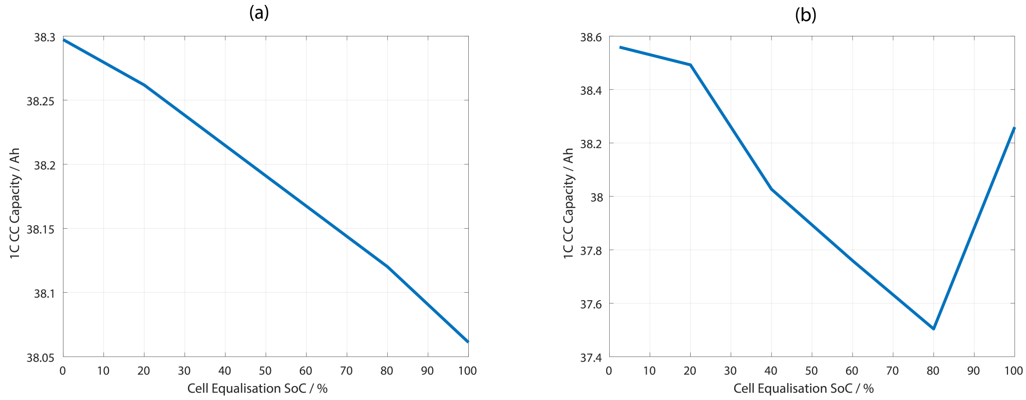

Figure 8.4: (a) Simulated and (b) Experimental 1C constant-current capacity for a Yuasa LIM50E ESS when cell equalisation is performed at different SoC's

The simulation shows that when the system is balanced at a lower SoC, the constant current capacity is higher. The experimental result generally agrees with this, however there is a lack of consistency where there is an increase in constant current capacity when the system is balanced at 100% compared to 80% SoC.

This could be due to inaccuracies in the model, but is more likely due to temperature, where as mentioned in chapter 6, there is no temperature control on the system and poor temperature measurement. As such, despite conditions being controlled as best as possible (windows closed throughout test regime, room HVAC set consistently, test performed at the same time each day), there were some temperature discrepancies. Regardless, for the test procedure in table 8.1, the simulation and experimental results agree that performing cell equalisation at near 0% SoC gives the greatest constant current capacity, likely due to the original hypothesis. An additional reason for the observed increased capacity when cell equalisation is performed at a low SoC is there due to being a greater $\frac{dV}{dSoC}$ at low SoC. This means that for the 1mV precision in voltage measurement, the cells will be at a closer SoC range when balanced to within 2mV at a low SoC compared to a high SoC.

Next, performing a test where the lower cell limits cannot be reached, as with WESS, should show a different result, as the lower voltage limit may not be reached. To consider this, the Yuasa ESS will be tested limiting the system voltage to 537.6V (average 3.2V/cell). This value was chosen as below this, the $\frac{dV}{dSoC}$ becomes much higher, so there is only a small loss in SoC range. The new procedure for this is shown in table 8.2.

Test phase	#	**Sequence**	**Limits**	**End Condition**
Cell Voltage Equalisation	1	CV at fixed SoC	V = V_{SoC}, I_{max} = 0.9C	V_{max} -V_{min} <2mV
CC Cycles	2	CC Charge	V = System max, I = 0.9C	V_{max} >= 4.1V
	3	CC Discharge	V = 537.6, I = 0.9C	V_{min} <= 2.75V or V_{avg} <= 3.2V
	4	Loop	Loop to #2	3 Loops
Repeat	5	Loop	Loop to #1	All SoC's tested (0% - 100%, 20% steps)

Table 8.2: Test procedure for comparing constant current capacity of a pack when balanced at different SoC's, limiting the system voltage to 537.6 (3.2V/cell average)

This procedure was again performed as a simulation and experimentally, with results shown in figure 8.5

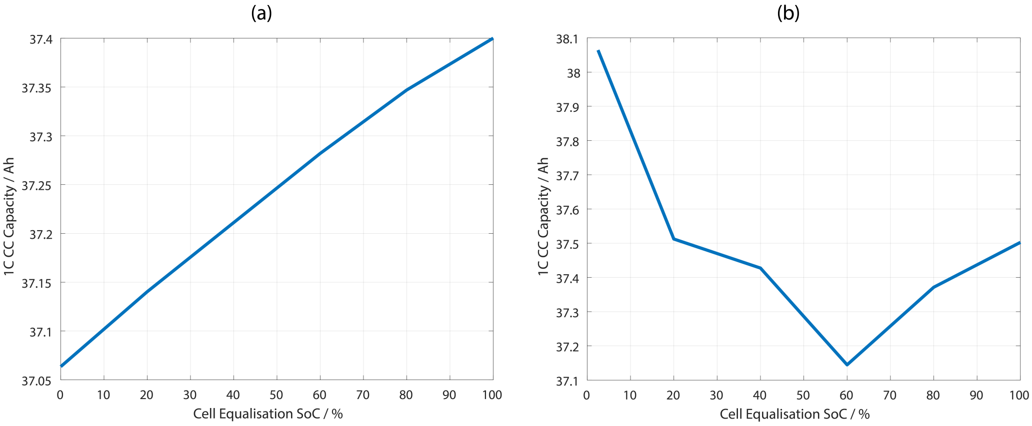

Figure 8.5: (a)Simulated and (b) Experimental 1C constant-current capacity for a Yuasa LIM50E ESS when cell equalisation is performed at different SoC's, where the ESS is limited to a minimum of 537.6V (3.2V/cell average)

It can be seen from the figure 8.5 (a) that with the new procedure, the opposite trend is true, with around 1% difference in capacity. This is due to the fact that the lower voltage limits are never reached by any cell, so the cell voltage imbalance is irrelevant when ending a discharge cycle. However, the top cell voltage limits are reached, so it is preferable to perform cell equalisation at 100% SoC in order to maximise cell utilisation.

Considering the experimental result in figure 8.5 (b), the trend does not quite agree. it is expected that at a lower SoC, where the $\frac{dV}{dSoC}$ is higher (see figure 5.29 for OCV curve), the pack is better balanced due to the voltage resolution, as in the previous example. For example, in the test procedure, cell voltage equalisation was performed until there was 2mV difference between cell voltages. At 2.5% SoC, a difference of 2mV between cells, would mean an SoC imbalance of 0.02%. At 60%, where the $\frac{dV}{dSoC}$ is lower - i.e. the OCV-SoC curve is flatter, a 2mV difference in cell voltage would mean a difference of 0.5% SoC. With <1% expected difference in capacity, it is likely that the $\frac{dV}{dSoC}$ is the driving factor affecting the ESS capacity when considering cell voltage imbalance.

8.2.0.2 Considering Variance

The results shown for the two experiments and simulations are useful, however results may be better or worse (i.e. more improvement in capacity is possible) should the cells have a greater variance between them. It will be considered through simulation how changing the capacity variance affects the result.

To do this, initially the capacity and impedance distributions are found (results for which are presented in chapter 6). Then the "randraw" function in MATLAB is used to produce datasets which match the impedance distribution, but has a changing capacity variance in each dataset. The mean capacity remains constant. To give a useful range, the variances used are: 0, 0.25, 0.5, 0.75, 1, 2, 3 - as a percentage of the mean. The simulations were performed according to the procedure shown in tables 8.1 and 8.2. Results for these are presented in figures 8.6 and 8.7.

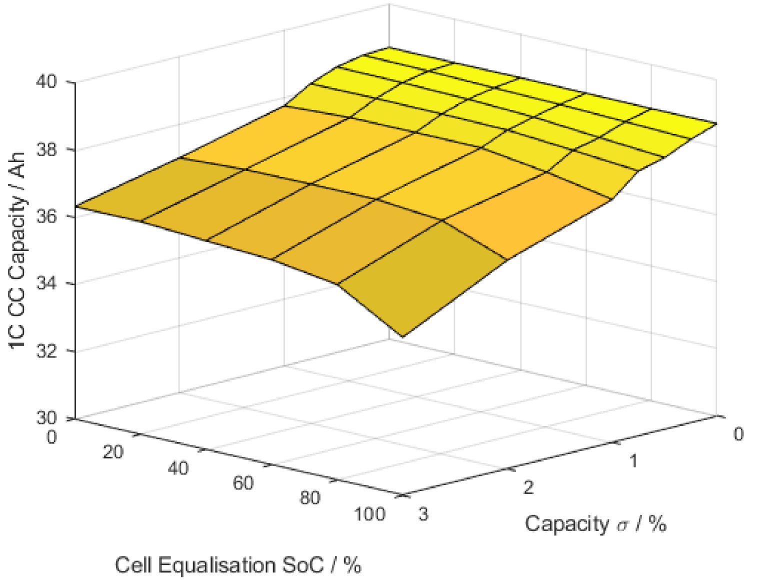

Figure 8.6: Simulated 1C constant-current capacity for a Yuasa LIM50E ESS when cell equalisation is performed at different SoC's and with a different capacity variance (σ)

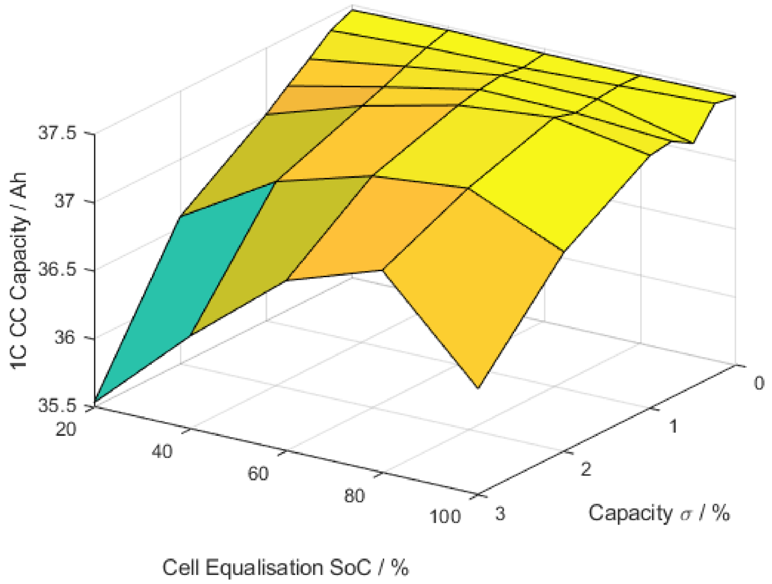

Figure 8.7: Simulated 1C constant-current capacity for a Yuasa LIM50E ESS when cell equalisation is performed at different SoC's and with a different capacity variance (σ), where the ESS is limited to a minimum of 537.6V (3.2V/cell average)

It can be seen that for a system that can reach the full cell voltage range, it is beneficial to perform cell equalisation at a lower state-of-charge, with larger improvements expected where there is a greater capacity variance. When a system cannot reach the lower cell voltage range, there is an improvement to be gained from performing cell equalisation at a high SoC. Again, this is more pronounced where there is a greater variance.

In summary, regardless of the system (except for a system with no variations between cells), there is an improvement to be gained from the correct selection of SoC to perform cell equalisation at. With the Yuasa LIM50 ESS, it was found experimentally that when the full voltage range is useable, there is 3% difference in capacity depending upon the balancing SoC. When the bottom limit cannot be reached, the difference is smaller at 0.7%.

Many variables will vary the amount of percentage gain (between the worst SoC to perform cell equalisation and the best) that is able to be achieved. It is expected that there will be a difference depending upon C-rate, likely more potential gain at a higher C-rate. Additionally, alternate chemistries may exhibit a different behaviour, due to different impedance / SoC relationships during charge and discharge. The difference occurs under load, so a different impedance will give a different voltage drop, and therefore a different set of results.

8.3 Cell position

As well as optimising cells already in place by changing the balancing mechanism, a battery can be optimised in how it is arranged. It is noted in [121] that there are (m x n)! ways of arranging cells in a pack (where m is the number of series connections and n is the number of parallel connections). As a factorial relationship, this is a vast number of ways which cells can be arranged. As an example for WESS with 264 series and 40 parallel connections, there are approximately $1.4 * 10^{37906}$ combinations. Additionally, the number of series and parallel connections can be adjusted, further increasing the number of configurations of cells, though this is beyond the scope of this work. This section will consider whether there is a change in available energy depending upon the physical location of each cell in the circuit

According to the assumptions made throughout literature and throughout this thesis in the models used, current is constant between cells in a series string. This means that for a pack consisting of just one series string, or parallel groups of cells connected in series, the position of cells or cell groups in the circuit will not make a difference to the system capacity, as the cells experience the same charge throughput regardless of position, purely considering the electrical behaviour.

Conversely, for systems with series strings connected in parallel, arranging the cells in different strings should give differing capacities. This is because the voltages of each string will be equal, due to the fact that they are connected in parallel and as such, a string with a lower capacity should have a lower current throughput, for voltage balance to be maintained.

This is demonstrated in figure 8.8, where two cells are simulated being connected in parallel. To exaggerate the point, the cells have very different capacities (30Ah and 50Ah) and are modelled as Yuasa LIM50 cells with changed capacities. An 80A (1C average) cycle shows the voltage and current profiles, where it is clear that there is a lower current throughput for the lower capacity cell. This agrees with results from a similar experimental test presented in [72], with a simulation and experiment of a new and aged cell connected in parallel showing the same trend.

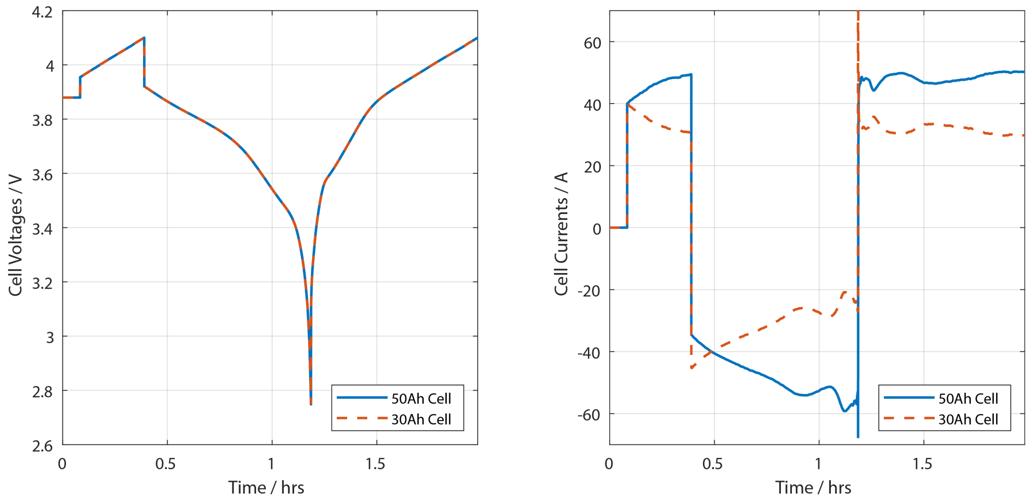

Figure 8.8: Simulation of two cells with differing capacities, demonstrating the lower current throughput of a lower capacity cell when connected in parallel.

Given that the terminal voltage of each string balances due to the nature of being connected in parallel and demonstrated in figure 8.8, an optimisation involves having cells in each string as well matched as possible. Matching would involve grouping the most similar cells together. It has been shown in literature in chapter 2 and experimentally in chapter 5, that the differences between impedance and capacity are not related. Therefore, the most similar cells can be most similar in terms of capacity, impedance, or a separate measure for ranking the cell could be calculated based on both the impedance and capacity to determine the most similar cells. One example of this would be the 1C, CC capacity of the cell, which is dependant on both capacity and impedance.

In order to determine how a system can be optimised by matching strings, simulations will be performed using the experimental cell data from WESS for the six strings discussed in chapter 6, and arranging the cells in the six strings measured to maximise the overall available energy for these six strings. As the cells are fixed in modules of 12 cells, the cells can only be arranged as part of their module. Therefore, each module is ranked. Figure 8.9 shows the rank of each module, where in this example the rank is calculated as the average capacity of the cells in the module. They are shown in the physical position in each string.

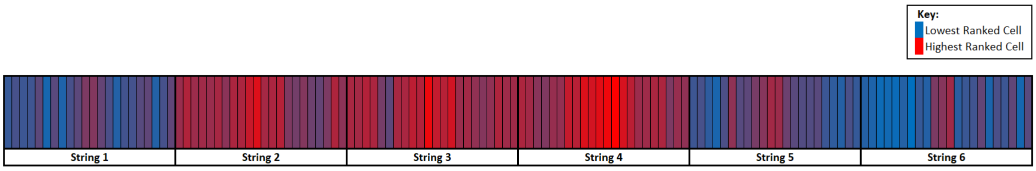

Figure 8.9: Diagram depicting the rank of each module in WESS, divided into strings. The rank shown is the average capacity of the cells in each module, in the measured positions

Once the cells are ranked, it is proposed that the cells are arranged into strings according to their rank. With the cell positions chosen, the system is simulated, with every cell being modelled, as per the cell model in chapter 6, shown in figure 6.1. Due to current operational and safety constraints, this cannot be performed experimentally, however, the simulation should provide a strong indication of the expected experimental results. Several parameters will be compared for ranking the modules which will be simulated. These are:

- Capacity
- R_{DCIR} at 50% SoC Charge
- R_{DCIR} at 50% SoC Discharge
- 1C CC Capacity

The 1C CC capacity will be estimated through a simulation of each cell, using the experimentally found parameters. As mentioned, this aims to be a parameter which is dependant on both capacity and impedance. For each parameter, 3 different ranking methods can be found:

1. Every Cell is ranked
2. Modules are ranked by worst ranked cell in module
3. Modules are ranked by average of cells in module

Using the ranking parameters and methods, two cell arrangement methods are proposed - matching similarly ranked cells together, and arranging by temperature. For each of the two arrangements, a number of simulations are performed, using each ranking parameter with each ranking method. For arranging modules by temperature, additional arrangements are used considering different measurements of temperature.

8.3.1 Matching strings

The first proposed method for arranging modules or cells involves arranging the pack with the most similarly ranked modules or cells in the same string. Using the ranking in figure 8.9 as an example, modules can be sorted by rank from lowest to highest and then divided into strings. This is depicted in figure 8.10.

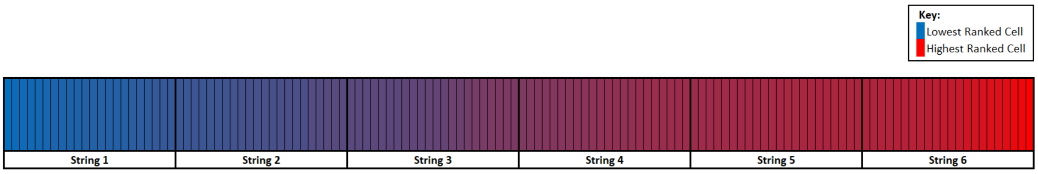

Figure 8.10: Diagram depicting the rank of each module in WESS, divided into strings, sorted by rank to best match the cells in each string. The rank shown is the average capacity of the cells in each module.

Applying the different ranking methods with the different ranking parameters and running simulations of 1C, constant-current cycles, produces the results comparing the achieved 1C capacity using different arrangements. Additionally, simulations were performed where the cells were randomly arranged and modules were randomly arranged. These results are shown in figure 8.11, where results are shown as a comparison to a simulation performed with the modules in their existing positions.

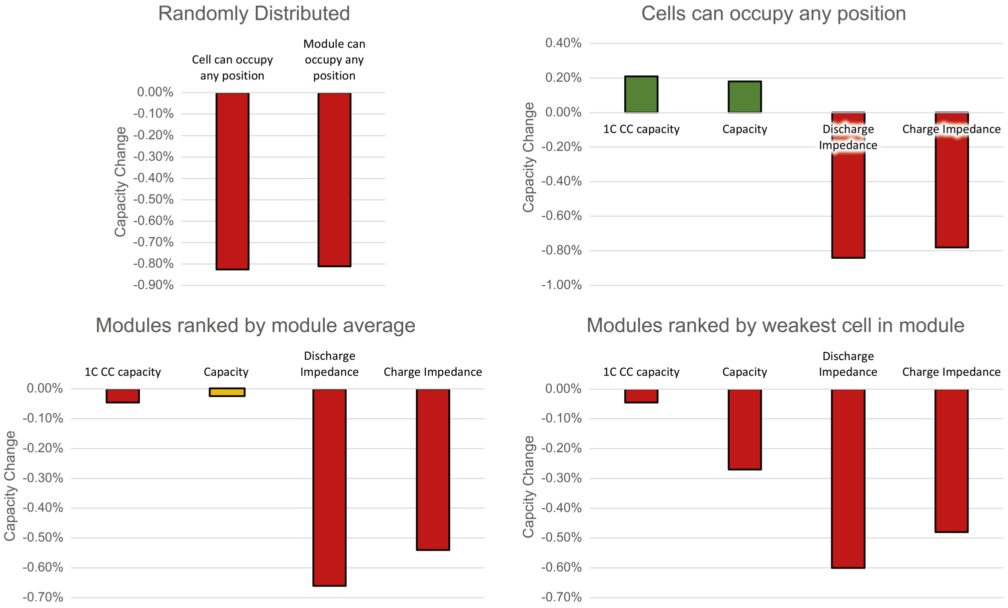

Figure 8.11: Results of simulations comparing different ranking methods and ranking parameters when sorting cells into strings matched by their rank.

It can be seen from using this arrangement method that applying the ranking parameter of capacity and 1C CC capacity, and allowing any cell to take any position, an improvement of around 1% can be achieved, compared to randomly distributing the cells. Compared to the existing arrangement, this is only 0.2%.

Unfortunately, locating cells in any position is not practically achievable, as cells are welded in place in the modules. Instead, only the same 1C CC capacity can be achieved comparing to the existing arrangement when only arranging modules. This is achieved through taking the average capacity of the cells in each module to rank the modules, and sorting as per figure 8.10.

It is noted that during commissioning of the battery system, the modules were arranged over a series of tests spanning several weeks, where the commissioning team tested modules individually before arranging the modules into the system. It is expected that the method finally used for arranging the modules is by sorting modules with similar capacity into the same string, as performed in the best simulation. This is apparent from figure 8.9.

8.3.2 Considering Temperature

It is clear that there is little to be gained over what manufacturers are already doing in terms of arranging cells using the string matching method, yet temperature is not considered. In WESS, strings are arranged vertically inside a cabin with an HVAC system. Despite the HVAC system, certain cells and modules tend to be warmer throughout a cycle. This could either be due to the fact that the warmer air in the cabin rises, so the modules physically located vertically higher are warmer. Or, there is worse airflow at the top, increasing the temperature. The distribution of temperature in the six strings measured is shown in figure 8.12, where the temperature given is the average temperature in each module across a 1C, CC cycle.

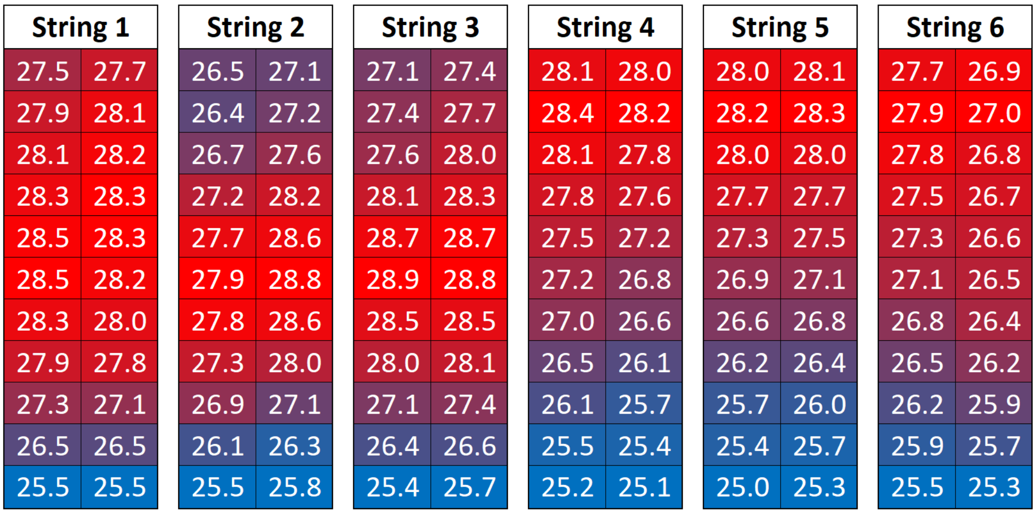

String 1		String 2		String 3		String 4		String 5		String 6	
27.5	27.7	26.5	27.1	27.1	27.4	28.1	28.0	28.0	28.1	27.7	26.9
27.9	28.1	26.4	27.2	27.4	27.7	28.4	28.2	28.2	28.3	27.9	27.0
28.1	28.2	26.7	27.6	27.6	28.0	28.1	27.8	28.0	28.0	27.8	26.8
28.3	28.3	27.2	28.2	28.1	28.3	27.8	27.6	27.7	27.7	27.5	26.7
28.5	28.3	27.7	28.6	28.7	28.7	27.5	27.2	27.3	27.5	27.3	26.6
28.5	28.2	27.9	28.8	28.9	28.8	27.2	26.8	26.9	27.1	27.1	26.5
28.3	28.0	27.8	28.6	28.5	28.5	27.0	26.6	26.6	26.8	26.8	26.4
27.9	27.8	27.3	28.0	28.0	28.1	26.5	26.1	26.2	26.4	26.5	26.2
27.3	27.1	26.9	27.1	27.1	27.4	26.1	25.7	25.7	26.0	26.2	25.9
26.5	26.5	26.1	26.3	26.4	26.6	25.5	25.4	25.4	25.7	25.9	25.7
25.5	25.5	25.5	25.8	25.4	25.7	25.2	25.1	25.0	25.3	25.5	25.3

Figure 8.12: Difference in temperature of modules in the six strings measured during a 1C CC cycle. The warmest module is 28.9°C and the coolest module is 25.0 °C. Note that the diagram depicts the physical vertical layout of each string.

The work performed in chapter 6 showed that the capacity for a cell increased and impedance for a cell decreased (for the WESS cells) as cell temperature increased. Therefore, it is proposed that performance can be improved by locating the worst ranked cells in the warmest physical positions. It is hoped that this will improve the overall cell utilisation and therefore the capacity of the pack.

To do this, as well as each cell being ranked, each cell or module position is ranked. Each module position is either ranked by the maximum or average temperature of that module, where the temperature used is the average temperature during a 1C CC Cycle. The lowest ranked cell or module is then located in the highest rank cell or module position and so on. For each of the temperature rankings, the same tests are performed as those done previously in section 8.3.1.

Results for arranging any cell into any position based on the cell temperature are shown in figure 8.13, results for arranging modules into positions based on average module temperature is shown in figure 8.14 and results for arranging modules into positions based on maximum module temperature is shown in figure 8.15.

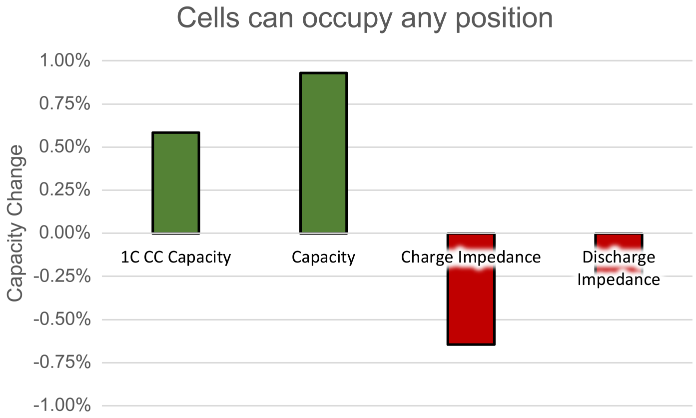

Figure 8.13: Results of simulations comparing different ranking methods when sorting weakest ranked cells into the warmest cell positions.

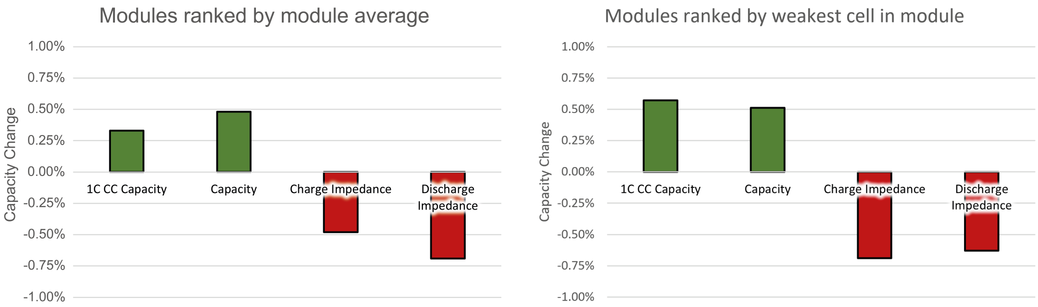

Figure 8.14: Results of simulations comparing different ranking methods when sorting modules into different positions based on the average temperature of cells in each module position.

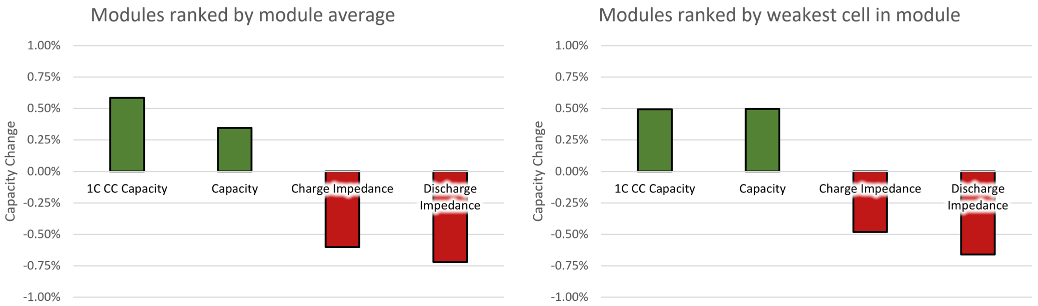

Figure 8.15: Results of simulations comparing different ranking methods when sorting modules into different positions based on the maximum temperature of a cell in each module position.

These results show an improvement over sorting similar modules into strings and an improvement over the existing arrangement of the modules - up to 0.6% when rearranging modules. The best method here appears to be ranking by the average 1C CC capacity of the cells within a module and module positions ranked by maximum temperature.

8.3.2.1 Sensitivity Analysis

The cells within WESS are all relatively similar, with a variance in capacity of 0.6% of the mean, and a variance in impedance of 4.3% of the mean. This is a value which is unique to this system, and so to consider different systems, datasets with different variances will be considered. Considering an impedance variance of 0-50% and a capacity variance of 0-5%, 81 datasets were produced. As the best ranking, the 1C CC capacity is used, where each position is ranked by the maximum temperature in each module.

Two simulations for each dataset were performed - random positions for each module and the optimised positions based on the temperature. This was repeated five times and the average was taken. The results in figure 8.16 shows the improvement between the random module location and the optimised location based on the temperature. Figure 8.17 shows a linear fit of the data, giving an impression of the general trend.

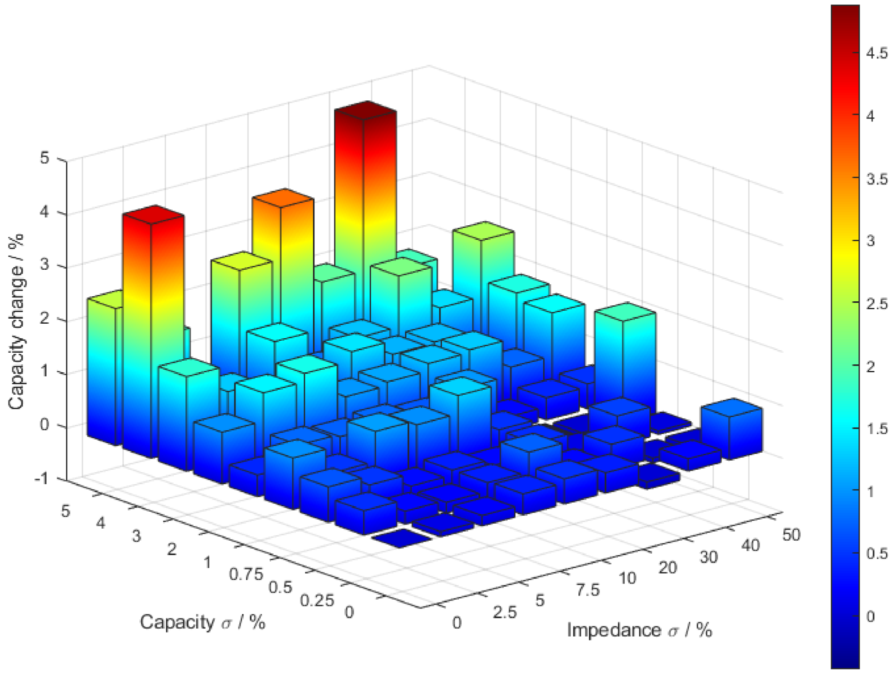

Figure 8.16: Results of simulations showing the capacity change between distributing modules randomly and ranking modules by 1C CC capacity and locating the highest ranked module in the warmest position.

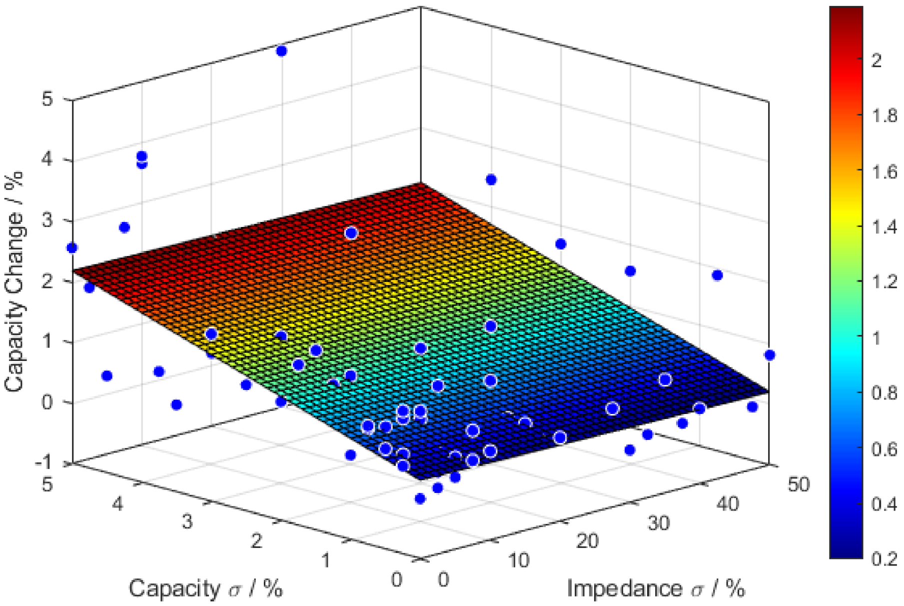

Figure 8.17: Linear fit of the results of simulations, showing the capacity change between distributing modules randomly and ranking modules by 1C CC capacity and locating the highest ranked module in the warmest position.

It can be seen from the figures that most improvements can be gained as the capacity variance increases. On the other hand, it is clear from the linear fit that little improvement is possible with an increased impedance variance. This is likely due to the impedance being very small compared to the capacity of these cells, and so the 1C CC Capacity is much more dependant on the overall capacity compared with the impedance.

Overall, this simulation work shows improvements of up to 5% with this cell type by optimising the cell arrangement when there is a large capacity variance. While there is currently a small capacity variance, it is likely that this will increase with degradation as discussed in chapter 2, so may become more relevant as the system ages. Practically, for WESS, according to the six strings measured, an improvement of around 0.5% could potentially be achieved through the best proposed method over the current arrangement. Naturally, the optimisation method involving temperature relies on there being a consistent variation in temperature that is dependant on the physical position. If this were not the case then this optimisation would not work. Concerning WESS, the assumption has been made that the temperature variation is consistent and dependant on the physical position of the module as opposed to factors intrinsic to the module. Further work is required to verify this, and ensure that the same trend is observed under different cycle types.

8.4 Discussion

The two optimisations discussed in this chapter show means for improving the performance of a battery system. It has been shown in both optimisations that greater capacity variance lends itself to a potential for greater improvement. Work in [15] suggests that as cells degrade, the variance increases - likely due to cells degrading at different rates. This will in turn lead to a greater variance. Therefore the optimisations are more relevant for second life systems. Additionally, due to uneven degradation, optimisation of cell arrangement should be performed at various points throughout a system's life, as the optimisation may not hold after some degradation.

Additionally, the optimisations proposed do not consider degradation. It is understood that degradation occurs faster at higher temperatures [166, 167]. Therefore, by positioning 'weak' cells in warmer positions, increased degradation may be seen in those cells, potentially reducing the system life. This would need to be considered when implementing the optimisation in a system.

Some of the proposed methods may be unsuitable when considering practical operation. For example, performing balancing at a low SoC can be risky. This is because there is little remaining capacity to provide a buffer for system self-discharge. Further, many applications require a battery to spend most of the time away from 0% SoC. In these cases, an algorithm for cell balancing would have to consider these limitations when implementing balancing control.

8.5 Conclusion

In conclusion, some improvements can be achieved by using the optimisations presented in this chapter. It has been shown that the amount of improvement possible is highly system dependant. For the Yuasa ESS, around 3% improvement can be achieved by choosing the correct SoC to balance at compared to the worst. Limiting the lower voltage of the overall pack, a smaller improvement is expected of around 1%. The results shown weren't perfect however, likely due to the limitation in the voltage resolution, meaning the cells were better equalised where there was a high $\frac{dV}{dSoC}$ at lower SoCs.

It was considered how the position of cells and modules can influence the overall power capabilities of a battery, using WESS as a case study. Rearranging modules by grouping similar modules together by capacity resulted in a 0.8% improvement over arranging modules randomly, but the same capacity as with the existing module positions. This is due to the commissioning process arranging modules in this way. However, putting the "weakest" modules in the warmest positions would result in a notable instantaneous improvement - a 1.4% improvement over randomly arranging modules and 0.6% improvement over the commissioned arrangement.

Chapter 9

Conclusions & Further Work

9.1 Chapter 4: Investigation into Cell Voltage Imbalance in Grid-Connected Batteries

This chapter presents system level data from an operational 2MW, 1MWh grid-connected battery. This includes a reading for cell voltage imbalance. Results for two different cycle types of shown - high DoD cycling and large power changes, where there is a large increase in cell voltage imbalance.

These observations were reported using two modules from WESS in series, giving cell level data for a 24s pack. A similar trend was observed, and cell voltage imbalance during high DoD cycling was accounted for. The same observations were not seen in the lab tests as with the large system during large power changes. This is as there is an error in sampling the cell voltages in the system, causing an erroneous increase in the cell voltage imbalance.

This was repeated with modules of a different chemistry, where similar cell voltage imbalance trends were observed. For both chemistries, it was noteworthy that the same cell reached both maximum and minimum cell voltages. This meant that the pack capacity was limited by that cell.

This work shows that relying on the nominal capacity of the battery and current SoC is not enough, as early termination of a cycle due to cell voltage limits being reached also limits the available energy. This could be estimated through empirical modelling based on the system power and energy. Alternatively, a more mechanistic model which considers individual cell behaviour could be used, which is the method used in subsequent chapters.

Further work into this could involve repeating the experiment with modules connected in parallel, in order to determine whether a single cell still limits the pack in this case. Additionally, analysis of cell level data from a large system such as WESS could give further insight.

9.2 Chapter 5: An fast variance based Grid Scale Battery Model

This chapter builds on chapter 4 by using the principle of a single cell limiting the capacity of a pack. It proposes a novel model for a large battery which models any size battery with 9 cell-models.

The model was verified using a 3s3p pack, where each cell-model represented one cell. This proved the model to be a good representation of the pack. From this, it was discussed how the model should be populated from a sample of cells. It was shown that the capacity and impedance for a sample of cells both fit a distribution, and this can be used to produce a new sample. This is particularly useful if only a small number of cells from a pack are available for test. A process was devised to divide the cells into the nine cell- models, to represent the pack.

This was then tested and experimentally verified under controlled conditions using a 12s4p pack. It was shown that the 9 cell-model performed equally to modelling all cells yet performed a simulation approximately 20 times quicker. The results using cell parameters generated from a distribution produced comparable results returning a slightly lower capacity (0.5-1%) than the experimental pack

The cell model used here is a simple Rint model and therefore lacks the accuracy of ECMs with several RC branches. Future work will involve reproducing the model with a better cell model to observe whether this improves the performance.

9.3 Chapter 6: In-situ Parameter Identification of Cells in Grid Connected batteries.

Chapter 6 shows the methods used to experimentally identify parameters for cells used in literature. These are used to propose a procedure for identifying parameters for all cells in a large battery whilst the cells remain in the pack.

This is initially tested with a 168s pack, comparing the results with a 12s module removed from the pack, and a single cell removed from that module. The 168s pack and 12s module were tested using the same power supply and had similar results. The cell showed a better performance likely due to the different testing hardware being more accurate.

The procedure was then tested using 6 strings from WESS, which showed expected results when compensating for temperature. The test cell was a new sample cell provided by the manufacturer and showed a higher capacity due to WESS being slightly degraded over its lifetime.

These results showed the viability of the method and demonstrated that the parameters found are ideal for battery modelling. This was shown with the 168s pack, where inaccuracies of the test system skewed results. This skew of results is then “baked in” to the model parameters, and as such the model will better track the observed behaviour.

Building upon this in the future would include identifying parameters for ECMs with multiple RC elements. Further, an adaptive method (i.e. Kalman filter) could be explored to give cell parameters without specific test cycles.

9.4 Chapter 7: Online parameter estimation for grid connected batteries

The penultimate chapter ties together chapters 4 through to 6 by taking the knowledge learned to create a new open-loop estimator. This was used to demonstrate the feasibility of using cell-level data to inform a model for real-time state estimation of large batteries.

A simple thermal model was added to the system which improved the ability of the model to determine whether a particular cycle is feasible. A more complex model could be used to further improve this, although it would likely require increased sensing on the system. A method for detecting cycles to automatically perform the in-situ parameter identification from chapter 6 was demonstrated.

The estimates shown by the CPE were somewhat different to what is estimated by the BMS, both for SoC and SoP. These are expected, as the way in which SoC and SoP is calculated is different. Ultimately, so long as the SoP is correct for the estimated SoC, this is sufficient, as it indicates the operating window for the battery relative to the CPE SoC.

This has scope for development - future work involves implementing improved models (with multiple RC elements) and using an adaptive estimator to update parameters in real time. It is unknown if this is practically feasible, due to the data requirements of cell level data, however a solution to this is worth exploring.

The work highlights some need for investigation into the power curtailment of WESS, where the cell voltage imbalance is much higher than the CPE estimate. This suggests that the system is fairly unbalanced, but also that this imbalance is not reflected by the model. Future work should reconsider how the cell model is populated, or consider an adaption of the model to better represent a large battery.

9.5 Chapter 8: Optimising energy storage capability of grid connected batteries

This chapter considering optimising large batteries explored two methods for optimising large batteries without changing the topology of the system (changing the numbers of series and parallel connections).

Firstly, using the Yuasa ESS as an example, a 3% difference in CC capacity could be expected between the best and worst options, depending upon the system operating parameters. It was found that practically, a large difference was observed from performing cell equalisation at a low SoC, due to the high $\frac{dV}{dSoC}$ at that point. This essentially gave the best SoC resolution in terms of bringing all cells to the same SoC.

Secondly, using WESS as an example, it was shown that a good choice of module position based on grouping modules of a similar capacity could give and improvement of 0.8% compared to randomly distributed modules. However, using this method, no improvements were possible over the existing configuration thanks to the manufacturer commissioning process. Instead, by arranging lower capacity modules into the warmer areas of the battery, an improvement of up to 0.6 % could be achieved compared to the existing configuration according to simulation and is shown for the first time. This is an improvement of 1.4% compared to randomly positioning modules. Additionally, using the in-situ parameter identification technique with this optimisation can mean a faster commissioning process for a new system, avoiding the need to test cells and modules individually.

Moving forward with this work, next steps will involve performing experiments with WESS through rearranging modules. This will involve determining safe procedures to safely attempt to swap module positions to verify this simulated work. Furthermore, more simulation work could be performed to consider the degradation of the system when performing the proposed optimisation.

References

[1] S&P Global Market Intelligence, "Top electric vehicle markets dominate lithium-ion battery capacity growth," 2021. [Online]. Available: https://www.spglobal.com/marketintelligence/en/news-insights/blog/top-electric-vehicle-markets-dominate-lithium-ion-battery-capacity-growth

[2] U. Gulzar, S. Goriparti, E. Miele, T. Li, G. Maidecchi, A. Toma, F. De Angelis, C. Capiglia, and R. P. Zaccaria, "Next-generation textiles: From embedded supercapacitors to lithium ion batteries," *Journal of Materials Chemistry A*, vol. 4, no. 43, pp. 16 771–16 800, 2016.

[3] C. Liu, Z. G. Neale, and G. Cao, "Understanding electrochemical potentials of cathode materials in rechargeable batteries," *Materials Today*, vol. 19, no. 2, pp. 109–123, 2016.

[4] W. Li, J. R. Dahn, and D. S. Wainwright, "Rechargeable Lithium Batteries with Aqueous Electrolytes," *Science*, vol. 264, no. 5162, pp. 1115–1118, 1994. [Online]. Available: http://science.sciencemag.org/content/264/5162/1115

[5] K. Ozawa, "Lithium-ion rechargeable batteries with LiCoO2 and carbon electrodes: the LiCoO2/C system," *Solid State Ionics*, vol. 69, no. 3, pp. 212–221, 1994.

[6] V. H. Vu, A. Kaplan, and W. T. McHugh, "Prismatic Cell Construction," 1998. [Online]. Available: https://patents.google.com/patent/US5958088A/en

[7] A. Kwade, W. Haselrieder, R. Leithoff, A. Modlinger, F. Dietrich, and K. Droeder, "Current status and challenges for automotive battery production technologies," *Nature Energy*, vol. 3, pp. 290–300, 2018.

[8] S. Nejad, D. T. Gladwin, and D. A. Stone, "A systematic review of lumped-parameter equivalent circuit models for real-time estimation of lithium-ion battery states," *Journal of Power Sources*, vol. 316, pp. 183–196, 2016.

[9] S. Piller, M. Perrin, and A. Jossen, "Methods for state-of-charge determination and their applications," *Journal of Power Sources*, vol. 96, no. 1, pp. 113–120, 2001.

[10] H. Rathmann, C. Weber, W. Benecke, J. Eichholz, and D. Kaehler, "Novel methode of state-of-charge estimation using in-situ impedance measurement: Single cells in-situ impedance measurement based state-of-charge estimation for LiFePO4 – Li2TO3 Battery Cells with a real BMS," in *IECON 2014 - 40th Annual Conference of the IEEE Industrial Electronics Society*, 2014, pp. 2192–2198.

[11] C. Zhang, J. Jiang, L. Zhang, S. Liu, L. Wang, and P. C. Loh, "A generalized SOC-OCV model for lithium-ion batteries and the SOC estimation for LNMCO battery," *Energies*, vol. 9, no. 11, p. 900, 2016.

[12] X. Lin, Y. Kim, S. Mohan, J. B. Siegel, and A. G. Stefanopoulou, "Modeling and Estimation for Advanced Battery Management," *Annual Review of Control, Robotics, and Autonomous Systems*, vol. 2, no. 1, pp. 393–426, 2019.

[13] C. R. Birkl, M. R. Roberts, E. McTurk, P. G. Bruce, and D. A. Howey, "Degradation diagnostics for lithium ion cells," *Journal of Power Sources*, vol. 341, pp. 373–386, 2017.

[14] T. Baumhöfer, M. Brühl, S. Rothgang, and D. U. Sauer, "Production caused variation in capacity aging trend and correlation to initial cell performance," *Journal of Power Sources*, vol. 247, pp. 332–338, 2014.

[15] S. F. Schuster, M. J. Brand, C. Campestrini, M. Gleissenberger, and A. Jossen, "Correlation between capacity and impedance of lithium-ion cells during calendar and cycle life," *Journal of Power Sources*, vol. 305, pp. 191–199, 2016.

[16] M. Daowd, N. Omar, P. van den Bossche, and J. van Mierlo, "A review of passive and active battery balancing based on MATLAB/Simulink," *International Review of Electrical Engineering*, vol. 6, no. 7, pp. 2974–2989, 2011.

[17] APX Group, "EPEX Spot Power UK Spot," 2017. [Online]. Available: http://www.apxgroup.com/market-results/apx-power-uk/dashboard/

[18] B. M. Gundogdu, "Control Analysis for Grid Tied Battery Energy Storage System for SOC and SOH Management," Ph.D. dissertation, University of Sheffield, 2019.

[19] R. Hollies, "When is a 41MW battery asset not a 41MW asset?" 2021. [Online]. Available: https://www.linkedin.com/feed/update/urn:li:activity:6773009539760558080/

[20] A. Burke and M. Miller, "Performance characteristics of lithium-ion batteries of various chemistries for plug-in hybrid vehicles," *24th International Battery, Hybrid and Fuel Cell Electric Vehicle Symposium and Exhibition 2009, EVS 24*, vol. 2, pp. 816–828, 2009.

[21] UNFCCC, "The Paris Agreement," 2020. [Online]. Available: https://unfccc.int/process-and-meetings/the-paris-agreement/the-paris-agreement

[22] S. Moores, "The global battery arms race: lithium-ion battery gigafactories and their supply chain," *Forum - The Oxford Institute for Energy Studies*, no. February, pp. 1–5, 2021. [Online]. Available: https://www.oxfordenergy.org/wpcms/wp-content/uploads/2021/02/THE-GLOBAL-BATTERY-ARMS-RACE-LITHIUM-ION-BATTERY-GIGAFACTORIES-AND-THEIR-SUPPLY-CHAIN.pdf

[23] F. . Sullivan, “Renewables and Cost Reductions Drive Battery Energy Storage,” 2021. [Online]. Available: https://www.frost.com/news/press-releases/expansion-of-renewables-and-cost-reductions-drive-battery-energy-storage-to-forefront-of-national-energy-plans/

[24] T. Bruen and J. Marco, “Modelling and experimental evaluation of parallel connected lithium ion cells for an electric vehicle battery system,” *Journal of Power Sources*, vol. 310, pp. 91–101, 2016.

[25] D. Baek, Y. Chen, N. Chang, E. Macii, and M. Poncino, “Battery-aware electric truck delivery route exploration,” *Energies*, vol. 13, no. 8, pp. 1–18, 2020.

[26] T. Feehally, D. Gladwin, R. Todd, A. Forsyth, M. Foster, D. Strickland, and D. Stone, “Battery energy storage systems for the electricity grid: UK research facilities,” *The 8th IET International Conference on Power Electronics, Machines and Drives (PEMD 2016)*, pp. 1–6, 2016.

[27] F. Milano and Á. O. Manjavacas, *Converter-interfaced energy storage systems: Context, modelling and dynamic analysis.* Cambridge University Press, 2019.

[28] Neoen, “Hornsdale Power Reserve — South Australia’s Big Battery.” [Online]. Available: https://hornsdalepowerreserve.com.au/

[29] N. Nitta, F. Wu, J. T. Lee, and G. Yushin, “Li-ion battery materials: present and future,” *Materials Today*, vol. 18, no. 5, pp. 252–264, 2015.

[30] J.-M. Tarascon and M. Armand, “Issues and challenges facing rechargeable lithium batteries,” *Nature*, vol. 414, p. 359, nov 2001.

[31] J. W. Choi and D. Aurbach, “Promise and reality of post-lithium-ion batteries with high energy densities,” *Nature Reviews Materials*, vol. 1, p. 16013, mar 2016.

[32] B. A. Johnson and R. E. White, "Characterization of commercially available lithium-ion batteries," *Journal of Power Sources*, vol. 70, no. 1, pp. 48–54, 1998.

[33] J. Deng, C. Bae, J. Marcicki, A. Masias, and T. Miller, "Safety modelling and testing of lithium-ion batteries in electrified vehicles," *Nature Energy*, vol. 3, no. 4, pp. 261–266, 2018.

[34] K. Sit, P. K. C. Li, C. W. Ip, C. W. Li, L. Wan, Y. F. Lam, P. Y. Lai, J. Fan, and D. Magnuson, "Studies of the energy and power of current commercial prismatic and cylindrical Li-ion cells," *Journal of Power Sources*, vol. 125, no. 1, pp. 124–134, 2004.

[35] S. Jaiser, M. Müller, M. Baunach, W. Bauer, P. Scharfer, and W. Schabel, "Investigation of film solidification and binder migration during drying of Li-Ion battery anodes," *Journal of Power Sources*, vol. 318, pp. 210–219, 2016. [Online]. Available: http://dx.doi.org/10.1016/j.jpowsour.2016.04.018

[36] A. Schilling, J. Schmitt, F. Dietrich, and K. Dröder, "Analyzing Bending Stresses on Lithium-Ion Battery Cathodes induced by the Assembly Process," *Energy Technology*, vol. 4, no. 12, pp. 1502–1508, 2016.

[37] M. Doyle, T. F. Fuller, and J. Newman, "Modeling of Galvanostatic Charge and Discharge of the Lithium/Polymer/Insertion Cell," *Journal of The Electrochemical Society*, vol. 140, no. 6, pp. 1526–1533, 1993.

[38] P. Kemper, S. E. Li, and D. Kum, "Simplification of pseudo two dimensional battery model using dynamic profile of lithium concentration," *Journal of Power Sources*, vol. 286, pp. 510–525, 2015.

[39] Y. Merla, B. Wu, V. Yufit, R. F. Martinez-Botas, and G. J. Offer, "An easy-to-parameterise physics-informed battery model and its application towards lithium-ion battery cell design, diagnosis, and degradation," *Journal of Power Sources*, vol. 384, no. November 2017, pp. 66–79, 2018.

[40] B. Sun, J. Bian, H. Ruan, W. Zhang, P. Ren, and X. Cong, "Modeling Study for Li-ion Batteries Considering High-frequency Inductance Characteristics Based on Electrochemical Impedance Spectroscopy Modeling Study for Li-ion Batteries Considering High-frequency Inductance Characteristics Based on Electrochemical Impedance Spectroscopy," *2018 Joint International Conference on Energy, Ecology and Environment (ICEEE)*, no. April, 2018.

[41] X. Lai, Y. Zheng, and T. Sun, "A comparative study of different equivalent circuit models for estimating state-of-charge of lithium-ion batteries," *Electrochimica Acta*, vol. 259, pp. 566–577, 2018.

[42] J. M. Reniers, G. Mulder, S. Ober-Blöbaum, and D. A. Howey, "Improving optimal control of grid-connected lithium-ion batteries through more accurate battery and degradation modelling," *Journal of Power Sources*, vol. 379, no. September 2017, pp. 91–102, 2018.

[43] D. D. Domenico, A. Stefanopoulou, and G. Fiengo, "Lithium-Ion Battery State of Charge (SOC) and Critical Surface Charge (CSC) Estimation using an Electrochemical Model-driven Extended Kalman Filter," *Journal of Dynamic Systems, Measurement, and Control*, vol. 132, no. 6, p. 061302, 2010. [Online]. Available: https://doi.org/10.1115/1.4002475

[44] M. Dubarry, V. Svoboda, R. Hwu, and B. Y. Liaw, "Capacity loss in rechargeable lithium cells during cycle life testing: The importance of determining state-of-charge," *Journal of Power Sources*, vol. 174, no. 2, pp. 1121–1125, 2007.

[45] G. Han, J. Yan, Z. Guo, D. Greenwood, J. Marco, and Y. Yu, "A review on various optical fibre sensing methods for batteries," *Renewable and Sustainable Energy Reviews*, vol. 150, no. July, p. 111514, 2021.

[46] J.-j. Chang, X.-f. Zeng, and T.-l. Wan, "Real-time measurement of lithium-ion batteries ' state-of-charge based on air-coupled ultrasound," *AIP Advances*, vol. 085116, pp. 1–6, 2019.

[47] K. S. Ng, C.-S. Moo, Y.-P. Chen, and Y.-C. Hsieh, “Enhanced coulomb counting method for estimating state-of-charge and state-of-health of lithium-ion batteries,” *Applied Energy*, vol. 86, no. 9, pp. 1506–1511, 2009.

[48] S. Pang, J. Farrell, J. Du, and M. Barth, “Battery state-of-charge estimation,” in *Proceedings of the 2001 American Control Conference. (Cat. No.01CH37148)*, vol. 2, 2001, pp. 1644–1649 vol.2.

[49] X. Tang, X. Mao, J. Lin, and B. Koch, “Li-ion battery parameter estimation for state of charge,” in *Proceedings of the 2011 American Control Conference*, 2011, pp. 941–946.

[50] X. Lin, A. Stefanopoulou, P. Laskowsky, J. Freudenberg, Y. Li, and R. D. Anderson, “State of charge estimation error due to parameter mismatch in a generalized explicit lithium ion battery model,” *ASME 2011 Dynamic Systems and Control Conference and Bath/ASME Symposium on Fluid Power and Motion Control, DSCC 2011*, vol. 1, pp. 393–400, 2011.

[51] P. P. Mishra, M. Garg, S. Mendoza, J. Liu, C. D. Rahn, and H. K. Fathy, “How Does Model Reduction Affect Lithium-Ion Battery State of Charge Estimation Errors? Theory and Experiments,” *Journal of The Electrochemical Society*, vol. 164, no. 2, pp. A237–A251, 2017.

[52] C. Jiang, A. Taylor, C. Duan, and K. Bai, “Extended Kalman Filter based battery state of charge(SOC) estimation for electric vehicles,” in *2013 IEEE Transportation Electrification Conference and Expo (ITEC)*, 2013, pp. 1–5.

[53] S. J. Moura, N. A. Chaturvedi, and M. Krstí, “Adaptive PDE Observer for Battery SOC/SOH Estimation via an Electrochemical Model,” *Journal of Dynamic Systems, Measurement, and Control*, vol. 136, no. 1, pp. 1–14, 2013.

[54] W.-Y. Chang, “The State of Charge Estimating Methods for Battery: A Review,” *ISRN Applied Mathematics*, pp. 1–7, 2013.

[55] Z. Guo, X. Qiu, G. Hou, B. Y. Liaw, and C. Zhang, “State of health estimation for lithium ion batteries based on charging curves,” *Journal of Power Sources*, vol. 249, pp. 457–462, 2014.

[56] E. Meissner and G. Richter, “Battery Monitoring and Electrical Energy Management precondition for future vehicle electric power systems,” *Journal of Power Sources*, vol. 116, no. 1-2, pp. 79–98, 2003.

[57] P. J. van Bree, A. Veltman, W. H. Hendrix, and P. P. van den Bosch, “Prediction of battery behavior subject to high-rate partial state of charge,” *IEEE Transactions on Vehicular Technology*, vol. 58, no. 2, pp. 588–595, 2009.

[58] G. L. Plett, “High-performance battery-pack power estimation using a dynamic cell model,” *IEEE Transactions on Vehicular Technology*, vol. 53, no. 5, pp. 1586–1593, 2004.

[59] S. Nejad, D. T. Gladwin, and D. A. Stone, “Sensitivity of lumped parameter battery models to constituent parallel-RC element parameterisation error,” *IECON Proceedings (Industrial Electronics Conference)*, pp. 5660–5665, 2014.

[60] L. W. Juang, P. J. Kollmeyer, T. M. Jahns, and R. D. Lorenz, “Implementation of online battery state-of-power and state-of-function estimation in electric vehicle applications,” *2012 IEEE Energy Conversion Congress and Exposition, ECCE 2012*, pp. 1819–1826, 2012.

[61] B. Lunz, Z. Yan, J. B. Gerschler, and D. U. Sauer, “Influence of plug-in hybrid electric vehicle charging strategies on charging and battery degradation costs,” *Energy Policy*, vol. 46, pp. 511–519, 2012.

[62] Z. P. Cano, D. Banham, S. Ye, A. Hintennach, J. Lu, M. Fowler, and Z. Chen, “Batteries and fuel cells for emerging electric vehicle markets,” *Nature Energy*, vol. 3, no. 4, pp. 279–289, 2018.

[63] J. Vetter, P. Novák, M. R. Wagner, C. Veit, K.-C. Möller, J. O. Besenhard, M. Winter, M. Wohlfahrt-Mehrens, C. Vogler, and A. Ham-

mouche, “Ageing mechanisms in lithium-ion batteries,” *Journal of Power Sources*, vol. 147, no. 1, pp. 269–281, 2005.

[64] G. Ning, B. Haran, and B. N. Popov, “Capacity fade study of lithium-ion batteries cycled at high discharge rates,” *Journal of Power Sources*, vol. 117, no. 1, pp. 160–169, 2003.

[65] A. Millner, “Modeling Lithium Ion battery degradation in electric vehicles,” in *2010 IEEE Conference on Innovative Technologies for an Efficient and Reliable Electricity Supply*, 2010, pp. 349–356.

[66] J. Shim, R. Kostecki, T. Richardson, X. Song, and K. A. Striebel, “Electrochemical analysis for cycle performance and capacity fading of a lithium-ion battery cycled at elevated temperature,” *Journal of Power Sources*, vol. 112, no. 1, pp. 222–230, 2002.

[67] S. Tippmann, D. Walper, L. Balboa, B. Spier, and W. G. Bessler, “Low-temperature charging of lithium-ion cells part I: Electrochemical modeling and experimental investigation of degradation behavior,” *Journal of Power Sources*, vol. 252, pp. 305–316, 2014.

[68] H. A. Gabbar, A. M. Othman, and M. R. Abdussami, “Review of Battery Management Systems (BMS) Development and Industrial Standards,” *Technologies*, vol. 9, no. 2, p. 28, 2021.

[69] K. W. E. Cheng, B. P. Divakar, H. Wu, K. Ding, and H. F. Ho, “Battery-Management System (BMS) and SOC Development for Electrical Vehicles,” *IEEE Transactions on Vehicular Technology*, vol. 60, no. 1, pp. 76–88, 2011.

[70] S. F. Schuster, M. J. Brand, P. Berg, M. Gleissenberger, and A. Jossen, “Lithium-ion cell-to-cell variation during battery electric vehicle operation,” *Journal of Power Sources*, vol. 297, pp. 242–251, 2015.

[71] S. Paul, C. Diegelmann, H. Kabza, and W. Tillmetz, “Analysis of ageing inhomogeneities in lithium-ion battery systems,” *Journal of Power Sources*, vol. 239, pp. 642–650, 2013.

[72] F. An, J. Huang, C. Wang, Z. Li, J. Zhang, S. Wang, and P. Li, “Cell sorting for parallel lithium-ion battery systems: Evaluation based on an electric circuit model,” *Journal of Energy Storage*, vol. 6, pp. 195–203, 2016.

[73] I. Zilberman, S. Ludwig, and A. Jossen, “Cell-to-cell variation of calendar aging and reversible self-discharge in 18650 nickel-rich, silicon–graphite lithium-ion cells,” *Journal of Energy Storage*, vol. 26, no. August, p. 100900, 2019.

[74] D. Oeser, A. Ziegler, and A. Ackva, “Single cell analysis of lithium-ion e-bike batteries aged under various conditions,” *Journal of Power Sources*, vol. 397, no. May, pp. 25–31, 2018.

[75] S. W. Moore and P. J. Schneider, “A Review of Cell Equalization Methods for Lithium Ion and Lithium Polymer Battery Systems,” in *SAE 2001 World Congress*. SAE International, 2001.

[76] W. F. Bentley, “Cell balancing considerations for lithium-ion battery systems,” in *The Twelfth Annual Battery Conference on Applications and Advances*, 1997, pp. 223–226.

[77] S. J. Harris, D. J. Harris, and C. Li, “Failure statistics for commercial lithium ion batteries: A study of 24 pouch cells,” *Journal of Power Sources*, vol. 342, pp. 589–597, 2017.

[78] Z. B. Omariba, L. Zhang, and D. Sun, “Review of Battery Cell Balancing Methodologies for Optimizing Battery Pack Performance in Electric Vehicles,” *IEEE Access*, vol. 7, no. February 2017, pp. 129 335–129 352, 2019.

[79] Amin, K. Ismail, A. Nugroho, and S. Kaleg, “Passive balancing battery management system using MOSFET internal resistance as balancing resistor,” *ICSEEA 2017 International Conference on Sustainable Energy Engineering and Application: ”Continuous Improvement of Sustainable Energy for Eco-Mobility”*, pp. 151–155, 2017.

[80] S. D'Arco, L. Piegari, and P. Tricoli, "A modular converter with embedded battery cell balancing for electric vehicles," in *Electrical Systems for Aircraft, Railway and Ship Propulsion, ESARS*. IEEE, 2012, pp. 1–6.

[81] D. V. Cadar, D. M. Petreus, and T. M. Patarau, "An energy converter method for battery cell balancing," in *33rd International Spring Seminar on Electronics Technology, (ISSE)*, 2010, pp. 290–293.

[82] M. Daowd, M. Antoine, N. Omar, P. van den Bossche, and J. van Mierlo, "Single switched capacitor battery balancing system enhancements," *Energies*, vol. 6, no. 4, pp. 2149–2179, 2013.

[83] W. Diao, N. Xue, V. Bhattacharjee, J. Jiang, O. Karabasoglu, and M. Pecht, "Active battery cell equalization based on residual available energy maximization," *Applied Energy*, vol. 210, no. August 2017, pp. 690–698, 2018.

[84] A. M. Imtiaz and F. H. Khan, ""Time shared flyback converter" based regenerative cell balancing technique for series connected li-ion battery strings," *IEEE Transactions on Power Electronics*, vol. 28, no. 12, pp. 5960–5975, 2013.

[85] L. McCurlie, M. Preindl, and A. Emadi, "Fast Model Predictive Control for Redistributive Lithium-Ion Battery Balancing," *IEEE Transactions on Industrial Electronics*, vol. 64, no. 2, pp. 1350–1357, 2017.

[86] V. L. Pham, V. T. Duong, and W. Choi, "A low cost and fast cell-to-cell balancing circuit for lithium-ion battery strings," *Electronics (Switzerland)*, vol. 9, no. 2, p. 248, 2020.

[87] C. Piao, Z. Wang, J. Cao, W. Zhang, and S. Lu, "Lithium-Ion Battery Cell-Balancing Algorithm for Battery Management System Based on Real-Time Outlier Detection," *Mathematical Problems in Engineering*, vol. 2015, pp. 1–13, 2015.

[88] F. Porpora, U. Abronzini, C. Attaianese, M. Di Monaco, and G. Tomasso, "Real time balancing for modular passive battery management system," *PCIM Europe Conference Proceedings*, no. May, pp. 1140–1145, 2019.

[89] H. Ren, Y. Zhao, S. Chen, and T. Wang, "Design and implementation of a battery management system with active charge balance based on the SOC and SOH online estimation," *Energy*, vol. 166, pp. 908–917, 2019.

[90] A. Tavakoli, S. Ali Khajehoddin, and J. Salmon, "Control and Analysis of a Modular Bridge for Battery Cell Voltage Balancing," *IEEE Transactions on Power Electronics*, vol. 33, no. 11, pp. 9722–9733, 2018.

[91] M. M. Ur Rehman, F. Zhang, M. Evzelman, R. Zane, and D. Maksimovic, "Control of a series-input, parallel-output cell balancing system for electric vehicle battery packs," *2015 IEEE 16th Workshop on Control and Modeling for Power Electronics, COMPEL 2015*, pp. 1–7, 2015.

[92] M. M. Ur. Rehman, M. Evzelman, K. Hathaway, R. Zane, G. L. Plett, K. Smith, E. Wood, and D. Maksimovic, "Modular approach for continuous cell-level balancing to improve performance of large battery packs," *2014 IEEE Energy Conversion Congress and Exposition, ECCE 2014*, pp. 4327–4334, 2014.

[93] J. Xu, X. Mei, and J. Wang, "A high power low-cost balancing system for battery strings," *Energy Procedia*, vol. 158, pp. 2948–2953, 2019.

[94] Z. Zhang, L. Zhang, L. Hu, and C. Huang, "Active cell balancing of lithium-ion battery pack based on average state of charge," *International Journal of Energy Research*, vol. 44, no. 4, pp. 2535–2548, 2020.

[95] D. M. Davies, M. G. Verde, O. Mnyshenko, Y. R. Chen, R. Rajeev, Y. S. Meng, and G. Elliott, "Combined economic and technological evaluation of battery energy storage for grid applications," *Nature Energy*, vol. 4, no. 1, pp. 42–50, 2019.

[96] M. Faisal, M. A. Hannan, P. J. Ker, A. Hussain, M. B. Mansor, and F. Blaabjerg, “Review of energy storage system technologies in microgrid applications: Issues and challenges,” *IEEE Access*, vol. 6, pp. 35 143–35 164, 2018.

[97] C. N. Truong, M. Naumann, R. C. Karl, M. Müller, A. Jossen, and H. C. Hesse, “Economics of residential photovoltaic battery systems in Germany: The case of tesla’s powerwall,” *Batteries*, vol. 2, no. 2, pp. 1–17, 2016.

[98] J. A. Sanguesa, V. Torres-Sanz, P. Garrido, F. J. Martinez, and J. M. Marquez-Barja, “A Review on Electric Vehicles: Technologies and Challenges,” *Smart Cities*, vol. 4, no. 1, pp. 372–404, 2021.

[99] T. Earl, L. Mathieu, S. Cornelis, S. Kenny, C. C. Ambel, and J. Nix, “Analysis of long haul battery electric trucks in EU: Marketplace and technology, economic, environmental, and policy perspectives,” *European Federation for Transport and Environment*, no. May, pp. 17–18, 2018. [Online]. Available: https://ec.europa.eu/inea/en/ten-t/ten-t-projects

[100] S. G. Sjøtun, “A ferry making waves: A demonstration project ‘doing’ institutional work in a greening maritime industry,” *Norsk Geografisk Tidsskrift*, vol. 73, no. 1, pp. 16–28, 2019.

[101] C. Marmaras, A. Javed, L. Cipcigan, and O. Rana, “Predicting the energy demand of buildings during triad peaks in GB,” *Energy and Buildings*, vol. 141, pp. 262–273, 2017.

[102] Flextricity, “Why has Flextricity never missed a traid?” 2016. [Online]. Available: https://www.flexitricity.com/more/blog/why-has-flexitricity-never-missed-triad/

[103] H. He, R. Xiong, and J. Fan, “Evaluation of lithium-ion battery equivalent circuit models for state of charge estimation by an experimental approach,” *Energies*, vol. 4, no. 4, pp. 582–598, 2011.

[104] R. Xiong, H. He, F. Sun, X. Liu, and Z. Liu, "Model-based state of charge and peak power capability joint estimation of lithium-ion battery in plug-in hybrid electric vehicles," *Journal of Power Sources*, vol. 229, pp. 159–169, 2013.

[105] C. Burgos-Mellado, M. E. Orchard, M. Kazerani, R. Cárdenas, and D. Sáez, "Particle-filtering-based estimation of maximum available power state in Lithium-Ion batteries," *Applied Energy*, vol. 161, pp. 349–363, 2016.

[106] S. Li, H. He, C. Su, and P. Zhao, "Data driven battery modeling and management method with aging phenomenon considered," *Applied Energy*, vol. 275, no. March, p. 115340, 2020.

[107] A. Purwadi, A. Rizqiawan, A. Kevin, and N. Heryana, "State of charge estimation method for lithium battery using combination of coulomb counting and adaptive system with considering the effect of temperature," *Proceedings - ICPERE 2014: 2nd IEEE Conference on Power Engineering and Renewable Energy 2014*, pp. 91–95, 2014.

[108] Q. Yu, R. Xiong, R. Yang, and M. G. Pecht, "Online capacity estimation for lithium-ion batteries through joint estimation method," *Applied Energy*, vol. 255, no. 5, p. 113817, 2019.

[109] W. Su and M. Y. Chow, "Sensitivity analysis on battery modeling to large-scale PHEV/PEV charging algorithms," *IECON Proceedings (Industrial Electronics Conference)*, pp. 3248–3253, 2011.

[110] S. Thanagasundram, R. Arunachala, K. Makinejad, T. Teutsch, and A. Jossen, "A Cell Level Model for Battery Simulation," *European Electric Vehicle Congress*, no. November, pp. 1–13, 2012.

[111] C. Guenther, J. K. Barillas, S. Stumpp, and M. A. Danzer, "A dynamic battery model for simulation of battery-to-grid applications," *IEEE PES Innovative Smart Grid Technologies Conference Europe*, pp. 1–7, 2012.

[112] C. Hill and D. Chen, “Development of a real-time testing environment for battery energy storage systems in renewable energy applications,” *IEEE Power and Energy Society General Meeting*, pp. 1–8, 2011.

[113] M. Mathew, S. Janhunen, M. Rashid, F. Long, and M. Fowler, “Comparative analysis of lithium-ion battery resistance estimation techniques for battery management systems,” *Energies*, vol. 11, no. 6, p. 1490, 2018.

[114] M. Sitterly, L. Y. Wang, G. G. Yin, and C. Wang, “Enhanced identification of battery models for real-time battery management,” *IEEE Transactions on Sustainable Energy*, vol. 2, no. 3, pp. 300–308, 2011.

[115] F. Baronti, R. Di Rienzo, N. Papazafiropulos, R. Roncella, and R. Saletti, “Investigation of series-parallel connections of multi-module batteries for electrified vehicles,” *2014 IEEE International Electric Vehicle Conference, IEVC 2014*, pp. 1–7, 2014.

[116] C. Sen and N. C. Kar, “Battery pack modeling for the analysis of battery management system of a hybrid electric vehicle,” *5th IEEE Vehicle Power and Propulsion Conference, VPPC ’09*, pp. 207–212, 2009.

[117] M. Mathew, Q. H. Kong, J. McGrory, and M. Fowler, “Simulation of lithium ion battery replacement in a battery pack for application in electric vehicles,” *Journal of Power Sources*, vol. 349, pp. 94–104, 2017.

[118] T. L. Fantham and D. T. Gladwin, “An overview of safety for laboratory testing of lithium-ion batteries,” *Energy Reports*, vol. 7, pp. 2–8, 2021.

[119] P. V. Brogan, R. Best, J. Morrow, R. Duncan, and M. Kubik, “Stacking battery energy storage revenues with enhanced service provision,” *IET Smart Grid*, vol. 3, no. 4, pp. 520–529, 2020.

[120] G. House, "Gresham House Energy Storage Fund plc. Annual Report 2020," 2020. [Online]. Available: https://greshamhouse.com/wp-content/uploads/2021/04/Gresham-House-Energy-Storage-Fund-plc-Annual-Report-2020-1820-27.4.21.pdf

[121] M. Ye, X. Song, R. Xiong, and F. Sun, "A Novel Dynamic Performance Analysis and Evaluation Model of Series-Parallel Connected Battery Pack for Electric Vehicles," *IEEE Access*, vol. 7, pp. 14 256–14 265, 2019.

[122] R. Xiong, F. Sun, and H. He, "State-of-charge estimation of lithium-ion batteries in electric vehicles based on an adaptive extended Kalman filter," *Gaojishu Tongxin/Chinese High Technology Letters*, vol. 22, no. 2, pp. 198–204, 2012.

[123] X. Zeng, M. Li, D. Abd El-Hady, W. Alshitari, A. S. Al-Bogami, J. Lu, and K. Amine, "Commercialization of Lithium Battery Technologies for Electric Vehicles," *Advanced Energy Materials*, vol. 9, no. 27, pp. 1–25, 2019.

[124] C. Pastor-Fernández, W. Widanage, G. Chouchelamane, and J. Marco, "A SoH Diagnosis and Prognosis Method to Identify and Quantify Degradation Modes in Li-ion Batteries using the IC/DV technique," *6th Hybrid and Electric Vehicles Conference (HEVC 2016)*, no. 1, pp. 1–6, 2017.

[125] A. Barai, K. Uddin, W. D. Widanage, A. McGordon, and P. Jennings, "A study of the influence of measurement timescale on internal resistance characterisation methodologies for lithium-ion cells," *Scientific Reports*, vol. 8, no. 1, pp. 1–13, 2018.

[126] H. He, R. Xiong, H. Guo, and S. Li, "Comparison study on the battery models used for the energy management of batteries in electric vehicles," *Energy Conversion and Management*, vol. 64, pp. 113–121, 2012.

[127] N. S. Zhai, M. W. Li, W. L. Wang, D. L. Zhang, and D. G. Xu, "The application of the EIS in Li-ion batteries measurement," *Journal of Physics: Conference Series*, vol. 48, no. 1, pp. 1157–1161, 2006.

[128] S. S. Zhang, K. Xu, and T. R. Jow, "EIS study on the formation of solid electrolyte interface in Li-ion battery," *Electrochimica Acta*, vol. 51, no. 8-9, pp. 1636–1640, 2006.

[129] Z. Xia and J. A. Abu Qahouq, "State of Health Estimation of Lithium-Ion Batteries Using Neuron Network and 1kHz Impedance Data," *ECCE 2020 - IEEE Energy Conversion Congress and Exposition*, pp. 1968–1972, 2020.

[130] W. Waag, S. Käbitz, and D. U. Sauer, "Experimental investigation of the lithium-ion battery impedance characteristic at various conditions and aging states and its influence on the application," *Applied Energy*, vol. 102, pp. 885–897, 2013.

[131] J. C. Burns, G. Jain, A. J. Smith, K. W. Eberman, E. Scott, J. P. Gardner, and J. R. Dahn, "Evaluation of Effects of Additives in Wound Li-Ion Cells Through High Precision Coulometry," *Journal of The Electrochemical Society*, vol. 158, no. 3, p. A255, 2011.

[132] X. Ni, Y. He, and H. Wang, "Expanding the metrology of Coulombic efficiency using neutron depth profiling," *Radiation Effects and Defects in Solids*, vol. 175, no. 3-4, pp. 356–366, 2020.

[133] F. Yang, D. Wang, Y. Zhao, K. L. Tsui, and S. J. Bae, "A study of the relationship between coulombic efficiency and capacity degradation of commercial lithium-ion batteries," *Energy*, vol. 145, pp. 486–495, 2018.

[134] E. Namor, D. Torregrossa, F. Sossan, R. Cherkaoui, and M. Paolone, "Assessment of battery ageing and implementation of an ageing aware control strategy for a load leveling application of a lithium titanate battery energy storage system," *2016 IEEE 17th Workshop on Control and Modeling for Power Electronics, COMPEL 2016*, pp. 1–6, 2016.

[135] X. Tan, Y. Wu, and D. H. Tsang, “A Stochastic Shortest Path Framework for Quantifying the Value and Lifetime of Battery Energy Storage under Dynamic Pricing,” *IEEE Transactions on Smart Grid*, vol. 8, no. 2, pp. 769–778, 2017.

[136] J. D. Bishop, C. J. Axon, D. Bonilla, M. Tran, D. Banister, and M. D. McCulloch, “Evaluating the impact of V2G services on the degradation of batteries in PHEV and EV,” *Applied Energy*, vol. 111, pp. 206–218, 2013.

[137] S. S. Lee, T. H. Kim, S. J. Hu, W. W. Cai, and J. A. Abell, “Joining technologies for automotive lithium-ion battery manufacturing - A review,” *ASME 2010 International Manufacturing Science and Engineering Conference, MSEC 2010*, vol. 1, pp. 541–549, 2010.

[138] Z. Zhang, X. Cheng, Z. Y. Lu, and D. J. Gu, “SOC Estimation of Lithium-Ion Battery Pack Considering Balancing Current,” *IEEE Transactions on Power Electronics*, vol. 33, no. 3, pp. 2216–2226, 2018.

[139] H. Dai, X. Zhang, X. Wei, Z. Sun, J. Wang, and F. Hu, “Cell-BMS validation with a hardware-in-the-loop simulation of lithium-ion battery cells for electric vehicles,” *International Journal of Electrical Power and Energy Systems*, vol. 52, no. 1, pp. 174–184, 2013.

[140] R. Jackey, M. Saginaw, P. Sanghvi, J. Gazzarri, T. Huria, and M. Ceraolo, “Battery model parameter estimation using a layered technique: An example using a lithium iron phosphate cell,” *SAE Technical Papers*, vol. 2, no. April 2015, pp. 1–14, 2013.

[141] V. H. Johnson, A. a. Pesaran, and B. Court, “Temperature-Dependent Battery Models for High-Power Lithium-Ion Batteries,” *Power*, no. January, pp. 1–15, 2000. [Online]. Available: http://www.nrel.gov/vehiclesandfuels/energystorage/pdfs/evs17paper2.pdf

[142] M. Dubarry, A. Devie, and B. Y. Liaw, “Cell-balancing currents in parallel strings of a battery system,” *Journal of Power Sources*, vol. 321, pp. 36–46, 2016.

[143] J. R. Belt, C. D. Ho, T. J. Miller, M. A. Habib, and T. Q. Duong, “The effect of temperature on capacity and power in cycled lithium ion batteries,” *Journal of Power Sources*, vol. 142, no. 1-2, pp. 354–360, 2005.

[144] L. Ran, W. Junfeng, W. Haiying, and L. Gechen, “Prediction of state of charge of Lithium-ion rechargeable battery with electrochemical impedance spectroscopy theory,” in *2010 5th IEEE Conference on Industrial Electronics and Applications*, jun 2010, pp. 684–688.

[145] P. Liu, J. Wang, J. Hicks-Garner, E. Sherman, S. Soukiazian, M. Verbrugge, H. Tataria, J. Musser, and P. Finamore, “Aging Mechanisms of LiFePO4 Batteries Deduced by Electrochemical and Structural Analyses,” *Journal of The Electrochemical Society*, vol. 157, no. 4, p. A499, 2010.

[146] S. Panchal, J. Mcgrory, J. Kong, R. Fraser, M. Fowler, I. Dincer, and M. Agelin-Chaab, “Cycling degradation testing and analysis of a LiFePO4 battery at actual conditions,” *International Journal of Energy Research*, vol. 41, no. 15, pp. 2565–2575, 2017.

[147] Y. Huang, Y. Li, L. Jiang, X. Qiao, Y. Cao, and J. Yu, “Research on Fitting Strategy in HPPC Test for Li-ion battery,” *iSPEC 2019 - 2019 IEEE Sustainable Power and Energy Conference: Grid Modernization for Energy Revolution, Proceedings*, pp. 1776–1780, 2019.

[148] P. Keil, S. F. Schuster, J. Wilhelm, J. Travi, A. Hauser, R. C. Karl, and A. Jossen, “Calendar Aging of Lithium-Ion Batteries,” *Journal of The Electrochemical Society*, vol. 163, no. 9, pp. A1872–A1880, 2016.

[149] M. J. Brand, S. F. Schuster, T. Bach, E. Fleder, M. Stelz, S. Gläser, J. Müller, G. Sextl, and A. Jossen, “Effects of vibrations and shocks on lithium-ion cells,” *Journal of Power Sources*, vol. 288, pp. 62–69, 2015.

[150] M. J. Brand, M. H. Hofmann, S. S. Schuster, P. Keil, and A. Jossen, “The Influence of Current Ripples on the Lifetime of Lithium-Ion Batteries,” *IEEE Transactions on Vehicular Technology*, vol. 67, no. 11, pp. 10 438–10 445, 2018.

[151] A. R. Mandli, A. Kaushik, R. S. Patil, A. Naha, K. S. Hariharan, S. M. Kolake, S. Han, and W. Choi, “Analysis of the effect of resistance increase on the capacity fade of lithium ion batteries,” *International Journal of Energy Research*, vol. 43, no. 6, pp. 2044–2056, 2019.

[152] A. Farmann, W. Waag, A. Marongiu, and D. U. Sauer, “Critical review of on-board capacity estimation techniques for lithium-ion batteries in electric and hybrid electric vehicles,” *Journal of Power Sources*, vol. 281, pp. 114–130, 2015.

[153] M. Einhorn, F. V. Conte, C. Kral, and J. Fleig, “A method for online capacity estimation of lithium ion battery cells using the state of charge and the transferred charge,” *IEEE Transactions on Industry Applications*, vol. 48, no. 2, pp. 736–741, 2012.

[154] H. P. Beelen, L. H. Raijmakers, M. C. Donkers, P. H. Notten, and H. J. Bergveld, “A comparison and accuracy analysis of impedance-based temperature estimation methods for Li-ion batteries,” *Applied Energy*, vol. 175, pp. 128–140, 2016.

[155] R. R. Richardson and D. A. Howey, “Sensorless Battery Internal Temperature Estimation Using a Kalman Filter with Impedance Measurement,” *IEEE Transactions on Sustainable Energy*, vol. 6, no. 4, pp. 1190–1199, 2015.

[156] A. Senyshyn, M. J. Mühlbauer, O. Dolotko, and H. Ehrenberg, “Low-temperature performance of Li-ion batteries: The behavior of lithiated graphite,” *Journal of Power Sources*, vol. 282, pp. 235–240, 2015.

[157] F. Hall, J. Touzri, S. Wußler, H. Buqa, and W. G. Bessler, “Experimental investigation of the thermal and cycling behavior of a lithium

titanate-based lithium-ion pouch cell," *Journal of Energy Storage*, vol. 17, pp. 109–117, 2018.

[158] B. Gyenes, D. A. Stevens, V. L. Chevrier, and J. R. Dahn, "Understanding Anomalous Behavior in Coulombic Efficiency Measurements on Li-Ion Batteries," *Journal of The Electrochemical Society*, vol. 162, no. 3, pp. A278–A283, 2015.

[159] X. Lin, H. E. Perez, S. Mohan, J. B. Siegel, A. G. Stefanopoulou, Y. Ding, and M. P. Castanier, "A lumped-parameter electro-thermal model for cylindrical batteries," *Journal of Power Sources*, vol. 257, pp. 12–20, 2014.

[160] S. M. Islam and S. Y. Park, "Quantification of heat loss for different charging profiles in a Li-Ion Battery," *IEEE Transactions on Energy Conversion*, vol. 36, no. 3, pp. 1831–1840, 2020.

[161] J. P. Schmidt, A. Weber, and E. Ivers-Tiffée, "A novel and precise measuring method for the entropy of lithium-ion cells: Δs via electrothermal impedance spectroscopy," *Electrochimica Acta*, vol. 137, pp. 311–319, 2014.

[162] N. Damay, C. Forgez, M. P. Bichat, and G. Friedrich, "Thermal modeling of large prismatic LiFePO4/graphite battery. Coupled thermal and heat generation models for characterization and simulation," *Journal of Power Sources*, vol. 283, pp. 37–45, 2015.

[163] Z. Wang, D. T. Gladwin, M. J. Smith, and S. Haass, "Practical state estimation using Kalman filter methods for large-scale battery systems," *Applied Energy*, vol. 294, no. April, p. 117022, 2021.

[164] L. Pelletier, F. A. Lebel, C. H. Antunes, and J. P. F. Trovao, "Sizing of a battery pack based on series/parallel configurations for a high-power electric vehicle as a constrained optimization problem," *IEEE Transactions on Vehicular Technology*, vol. 69, no. 12, pp. 14 150–14 159, 2020.

[165] M. Fernandez-Montoya, A. Arias-Rosales, O.-G. Gilberto, and R. Mejia-Gutierrez, "Nominal energy optimisation method of constrained battery packs through the iteration of the series-parallel topology," *International Journal of Energy Research*, vol. 41, pp. 1709–1729, 2012.

[166] B. Xu, A. Oudalov, A. Ulbig, G. Andersson, and D. S. Kirschen, "Modeling of lithium-ion battery degradation for cell life assessment," *IEEE Transactions on Smart Grid*, vol. 9, no. 2, pp. 1131–1140, 2018.

[167] W. Diao, Y. Xing, S. Saxena, and M. Pecht, "Evaluation of present accelerated temperature testing and modeling of batteries," *Applied Sciences (Switzerland)*, vol. 8, no. 10, pp. 1–10, 2018.